UNIVERSITY OF OKLAHOMA

GRADUATE COLLEGE

TEMPERATURE-INDUCED SPECTRAL ARTIFACTS IN FOURIER TRANSFORM INFRARED (FTIR) SPECTROSCOPY. OPTIMIZATION OF VARIABLE TEMPERATURE DIFFUSE REFLECTION FTIR SPECTROSCOPY INSTRUMENTATION

A DISSERTATION

SUBMITTED TO THE GRADUATE FACULTY

in partial fulfillment of the requirements for the

Degree of

DOCTOR OF PHILOSOPHY

By

DALIA KAZEVNA MARAOULAITE
Norman, Oklahoma
2016

TEMPERATURE-INDUCED SPECTRAL ARTIFACTS IN FOURIER TRANSFORM INFRARED (FTIR) SPECTROSCOPY. OPTIMIZATION OF VARIABLE TEMPERATURE DIFFUSE REFLECTION FTIR SPECTROSCOPY INSTRUMENTATION

A DISSERTATION APPROVED FOR THE
DEPARTMENT OF CHEMISTRY AND BIOCHEMISTRY

BY

_____
Dr. Robert L. White, Chair

_____
Dr. Wai Tak Yip

_____
Dr. Shaorong Liu

_____
Dr. Charles V. Rice

_____
Dr. Mark A. Nanny

I would like to dedicate this work to my parents, Olga Maraoulene and Kazis Maraoulas, who raised me with love and discipline, taught me independence and responsibility, set the bar high, and worked hard to provide for me and my brother the opportunities for growth and achievement. I miss you both and I thank you for my adventurous life and the strength you give me.

Acknowledgements

I would like to thank my advisor, Dr. Robert White, for his invaluable mentorship, expertise, constructive criticism, all his help, and perhaps most importantly, his patience and kindness. I deeply respect Dr. White's research tactics and ethics and am truly grateful to have had the opportunity to be a part of his research team. I would like to thank all those who served on my graduate committee over the years: Dr. Wai Tak Yip, Dr. Shaorong Liu, Dr. Mark Nanny, Dr. Charles Rice, Dr. Friederike Jentoft, and Dr. LeRoy Blank, for the support and guidance through the grueling graduate school experience. Your dedication to the success of the students is evident, and I want to thank you for your efforts dedicated to preparing us for the professional environment and productive careers in science. I would also like to thank Dr. Audrey L. Ingram, Dr. Tara M. Nickels, and Dr. Katie Foster for stimulating discussion, help in research and writing, and camaraderie on this journey.

I would like to thank my family, especially my grandmother Svetlana Pimenova, a wise lady whose strength and determination have been truly encouraging, and whose help has been invaluable. I would like to thank my closest friends, Olga Hayes (Verbovaya), Lyubov Frankevich, and Dr. Deann Gattis, whose words of encouragement have kept me going to the finish line. May your life be full of good for all the good you do.

Table of Contents

List of Tables

List of Figures

Abstract

High stability Fourier transform infrared (FT-IR) interferometers make it possible to conduct experiments designed to identify subtle sample structure changes resulting from external perturbations. In particular, variable temperature diffuse reflection infrared Fourier transform spectroscopy (VT-DRIFTS) can be used to associate specific structure changes with incremental additions of thermal energy by observing the sample *in-situ* while heating, eliminating the need for separate measurements that can introduce error. This fast, low cost spectroscopic technique requires a small sample and little preparation, but is complicated by the fact that when the sample is heated, the system is also perturbed rendering the data difficult to interpret due to so-called "thermal artifacts." Until now little has been done to understand the effect of thermal fluctuations on IR spectra due to instrument response. In this study a thorough characterization of the VT-DRIFTS system led to the identification of the key sources of spectral changes, minimization of thermal artifacts, and development of a data processing method. Experimental studies have shown that the main causes of temperature-induced artifacts are thermal expansion-related alignment changes in the optical transmission system, especially near the sample holder and the interferometer, and modulated and unmodulated thermal emission from the sample itself and instrument components, which affect the detector response at high temperatures. Incorporating thermal barriers and redesigning the sample holder to incorporate quartz has decreased temperature-induced alignment changes. Incorporating cube-corner mirrors at the interferometer and blocking 1/2 the IR beam between the interferometer and the sample solves the modulated thermal emission problem by the method of

destructive interference of the noise waives. Unmodulated emission (basically, excess heat) can be accounted for by scaling the data post-collection using computational macros. Thus, the effects of temperature on IR spectra have been characterized, and solutions have been proposed for variable temperature instrument optimization. Capabilities of the VT-DRIFTS methodology are demonstrated in this work.

Chapter 1: Introduction

1.1 Spectrochemical Analysis

In science the ability to measure properties of matter indirectly based on the interaction of radiant energy with physical matter is of utmost importance. A number of analytical techniques rely on the properties of interaction of electromagnetic radiation with a sample, and they are collectively known as Spectrochemical methods of analysis. These systems employ a source of electromagnetic energy, an optical system to deliver and capture electromagnetic waves, a detector, and a means of placing the sample in the path of the electromagnetic radiation beam.

1.1.1 Spectral Range

The wavelength (or frequency) of electromagnetic radiation is one factor that determines the type of information obtained during Spectrochemical analysis. For example, X-ray diffraction can be used to measure interatomic distances in a crystal to determine its structure, or its identity based on comparisons with previously published data; near infrared (near-IR) spectroscopy can be used to detect overtone and combination vibrations for qualitative and quantitative analysis of organic and inorganic molecules; ultraviolet-visible (UV-vis) spectroscopy measures electron transitions from ground energy states to excited states; gamma-ray spectroscopy provides information

regarding gamma-emitters in the sample; and mid infrared (mid-IR) spectroscopy measures absorption of radiation resulting in changes to molecular rotations and fundamental vibrations, providing insight into the identity of the species present, their amounts, and their chemical environments.

Above absolute zero temperature, all atoms in molecules experience a periodic motion known as a "molecular vibration." These vibrations depend on the mass of the atoms and their interactions with other atoms in the molecule and the local environment. Infrared electromagnetic radiation wavelengths extend from the nominal red edge of the visible spectrum at 700 nm to about 1 mm (a frequency range from ~430 THz to ~300 GHz), and includes most of the thermal radiation emitted by objects near room temperature due to molecular vibrations. For mid-IR spectroscopy, the instrument range is typically 484 to 4033 cm^{-1}.[1]

Infrared radiation is emitted or absorbed by molecules when they change rotational-vibrational energy states. Thus, determining the vibrational spectrum of a material can provide information about molecular bonding, which can aid in determining structure and composition.

1.1.2 Samples for Spectrochemical Analysis

The physical form of the sample is another factor to consider when choosing a spectroscopic analysis method, because it determines the most appropriate type of measurement technique. Gasses can be analyzed in sealed cells or flow cells, liquids can be held in transparent cuvettes or flow cells, and solids are generally analyzed in

pellet, film, crystal, or powder forms. The optical systems used for analyses are dictated by the type of sample holder employed.

The mode of interaction between electromagnetic radiation energy and sample also varies with spectroscopic techniques. In emission spectroscopy, electromagnetic radiation is emitted from excited samples as they return to ground state energies. In elastic scattering spectroscopy, the sample reflects the radiation beam, causing it to deviate from its original path, providing information regarding the morphology of the sample. In absorption spectroscopy, radiation irradiates the sample and some wavelengths are absorbed. The wavelength and amount of absorbed radiation are related to the identity and concentration of particular sample components. Transmission spectroscopy is most suitable for solutions and gaseous mixtures; attenuated total reflection spectroscopy is used for samples with negligible transmittance and reflectance properties, such as organic solids; and reflection spectroscopy (diffuse and specular) is employed to analyze the composition of powders and rough surfaces.

1.1.3 Diffuse Reflection Fourier Transform Infrared Spectroscopy (DRIFTS)

Diffuse reflection infrared Fourier transform spectroscopy (DRIFTS) is used to analyze powder samples or rough surfaces by irradiating them with infrared radiation. Diffusely reflected radiation is collected, and absorption band wavenumber and intensity provides qualitative and quantitative information about the solid sample.

In general, infrared spectroscopy is used to observe molecular vibrations. Variable temperature diffuse reflection infrared Fourier transform spectroscopy (VT-DRIFTS) is a method used for analysis of solid samples in powder form that requires

little sample preparation. [2] VT-DRIFTS represents a unique approach to thermal analysis, and can be used to monitor real-time changes in chemical interactions between sample constituents and their environments.[3-12]

Diffuse reflection FTIR spectroscopy has been used for qualitative analyses (when absorption band frequencies are used to identify sample constituents), quantitative analysis (when absorption band intensities are correlated with the concentrations of various sample components),[13] and for structural analysis (when absorption band frequencies provide information regarding chemical bonding in the sample).[7, 9-12, 14] In conjunction with thermogravimetry (TG) and differential scanning calorimetry (DSC), VT-DRIFTS can be used for temperature-dependent structural characterizations of solid samples,[3, 4, 15] whereas TG combined with mass spectrometry (TG-MS) provides complementary structural information regarding evolved products.[6, 8] VT-DRIFTS has been employed to study water desorption and readsorption,[10, 16] thermal decomposition processes,[17] and solid state chemical reactions.[7, 8] In addition, quantitative VT-DRIFTS analyses have been used to determine chemical reaction activation energies.[3] VT-DRIFTS in combination with TG-MS has been used in our research group to study the interactions of clays with benzoic acid, salicylic acid, and acetylsalicylic acid by observing dehydration processes, and thermal desorption mechanisms of various organic compounds adsorbed on clays. [2, 10-12, 18]

1.2 Theory of DRIFTS

1.2.1 Kubelka-Munk Theory of Diffuse Reflection

Due to the fact that powders are inhomogeneous on the scale of light wavelengths, every diffuse reflectance spectrum depends not only on the properties that govern interactions between light and matter, but also the scattering characteristics of the specific sample.[19] This makes the diffuse reflection light-sample interaction model complex, and, of the many diffuse reflection theories, the Kubelka-Munk description is the most widely accepted.

Diffuse reflection theory can be described by comparisons to the theory of absorbance. In absorbance, radiation intensity decreases exponentially as a function of the distance that light travels through a sample. A constant fraction of radiation is absorbed after each infinitesimal step through the sample. Thus, longer radiation travel distances to a particular sample location result in smaller amounts of light reaching that point, and thus, less radiation is available to be absorbed or transmitted from that point forward.

The same is true for scattering. As the beam penetrates into the sample, it is scattered at the first grain boundary that it encounters. Thus, like absorption, only a fraction of the incident radiation continues to travel along the same path, and the intensity of radiation available for scattering at the next grain boundary becomes smaller. The rate of change of the intensity of scattered radiation at point x along the beam path is a negative function of the incident radiation that made it to point x.[19]

$$dI_s(x) / dx = -I(x) \tag{1.1}$$

At the interface between two transparent media, incident radiation will be partially transmitted and partially reflected. The relative intensities of the reflected and transmitted beams will depend on the refractive indices of the two transparent media and the angle of incidence.

The angle of refraction for the transmitted portion of the beam can be calculated by Snell's law:[20]

$$n_1 \sin \theta = n_2 \sin \varphi \tag{1.2}$$

where n_1 and n_2 are the refractive indices of the two media, θ is the angle of incidence, and φ is the angle of refraction.

The incident beam is characterized by the amplitude of the perpendicular component (perpendicularly polarized radiation, i.e. transverse electric, s (senkrecht) waves, wherein the electric field oscillates in the direction perpendicular to the plane of incidence) and the parallel component (parallel polarized radiation, i.e. transverse magnetic or p (parallel) waves), wherein the electric field oscillates in the direction parallel to the plane of incidence.

Because the angle of refraction is related to the refractive indices of the media, the amplitude of the reflected portion of the beam can be calculated from the angle of incidence and angle of refraction by Fresnel equations for the parallel and perpendicular components of the beam:

$$r_s = -(\sin(\varphi - \theta)/\sin(\varphi + \theta)) \tag{1.3}$$

for the perpendicular component, and

$$r_p = \tan(\varphi - \theta)/\tan(\varphi + \theta) \tag{1.4}$$

for the parallel component.

The Kubelka-Munk theory requires that the particle size is much smaller than the sample thickness, and that the absorbing and scattering media are uniformly distributed throughout the sample. After incident radiation penetrates into the sample, it is scattered at many points, indicating changes in direction of the radiation and an increase in its path length through the sample. The Kubelka-Munk theory results in a mathematical relationship between the scattering and absorption coefficients of the sample and the reflectance of the sample:

$$k/s = (1 - R)^2/(2R), \tag{1.5}$$

where k is sample absorption coefficient, s is the sample scattering coefficient, and R is the sample reflectance. Note that as the k/s ratio approaches zero, reflectance (R) tends towards unity, suggesting high sensitivity discrimination of diffuse reflection for weak absorbers.[19]

A fine powder is made up of small particles of solids. Each particle has many edges, creating localized non-uniformities throughout the sample that deflect the incident beam, causing scattering. Radiation reflected back at an angle equal to the incident angle is specularly reflected. In this case, the beam does not penetrate into the sample and thus the reflected beam does not contain any absorption information about the sample. In contrast, diffusely reflected radiation penetrates individual particles. Therefore it contains qualitative and quantitative information about the sample.

1.2.2 Derivation of the Kubelka-Munk Theory of Diffuse Reflection

The importance of the Kubelka-Munk theory is in the ability to extract *quantitative* information about a sample from reflectance data. For comparison, quantitative absorption spectroscopy relies on the use of Beer's Law,

$$\alpha(T,\lambda) = abC \tag{1.6}$$

which states that absorbance of electromagnetic radiation by a chemical species is directly proportional to sample absorptivity (a), the beam path length through the sample (b), and the absorber concentration (C). For powder samples and rough surfaces, the beam path is not straight due to multiple reflections in random directions.

After interacting with a rough surface or powder solid sample, the beam is scattered at multiple grain boundaries, and the beam path length for different packets of radiation interacting with the sample varies, depending on sample characteristics. Although absorption band information can be determined by comparing incident beam intensity (I_{IN}) with the reflected beam intensity (I_R) by the I_R/I_{IN} ratio, extracting quantitative information regarding concentrations of absorbing species is more complex for diffusely scattering samples.

The Kubelka-Munk function:

$$f\big(R_\infty(\lambda)\big) = \frac{k(\lambda)}{s(\lambda)} = \frac{2.303a(\lambda)C}{s(\lambda)} = \frac{\big(1-R_\infty(\lambda)\big)^2}{2R_\infty(\lambda)} \tag{1.7}$$

relates absolute reflectance ($R_\infty(\lambda)$) to absorber concentration (C). In equation (1.7), the absorbance coefficient $k(\lambda)$ can be derived from $2.303a(\lambda)C$, where $a(\lambda)$ is the absorptivity of the sample, and C is its concentration.[21-23]

Originally developed for the analysis of paint films,[24] the Kubelka-Munk theory is one of several approximation models that relate sample concentration to

sample reflection properties.[19] Although all models provide approximations of diffuse scattering theory, the Kubelka-Munk model is the most widely accepted and has been applied to the analysis of various sample types, including: paints, powders, papers, and textiles.[3, 6, 7, 9-11, 19, 23, 25-28]

The complexity of diffuse reflectance stems from the fact that powders are not homogeneous on a scale comparable to the wavelength of radiation. Scattering is affected by particle size, and radiation scatters from multiple points inside the sample. So, diffusely reflected radiation intensity depends not only on the properties that govern the interactions between light and matter, but also on the characteristics of the particular sample (e.g. particle size).

Due to the inherent complexity of the problem, diffuse reflection theories rely on a number of assumptions. The main assumptions are that the thickness of the sample layer probed by radiation is very small, and that the thickness of the sample is infinitely greater than the radiation penetration distance.[24] This is applicable to powders because only the surface and near-surface layers of the sample are exposed to the incident beam. The particles in the region exposed to radiation must be much smaller than the thickness of the radiation penetration distance. Both the absorbing and scattering media must be uniformly distributed through this region. The Kubelka-Munk theory is based on the assumption that incident radiation consists of diffuse monochromatic light, and that all detected radiation results from diffuse reflectance. The theory works best when samples reflect most of the incident radiation (i.e. >50%).

The Kubelka-Munk theory describes diffusely reflected radiation as the intensity of light propagating through an inhomogeneous medium of randomly oriented particles

as a consequence of grain boundary reflections. The phase angles of scattered electromagnetic waves sum to a time average of zero, so diffuse reflectance can be characterized by the intensity of the scattered light, thereby rendering the path of the beam irrelevant to the derivation. The intensity of radiation travelling both downward and upward within a sample represents the total intensity reflected, refracted, and diffracted.[24] The amount of radiation scattered (I_s) is proportional to the incident radiation intensity (I) multiplied by the scattering coefficient s

$$I_s \propto sI \tag{1.8}$$

$$\frac{dI_s(x)}{dx} = -I(x) \tag{1.9}$$

This equation is analogous to the absorption law:

$$\frac{dI_{abs}(x)}{dx} = -I(x) \tag{1.10}$$

However, there is an important difference: incident radiation decreases at each interface where radiation is absorbed, but scattered radiation does not "disappear". Instead, it continues within the sample medium when it reflects at interface boundaries. Thus, the total intensity of scattered radiation decreases only because of radiation absorption.

The following derivation is an adaptation from Milosevic, et al. [19], which was based on the original Kubelka and Munk publication.[24] First, we define the following variables:

k absorption coefficient,

s scattering coefficient,

I_+ radiation travelling downward ("transmitted"),

I_- radiation travelling upward ("reflected"),

x coordinate along the beam path at a specific depth.

By scattering in various directions, the effective path length of the beam increases. In a semi-infinite sample illuminated from above, there are two general beam components: $I_+(x)$ propagating downward and $I_-(x)$ propagating upward. The intensities of these two components can be expressed in terms of the sample absorption coefficient (k) and the sample scattering coefficient (s).

As radiation travels into a sample, and as it is reflected back towards the incident beam, intensity decreases due to absorption and scattering, which is represented by the first terms in equations (1.11) and (1.12). However, scattered radiation remains within the sample and simply changes direction, contributing to an increase in intensity of the beam travelling in the opposite direction.

$$\frac{dI_+(x)}{dx} = -(k+s)I_+(x) + sI_-(x) \tag{1.11}$$

$$\frac{dI_-(x)}{dx} = -(k+s)I_-(x) - sI_+(x) \tag{1.12}$$

The reversal of the sign in equation (1.12) is due to the opposite direction of travel of reflected radiation.

The total intensity can be expressed as a single first order differential equation with a constant coefficient ($\boldsymbol{A}$):

$$\frac{d}{dz}\begin{pmatrix} I_+ \\ I_- \end{pmatrix} = \begin{pmatrix} -(k+s) & s \\ -s & (k+s) \end{pmatrix}\begin{pmatrix} I_+ \\ I_- \end{pmatrix} = \boldsymbol{A}\begin{pmatrix} I_+ \\ I_- \end{pmatrix} \tag{1.13}$$

The solution is

$$I(x) = e^{\boldsymbol{A}x}I(0) \tag{1.14}$$

$$\boldsymbol{A}x = -(k+s)x\begin{pmatrix} 1 & 0 \\ 0 & -1 \end{pmatrix} + sx\begin{pmatrix} 0 & 1 \\ -1 & 0 \end{pmatrix} \tag{1.15}$$

thus,

$$e^{\boldsymbol{A}x} = \begin{pmatrix} cosh\sqrt{\frac{k}{s}\left(\frac{k}{s}+2\right)}\,sx - \frac{\frac{k}{s}+1}{\sqrt{\frac{k}{s}\left(\frac{k}{s}+2\right)}}sinh\sqrt{\frac{k}{s}\left(\frac{k}{s}+2\right)}\,sx & \frac{1}{\sqrt{\frac{k}{s}\left(\frac{k}{s}+2\right)}}sinh\sqrt{\frac{k}{s}\left(\frac{k}{s}+2\right)}\,sx \\ -\frac{1}{\sqrt{\frac{k}{s}\left(\frac{k}{s}+2\right)}}sinh\sqrt{\frac{k}{s}\left(\frac{k}{s}+2\right)}\,sx & cosh\sqrt{\frac{k}{s}\left(\frac{k}{s}+2\right)}\,sx + \frac{\frac{k}{s}+1}{\sqrt{\frac{k}{s}\left(\frac{k}{s}+2\right)}}sinh\sqrt{\frac{k}{s}\left(\frac{k}{s}+2\right)}\,sx \end{pmatrix} \tag{1.16}$$

or,

$$e^{\boldsymbol{A}x} = \begin{pmatrix} a_{11} & a_{12} \\ a_{21} & a_{22} \end{pmatrix} \tag{1.17}$$

where

$$a_{11} = cosh\sqrt{\frac{k}{s}\left(\frac{k}{s}+2\right)}\,sx - \frac{\frac{k}{s}+1}{\sqrt{\frac{k}{s}\left(\frac{k}{s}+2\right)}}sinh\sqrt{\frac{k}{s}\left(\frac{k}{s}+2\right)}\,sx \tag{1.18}$$

$$a_{12} = \frac{1}{\sqrt{\frac{k}{s}\left(\frac{k}{s}+2\right)}}sinh\sqrt{\frac{k}{s}\left(\frac{k}{s}+2\right)}\,sx \tag{1.19}$$

$$a_{21} = -\frac{1}{\sqrt{\frac{k}{s}\left(\frac{k}{s}+2\right)}}sinh\sqrt{\frac{k}{s}\left(\frac{k}{s}+2\right)}\,sx \tag{1.20}$$

$$a_{22} = cosh\sqrt{\frac{k}{s}\left(\frac{k}{s}+2\right)}\,sx + \frac{\frac{k}{s}+1}{\sqrt{\frac{k}{s}\left(\frac{k}{s}+2\right)}}sinh\sqrt{\frac{k}{s}\left(\frac{k}{s}+2\right)}\,sx \tag{1.21}$$

For a sample of thickness t we can rewrite equation (1.13) as

$$\begin{pmatrix} I_t \\ 0 \end{pmatrix} = \boldsymbol{A}\begin{pmatrix} I_{IN} \\ I_R \end{pmatrix} \tag{1.22}$$

and redefine the upward and downward components to represent radiation intensity incident on the sample (I_{IN}), radiation intensity transmitted (I_T) through the sample of thickness (t), and radiation intensity reflected (I_R) as

$$I_{IN} = I_+(0) \tag{1.23}$$

$$I_T = I_+(t) \tag{1.24}$$

$$I_R = I_-(0) \tag{1.25}$$

Because no radiation enters the sample from the side opposite the incident beam,

$$I_-(t) = 0 \tag{1.26}$$

With these definitions, equations (1.18 – 1.21) can be rewritten as:

$$I_T = a_{11} I_{IN} + a_{12} I_R \tag{1.27}$$

$$0 = a_{21} I_{IN} + a_{22} I_R \tag{1.28}$$

Overall sample reflectance and transmittance are defined in terms of the incident radiation intensity

$$R = \frac{I_R}{I_{IN}} = \frac{I_-(0)}{I_+(0)} \tag{1.29}$$

$$T = \frac{I_T}{I_{IN}} = \frac{I_+(t)}{I_+(0)} \tag{1.30}$$

However, *T* can also be expressed as:

$$T = a_{11} - \frac{a_{12} a_{21}}{a_{22}} \tag{1.31}$$

which, for a sample of thickness *t,* can be defined as absolute reflectance R_∞ when $t \to \infty$. This yields the Kubelka-Munk result:

$$R_\infty = \frac{1}{1+\frac{k}{s}+\sqrt{\frac{k}{s}\left(\frac{k}{s}+2\right)}} = 1 + \frac{k}{s} - \sqrt{\frac{k}{s}\left(\frac{k}{s}+2\right)} \tag{1.32}$$

Note that as $\frac{k}{s}$ approaches zero, R_∞nears unity. Also, as $\frac{k}{s}$ increases from zero, the absolute reflectance (R_∞) decreases sharply. Thus, the theory predicts that large sample reflectivity changes will result from small changes in concentration for weak absorbers.

Reflected radiation can be measured, and, using the derived relationship, absorption characteristics of the sample can be extracted from these measurements. Thus, to obtain a spectrum for which a plotted variable is directly proportional to the

concentration of the absorbing species, as is the case for Beer's Law ($A = abC$), the $\frac{k}{s}$ ratio must be expressed in terms of reflectance (R).

Rearranging equation (1.32) yields the well-known Kubelka-Munk transform:

$$\frac{k}{s} = \frac{(1-R_\infty)^2}{2R_\infty} \tag{1.33}$$

This equation describes the reflectance of a sample of semi-infinite thickness with negligible front surface (i.e. specular) reflectance. This diffuse reflectance transform is widely incorporated into software for commercial instruments.[19]

Note that as $k \to 0$, $R_\infty \to 1$, (i.e. all the incident radiation is eventually reflected),

$$\frac{dI_+(x)}{dx} = -(k+s)I_+(x) + sI_-(x) \tag{1.34}$$

$$\frac{dI_-(x)}{dx} = -(k+s)I_-(x) - sI_+(x) \tag{1.35}$$

When $k = 0$, these equations become:

$$\frac{dI_+(x)}{dx} = -sI_+(x) + sI_-(x) \tag{1.36}$$

$$\frac{dI_-(x)}{dx} = -sI_-(x) - sI_+(x) \tag{1.37}$$

Also, at any point x within the sample, the intensity of the downward travelling beam, $I_+(x)$, is equal to the intensity of the upward travelling component, $I_-(x)$, due to similar reflection, refraction, and diffraction processes

$$I_\pm(x) = I_\pm(0) \tag{1.38}$$

Reflected radiation has two basic components: radiation diffusely reflected from the sample surface and specular front surface reflection (I_S), and radiation diffusely

reflected after penetrating into the sample, where it was scattered by particles back to the surface (I_{DIFF}).

$$R = I_S + I_{DIFF} \tag{1.39}$$

As stated earlier, in diffuse reflectance measurements, samples should be illuminated with diffuse radiation, and diffusely scattered radiation should then be detected. Specularly reflected radiation does not penetrate the sample, and therefore does not carry information regarding the absorption properties of the sample. However, specular reflection increases the magnitude of reflected radiation reaching the detector, which creates unwanted spectral artifacts. Therefore, it is imperative that the specular component of reflected radiation be removed or suppressed. This dictates the design of diffuse reflection optics. For example, in an integrating sphere, the sample can be irradiated with diffuse radiation, thus suppressing the intensity of the specular component. In the "Praying Mantis" diffuse reflection accessory (DRA) used in this research, sample illumination and radiation collecting optics are designed so that the specular reflection component is not directed to the detector.

1.2.3 Diffuse Reflection Accessories

Diffuse reflection accessories are designed for analyses of materials that scatter incident radiation. Many materials exhibit diffuse reflection, including powders, solids, films, and emulsion samples. In diffuse reflection spectroscopy, the specular reflection component should be excluded from detection, when possible.

For the analysis of powder samples, the optical system employed in this study includes the "Praying Mantis" (PM) optics, which incorporates elliptical aluminum-

coated mirrors rather than an integrating sphere. There are several advantages to using the PM optical system instead of an integrating sphere. First, the focal point of the PM has a small diameter, allowing for analyses of samples as small as 3 mm in diameter and 1 mm thick. In contrast, diffuse reflection measurements made by using an integrating sphere require samples that are ~12 mm in diameter and several millimeters thick. Second, the sample is orientated horizontally, rather than vertically, as in an integrating sphere, allowing for a range of sample types including powders, films, emulsions, and solids, and better facilitating powder analyses. Third, the PM accessory is more compact than an integrating sphere, allowing it to occupy the sample compartment of commercial instruments more readily.

1.2.4 Fourier Transform IR Spectroscopy

A Fourier transform infrared (FTIR) spectrometer is used to obtain broadband infrared spectra. Unlike a dispersive IR spectrometer, which employs a monochromator for wavelength selection, an FTIR instrument detects radiation at all wavelengths simultaneously. This is known as the multiplex or Felgett Advantage.[20] An FTIR is equipped with a Michelson interferometer, which modulates source radiation and permits scanning over the entire spectral range in a few seconds. The modulated signal reaching the detector yields an interference pattern, which is converted into a 2-dimensional plot of detector signal versus interfering beam retardation called an "interferogram" (*vide infra*). The Fourier transform algorithm is used to convert interferograms into "single beam spectra." Measured spectra are "single" beam because there is only one path between the radiation source and detector.

In order to obtain sample absorbance information from FTIR measurements, a reference single beam spectrum representing the maximum radiation intensity that can reach the detector is needed for comparison. The ratio of a sample single beam spectrum to a reference single beam spectrum is computed to produce transmittance or reflectance spectra, depending on the measurement methodology. When diffuse reflection is employed, the ratio of these single beam spectra yields a reflectance spectrum. Although both transmittance and reflectance spectra can be converted to absorbance by computing $-\log_{10}$, absorbance is not proportional to concentration when diffuse reflectance measurements are made. Instead, reflectance spectra are converted to Kubelka-Munk format.

In general, the reference spectrum can either be collected separately (in a single beam instrument) or simultaneously with the sample measurement (in a double beam instrument). In UV/vis spectrometry, it is common practice to collect sample and reference spectra simultaneously by splitting the source beam and irradiating the sample and the reference at the same time. Double beam operation is very effective, as it compensates for atmospheric absorption interferences, alleviating the need to purge the instrument, and eliminates effects due to temperature and atmospheric pressure fluctuations, which may affect measurements. In contrast, the use of double-beam instruments is very uncommon in FTIR. Methods for splitting radiation exiting the interferometer involve complicated moving optical components, resulting in alignment issues that increase measurement noise. Thus, in a typical single-beam FTIR spectrometer, the reference spectrum is collected separately from the sample spectrum.

Therefore, a different approach is needed to compensate for spectral variations caused by environmental variations that occur between reference and sample measurements.

To eliminate fluctuations in atmospheric absorptions, the instrument chamber is purged with an inert gas or dry and CO_2-free air. Wavelength-dependence of the source spectral radiance, detector responsivity (also a function of the wavelength of incident radiation), and optical efficiency of the instrument mirrors are assumed to be constant when analyzing the sample and the reference. However, when this is not true, source and detector instabilities are not compensated by single beam operation. Signal averaging scans helps to minimize effects caused by short-term instabilities, but may not completely eliminate their effects on the spectra. The instrument employed in this study was typically used to signal average 175 scans to obtain single beam spectra, which required about 1 min. Single beam spectra were ratioed to a reference spectrum to obtain reflectance spectra, which were then converted to Kubelka-Munk format. The relevant instrument-specific file type designations and conversions are described in Appendix A.

1.3 Research Objectives

In addition to the factors that must be considered for high-quality isothermal analyses by DRIFTS, VT-DRIFTS measurement artifacts can occur due to effects from *in-situ* sample heating. While heating the sample, temperature changes to the instrument components can affect spectra. In fact, heating samples to high temperatures significantly decreases the quality of VT-DRIFTS spectra, complicating data

interpretations and obscuring important spectral features associated with chemical and physical changes in the sample.[29, 30]

The goal of this study is to identify the main causes of temperature-induced spectral artifacts in VT-DRIFTS spectra, and to develop solutions for the prevention, elimination, or reduction of temperature-induced spectral artifacts. This can be done by proper sample preparation, improving instrument component efficiencies, and by creating software for post-collection data manipulations. Eliminating spectral artifacts permits observation of subtle chemical changes that would otherwise not be detected.[9, 10]

1.4 References

1. Skoog, D.A., F.J. Holler, and S.R. Crouch, *Principles of Instrumental Analysis*, 6th ed., Thompson Brooks/Cole: Belmont, CA (2007).

2. Maraoulaite, D.K., T.M. Nickels, A.L. Ingram, and R.L. White, VT-DRIFTS Investigations of Interactions Between Benzoic Acid and Montmorillonite Clay*, Spectroscopy*, **30**(10), p. 2-8 (2015).

3. White, D.R. and R.L. White, Isoconversion effective activation energy profiles by variable temperature diffuse reflection infrared spectroscopy*, Applied Spectroscopy*, **62**(1), p. 116-120 (2008).

4. White, R.L., Variable Temperature Infrared Study of Copper Sulfate Pentahydrate Dehydration*, Thermochimica Acta*, **528**, p. 58-62 (2012).

5. White, R.L., VT-DRIFTS: A Two-Dimensional Infrared Thermal Analysis Method*, Applied Spectroscopy*, **47**(9), p. 1492-1496 (1993).

6. White, R.L. and J. Ai, Variable-Temperature Diffuse Reflectance Infrared Studies of Calcium Oxalate Monohydrate*, Applied Spectroscopy*, **46**(1), p. 93-99 (1992).

7. White, R.L. and A. Nair, Diffuse Reflectance Infrared Spectroscopic Characterization of Silica Dehydroxylation*, Applied Spectroscopy*, **44**(1), p. 69-75 (1990).

8. White, R.L. and A. Nair, Effect of Silica on the Thermal Degradation of Poly(vinyl butyral)*, Chemistry of Materials*, **2**(6), p. 742-748 (1990).

9. Ingram, A.L., T.M. Nickels, D.K. Maraoulaite, and R.L. White, Variable Temperature Infrared Spectroscopy Studies of Aromatic Acid Adsorbate Effects on Montmorillonite Dehydration, *Applied Spectroscopy*, published online July 25, 2016. doi: 10.1177/0003702816654155.

10. Nickels, T.M., A.L. Ingram, D.K. Maraoulaite, and R.L. White, Variable Temperature Infrared Investigation of Benzoic Acid Interactions with Montmorillonite Clay Interlayer Water*, Applied Spectroscopy*, **69**(7), p. 850-856 (2015).

11. Nickels, T.M., A.L. Ingram, D.K. Maraoulaite, and R.L. White, Variable Temperature Infrared Spectroscopy Investigations of Benzoic Acid Desorption from Sodium and Calcium Montmorillonite Clays*, Applied Spectroscopy*, **69**(12), p. 1381-1389 (2015).

12. Nickels, T.M., D.K. Maraoulaite, A.L. Ingram, and R.L. White, *Infrared Studies of Benzoic Acid Interactions with Montmorillonite Clay*, in *248th ACS National Meeting & Exposition*: San Francisco, CA, United States, p. ANYL-226 (2014).

13. Murthy, R.S.S., J.P. Blitz, and D.E. Leyden, Quantitative Variable-Temperature Diffuse Reflectance Infrared Fourier-Transform Spectrometric Studies of Modified Silica-Gel Samples*, Analytical Chemistry*, **58**(14), p. 3167-3172 (1986).

14. Spiridon, I., C.A. Teaca, and R. Bodirlau, Structural Changes Evidenced by Ftir Spectroscopy in Cellulosic Materials after Pre-Treatment with Ionic Liquid and Enzymatic Hydrolysis*, BioResources*, **6**(1), p. 400-413 (2011).

15. Clegg, F., C. Breen, M.A. Carter, C. Ince, S.D. Savage, and M.A. Wilson, Dehydroxylation and Rehydroxylation Mechanisms in Fired Clay Ceramic: A TG-MS and DRIFTS Investigation*, Journal of the American Ceramic Society*, **95**(1), p. 416-422 (2012).

16. Chandrasekharan, R., R.I. Masel, and M.A. Shannon, Experimental technique using FTIR to estimate IR optical properties at variable temperatures: Application to PMDA-ODA polyimide thin films from 100 to 380 degrees C*, Review of Scientific Instruments*, **78**(053105), p. 1-8 (2007).

17. Henderson, D.O., R. Mu, Y.S. Tung, and G.C. Huston, Decomposition Kinetics of EGDN on ZnO by Diffuse Reflectance Infrared Fourier Transform Spectroscopy*, Applied Spectroscopy*, **49**(4), p. 444-450 (1995).

18. Nickels, T.M., A.L. Ingram, D.K. Maraoulaite, and R.L. White, Thermogravimetry-Mass Spectrometry Investigations of Benzoic Acid Interactions with Sodium and Calcium Montmorillonites*., Thermochimica Acta*, **614**, p. 157-162 (2015).

19. Milosevic, M. and S.L. Berets, A review of FT-IR diffuse reflection sampling consideration*, Applied Spectroscopy Reviews*, **37**(4), p. 347-364 (2002).

20. Ingle, J.D. and S.R. Crouch, *Spectrochemical Analysis*, Prentice Hall: New Jersey (1988).

21. Fuller, M.P. and P.R. Griffiths, Diffuse Reflectance Measurements by Infrared Fourier-Transform Spectrometry*, Analytical Chemistry*, **50**(13), p. 1906-1910 (1978).

22. Brimmer, P.J. and P.R. Griffiths, Angular Dependence of Diffuse Reflectance Infrared Spectra. Part III: Linearity of Kubelka-Munk Plots*, Applied Spectroscopy*, **42**(2), p. 242-247 (1988).

23. Tsuge, A., Y. Uwamino, T. Ishizuka, and K. Suzuki, Quantitative Analysis of Powdery Sample by Diffuse Reflectance Infrared Fourier Transform Spectrometry: Determination of the α-Component in Silicon Nitride*, Applied Spectroscopy*, **45**(8), p. 1377-1380 (1991).

24. Kubelka, P. and F. Munk, Ein Beitrag zur Optik der Farbanstriche*, Zeitschrift für Technische Physik*, **12**, p. 593-601 (1931).

25. Gunde, M.K., J.K. Logar, Z.C. Orel, and B. Orel, Application of the Kubelka-Munk Theory to Thickness-Dependent Diffuse-Reflectance of Black Paints in the Mid-Ir*, Applied Spectroscopy*, **49**(5), p. 623-629 (1995).

26. Gunde, M.K., Z.C. Orel, J.K. Logar, and B. Orel, Flocculation gradient technique in terms of Kubelka-Munk coefficients: Quantifying black-pigmented dispersions*, Applied Spectroscopy*, **49**(12), p. 1756-1761 (1995).

27. Bak, J. and B. Kindl, Quantitative analysis of mineral powders by DRIFTS: Determination of SrCO3 in superconductor precursor powders*, Applied Spectroscopy*, **51**(11), p. 1730-1735 (1997).

28. Blitz, J.P. and S.M. Augustine, Characterization of Heterogeneous Catalysts by Ft-Ir Diffuse-Reflectance Spectroscopy*, Spectroscopy*, **9**(8), p. 28-34 (1994).

29. White, R.L., Removal of Baseline Artifacts from Variable-Temperature Diffuse Reflectance Infrared Spectra*, Analytical Chemistry*, **64**(17), p. 2010-2013 (1992).

30. Lin, R. and R.L. White, Effect of Diffuse Reflectance Fourier Transform Infrared Spectroscopy Sample Temperature on Photoconducting Semiconductor and Pyroelectric Infrared Detectors*, Analytical Chemistry*, **66**(18), p. 2976-2980 (1994).

Chapter 2: System Components

2.1 VT-DRIFTS Apparatus and Data Collection

Infrared spectra were collected by using a Mattson Instruments Inc., Nova Cygni 120 FTIR system. The apparatus is described in detail elsewhere[1], and a schematic of the experimental setup is provided in Figure 2.1. The sample compartment of this instrument is large enough to hold the diffuse reflection optics and the sample holder environmental chamber. A Harrick Scientific Inc. environmental chamber (Figures 2.3 and 2.4) was modified to incorporate a nichrome wire heater (Figures 2.2 and 2.3) and a K-type thermocouple (Figure 2.2) connected to a Eurotherm 818 Series Temperature Controller/Programmer for sample heating (Figure 2.1). A software macro program was used to mediate the actions of the temperature controller and the FTIR to streamline experiments.

VT-DRIFTS instrument control by the macro program is described in Appendix B.1, and the macro program is provided in Appendix B.2. Executable programs utilized by the macro program are listed in Appendices B.3-B.7.

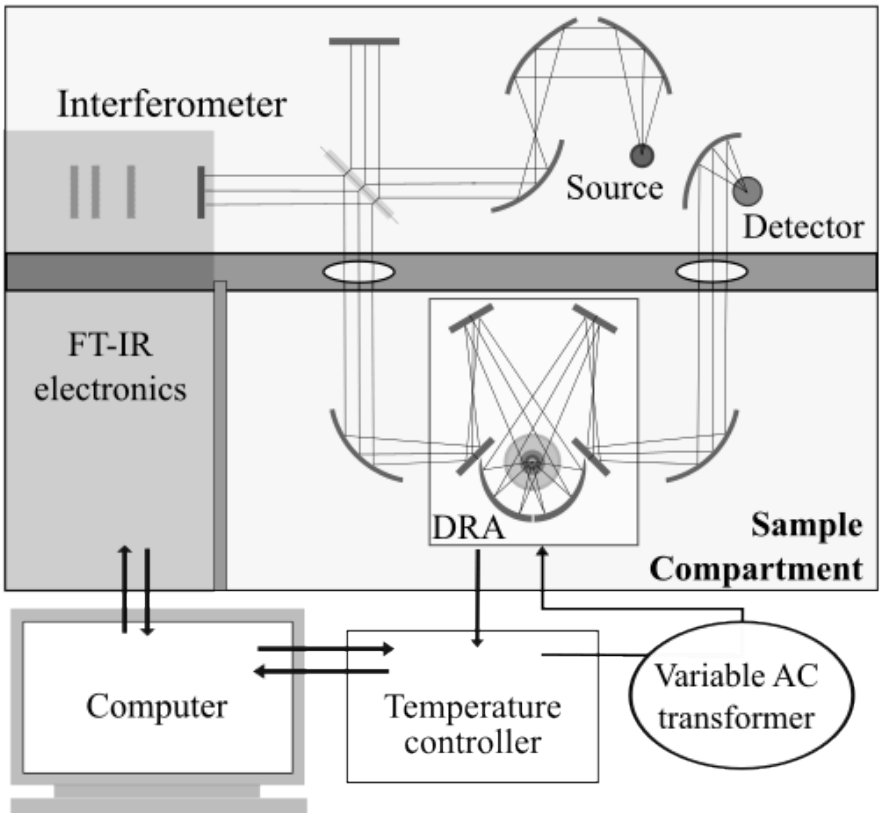

Figure 2.1 VT-DRIFTS schematic representation.

2.1.1 Reflectance Spectrum Measurements

After data collection, the operator processes the interferogram data to produce single beam spectra, which are ratioed to a reference single beam spectrum to create reflectance spectra. When analyzing variable temperature spectra, two approaches for selection of reference spectra are viable.

In one method, a series of reference single beam spectra are collected for a non-absorbing material in the sample holder by means of a heating ramp, producing a set of reference spectra analogous to the sample spectra but lacking absorption bands. Macro program commands can be used to retrieve sample and reference single beam spectra

measured at similar temperatures and then ratio these spectra to produce reflectance spectra. Although this method is somewhat effective for temperature artifact compensation, it results in a loss of signal-to-noise ratio (SNR) with increasing sample temperature, because an overall decrease in interferogram signal intensity is one of the most apparent temperature-induced artifacts in VT-DRIFTS. In addition, sample particle physical changes caused by thermal expansion and cooling may affect spectra and are not necessarily reproducible between experiments.

In another method, reflectance spectra are calculated by ratioing VT-DRIFTS sample single beam spectra to the same reference single beam spectrum, which was measured at ambient temperature. Although temperature-dependent artifacts remain in reflectance spectra generated in this manner, particularly for high-temperature measurements, spectral signal-to-noise ratio (SNR) is greater and spectra are more reproducible because only sample single beam spectrum variations contribute to reflectance spectra changes.

The macro program used for computing the ratio of sample single beam spectra to a single reference spectrum is provided in Appendix B.8. This software can be modified to ratio VT-sample single beam spectra to VT-reference single beam spectra by removing the # symbol from lines 27-43 of the code.

2.1.2 Sample Chamber Design. Heating the Sample

A modified Harrick Scientific Inc. environmental chamber was incorporated into the VT-DRIFTS instrument to facilitate sample heating (Figures 2.2 and 2.3). The original chamber was modified to incorporate a nichrome wire heater and a K-type

thermocouple for better heating efficiency and improved temperature control. The thermocouple was connected to a Eurotherm 818 Series Temperature Controller/Programmer. A stainless steel environmental chamber lid was used to isolate the sample holder for control of the gaseous environment (Figure 2.4).

The sample holder consisted of a steel post attached to the base of the environmental chamber. At the top of the post, a piece of Pt foil was held in place by a ring spacer. The platinum foil and ring attach to the steel post by two screws. The foil and ring create a shallow void to which sample was added (Figures 2.2 and 2.3). In addition to sample economy, the small sample size made it easier to obtain a smooth, homogenous sample surface, and reduced the energy needed to heat the sample.

Electrical leads for the thermocouple and the nichrome wire heater enter the chamber through the base (Figure 2.2). The thermocouple is in contact with the Pt foil at the bottom. A quartz tube was placed over the steel post to prevent electrical conduction with the heating element, which was nichrome wire wrapped around the tube. A larger quartz tube was placed over the wire to insulate the nichrome wire from the environmental chamber lid (Figure 2.3). Sample height adjustment screws are located at each side of the base.

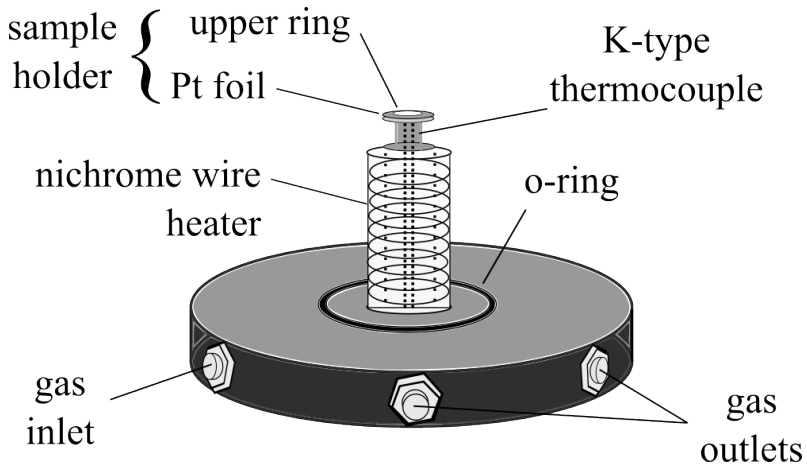

Figure 2.2 Diagram of the modified sample holder assembly.

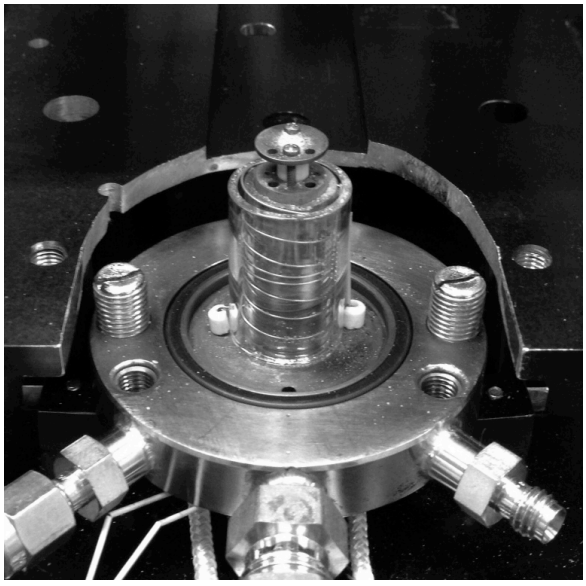

Figure 2.3 Modified sample holder assembly.

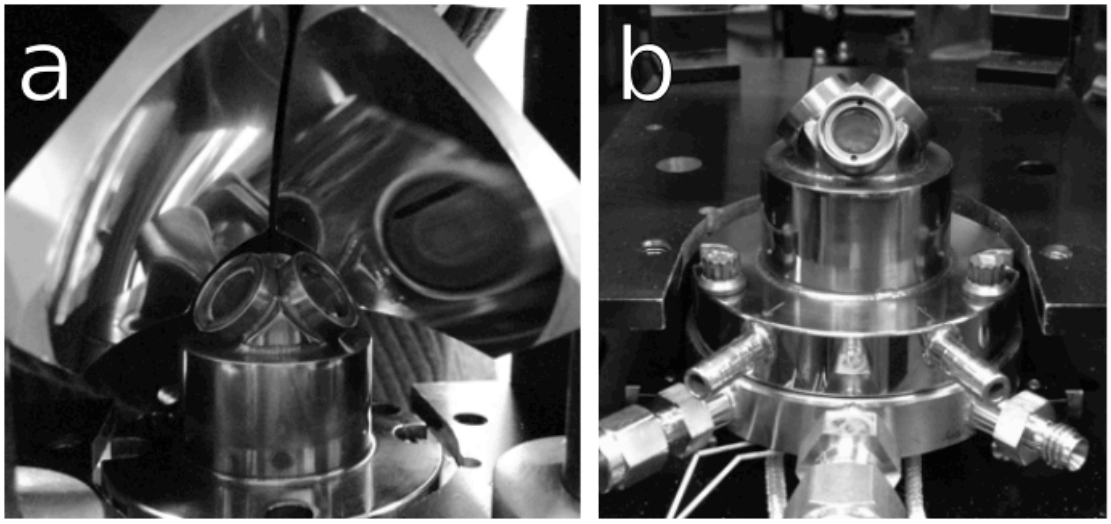

Figure 2.4 Harrick environmental chamber a) mounted in DRA optics, b) view with DRA optics removed.

By placing the thermocouple under the sample rather than at its surface, sample temperatures can be measured without blocking part of the incident infrared beam. However, due to its location, the temperature recorded by the thermocouple represents the temperature at the bottom of the sample, whereas the more important temperature measurement would be at the sample surface, where the infrared beam interacts with the material being studied (*vide infra*).

2.1.3 Sample Chamber Modifications for Alignment Optimization

The DRA optics focus the infrared beam on the sample with a focal point diameter of about 1/8 in. The sample holder size is close to the size of the focal point. Therefore, locating the sample at the optical focal point of the infrared beam is critical for proper alignment.

Horizontal sample location adjustments (i.e. in the xy-plane) were accomplished by mounting the sample holder on a moveable platform. Adjustment screws on each side of the sample holder were used for vertical alignment (i.e. the z-axis) (Figure 2.3). By using these adjustments, the sample location could be properly aligned with the infrared beam focal point. Optimum alignment was achieved by iterative mirror adjustments made while monitoring the interferogram signal intensity. Set-screws were used to secure the sample holder in place after attaining optical alignment.

2.1.4 Effects of Sample Purge

After loading the sample, the environmental chamber lid was installed and secured to seal the chamber (Figure 2.4), and the FTIR sample compartment cover was put in place so that the instrument could be purged with dry, CO_2-free air to minimize CO_2 and water background absorptions (Figure 2.5).

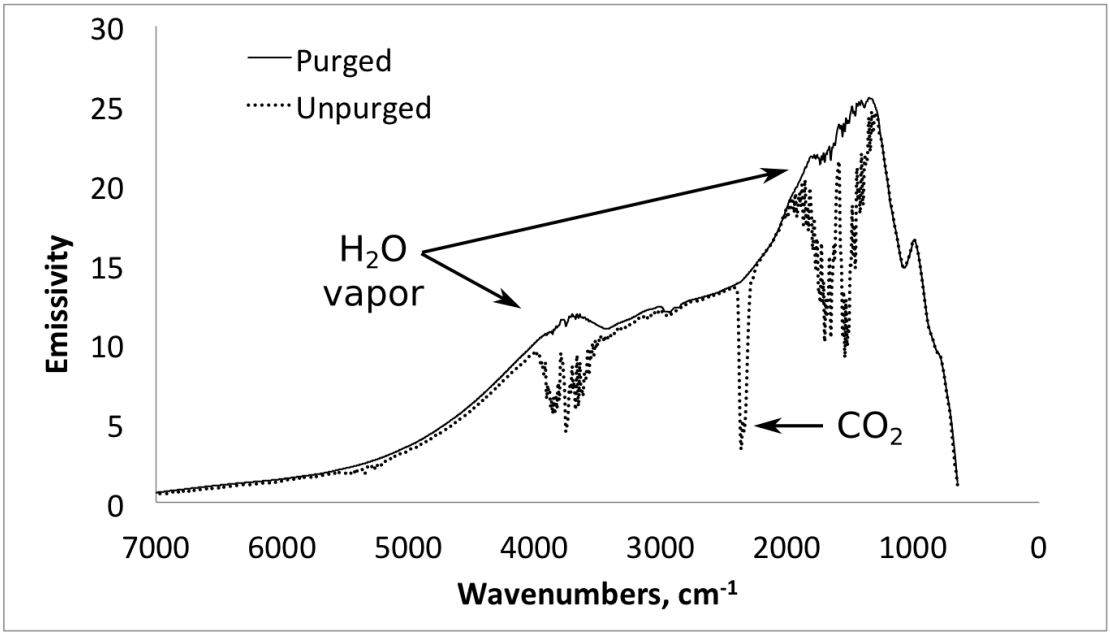

Figure 2.5 CO_2 and water vapor background absorptions.

The sample chamber was purged with a He gas flow to create an inert, oxygen-free environment. The purge gas inlet is shown in Figure 2.2. It is important to eliminate oxygen from the sample chamber to prevent combustion and oxidation reactions that may occur at high temperatures. In addition to sample degradation, the nichrome heater wire, environmental chamber base and lid o-rings, and the ZnSe windows can be damaged if the assembly is heated to high temperatures in the presence of oxygen. When temperature-dependent reactions occur during sample heating, He purge removes reaction products from the chamber. The gas outlet can be connected to other instruments (e.g. a gas chromatograph and/or mass spectrometer), for further analysis of the volatile products. Prior to VT-DRIFTS analysis, sufficient time must be allowed to efficiently purge the sample chamber and FTIR instrument. Typically, about one hour is sufficient for purging.

2.2 VT-DRIFTS Instrument Parameters

2.2.1 Interferogram Signal I(T, λ) and Radiant Power at the Detector $\Phi_D(T, \lambda)$

The interferogram signal $I(T, \lambda)$ used to calculate the single beam spectrum depends on the radiant power reaching the detector $\Phi_D(T, \lambda)$, and other parameters[2]:

$$I(T, \lambda) = \Phi_D(T, \lambda) R_D(\lambda) g H(T, \lambda) \quad (2.1)$$

where $R_D(\lambda)$ is the detector response function, g is the signal amplification gain factor of the detector electronics, and $H(T, \lambda)$ is the detector transfer function.[2] The radiant power reaching the detector is defined by a number of instrumental factors[2]:

$$\Phi_D(T, \lambda) = B(T_S, \lambda) A_S \Omega_L T_{OP}(T, \lambda) R(T, \lambda) \quad (2.2)$$

where $B(T_S, \lambda)$ is the infrared source radiance, A_S is the source area viewed, Ω_L is the limiting solid angle, $R(T, \lambda)$ is the reflectance of the material in the DRIFTS sample holder, and $T_{OP}(T, \lambda)$ is the transmission efficiency of the optical system. As indicated, the source radiance $B(T_S, \lambda)$ depends on the temperature of the source and the wavelength, whereas the reflectance of the material in the sample holder $R(T, \lambda)$, the transmission efficiency of the optical system $T_{OP}(T, \lambda)$, and the detector transfer function $H(T, \lambda)$ depend on ambient temperature and the wavelength.[3]

2.2.2 Infrared Source and Radiance $B(T_S, \lambda)$

The Nova Cygni 120 FTIR spectrometer is equipped with a Globar infrared source, which consists of a silicon carbide rod that is heated to 1000–1650 °C to produce radiation in the mid-infrared wavenumber range of ~ 400-4000cm^{-1}. Electrical current is passed through the rod, causing it to heat and emit radiation. The globar is a continuum source, producing a spectral continuum over a broad wavelength region, rather than narrow spectral lines. The globar is continuously heated and suitably stable for long-term measurements. The spectral radiance Φ of the source is frequency dependent and depends on the source temperature. At 1000 cm^{-1}, a typical globar spectral radiance Φ is approximately 10^{-4} W cm^{-2} nm^{-1} sr^{-1}.[4]

The globar source employed for studies described here was water-cooled to improve temperature stability, which is essential for high measurement reproducibility.[4] It is common to leave the source on when the instrument is not in use. This eliminates the time required for source temperature equilibration prior to

measurements and also continuously heats the KBr beamsplitter, which minimizes water absorption.

The radiant power spectrum of an infrared source depends on its temperature, the hotter the source, the more short-wavelength radiation it emits.[4] By placing a highly reflective medium (e.g. Ag powder) into the sample holder, a reference single beam spectrum can be obtained (Figure 2.6). Because of relative intensity variations, some spectral regions have higher SNR than others.

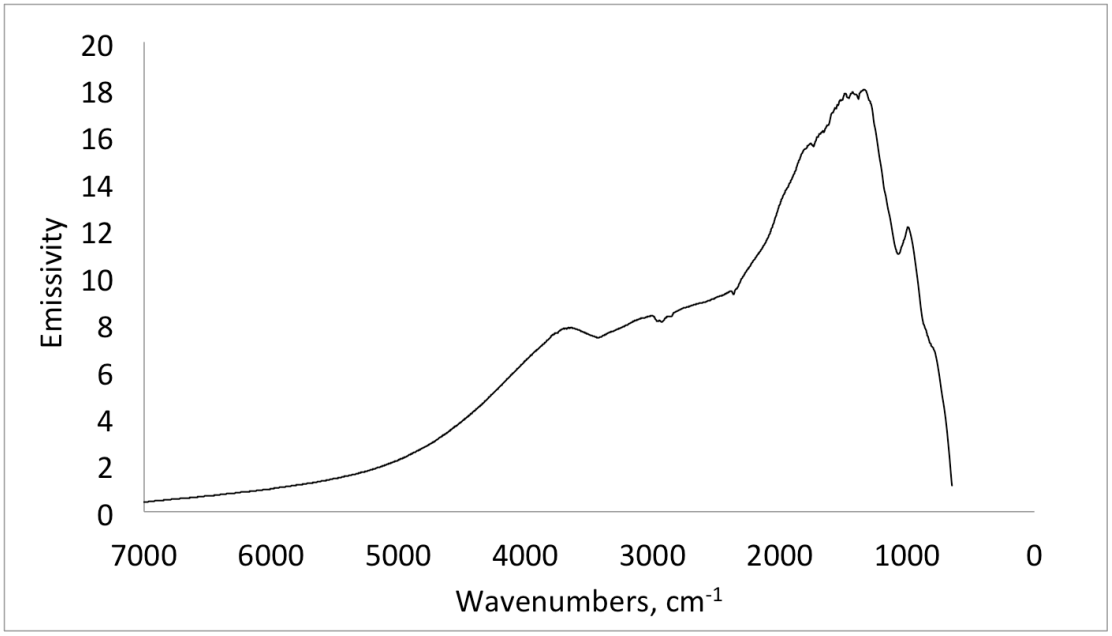

Figure 2.6 Single beam Ag powder spectrum measured at ambient temperature

The reference single beam spectrum in Figure 2.6 represents infrared radiation intensity (in units of emissivity) reaching the detector as a function of wavenumber between 7000 and 650 cm^{-1}. It is more common to use wavenumbers as the independent variable in spectrum plots than wavelengths in infrared spectroscopy. Wavenumbers are inversely proportional to wavelength and directly proportional to frequency and energy[5]:

$$E = h\nu = hc/\lambda = hc\sigma \quad (2.3)$$

where E is energy, h is Planck's constant, ν is frequency, c is the speed of light in a vacuum, λ is wavelength, and σ represents wavenumbers.

Due to the combined effects of the blackbody curve emitted by the source, reflection and absorption losses of the optics, and the response function of the detector, single beam spectrum intensity varies significantly as a function of wavenumber. Between 7000 and 4000 cm^{-1}, and below 500 cm^{-1}, detector signal intensity is relatively low. Due to the sharp drop in signal intensity below 800 cm^{-1} (see Figure 2.6), infrared measurements are less reliable in this wavenumber region. Likewise, spectral features above 4000 cm^{-1} are less reproducible and have lower SNR than those found in the 4000-800 cm^{-1} range.

Globar sources typically have a useful lifetime of a few years. Due to accumulation of impurities over time, electrical resistance decreases, resulting in a gradual decrease in temperature with time. An overlay of single beam spectra collected with an old and a new globar source is shown in Figure 2.7. With the new source, emissivity is greater above 2000 cm^{-1} compared to the old source.

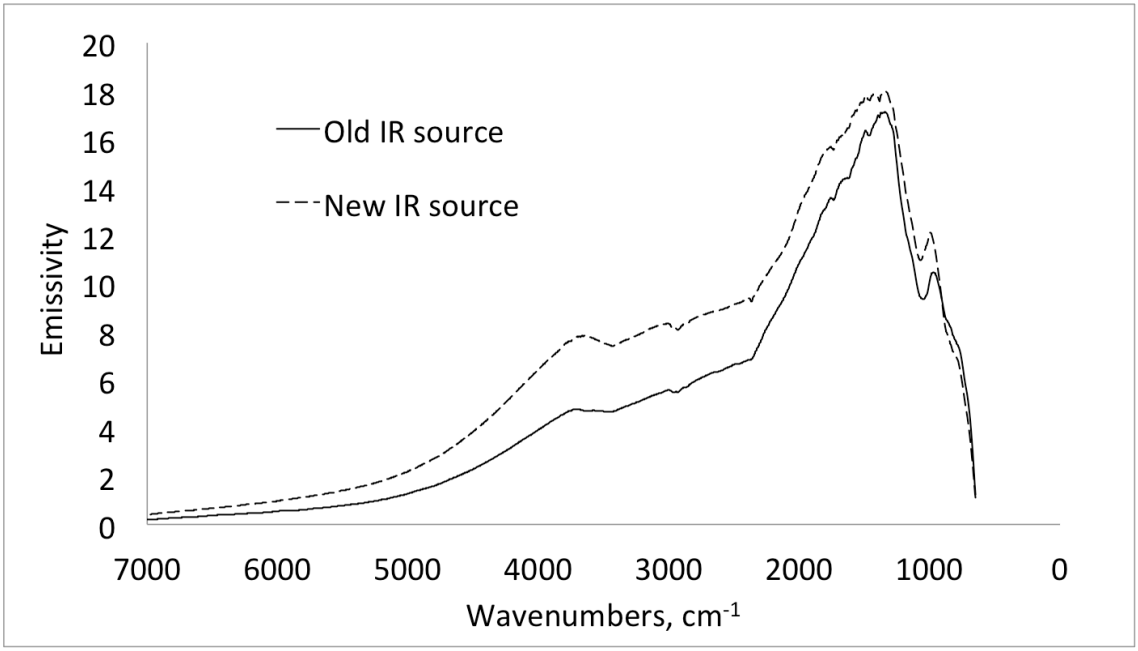

Figure 2.7 Overlay of ambient temperature single beam spectra measured with a new and old infrared source.

2.2.3 Detector and Radiant Power $\Phi_D(T, \lambda)$

A number of detectors are available for use with FTIR spectrometers. The deuterated triglycine sulfate (DTGS) detector operates at ambient temperature and does not respond to temperature changes in the same manner as the mercury cadmium telluride (MCT) detector, which must be cooled with liquid nitrogen to 77 K prior to operation. However, the overall sensitivity of MCT detectors is significantly greater than DTGS detectors, making them more suitable for the VT-DRIFTS technique, which requires detection of low detector signals (*vide infra*).

The instrument employed for studies described here was equipped with a mercury cadmium telluride HgCdTe (MCT) photoconductivity detector obtained from "Infrared Associates, Inc." (Cranbury, NJ), Model No. 0465-0034 (Serial No. N-

12804). HgCdTe is the most commonly employed variable gap semiconductor material used for infrared detection.[6] A large photoexcitation spectral range and a high quantum efficiency (the number of incident photons relative to the number of photons converted into electrons excited into the conduction band) yield high sensitivity and make the MCT detector the most popular choice for FTIR spectroscopy. Based on spectral response function,[7] the wavenumber range of MCT detectors is approximately 400 – 4500 cm^{-1},[7] which closely overlaps the spectral range emitted by a globar radiation source. Other detector materials are available for mid-infrared spectroscopy and provide competitive cost, stability, durability, and convenient mechanical properties, but performance characteristics of MCT detectors are typically the best.[6]

The MCT detector operates in photoconductive mode, wherein the conductance of the resistive element increases when infrared radiation is incident on the active area.[7] The detector employed for studies described here had a relatively small active area of about 0.0025 cm^2. In general, smaller active areas decrease detector response times. With increasing temperature, valence electrons are promoted into the conduction band. A constant current is passed through the detector, so the increase in conductance produces a voltage change. Modulating the incident radiation yields an AC electrical output.[7] The measured detector signal $S(x)$ is the amplified change in voltage of the photoconductive element. Plots of $S(x)$ as a function of interferometer moving mirror displacement (x) yield interferograms (equations (2.9) and (2.10)).

Detector cooling reduces effects from thermal excitation of electrons into the conduction band,[4] and therefore minimizes noise. The operating temperature of the

detector is 77 K, which is achieved with liquid nitrogen (LN_2). Resistance of the photoconductive element has been found to increase from 53.8 to 82.1 ohms when the detector is cooled from room temperature (300 K) to 77 K.[7]

The transfer function for the detector $H(T, \lambda)$ can be expressed by an equation or a plot of the electrical output (signal) versus radiant power Φ_λ incident on the detector. The rate of change of the electrical output signal in this plot represents the sensitivity $Q(\lambda)$ of the detector

$$Q(\lambda) = dS/d\Phi \tag{2.4}$$

i.e. the slope of a plot of electrical output S versus incident radiant power Φ. The magnitude of the electrical signal S (voltage) at any given incident radiant power Φ_λ is the responsivity, $R(\lambda)$, of the detector

$$R(\lambda) = \text{rms } S \,/\, \text{rms } \Phi_\lambda \tag{2.5}$$

Both sensitivity $Q(\lambda)$ and responsivity $R(\lambda)$ are wavelength dependent. These parameters change with temperature, bias voltage, component parameters, and time.[4] The detector signal increases with increasing bias current, and for the specific model used in this study, responsivity ranges from 3049 to 13451 V/W.[7]

The detectivity (D) is the measure of minimum detectability and is defined as

$$D = 1/\Phi_n \tag{2.6}$$

where Φ_n is noise equivalent power, which is the radiant power of the modulated beam incident on the detector that gives rise to a signal equivalent to the root-mean-square (rms) dark noise σ_d in a 1 Hz bandwidth.[4] The magnitude of σ_d can be calculated from values for $R(\lambda)$ and Φ_n:

$$\sigma_d = R(\lambda)\Phi_n \tag{2.7}$$

Normalized detectivity D^* takes into account the detector active area A and electrical bandwidth dependencies.[4]

$$D^* = DA^{1/2}(\Delta f)^{1/2} \tag{2.8}$$

where Δf is the noise equivalent bandwidth. From the technical data summary for the device employed for studies described here, $A = 0.0025$ cm^2, Φ_n at 1 KHz ranges from 2.79 to 14.42 nV/Hz$^{1/2}$, and the normalized spectral detectivity D^* ranges from 4.84 to 76.93 cmHz$^{1/2}$/W, depending on the bias voltage and electrical bandwidth.[7]

2.2.4 Reflectance of the Sample Material R(T, λ).

According to White[8], it is critical that reference spectra are measured under the same conditions as the sample. A highly reflective non-absorbing material is best suited as a reference material. DRIFTS samples are diluted in a highly reflective matrix to maximize the path length through the sample and satisfy the Kubelka-Munk theory assumption of infinite path length. The diluent should also have the desired properties of a reference material, including inertness.[8-11]

Because diffuse reflection spectroscopy requires significant reflection from samples, an ideal sample should have high reflectance properties and sharp, non-overlapping, absorption bands. Ideally, some radiation should pass to the detector at all measured wavenumbers. Unfortunately, some samples don't reflect very well, and instead absorb a significant portion of incident radiation. At wavenumbers at which the intensity of the signal reaching the detector is near zero, it is not possible to accurately represent absorption intensities. By using a highly reflective diluent, near zero detector signals can be avoided and SNR can be maximized. The diluent must not absorb

infrared radiation, be inert, and for variable temperature experiments, be stable at high temperatures. Some popular materials include KBr, KCl, and NaCl, but these salts are not suitable for dehydration reaction studies because they absorb water. Silver (Ag), gold (Au), and diamond ($C_{diamond}$) powders are also suitably non-absorbing and highly reflective materials that do not absorb water. Ag powder is more reflective than diamond powder, and also cheaper. Au powder is slightly more reflective than Ag powder, but is much more expensive. Thus, Ag was used to dilute samples because of its excellent reflection properties and cost effectiveness. In the mid-infrared range, Ag reflectance is between 99.2 – 99.5%.[12] The use of a highly reflecting diluent maximizes the path length through the sample, which increases absorbance and provides sharp, quantifiable, absorbance bands. Also, increased diffuse reflection maximizes the signal intensity at the detector, yielding greater SNR.

In studies described here, Ag powder (99.95% pure) was used as the reference, diluent, and as the sample material.

2.3 Optical System

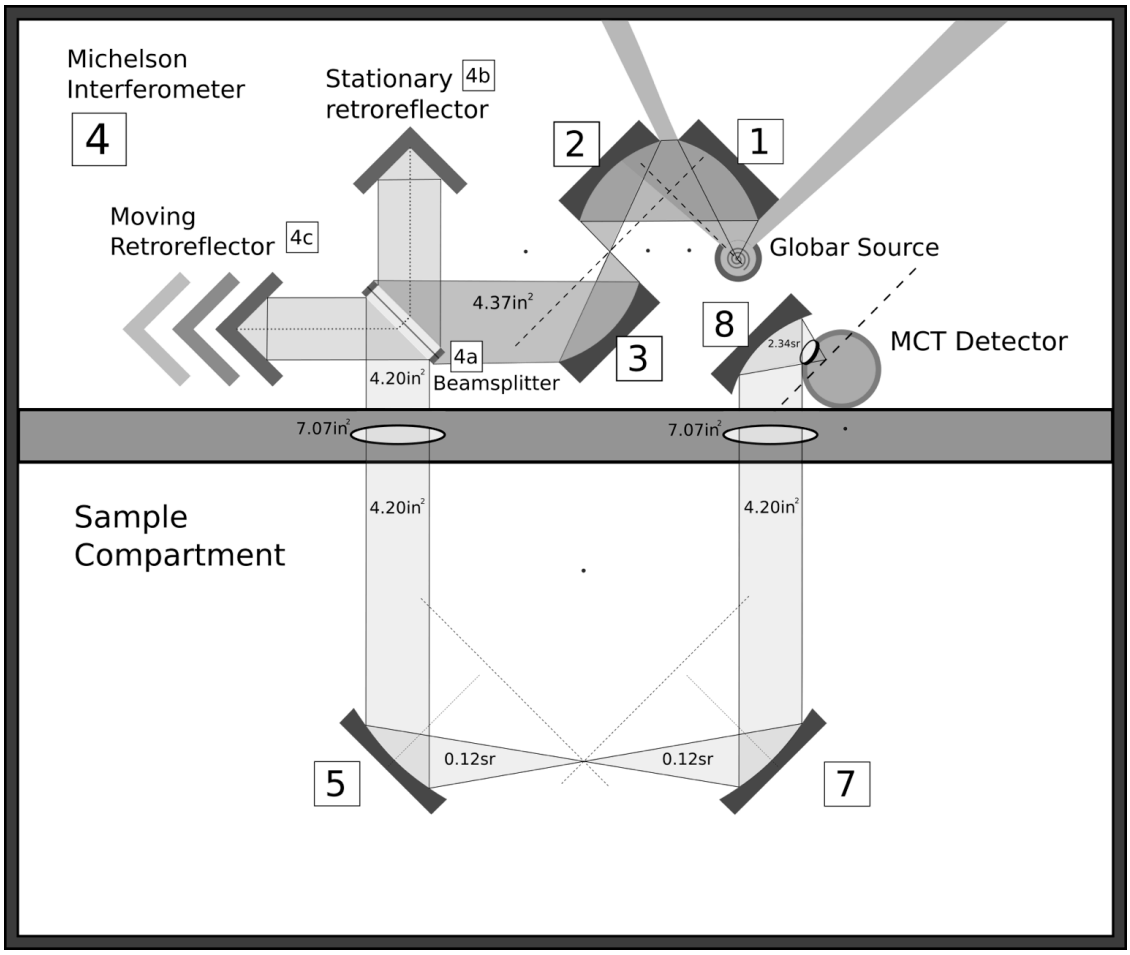

Figure 2.8 FTIR Optical system.

To direct infrared radiation from the source to the sample and the detector, the FTIR spectrometer is equipped with a series of front-reflection aluminum mirrors. The diagram in Figure 2.8 gives the layout of the optical components.

The infrared source is mounted off-axis relative to the collimating mirror (1) so that the source body does not block the collimated beam.[4] Mirrors (2) and (3) direct the collimated infrared beam to the interferometer, where the radiation is modulated. A

90° Michelson interferometer is employed in the Nova Cygni 120 spectrometer. Michelson interferometer principles of operation are discussed in section (2.3.1).

From the interferometer, the collimated and modulated infrared beam is directed into the sample compartment through a 3 in diameter round opening in the cover that separates the source, detector, and interferometer from the sample chamber. After entering the sample chamber, the beam encounters a concave aluminum mirror (5). This mirror allows the collimated infrared beam to make a 90° turn towards the diffuse reflection accessory (DRA), and focuses the beam on mirror (6-1).

Mirrors (6-1) through (6-6) are part of the diffuse reflectance accessory (DRA) (described in section 2.3.2 and shown in Figure 2.8). The purpose of the accessory is to direct source radiation to the sample and then collect radiation reflected from the sample surface and direct it to mirror (7). Mirror (7) is concave with the same focal length as mirror (5). When the beam encounters mirror (7), it makes a 90° turn and becomes collimated on its path to the detector. Mirror (8) has a short focal length and focuses the beam on the detector.

2.3.1 Michelson Interferometer

The Michelson interferometer is a two-beam interferometer that accepts all source radiation. The Michelson interferometer [(4) in Figure 2.7] incorporates a fixed cube corner retroreflector mirror, a moving cube corner retroreflector mirror, and a semi infrared-transparent (~ 50%) beamsplitter oriented at a 45° angle relative to the fixed and moving mirrors so that the beam from the source is split into two beams of

relatively equal intensity. The paths of the two 'half-beams' are at a 90° angle to each other.

An ideal beamsplitter reflects 50% of incident beam and transmits the other 50% without any absorption or scattering losses. A compensator (KBr optical flat) is attached to the beamsplitter to equalize the optical paths of the two 'half-beams.'

When the path length to the fixed mirror equals the path length to the moving mirror, the two 'half-beams' recombine in-phase and produce a bright image of the source at the detector. When the moving mirror is shifted by λ/4, the difference between path lengths becomes λ/2, and the two beams recombine out-of-phase with each other, resulting in darkness at the detector.[4] A He/Ne red (632.8 nm) laser is employed to precisely measure the interferometer moving mirror distance and is used to trigger detector signal data acquisitions.

The detector signal $S(x)$ can be expressed as a function of the source radiant power Φ_v, Φ_λ, or Φ_σ by: [4]

$$S(x) = K\,\Phi_v \cos(4\pi x v / c) = K\,\Phi_\lambda \cos(4\pi x / \lambda) = K\,\Phi_\sigma (4\pi x \sigma) \qquad (2.9)$$

where K is a constant determined by the detector response function and geometrical factors, x represents moving mirror displacement relative to the zero path difference point, v is the radiation frequency, σ is the wavenumber of the source radiation, λ is the corresponding wavelength, and c is the speed of light. The measured signal $S(x)$ plotted as a function of mirror displacement (x) constitutes an interferogram.

For a polychromatic radiation source, each frequency will be modulated as a separate cosine oscillation, and the interferogram represents the summation of all cosine oscillations produced by the radiation source. When the interferometer moving mirror

position is such that the path length of both interferometer 'half-beams' is identical, all cosine oscillations are in phase, and the detector sees a bright field corresponding to the highest signal voltage in the interferogram. As the mirror moves away from this zero path length difference position, detector signal drops to a relatively stable value between zero and the maximum signal value. The AC detector signal is the integral over all frequencies [4]:

$$S(x) = \int_{-\infty}^{+\infty} \Phi_\sigma \cos(4\pi x\sigma) d\sigma \tag{2.10}$$

2.3.2 "Praying Mantis" Diffuse Reflection Accessory

In 1991, Milosevic and Harrick patented an "Optical attachment for variable angle reflection spectroscopy." According to the authors, the attachment works for external, internal, and diffuse reflection techniques. Its main feature is that pre-focusing and post-collection mirrors can be rotated in unison to vary the incident and collection angles (between 5-85°) without misaligning the system, (i.e. without losing focus on the sample). The "Praying Mantis" DRA, which is based on this attachment, is a highly efficient system for spectroscopic analysis of powders and rough surfaces. It collects almost twice the diffusely reflected radiation when compared to an integrating sphere.[13]

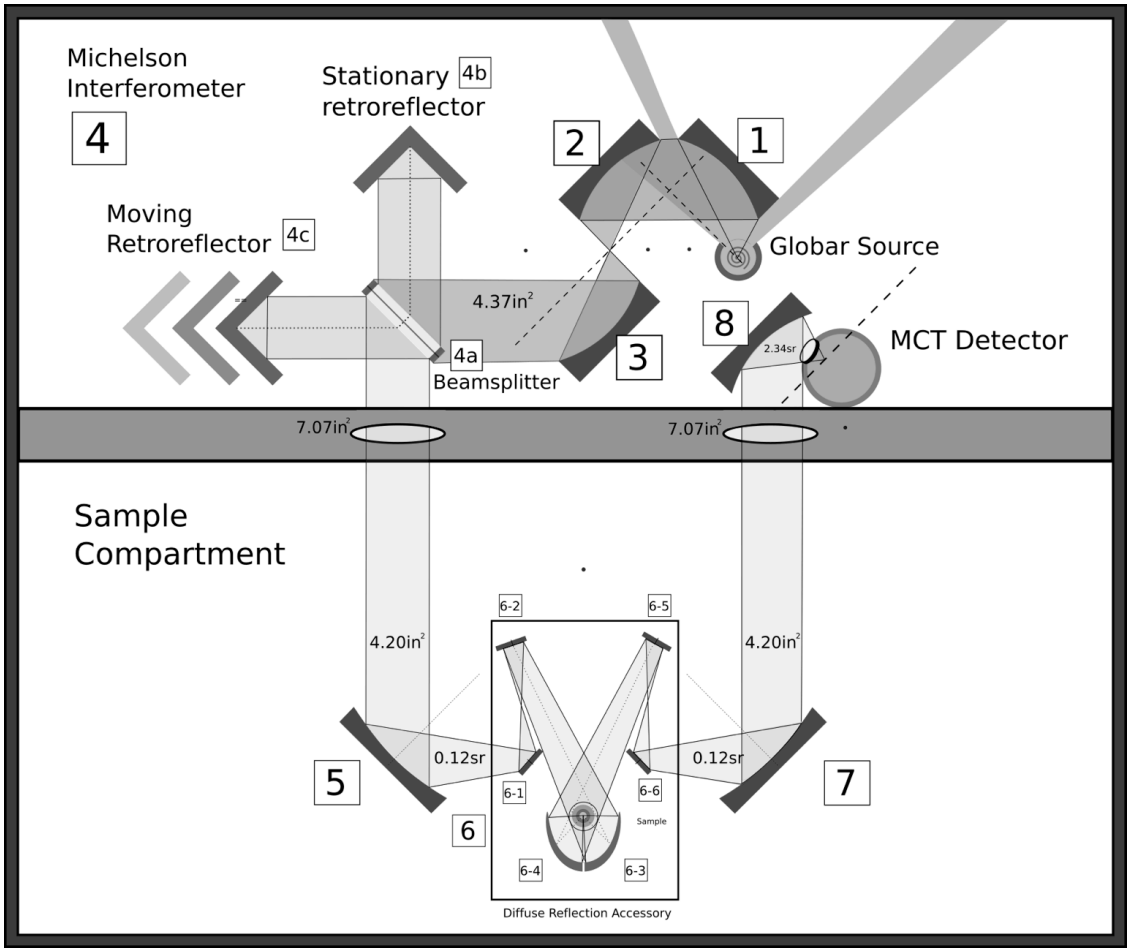

Figure 2.9 FTIR spectrometer equipped with the "Praying Mantis" diffuse reflection accessory.

The “Praying Mantis” DRA incorporates two 6:1 90° off-axis ellipsoid mirrors. One ellipsoid focuses the incident beam on the sample, and the second collects up to 20% of the radiation diffusely reflected from the sample.[14] The accessory gets its name from the visual appearance of the ellipsoid mirrors. These mirrors are labeled (6-3) and (6-4) in Figure 2.8. Both ellipsoid mirrors are stationary and are not designed to be moved (adjusted) by the operator.

Mirror (6-3) focuses the infrared beam onto the sample surface. The sample interacts with the beam, scattering some of the radiation. Mirror (6-4) collects the

scattered radiation and focuses it on mirror (6-5). Unlike an integrating sphere, when the PM-DRA is used, the specular component of the reflected beam is not collected by the ellipsoid mirrors.[14] Only diffusely reflected radiation is collected by mirror (6-4) and passed to the detector. Most other commercially available diffuse reflectance attachments collect radiation at an azimuthal angle of 180°, where the specular component and reststrahlen bands have the highest intensity.[14] In the PM-DRA, mirrors (6-3) and (6-4) are tilted forward, so that the diffusely reflected radiation is collected at an azimuthal angle of 120°. In this arrangement, the specular reflection component passes the ellipsoid mirrors and is not collected.[14]

In addition to the pair of ellipsoid mirrors, the DRA contains 4 plane mirrors. Mirror (6-1) is a small (less than 1 in^2) aluminum on glass front-reflection plane mirror that is extremely critical to the alignment of the sample. Small movements (a turn by only a few degrees) of this mirror can result in complete loss of signal at the detector. When mirror (6-1) is turned side-to-side by using the adjustment knob, the infrared source image at the sample moves along a circular trajectory in the *yz*-plane.

Mirror (6-2) is also a plane mirror with the same construction as (6-1), but, due to its location and pivot, it is somewhat less sensitive than mirror (6-1) for signal adjustments. A change in the rotation angle of mirror (6-2) results in a change in the detector signal intensity, but the change is not as much as the same rotation would cause for mirror (6-1). Mirror (6-2) is equipped with two adjustment knobs. One knob turns the mirror side-to-side, which moves the source image in a circular trajectory in the *xz*-plane. The other knob causes the mirror to pivot up and down, causing the infrared

source image to move in a plane along a one part of the circular trajectory, essentially back and forth along the *z*-axis.

The diffusely reflected radiation component collected by the ellipsoid mirrors is reflected onto mirror (6-5). Mirrors (6-2) and (6-5) have the same properties and are positioned on opposite sides of the DRA. They exhibit similar behaviors when adjusted. The same can be said regarding mirrors (6-1) and (6-6). Differences in these mirrors are mostly related to function: mirrors (6-1) and (6-2) bring the source radiation to the sample, whereas mirrors (6-5) and (6-6) transfer diffusely scattered radiation to the detector.

2.4 Transmission Efficiency of the Optical System $T_{OP}(T, \lambda)$

The transmission efficiency of an FTIR optical system rarely exceeds 10% due to the number of components in the optical system. The image of the source fills the detector area in a well-designed spectrometer, which means that the system should not be limited by source photon shot noise, but may be limited by detector background noise.[15] Although real instruments do not reach the performance characteristics of a shot noise limited system, even at transmission efficiencies of only a few percent and SNR limited to $1\text{-}5\times10^3$, which is far below the SNR expected for a shot noise limited system, FTIR systems exhibit high sensitivities.[16]

In order to observe sample chemical changes while heating them *in-situ*, additional optical components must be added that further decrease SNR. Moreover, the system undergoes temperature-induced changes that increase fluctuations in the signal

reaching the detector. In order to understand these effects and to propose improvements, it is important to examine the optical system in detail.

The optical system consists of a series of front surface aluminum mirrors, a germanium coated potassium bromide beamsplitter in the interferometer, zinc selenide windows in the environmental chamber housing the sample, and the detector window. The efficiency of the optical system can be estimated if the optical properties of the materials are known, and geometrical properties of the system are taken into account.

2.4.1 Materials Used for Optics

Aluminum reflection coefficients were obtained from the CRC Handbook of Chemistry and Physics.[12] Over the range of interest, reflectance varies from R_{Al} = 0.9906 at 484 cm^{-1} to R_{Al} = 0.9817 at 4033 cm^{-1}.[12, 17] Because there is no refraction at mirrors (there is no transmission) we can assume that reflection from the front surface of Al mirrors is the same regardless of the angle of incidence. This simplifies the problem of estimating reflection losses.

The beamsplitter is made from two relatively thick KBr windows with a layer of germanium coated on one of them. The beamsplitter efficiency should take into account the transmittance and reflectance properties of KBr and Ge. The transmittance of Ge (T_{Ge}) is about 47% and reflectance (R_{Ge}) is approximately 40% in the principal region of transparency, which is from 800 to 5000 cm^{-1},[17, 18] which also corresponds with the spectral range of the FTIR system employed for the studies described here. The transmittance of KBr (T_{KBr}) exceeds 87%, making it a practical window material in systems where sensitivity to moisture is unimportant. In fact, KBr

is the most commonly used material for FTIR beamsplitters.[19] Reflectance of KBr in the relevant spectral region (R_{KBr}) is about 7%.[17]

Zinc selenide is a practical environmental chamber window material because it is stable at high temperatures (melting point exceeds 1100 °C [12]) and does not absorb moisture, which may be released when some samples are heated. Transmission ranges for KBr and ZnSe extend beyond the wavenumber range of FTIR instruments. Within the most useful range of the instrument (4000 to 800 cm^{-1}), the transmittance of ZnSe (1 – 12 mm thick) (T_{ZnSe}) exceeds 72%.[20]

2.4.2 Maximum Optical Throughput of the FTIR Spectrometer

The opening in the water-cooled sleeve around the infrared source subtends a solid angle Ω that is large enough to expose the entire surface of mirror (1) to infrared radiation (Figures 2.7 and 2.8). The radiation collected by the first mirror represents the maximum radiant power for the spectrophotometer (Φ). Over the measurement wavenumber range (4000 to 800 cm^{-1}), and based on the wavenumber dependent reflectance of aluminum, at least 98% of the incident radiation will be reflected to mirror (2). The same is true for subsequent mirror reflections. By utilizing phosphor paper to visualize the infrared beam, it was apparent that the entire surface of mirrors (1) – (3) is irradiated with infrared radiation. Mirrors (1) and (2) are orientated at a 90° angle to each other, so that most of the collimated radiation reflected from mirror (1) is captured by mirror (2). Mirrors (2) and (3) are placed in parallel planes such that the focal points of the two mirrors are superimposed. A collimated beam irradiates mirror (2) and is focused at the focal point of mirror (3), so that the radiation leaving mirror (3)

and directed into the interferometer is also collimated (3). This design minimizes stray light passing to the interferometer, and provides a convenient location for an aperture (at the mirror (2) and (3) focal points), which could be used to control the amount of light passing through the instrument.

Thus, the fraction of infrared source radiance reaching the beamsplitter must be at least:

$$\Phi \times 0.98^3 = 0.94\Phi \tag{2.11}$$

Considering the interferometer (4), the incident collimated beam first strikes the beamsplitter (4a). To make sure the entire beamsplitter is irradiated in the interferometer, the diameter of the projected area of the beamsplitter opening is smaller than the diameter of the collimated beam. Based on the dimensions of mirror (3) and the beamsplitter, it is estimated that only ~ 96% of the beam from mirror (3) enters the interferometer (4) (see Appendix C.1 for calculations). Considering that only 0.94Φ was reflected from mirror (3), only

$$0.94\Phi \times 0.96 = 0.90\Phi \tag{2.12}$$

enters the interferometer (4).

The collimated beam from mirror (3) passes through the KBr layer and then is split into two fractions by the Ge layer. Thus, about ~ 50% of the radiation is reflected to the stationary cube corner retroreflector and ~ 50% is transmitted through the beamsplitter to the moving cube corner retroreflector. The fraction of incident radiation reflected to the stationary retroreflector can be approximated by taking into account the reflectance of KBr (R_{KBr}), transmittance through KBr (T_{KBr}), reflection from Ge (R_{Ge}), and subsequent transmission through KBr (T_{KBr}).

$$\text{Fraction reflected to (4b)} = R_{KBr} + T_{KBr}^2 \times R_{Ge} \quad (2.13)$$

The fraction transmitted through the beamsplitter and to the moving cube corner retroreflector can be approximated similarly by considering T_{KBr} and T_{Ge}:

$$\text{Fraction transmitted to (4c)} = T_{KBr}^2 \times T_{Ge} \quad (2.14)$$

At each cube corner retroreflector, the beam strikes a reflective surface (R(Al) = 0.98) twice, hence a 0.98^2 fraction of the beam is reflected from each retroreflector back to the beamsplitter. The radiation reflected from (4b) is split again when it returns to the beamsplitter (4a): one fraction is reflected back to the source, and another fraction is transmitted to mirror (5). Radiation reflected from (4c) is split similarly: a fraction is transmitted through the beamsplitter to the source, and a fraction reflects from the beamsplitter (4a) and is directed towards mirror (5). It follows that the intensity of the beam incident to mirror (5) is the sum of the intensities of the two half-beams, which recombines into a single collimated beam. When the two half-beams recombine, their intensities are practically equal, but only when the beams are in phase. Thus, considering that only 0.90 Φ undergoes modulation, the maximum amount of radiation reaching mirror (5) can be estimated as follows:

$$0.90\ \Phi \times 2 \times (R_{KBr} + T_{KBr}^2 \times R_{Ge}) \times R_{Al}^2 \times (T_{KBr} \times T_{Ge}) =$$

$$0.90\ \Phi \times 2 \times (0.07 + 0.87^2 \times 0.40) \times 0.98^2 \times (0.87^2 \times 0.47) = 0.23\ \Phi \quad (2.15)$$

Note that this estimate does not assume a thickness for the KBr optical flat or the Ge layer, and assumes that the radiation reflected from these surfaces is, in fact, directed towards the intended surfaces, rather than lost due to scattering or changes in direction due to refraction. Although the beamsplitter KBr windows correct for beam path shifting caused by the high refractive index of Ge (n = 4.0)[17] it is important to

remember that the optical properties of the beam and its mode of interaction with the window and mirror materials vary as a function of wavenumber.

There is a change in intensity of the beam when the two half-beams recombine in and out of phase with each other when the moving retroreflector is in motion. Tomas Hirschfeld postulated that the power (relative to input) of the transmitted (T) and reflected (R) beams can be determined from the beamsplitter reflectance R_B and the relative phase ϕ of the interferometer's moving mirror for each wavelength using the equations [21]:

$$T = 2R_B(1 - R_B)(1 + \cos\phi) \tag{2.16}$$

$$R = R_B^2 + (1 - R_B)^2 + 2R_B(1 - R_B)\cos\phi \tag{2.17}$$

Integrating these equations over many cycles of ϕ results in an average of 50% transmittance and reflectance over the entire spectral range. At each particular wavelength, T and R vary between 0 and 50%, depending on moving retroreflector position.

The diameter of the opening to the sample compartment is large enough to accommodate the collimated beam travelling from the interferometer (4) to mirror (5). Following the interferometer, aluminum front surface reflection mirror (5) is mounted at a 45° angle relative to the path of the collimated and modulated beam and the path to the sample holder, allowing the beam to make a 90° turn. Mirror (5) is large enough to capture the entire collimated beam, so the projected area of the beam is limited by the beamsplitter (see Appendix C.2). From mirror (5), the beam travels to mirror (7) when the DRA sample accessory is not installed. Mirrors (5) and (7) are F/1 mirrors. For an F/1 mirror, the focal length equals the limiting diameter.[4] The beam is transmitted in

the horizontal plane, so the width of the mirrors acts as the limiting diameter, and at 45° angles the projected area of the parabolic mirrors appears circular (i.e. the projected width and height are equal). Mirrors (5) and (7) share the same focal point, they are placed symmetrically about the optimal sample location, which is about 6.0 inches from the centers of both mirror (5) and mirror (7) (Appendix C.3) at 45° from the normal to each mirror surface, as shown in Figure 2.7.

Mirror (7) collimates the beam and reflects it to mirror (8), where the beam is focused on the detector window. Considering the dimensions of mirrors (7) and (8), as well as the dimensions of the aperture between the front and rear instrument compartments, it appears that there are no geometrical restrictions (apertures) in the path of the beam from mirror (5) to the detector (Appendix C.4). The detector window transmission efficiency is ~ 85% [15].

Thus, an estimated transmission efficiency for the FTIR optical system employed in these studies is 9.22% (Table 2.1), which is close to the a previously published estimate of 9.75% for a typical FTIR spectrophotometer.[15]

Table 2.1 Estimated Optical Transmission Efficiency of the FTIR Spectrometer.

Without the DRA:	Transmission efficiency factor	Percent Source Radiance Transmitted
Source radiance		100.00%
Mirror (1) R_{Al}	0.98	98.00%
Mirror (2) R_{Al}	0.98	96.04%
Mirror (3) R_{Al}	0.98	94.12%
Beamsplitter: $A_{p\,4a}$ / $A_{p\,M3}$, geometrical limitation	0.96	90.48%
Interferometer optics transmission	0.25	23.05%
Integrated intensity decrease due to interference of the two half-beams	0.5	11.52%
Mirror (5) R_{Al}	0.98	11.29%
Mirror (7) R_{Al}	0.98	11.07%
Mirror (8) R_{Al}	0.98	10.85%
Detector window	0.85	**9.22%**

2.4.3 Maximum Optical Throughput of the "Praying Mantis" Diffuse Reflection Accessory

When the "Praying Mantis" diffuse reflection accessory (DRA) is placed in the path of the infrared beam, optical throughput decreases. To estimate the transmission efficiency of the DRA optics, a sample reflectivity of 100% was assumed. When the diffuse reflection accessory is installed between mirror (5) and mirror (7) (Figure 2.8), the beam first encounters mirror (6-1), a small (less than 1 in^2) aluminum on glass front surface reflection plane mirror. The distance from mirror (5) to mirror (6-1), center to center, is about 4.40 in, and the angle between these mirrors is approximately 45° in the horizontal plane. The distance and angle vary somewhat depending on the position of

mirror (6-1), because it is adjustable. Based on these values, the area of mirror (6-1) is large enough to capture the beam from mirror (5) and transmit it to mirror (6-2) (Appendix C.5).

From mirror (6-1) the beam goes to mirror (6-2), which is a plane mirror with the same construction as mirror (6-1). The distance between mirror (6-1) and mirror (6-2), center to center, is 3.66 in. The 45° off-axis focal point of mirrors (5) and (7), which was at the sample holder without the DRA, is now between mirrors (6-1) and (6-2). Similar calculations were applied to determine that the dimensions of mirrors (6-2) and (6-3) are sufficient to transmit the beam from mirror (6-1) without geometrical losses (Appendix C.6).

Thus, the DRA does not pose geometrical limitations on the transmission of the infrared beam. However, each of the mirrors (6-1) – (6-6) reflects at most 98% of incident radiation due to aluminum reflectivity. As previously noted, the ellipsoid (6-3) focuses the beam on the sample, whereas mirror (6-4) is used to collect up to 20% of the radiation diffusely reflected from the sample. Thus, mirror (6-4) captures up to 20% of the 2π sr (hemisphere) reflection by the sample. Mirrors (6-5) and (6-6) are the same as mirrors (6-2) and (6-1), respectively, and direct the beam to mirror (7).

When the "Praying Mantis" diffuse reflection accessory is installed and aligned, the overall signal intensity should decrease because of a minimum of 82.28% reduction of the radiant power that was incident to mirror (6-1) (Table 2.2). The greatest loss of throughput occurs between the sample and ellipsoid mirror (6-4), which only collects 20% of the diffusely reflected radiation.

Table 2.2 Estimated Optical Transmission Efficiency of the "Praying Mantis" DRA.

"Praying Mantis" diffuse reflection accessory	Transmission efficiency factor	Percent Source Radiance Transmitted
Radiation incident on mirror (6-1)		100.00%
Mirror (6-1) R_{Al}	0.98	98.00%
Mirror (6-2) R_{Al}	0.98	96.04%
Mirror (6-3) R_{Al}	0.98	94.12%
Sample	1	94.12%
Mirror (6-4): $\Omega_{M(6-4)} / 2\pi$	0.2	18.82%
Mirror (6-4) R_{Al}	0.98	18.45%
Mirror (6-5) R_{Al}	0.98	18.08%
Mirror (6-6) R_{Al}	0.98	**17.72%**

2.4.4 Optical Throughput Losses in Variable Temperature Experiments

2.4.4.1 Environmental chamber

In order to conduct *in-situ* variable temperature experiments, the sample must be housed in an environmental chamber, which can be used to maintain a controlled atmosphere and/or non ambient temperatures and pressures.[22] The system characterized here was equipped with a modified Harrick Scientific Inc. vacuum chamber (HVC-DRP). The chamber and post-factory modifications are described in detail in section 2.1.2 and in [1]. The environmental chamber lid (Figure 2.4) incorporates two ZnSe windows positioned perpendicular to the radiation travelling between the ellipsoid mirrors and the sample to eliminate specularly reflected radiation at these windows.[22] The infrared beam passes through ZnSe twice, once when

travelling to the sample, and once from the sample to the radiation collecting ellipsoid (6-4).

According to the manufacturer,[22] the diameter of the ZnSe windows is 15 mm, and the windows are secured to the chamber with compression nuts with an inner diameter of 12 mm (measured). The visible area of each window is thus:

$$A_{ZnSe} = \pi\, r_{ZnSe}^2 = \pi\, (6\text{ mm})^2 = 113\text{ mm}^2 = 0.175\text{ in}^2 \qquad (2.18)$$

The ZnSe windows define the limiting solid angle of the radiation transmitted into the chamber from ellipsoid (6-3) and out of the chamber to the collecting ellipsoid (6-4). The measured distance from the sample to each of the ZnSe windows $r_{chamber}$ is about 12 mm. Thus, the limiting solid angle is:

$$\Omega_{ZnSe} = A_{ZnSe} / (r_{chamber})^2 = (113\text{ mm}^2) / (12\text{ mm})^2 = 0.785\text{ sr} \qquad (2.19)$$

Considering that each ellipsoid mirror subtends 20% of the 4π sr solid angle:

$$\Omega_{\text{ Ellipsoids}} = 0.2 \times 2\pi = 1.26\text{ sr} \qquad (2.20)$$

The decreased throughput through the windows, Ω_{ZnSe}, can be calculated by:

$$\Omega_{ZnSe} / \Omega_{\text{ Ellipsoids}} = 0.785\text{ sr} / 1.26\text{ sr} = 0.623 \qquad (2.21)$$

The optical properties of ZnSe further decrease optical throughput, because T_{ZnSe} = 0.72 in the wavelength range of interest.[12] However, refraction effects are negligible because radiation impinges on the windows at normal incidence.

Overall, when the environmental chamber is installed, optical throughput decreases by a factor of about 5, as shown by Table 2.3.

Table 2.3 Estimated Optical Transmission Efficiency of the Harrick Inc. Environmental Chamber.

Harrick Scientific Inc. environmental chamber	Transmission efficiency factor	Percent Source Radiance Transmitted
Radiation reflected from (6-3)		100.00%
Ω_{ZnSe} / $\Omega_{Ellipsoids}$ from (6-3) to sample	0.62	62.30%
T (ZnSe)	0.72	44.86%
Sample	1	44.86%
Ω_{ZnSe} / $\Omega_{Ellipsoids}$ from sample to (6-4)	0.62	27.95%
T (ZnSe)	0.72	**20.12%**

2.4.4.2 Thermal insulation of the rear instrument compartment

Experiments have shown that a thermal barrier between the sample chamber and the source-interferometer-detector compartment of the instrument is advantageous for VT-DRIFTS experiments. This decreases interferometer alignment variations and sample temperature induced decreases in signal intensity due to detector response from unmodulated infrared sample emission radiation.

Infrared transparent KBr windows were mounted between (4) and (5), and between (7) and (8) by using magnets to achieve attachment and seal, as shown in Figure 2.9.

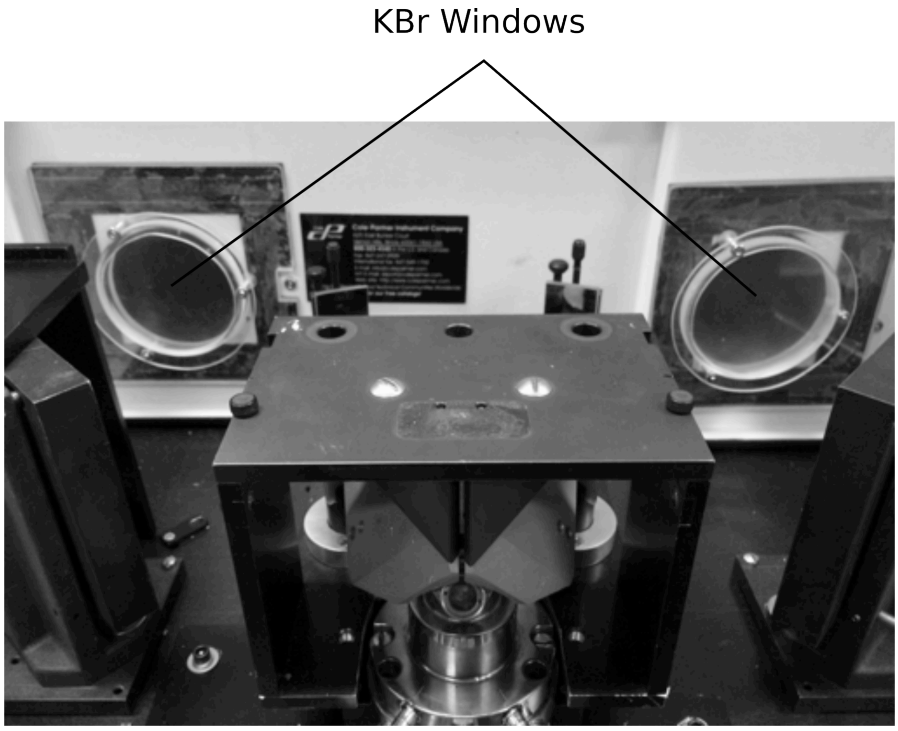

Figure 2.10 Sample compartment isolation by using KBr windows.

The diameter of the windows (3 in) yields a projected area (7.07 in^2) that is larger than the projected area of the collimated beam passing through them (4.20 in^2). However, some radiation intensity is lost due to limited KBr transmittance.

Because the collimated infrared beam is perpendicular to KBr window surfaces, refraction and reflection losses are minimal. Assuming that the thickness of the KBr windows has minimal effect on transmittance, then $T = 87\%$. Thus, these two KBr windows reduce optical throughput by 24.31% (Table 2.4).

Table 2.4 Optical Throughput of the KBr Windows Between Compartments.

KBr windows for thermal insulation of the rear instrument compartment.	Transmission efficiency factor	Percent Source Radiance Transmitted
Throughput without KBr separators		100.00%
T (KBr)	0.87	87.00%
T (KBr)	0.87	**75.69%**

2.4.4.3 Partially blocked beam method to eliminate sample emission artifacts

The "partially blocked beam method," [23], can be employed for interferometers incorporating cube corner retroreflectors to eliminate negative interferograms that result from sample emission at high temperatures. This method requires that one-half of the collimated beam be blocked, which eliminates the path for this unwanted radiation through the interferometer and back to the detector. When using this method, optical throughput is decreased by 50%.

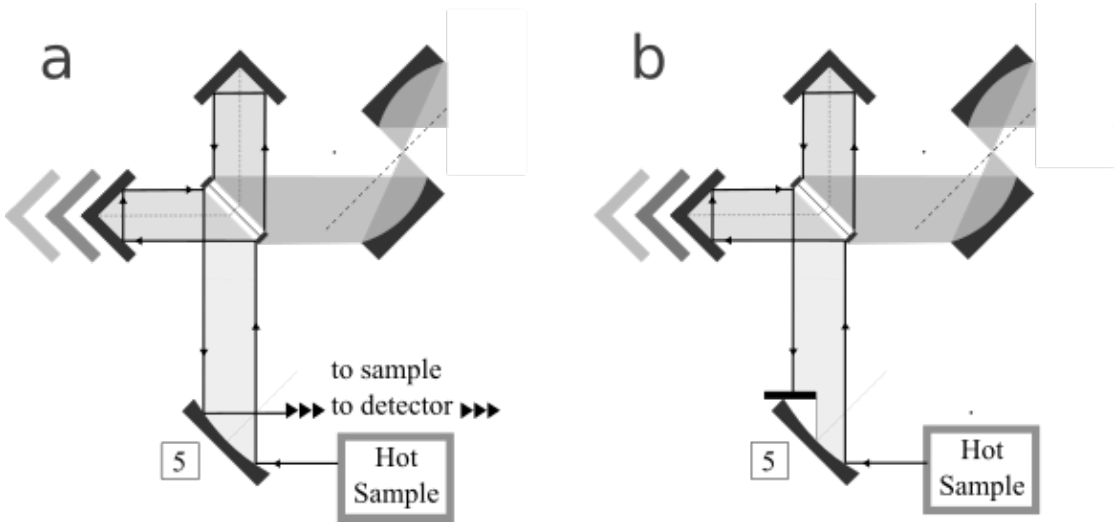

Figure 2.11 Illustration of the partially blocked beam method for eliminating modulated sample emission.

2.4.4.4 Summary

Based on estimates made here, the transmission efficiency of the FTIR optical system when equipped with the "Praying Mantis" DRA should be:

$$9.22\% \times 17.22\% = 1.59\% \tag{2.22}$$

When additional components are installed that are required for VT-DRIFTS measurements, transmission efficiency further decreases by more than a factor of 10:

$$1.59\% \times 20.12\% \times 75.69\% \times 50.00\% = 0.121\% \tag{2.23}$$

Due to high detector sensitivity[7, 10, 24] spectra collected at this low throughput are still informative [16]. However, with increasing sample temperatures, SNR rapidly decreases due to detector properties, alignment fluctuations, and other temperature-dependent changes. The VT-DRIFTS methodology is highly sensitive, detailed, informative, and convenient, but could be improved if the effects of sample heating were eliminated or reduced. This is the focus of the investigations described in this dissertation.

2.5 References

1. White, D.R. and R.L. White, Isoconversion effective activation energy profiles by variable temperature diffuse reflection infrared spectroscopy*, Applied Spectroscopy*, **62**(1), p. 116-120 (2008).

2. White, R.L., Removal of Baseline Artifacts from Variable-Temperature Diffuse Reflectance Infrared Spectra*, Analytical Chemistry*, **64**(17), p. 2010-2013 (1992).

3. White, R.L. and J. Ai, Variable-Temperature Diffuse Reflectance Infrared Studies of Calcium Oxalate Monohydrate*, Applied Spectroscopy*, **46**(1), p. 93-99 (1992).

4. Ingle, J.D. and S.R. Crouch, *Spectrochemical Analysis*, Prentice Hall: New Jersey (1988).

5. Skoog, D.A., F.J. Holler, and S.R. Crouch, *Principles of Instrumental Analysis*, 6th ed., Thompson Brooks/Cole: Belmont, CA (2007).

6. Rogalski, A., *Comparison of Photon and Thermal Detector Performance*, in *Handbook of Infrared Detection Technologies*, M. Henini and M. Razeghi, eds., Elsevier Advanced Technology: Oxford, UK (2002) p. 5-23.

7. *HgCdTe Detector. Serial # J-5385-2*, technical data, InfraRed Associates, Inc.: New Brunwick, NJ (1985).

8. White, R.L., Requirements for Thermal Analysis by Variable-Temperature Diffuse Reflectance Infrared Spectroscopy*, Applied Spectroscopy*, **46**(10), p. 1508-1513 (1992).

9. Handke, M., M. Milosevic, and N.J. Harrick, External Reflection Fourier-Transform Infrared-Spectroscopy - Theory And Experimental Problems*, Vibrational Spectroscopy*, **1**(3), p. 251-262 (1991).

10. Milosevic, M. and S.L. Berets, A review of FT-IR diffuse reflection sampling consideration*, Applied Spectroscopy Reviews*, **37**(4), p. 347-364 (2002).

11. Maraoulaite, D.K., T.M. Nickels, A.L. Ingram, and R.L. White, VT-DRIFTS Investigations of Interactions Between Benzoic Acid and Montmorillonite Clay, *Spectroscopy*, **30**(10), p. 2-8 (2015).

12. *CRC Handbook of Chemistry and Physics*, 96th ed., CRC Press, 2015-2016, www.hbcpnetbase.com. Accessed 6 Dec. 2015.

13. *UV-VIS Spectrophotometry: Diffuse Reflectance Accessories*, data sheet, Harrick Scientific Corporation: Ossining, NY (1985).

14. *Praying Mantis™ Diffuse Reflection Attachment*, data sheet, Harrick Scientific Corporation: Ossining, NY (1997).

15. Hirschfeld, T., Ideal FT-IR Spectrometers and the Efficiency of Real Instruments, *Applied Spectroscopy*, **40**(8), p. 1239-1240 (1986).

16. Nickels, T.M., A.L. Ingram, D.K. Maraoulaite, and R.L. White, Variable Temperature Infrared Investigation of Benzoic Acid Interactions with Montmorillonite Clay Interlayer Water, *Applied Spectroscopy*, **69**(7), p. 850-856 (2015).

17. Wakaki, M., K. Kudo, and T. Shibuya, *Physical Properties and Data of Optical Materials*, CRC Press, Taylor & Francis Group: Boca Raton, FL (2007).

18. *Germanium (Ge)*, data sheet, The University of Reading, Infrared Multilayer Laboratory, 2001, www.reading.ac.uk/infrared/library/infraredmaterials/ir-infraredmaterials-ge.aspx. Accessed 14 Dec. 2015.

19. *Potassium Bromide (KBr)*, data sheet, Crystran Ltd., 2012, www.crystran.co.uk/optical-materials/potassium-bromide-kbr. Accessed 6 Dec. 2015.

20. *Zinc Selenide (ZnSe)*, data sheet, Crystran Ltd., 2012, www.crystran.co.uk/optical-materials/zinc-selenide-znse. Accessed 6 Dec. 2015.

21. Hirschfeld, T., *Quantitative FT-IR: a Detailed Look at the Problems Involved*, in *Fourier Transform Infrared Spectroscopy*, J.R. Ferraro and L.J. Basile, eds., Academic Press, Inc.: London (1979) p. 193-242.

22. *Vacuum Chamber for DRA HVC-DRP*, data sheet, Harrick Scientific Corporation: Ossining, NY (1984).

23. Tripp, C.P. and R.A. McFarlane, Discussion of the Stray Light Rejection Efficiency of FT-IR Spectrometers: The Effects of Sample Emission on FT-IR Spectra*, Applied Spectroscopy*, **48**(9), p. 1138-1142 (1994).

24. *Mercury Cadmium Telluride Detectors*, data sheet, Teledyne Judson Technologies LLC: Mongomeryville, PA (2002).

Chapter 3: Effects of Sample Heating on Infrared Spectral Features

Experiments were conducted to assess the effects of DRIFTS sample holder and optics heating on infrared spectral features such as band intensity and band shape. Ideally, these tests could be performed by analyzing a sample by VT-DRIFTS that did not undergo a change in structure during heating. Unfortunately, the physical and/or chemical properties of most if not all powdered samples are temperature dependent. Even if no chemical structure changes occur, particles may move, cleave, or aggregate, resulting in a scattering coefficient change. Therefore, experiments were designed in which the sample holder and DRIFTS optics were heated, but the sample was not. Experiments were conducted by placing a polystyrene film sample in the beam path, but located away from the VT-DRIFTS sample holder and optics. In this way, a heating program could be executed, but the sample composition would not change, because it was not heated. Therefore, any observed spectral changes could be attributed to sample holder heating.

Silver powder (99.95% pure) was loaded into the sample holder to achieve maximum sample reflectance. The detector was cooled with liquid N_2, and the instrument was purged with CO_2-free dry air for about one hour prior to experiments.

A Nicolet matte finish polystyrene film (reference No. 018297) supported by a cardboard sleeve with a circular opening of 1 inch diameter was used for VT-DRIFTS studies. The matte finish reduced the amplitude of interference fringes that are characteristic of smooth films. These fringes are caused by interference between radiation internally reflected at film surfaces and radiation transmitted through the sample. The thickness of the film was unknown, but estimated to be in the range of 0.03-0.038 mm based on comparisons with published spectra and information for similar samples.[1] The best infrared beam location for the film was determined to be inside the sample compartment of the instrument between mirrors (7) and (8) (See instrument diagram, Figure 2.8), based on SNR optimization. Temperature measurements made by using a data logger during sample holder heating showed that the temperature increase was minimal at that location. By monitoring the interferogram signal in real time and adjusting the position of the sample in the plane perpendicular to the infrared beam path, the film was positioned so that the entire 3.14 in^2 aperture was irradiated. It was previously determined that the infrared beam cross-sectional area between mirrors (7) and (8) was 4.20 in^2. Thus, the film sample was the limiting aperture when it was present. The film was attached to the metal frame of the instrument at the round opening between the sample compartment and detector by using a magnet. A photograph of the mounted film is shown in Figure 3.1.

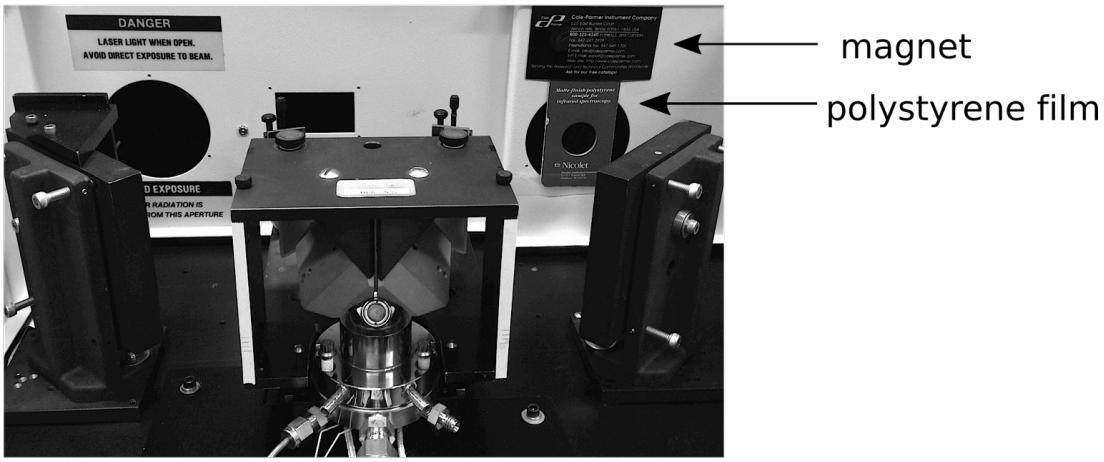

Figure 3.1 Experimental setup.

Figure 3.2 shows a diffuse reflectance spectrum of the polystyrene film measured at ambient temperature and represented in Kubelka-Munk units. The peaks in the spectrum were compared with information from the NIST.[2] The peaks are consistent with reference data with the exception of the peak at 1493.87 cm^{-1}, which may be due to UV-stabilizers or other additives often found in plastics. For spectrum evaluations, only peaks with intensity greater than 0.10 Kubelka-Munk units were used for comparisons.

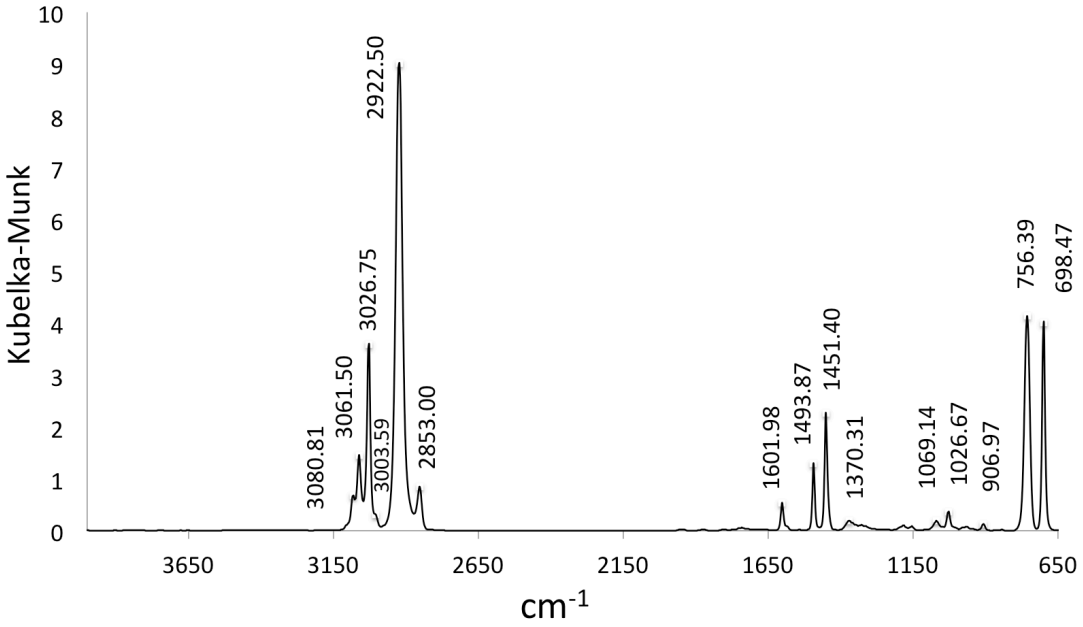

Figure 3.2 Kubelka-Munk spectrum of polystyrene film obtained at ambient temperature with Ag powder in the sample holder.

By identifying the wavenumbers with the highest absorption intensity closest to the corresponding polystyrene film absorptions reported by NIST, absorption peaks were identified in the spectrum (Table 3.1). The peak at 1493 cm^{-1} does not appear in the list of NIST peaks, but had high enough absorption intensity that it was included in the list.

Table 3.1 Polystyrene Absorption Peaks.

NIST Peak Location (cm^{-1})	Peak Location (cm^{-1})	Emissivity	Reflectance (%)	K-M Intensity
699.448	698.47	0.39	9.93	4.08
756.58	756.39	0.58	9.62	4.24
906.8025	906.97	5.55	59.39	0.13
1028.334	1026.67	4.98	43.16	0.37
1069.1485	1069.14	5.93	54.04	0.19
1368.527	1370.31	9.74	54.58	0.18
1449.675	1451.40	2.80	15.84	2.23
-	1493.87	4.09	23.03	1.28
1601.358	1601.98	6.21	36.95	0.53
2850.062	2853.00	2.45	29.43	0.84
2920.935	2922.50	0.35	4.49	10.30
3001.412	3003.59	3.87	46.38	0.30
3026.3975	3026.75	0.91	10.94	3.62
3060.025	3061.50	1.75	21.18	1.46
3082.208	3080.81	2.70	32.76	0.68

Peak locations (cm^{-1}) in Table 3.1 were determined by examining single beam spectra and identifying wavenumbers corresponding to the lowest emissivity over a small range of wavenumbers spanning each peak. For the small shoulder at 3003.59 cm^{-1}, the inflection point was used to identify the peak location. Due to the inherent laser reference wavelength calibration of FTIR instruments, spectrum wavenumber reproducibility was ± 0.02 cm^{-1}. For 50 measured spectra, peak minimum locations were 100% reproducible for all except for the peak at 2922.50 cm^{-1}.

The peak at 2922.50 cm^{-1} exhibited the highest absorptivity, therefore the signal reaching the detector was closest to zero (average emissivity at room temperature was

0.35). Over the 2864.58 – 2961.11 cm^{-1} range (approximate peak width at base) 26 data points defined this peak, and the lowest signal was found at 3 different wavenumbers (i.e. at 2918.64, 2922.5, and 2926.36 cm^{-1}) in the 50 acquired spectra. It is reasonable to select the middle of these values as the peak location for further discussion, and in fact, this value corresponded to the minimum in the majority of spectra. The peak at 698.47 cm^{-1} had a similar emissivity value (0.39), but this peak was narrower and spanned only 11 data points, so the minimum was more distinct. Figure 3.3 shows an overlay of the single beam spectra in the wavenumber regions near the 2922.50 (a) and 698.47 cm^{-1} (b) absorption peaks shown on the same scale (40 cm^{-1} width and emissivity range between 0.0 and 1.0). Figure 3.3 shows that absorption peak shape reproducibility can vary for peaks that have similar emissivities.

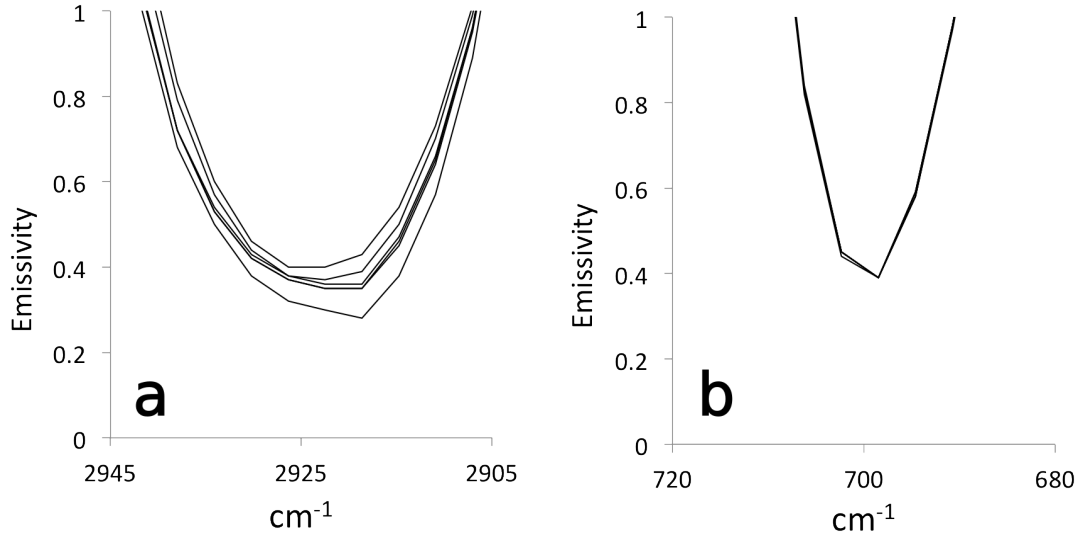

Figure 3.3 Overlay of single beam spectra a) centered at 2922.50 cm^{-1} and b) centered at 698.47 cm^{-1}.

A number of tools are available in the Mattson Instruments FTIR WinFirst operating software package for determining peak intensity. After the general location

of a peak is specified (by "point-and-click" or entering a wavenumber), the software either gives the y-value corresponding to the nearest data point (i.e. no peak picking filter), or calculates a value by spline interpolation or by finding the vertex of a parabola based on data points near the peak maximum. Although peak intensity values determined by the software were similar, calculated peak locations can vary. Table 3.2 lists the values obtained by the "peak picking" WinFirst tool.

Table 3.2 Calculated Peak Locations.

Peak picking filter	Peak wavenumber (cm^{-1})	Peak intensity, K-M
None	2922.50	9.02
3 point weighted average	2924.01	9.02
5 point weighted average	2923.99	9.02
Cubic spline fit	2924.05	9.07
½-max center (manual)	2923.61	9.03

3.1 Reproducibility at Ambient Temperature

To characterize instrument performance in the absence of sample heating, 50 spectra were successively collected (~ 1 spectrum/min) at ambient (i.e. room) temperature. Figure 3.4 shows an overlay of 6 single beam spectra over the 4000-650 cm^{-1} range collected in about 10 min increments. Polystyrene absorption peaks are clearly visible, and spectra overlay well, indicating high reproducibility at ambient temperature.

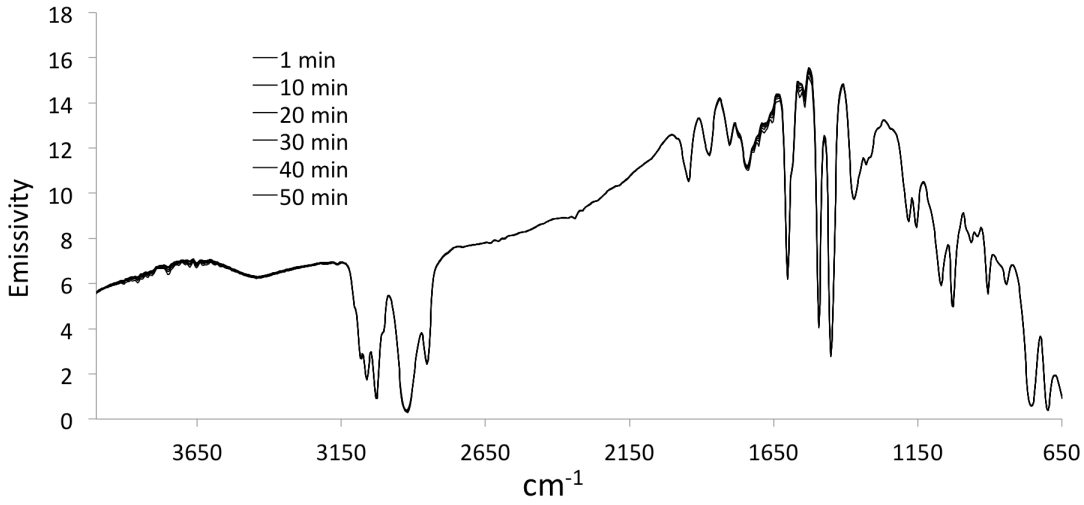

Figure 3.4 Overlay of single beam spectra collected at ambient temperature.

By dividing polystyrene film single beam spectra by a reference background spectrum (i.e. Ag powder at ambient temperature), reflectance spectra were obtained (Figure 3.5).

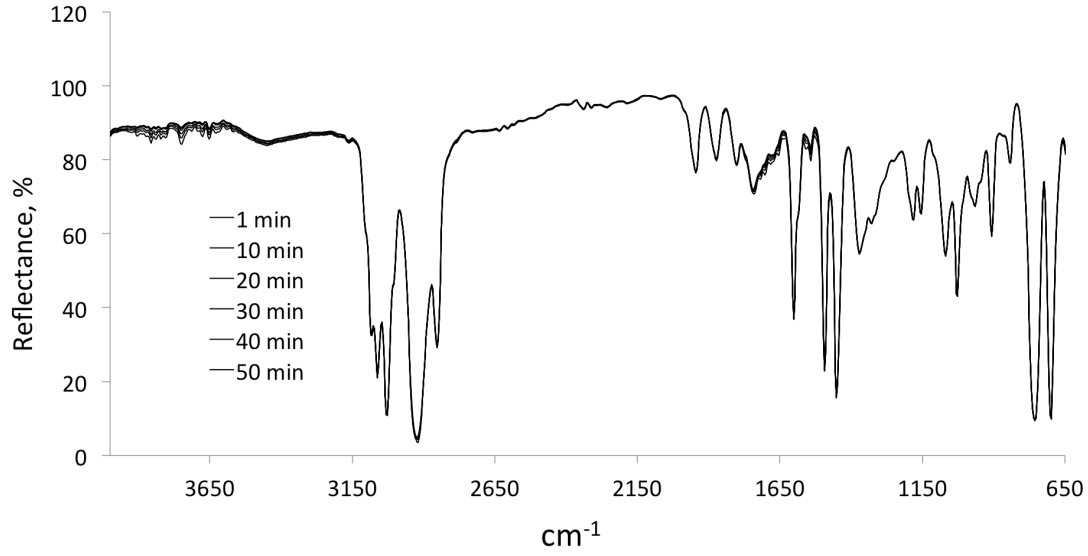

Figure 3.5 Overlay of reflectance spectra collected at ambient temperature.

Kubelka-Munk format spectra calculated from these reflectance spectra by using equation 1.33 are shown in Figure 3.6.

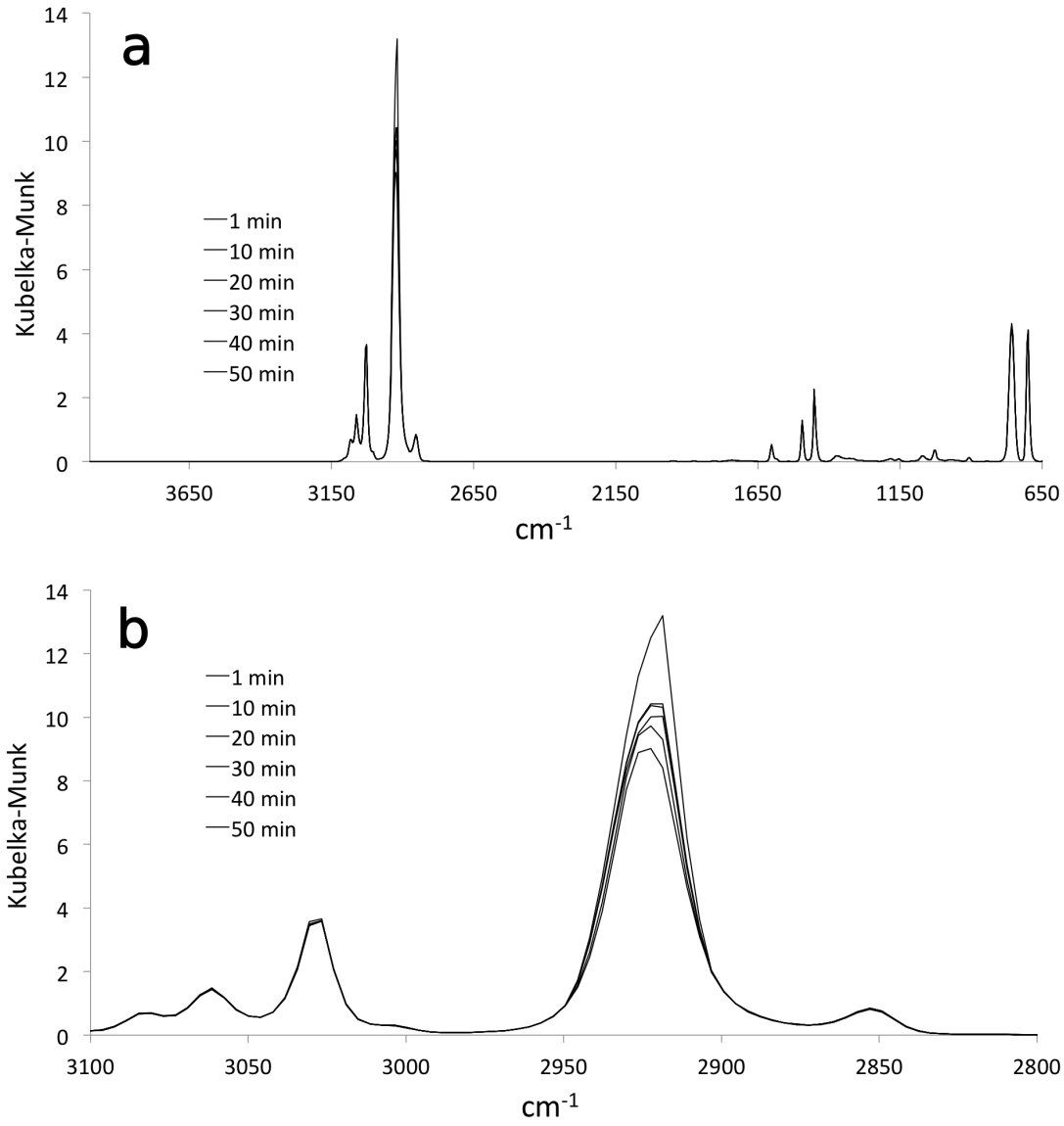

Figure 3.6 Overlay of diffuse reflectance spectra collected at ambient temperature; a) complete spectra and b) expansion of the C-H stretching region.

Although the overlaid spectra in Figures 3.4-3.6 should be identical, some differences in band intensities are apparent. To compare differences in peak reproducibility observed for various spectrum formats, C-H stretching regions of spectra are shown in emissivity, % reflectance, and Kubelka-Munk units in Figure 3.7.

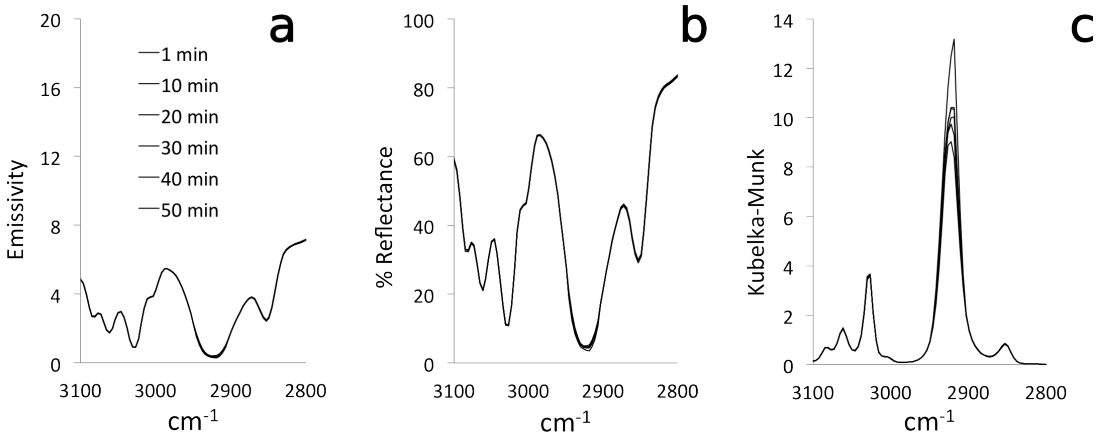

Figure 3.7 Overlay of the same ambient temperature C-H stretching region of spectra in a) emissivity, b) reflectance, and c) Kubelka-Munk format.

The differences in reproducibility apparent in Figure 3.7 can be quantified by computing point-by-point standard deviations for the 50 digitized spectra.

Figure 3.8 shows the single beam spectrum obtained by averaging all 50 single beam spectra (solid line) and a plot of standard deviations (dashed line) calculated at each digitized wavenumber. The largest emissivity changes were found near 1550 cm^{-1} and corresponded to the strongest absorptions. Fluctuations in the 3550 – 4000 and 1700 – 1500 cm^{-1} regions can be attributed to fluctuations in water vapor concentrations due to incomplete instrument purge.

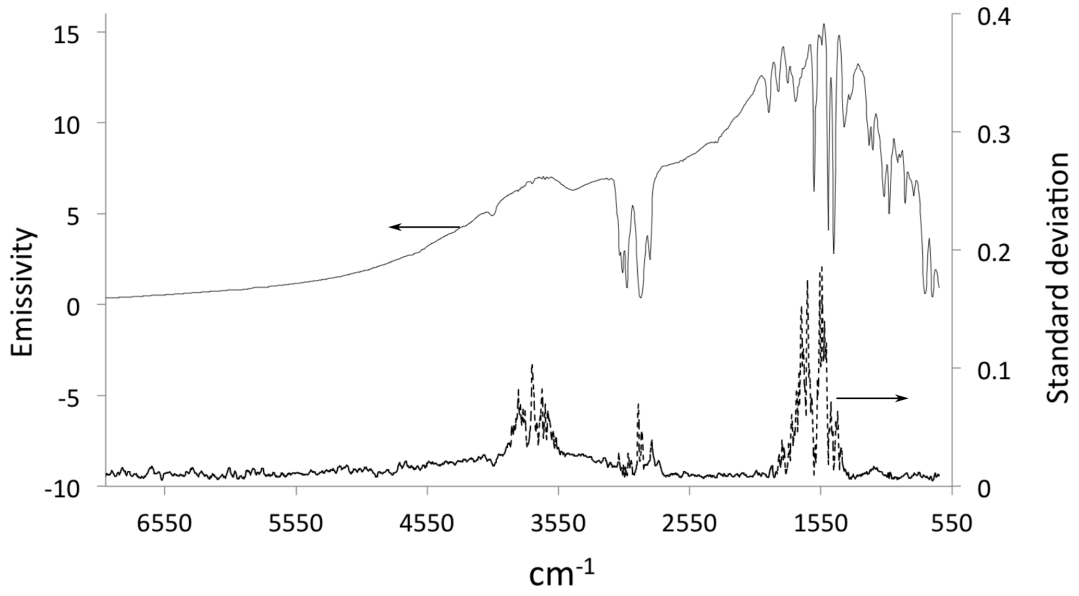

Figure 3.8 Average single beam spectrum and standard deviations at ambient temperature.

For reflectance spectra, similar fluctuations were observed. The average reflectance spectrum and the standard deviation plot are shown in Figure 3.9. Above 4000 cm^{-1}, reflectance spectrum noise increased because little radiation was reaching the detector at high wavenumbers (see section 2.2.2, Figures 2.5 and 2.6).

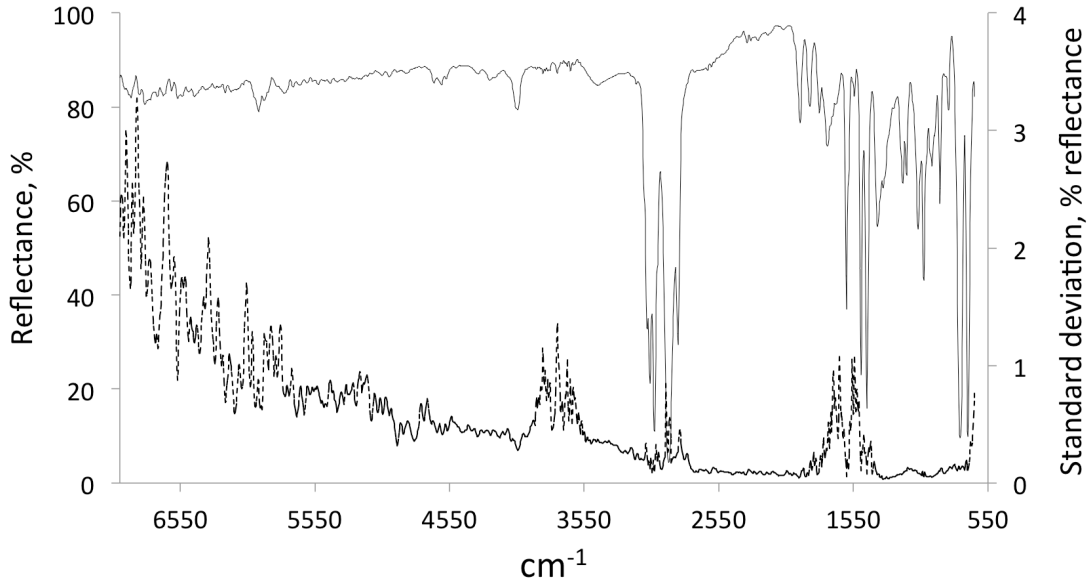

Figure 3.9 Average reflectance spectrum and standard deviations at ambient temperature.

For the 50 measured spectra, individual spectral intensities and associated standard deviations can be represented by: $I_{\mathrm{SBM}} \pm s_{\mathrm{SBM}}$, $I_{\mathrm{RAS}} \pm s_{\mathrm{RAS}}$, and $I_{\mathrm{DRT}} \pm s_{\mathrm{DRT}}$. I_{BKG} can be used to represent the background single beam spectrum intensity (i.e. reference) employed to convert single beam spectra to reflectance. Spectral fluctuations in reflectance and DRIFTS spectra can be estimated from error propagation calculations.[3]

When single beam spectra were converted to reflectance, relative standard deviation was conserved because the same reference single beam spectrum was used for all calculations (i.e. s_{BKG} was zero):

$$I_{\mathrm{RAS}} \pm s_{\mathrm{RAS}} = \frac{I_{\mathrm{SBM}} \pm s_{\mathrm{SBM}}}{I_{\mathrm{BKG}}\ (constant)} \tag{3.1}$$

$$\frac{s_{\mathrm{RAS}}}{I_{\mathrm{RAS}}} = \sqrt{\left(\frac{s_{\mathrm{SBM}}}{I_{\mathrm{SBM}}}\right)^2 + \left(\frac{0}{I_{BKG}}\right)^2} = \sqrt{\left(\frac{s_{\mathrm{SBM}}}{I_{\mathrm{SBM}}}\right)^2} = \frac{s_{\mathrm{SBM}}}{I_{\mathrm{SBM}}} \tag{3.2}$$

Accounting for error propagation when reflectance spectra were converted to Kubelka-Munk format, the relative standard deviation of intensities increased by a factor of 1.73:

$$I_{\mathrm{DRT}} \pm s_{\mathrm{DRT}} = \frac{(1 - I_{\mathrm{RAS}} \pm s_{\mathrm{RAS}})^2}{2\,(I_{\mathrm{RAS}} \pm s_{\mathrm{RAS}})} \tag{3.3}$$

$$\frac{s_{\mathrm{DRT}}}{I_{\mathrm{DRT}}} = \sqrt{\left(\frac{s_{\mathrm{RAS}}}{I_{\mathrm{RAS}}}\right)^2 + \left(\frac{s_{\mathrm{RAS}}}{I_{\mathrm{RAS}}}\right)^2 + \left(\frac{s_{\mathrm{RAS}}}{I_{\mathrm{RAS}}}\right)^2} = \sqrt{3\left(\frac{s_{\mathrm{RAS}}}{I_{\mathrm{RAS}}}\right)^2} = \sqrt{3}\,\frac{s_{\mathrm{RAS}}}{I_{\mathrm{RAS}}} \tag{3.4}$$

$$s_{\mathrm{DRT}} = \sqrt{3}\,\frac{s_{\mathrm{RAS}}}{I_{\mathrm{RAS}}}\,I_{\mathrm{DRT}} \tag{3.5}$$

Thus, for Kubelka-Munk spectra, absolute standard deviation is proportional to the intensity multiplied by 1.73 times the RSD of the corresponding reflectance. Thus, error is amplified in the Kubelka-Munk format and is larger for absorption bands with greater intensity. Consequently, the worst reproducibility was associated with the most intense absorption bands (Figure 3.10).

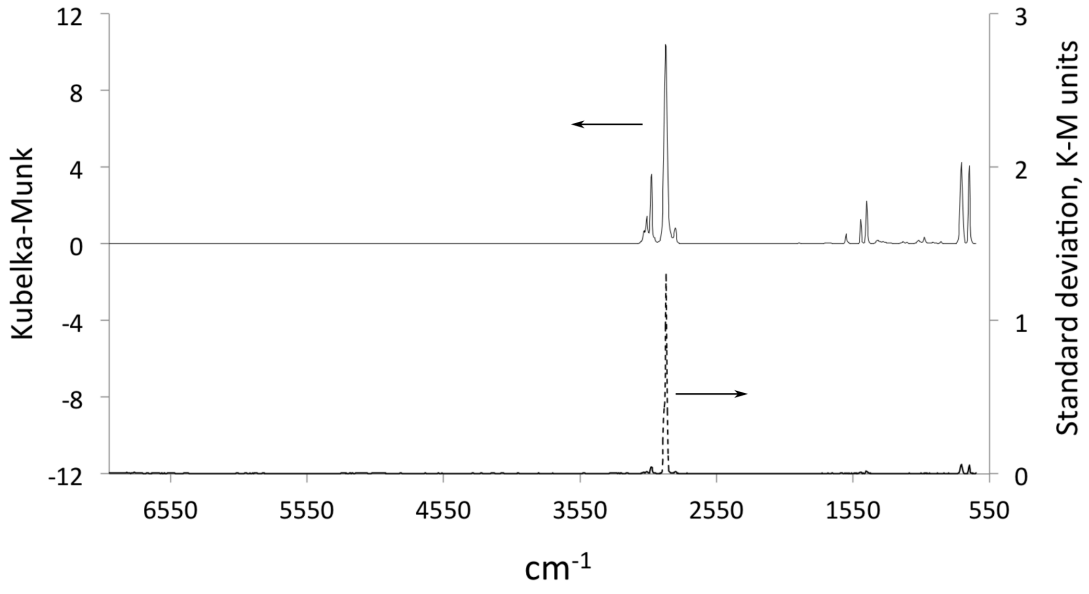

Figure 3.10 Average Kubelka-Munk spectrum and standard deviations at ambient temperature.

Therefore, small variations in signal intensity at the detector causes significant fluctuations in Kubelka-Munk spectrum peak intensity.

More detail regarding spectral fluctuations can be obtained by monitoring peak intensity changes as a function of time. Selected peak intensity trends are shown in Figure 3.11. The Kubelka-Munk intensity of the 2922.50 cm^{-1} peak is significantly greater than that for other peaks. Peak wavenumber locations are listed in the legend in decreasing order of absorption intensity. Changes were found to be largest for peaks with the greatest intensity.

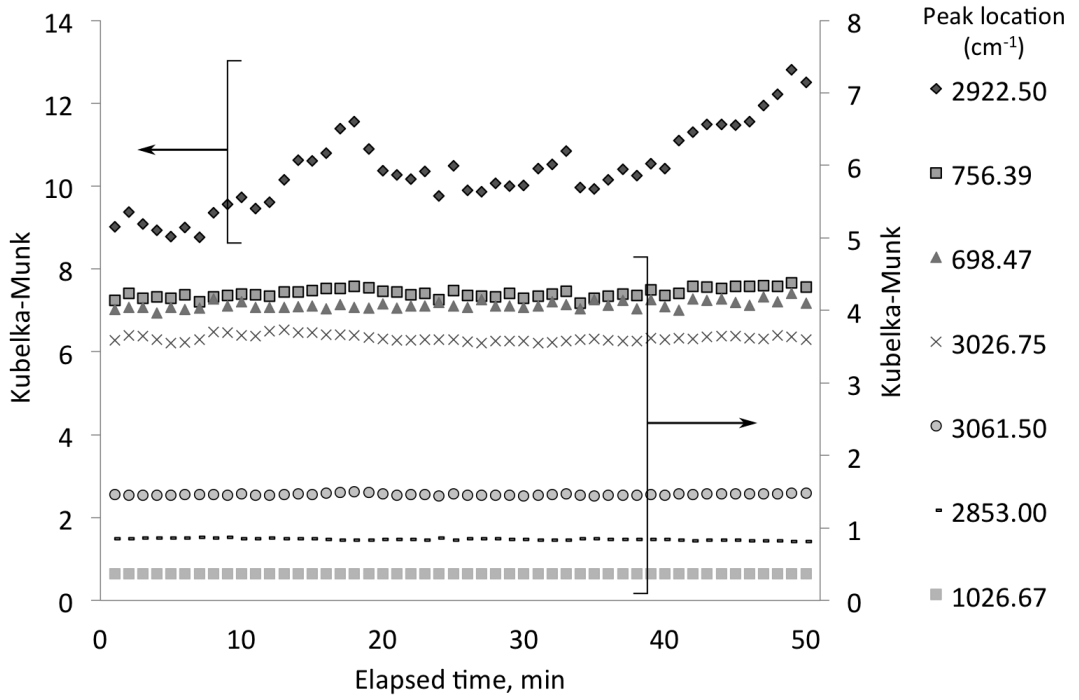

Figure 3.11 Elapsed time trends in Kubelka-Munk intensity at ambient temperature.

Whereas most peak intensity fluctuations represented small changes superimposed on a constant mean, a gradual increase in peak intensity was observed for the most intense peak (i.e. at 2922.50 cm^{-1}). Temperature-dependent factors may be responsible for this

gradual intensity increase. For example, if the liquid nitrogen cooled detector temperature was continuing to equilibrate over this period, interferogram voltages would gradually increase. This increase would preferentially impact more intense absorption peaks because less infrared radiation strikes the detector, so that small voltage changes would represent large relative signal fluctuations. This would explain why highly-absorbing peaks appear larger over time. In addition, gradual systematic spectral changes may be due to equilibration of the electronics temperature, which gradually increases with time to a constant value. Systematic changes to the instrument environment caused by purge gas temperature changes, or gradual source temperature changes could also affect peak intensities.

3.2 VT-DRIFTS Polystyrene Spectral Variations

After characterizing ambient temperature spectrum reproducibility, a heating program was initiated and 100 spectra were sequentially obtained while heating silver powder in the VT-DRIFTS sample holder from ambient temperature (26.4 °C) to 496.3 °C at 5 °C/min. Spectra were collected at about 1 minute intervals. Figure 3.12 shows that significant changes in single beam spectra over the 4000-650 cm^{-1} range occurred when the VT-DRIFTS sample holder was heated. Although polystyrene film absorptions were constant for all measurements, the single beam changes illustrated in Figure 3.12 lead to "apparent" reflectance spectrum changes.

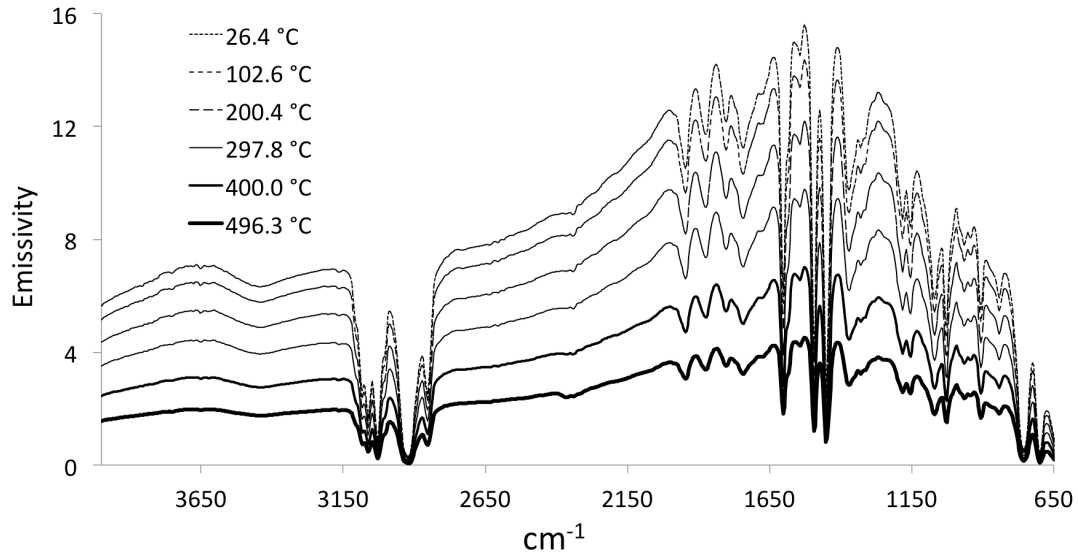

Figure 3.12 Overlay of polystyrene single beam spectra measured during VT-DRIFTS sample holder heating.

Results show that the single beam spectrum measured at ambient temperature exhibited the highest emissivity. Although absorption band locations appear to be the same in all spectra, the overall single beam intensity decreased significantly with increasing temperature.

Decreasing single beam intensity with increasing sample temperature has been previously reported for VT-DRIFTS measurements.[4, 5] It has been attributed to effects from unmodulated thermal emission and leads to a decrease in spectral SNR at higher temperatures. The magnitude of this effect depends on the type of detector employed.[4] With MCT detectors, as previously described, electrical conduction of the resistive element is positively correlated with the number of electrons promoted to the conduction band by heat energy. A constant current is passed through the detector (i.e. a DC bias), so the increase in conductance results in a voltage change.[6, 7] At higher detector temperatures (due to heating by unmodulated infrared emission)

background conductivity is higher than at ambient temperature, but infrared source emissivity remains constant. As a result, with increasing unmodulated radiation, the voltage change caused by modulated radiation incident to the resistive detector element decreases compared to its ambient temperature value, so the integrated area under the single beam spectrum decreases.

Converting single beam spectra into reflectance by dividing by a reference spectrum (Ag powder) produced the spectra shown in Figure 3.13. When spectra were divided by the reference, reflectance decreased with increasing temperature due to the gradual decrease in sample single beam emissivity with increasing sample holder temperature. This decreasing reflectance is also associated with a lower spectral SNR and baseline shifts. For the polystyrene reflectance spectra shown in Figure 3.13, baseline corrections can be achieved by adding back reflectance offset values. However, for real samples for which the baseline is obscured by absorption peaks, baseline changes may be more difficult to correct by post data collection methods.

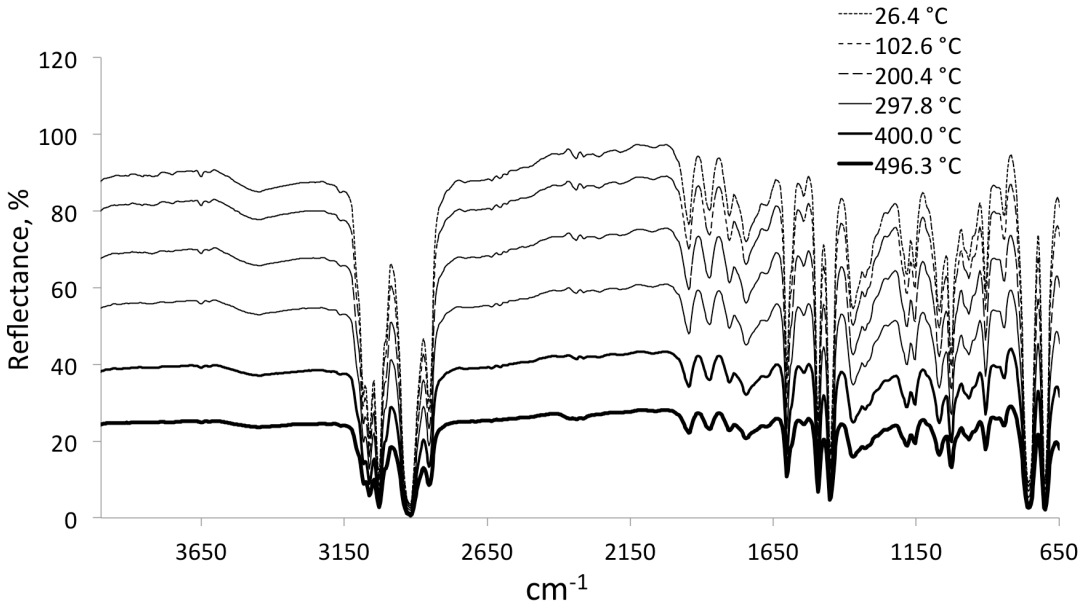

Figure 3.13 Overlay of VT-DRIFTS polystyrene reflectance spectra.

Transforming reflectance spectra with the Kubelka-Munk transform produced the results shown in Figure 3.14. Absorption band locations appear to be unchanged, but peaks and baselines do not overlap as well as when all measurements were made at ambient temperature. Kubelka-Munk spectral intensity significantly increased when single beam intensity decreased. For example, peak intensity for the largest peak (at 2922.50 cm^{-1}) was 12.8 Kubelka-Munk units at ambient temperature and 81.3 Kubelka-Munk units at 496.3 °C.

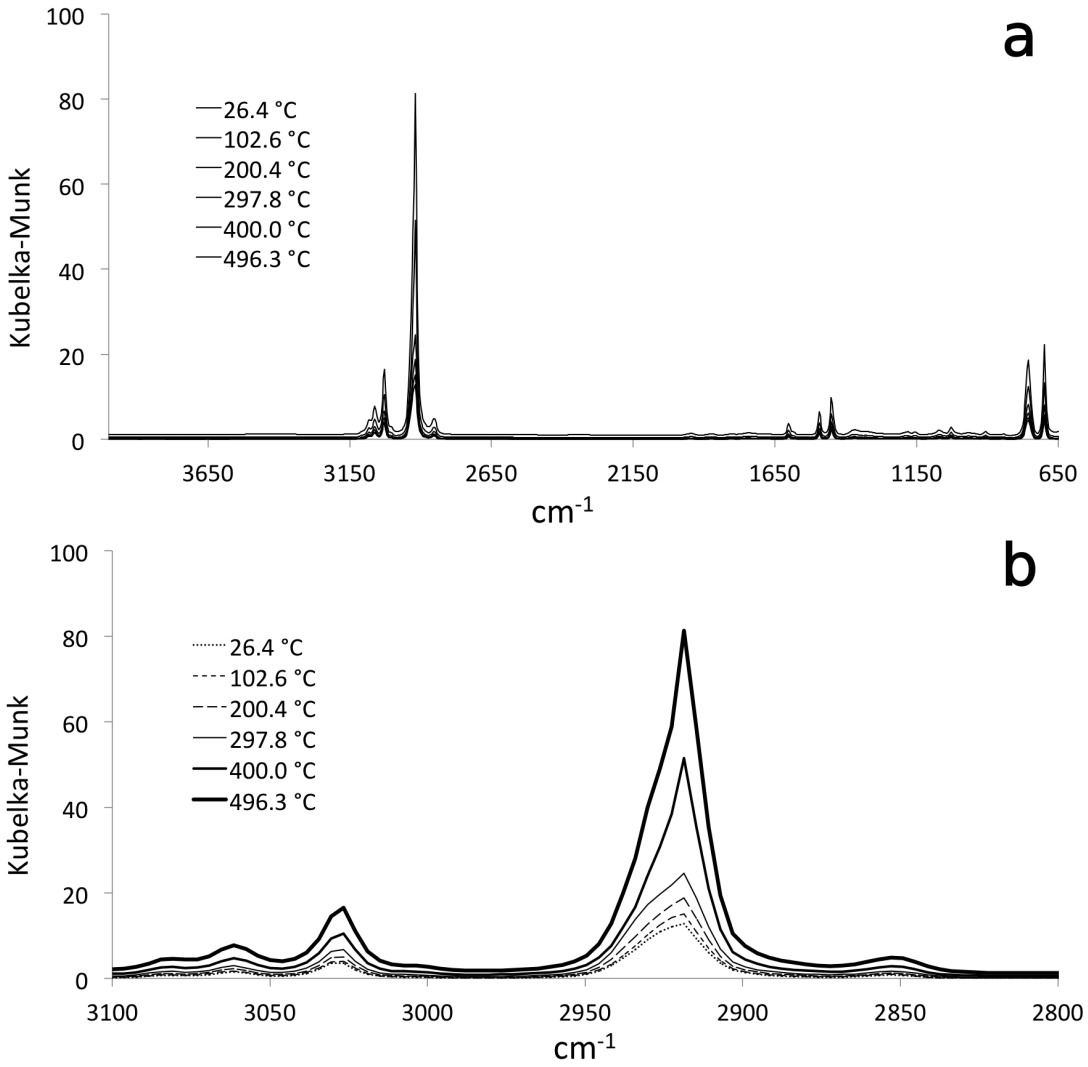

Figure 3.14 Overlay of VT-DRIFTS Kubelka-Munk results a) complete spectra and b) expansion of the C-H stretching region.

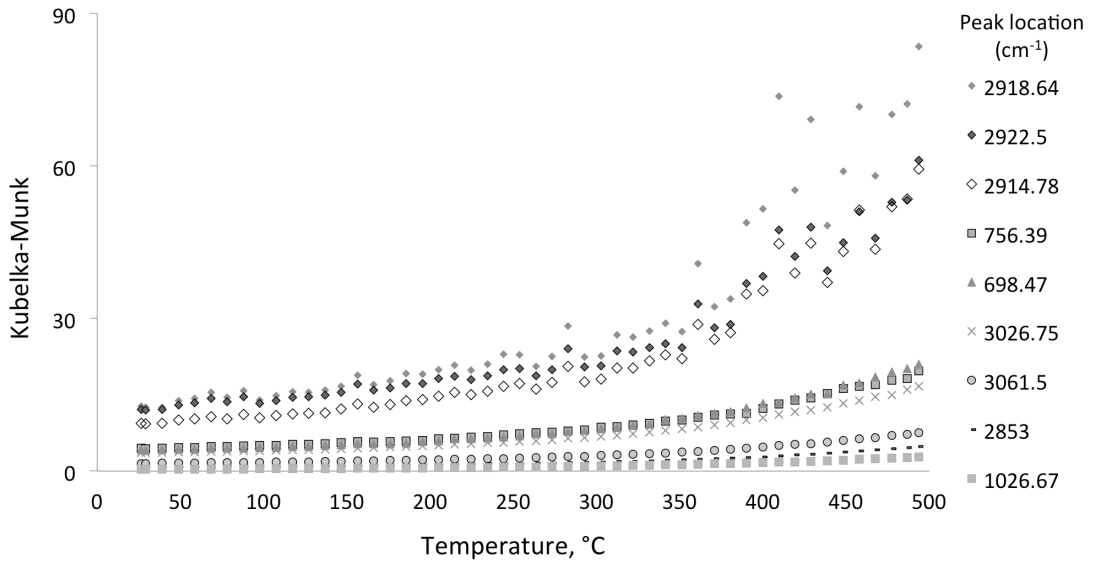

Figure 3.15 Temperature-dependent trends in polystyrene Kubelka-Munk spectral peak intensities.

Although peak intensity increased with increasing temperature, sample absorptions did not change, so peak shapes and magnitudes should not have varied. The maximum intensity in these spectra occurred at 2918.64 cm^{-1}, which was 4 cm^{-1} lower than 2922.50 cm^{-1}, which corresponded to the maximum for ambient temperature spectra. Temperature-dependent intensity trends for adjacent digitized spectrum values (i.e. at 2914.78 and 2922.50 cm^{-1}) are also shown in Figure 3.15. Intensities at all three wavenumber locations exhibited similar behavior, but changes were greatest at the absorption maximum.

In general, computational error propagation revealed that the largest fluctuations in VT-DRIFTS Kubelka-Munk spectra should be associated with the most intense absorption peaks. Compared to ambient temperature measurements, this error is significantly magnified when the sample holder was heated. This was most likely due to the detector voltage decrease caused by increasing unmodulated radiation produced

when the sample holder was heated. Figure 3.16 depicts the correlation between average Kubelka-Munk spectrum intensities and their standard deviations, comparing ambient temperature and variable temperature results. At ambient temperature, average Kubelka-Munk peak intensities were lower, and reproducibility was better than when the sample holder was heated.

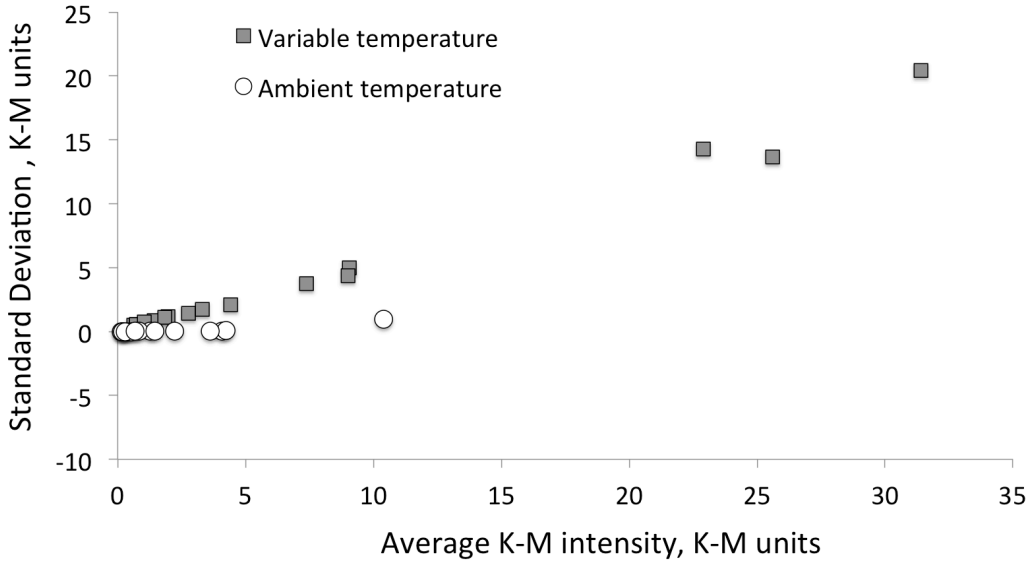

Figure 3.16 Standard deviation of Kubelka-Munk spectra peak intensities as a function of peak intensity for ambient and variable temperature measurements.

Because there is a systematic trend in Figure 3.16, specifically, a gradual increase in Kubelka-Munk intensities, methods for eliminating these variations were investigated.

3.3 Post-Collection Manipulation of Variable Temperature Spectra

Spectra can be scaled to remove baseline offsets by using a factor calculated from portions of single beam spectra that represent the baseline. A polynomial function that modeled systematic temperature-dependent trends was used to scale single beam

spectra collected at different temperatures. Scale factor variations with temperature were best determined by monitoring temperature-dependent trends in emissivity at single beam spectrum baseline locations.

3.3.1 Identifying Single Beam Spectrum Baseline Locations

Figure 3.17 illustrates the baseline wavenumber selection process. The first step in identifying spectrum baseline locations was to determine wavenumber locations that exhibited the lowest standard deviations when multiple spectra were measured. A single beam spectrum obtained with polystyrene in the beam is represented by short dashes in Figure 3.17. For comparison, the reference Ag powder spectrum also obtained at room temperature is shown by long dashes. The spectrum obtained with polystyrene in the beam was the result of averaging 50 spectra collected at ambient temperature. Wavenumbers corresponding to the lowest Kubelka-Munk intensity standard deviations were identified in these 50 spectra. Portions of single beam spectra corresponding to these wavenumbers are marked by the thick line on the polystyrene absorption single beam spectrum. The standard deviations are represented by open circles on the bottom (right y-axis). From those wavenumbers with the lowest relative standard deviations, some were selected to represent the baseline at various locations in the spectrum. These wavenumbers, which most closely match reference single beam spectrum values, are depicted by triangles and labeled with their corresponding wavenumbers.

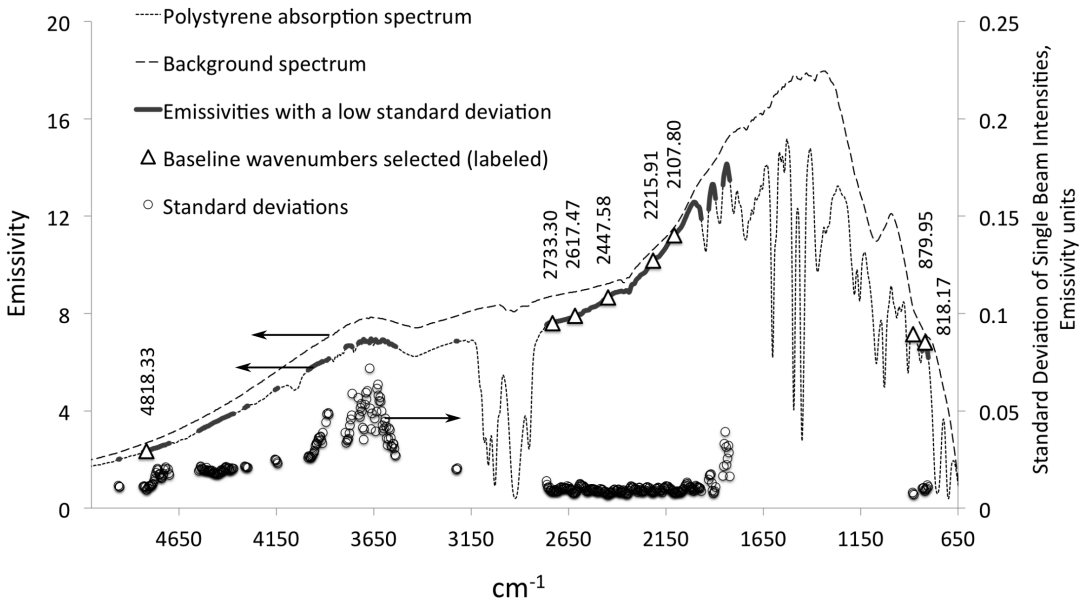

Figure 3.17 Baseline wavenumber selection process.

Selected baseline wavenumbers and their corresponding emissivity and standard deviations are listed in Table 3.3.

Table 3.3 Baseline Location Characteristics.

cm^{-1}	Average Baseline Point Intensities, Emissivity	Standard Deviation	RSD
818.17	6.81	0.00881	0.00129
879.95	7.13	0.00729	0.00102
2107.80	11.22	0.00784	0.00070
2215.91	10.18	0.00799	0.00078
2447.58	8.66	0.00678	0.00078
2617.47	7.92	0.00753	0.00095
2733.30	7.62	0.00822	0.00108
4818.33	2.36	0.00948	0.00401

Note that in the 1830-1950 and 3500-4000 cm^{-1} ranges, standard deviation significantly increases. This is most likely due to fluctuations in water vapor absorption bands and related to instrument purge (see Figure 2.5). Bands associated with water (1300-2045 cm^{-1} and 3200-4000 cm^{-1}) and carbon dioxide (2290 – 2395 cm^{-1}) exhibit greater signal fluctuations due to concentration variations inside the instrument. Therefore, these wavenumber ranges were not suitable for baseline characterizations.

3.3.2 Single Beam Scaling

Scaling factor temperature dependence was modeled by monitoring spectrum intensities at baseline locations with the highest emissivities and lowest standard deviations. Scaling factors appropriate for correcting spectra at each measured temperature were calculated by ratioing the sample single beam spectrum emissivity value at ambient temperature to the emissivity values at other temperatures. Figure 3.18 shows the trend in scaling factors as a function of temperature derived from different baseline locations. All curves exhibit similar shapes. However, the best fit trendline equation was generated from scaling factors calculated from 2107.80 cm^{-1} intensities. Based on these criteria, 2107.08 cm^{-1} was selected as the spectrum wavenumber from which scale factors were derived. The WinFirst macro "scale.mac" (Appendix D) was used to scale individual single beam spectra.

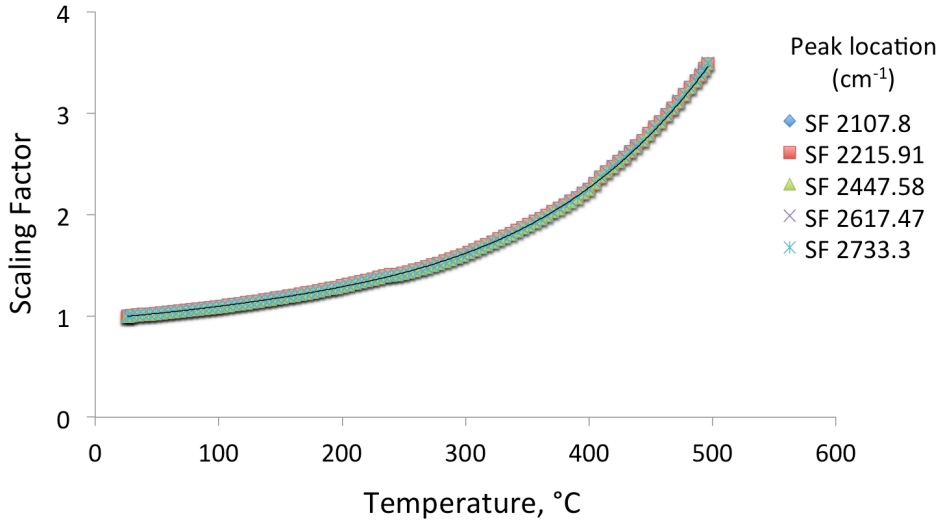

Figure 3.18 Temperature-dependent scaling factors calculated at different baseline locations.

Figure 3.19 shows an overlay of single beam spectra collected at different temperatures after the scaling procedure. Spectra exhibit some variation on both sides of the baseline location selected for determining scaling factors (2107.80 cm^{-1}). For comparison, Figure 3.20 shows an overlay of single beam spectra collected at ambient temperature at 10 min intervals. Ambient temperature spectra overlay well in the 650-1500 cm^{-1} and 2000-2800 cm^{-1} spectral ranges. However, more variation was observed in the water absorption ranges, most likely because of changes in instrument purge.

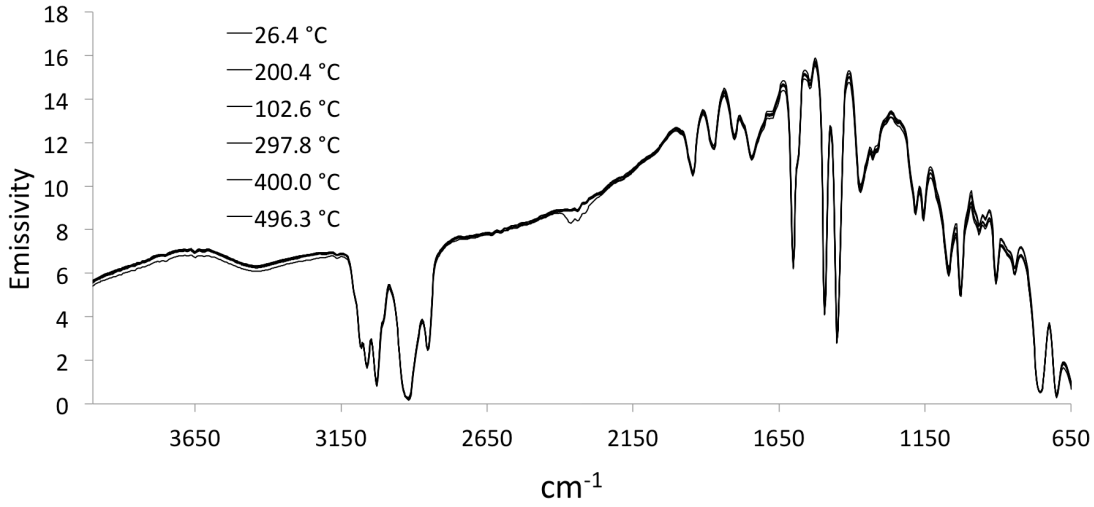

Figure 3.19 Overlay of scaled VT-DRIFTS sample single beam spectra.

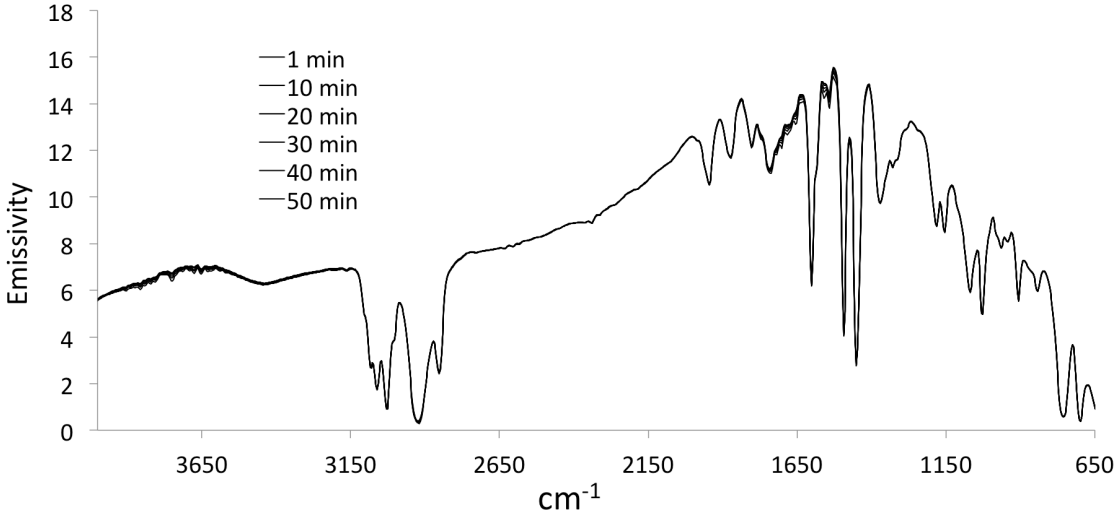

Figure 3.20 Overlay of DRIFTS sample single beam spectra collected at ambient temperature.

Reflectance spectra calculated as a ratio of a variable temperature polystyrene single beam spectrum to the ambient temperature Ag reference single beam spectrum exhibited baseline offsets, as shown in Figure 3.21. The ambient temperature spectrum is depicted by a thick line. It is notable that the thin line representing the measurement

made at 496.3 °C is below the ambient temperature spectrum in the higher wavenumber region but above the ambient temperature spectrum in the low wavenumber region. In contrast, the scaled spectrum obtained at 297.8 °C overlaps with the room temperature spectrum relatively well. Thus, it is plausible that a change in the Ag powder contained in the sample holder occurred above 300 °C, causing a redistribution in signal intensities and creating a temperature-induced baseline slope.

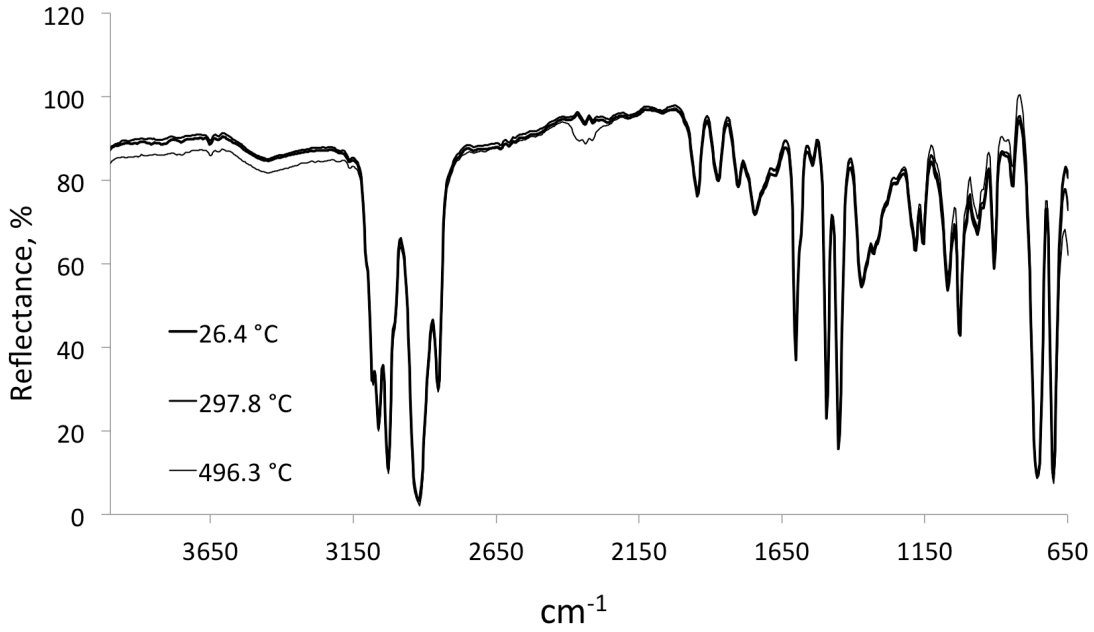

Figure 3.21 Overlay of scaled VT-DRIFTS polystyrene reflectance spectra.

Although baseline changes appear to be small in reflectance spectra, conversion to Kubelka-Munk format amplifies these variations and affects relative peak intensities, rendering results less accurate for quantitative analyses. Figure 3.22 is an overlay of scaled spectra after conversion to Kubelka-Munk format. Note the poor peak height reproducibility, which is particularly evident in Figure 3.22b.

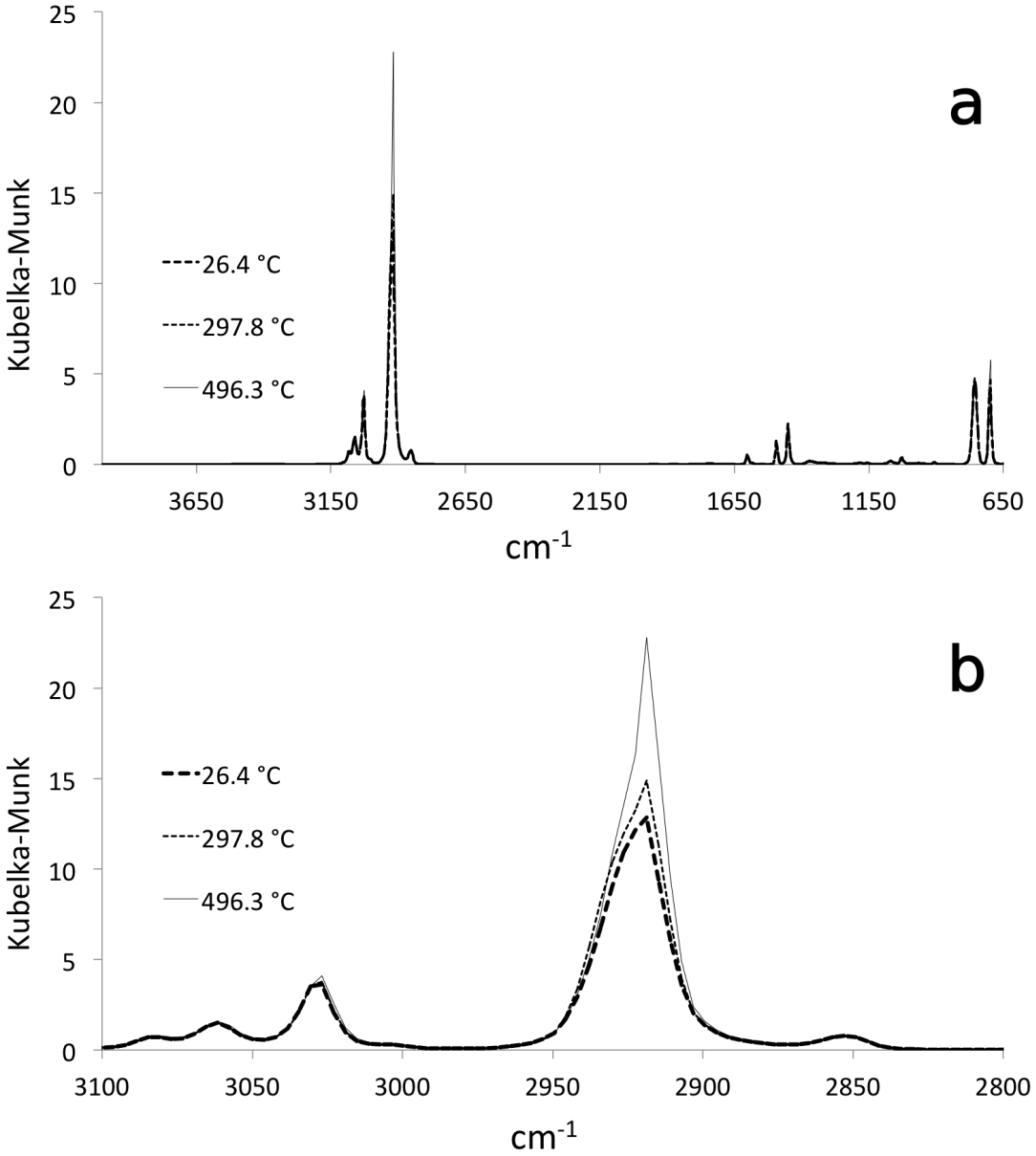

Figure 3.22 Overlay of scaled VT-DRIFTS polystyrene spectra in Kubelka-Munk format: a) complete spectrum and b) expansion in the C-H stretching region

3.3.3 Baseline Offset

Sloping lines were subtracted from spectra prior to conversion to Kubelka-Munk format by using a WinFirst macro command and selecting 2 absorption spectrum baseline locations. The "slope.mac" macro program code can be found in Appendix E.

The effectiveness of slope removal by using various baseline locations was compared. The best baseline location choices yielded the lowest peak maximum standard deviations and near-zero baseline slopes in corrected reflectance spectra.

Thus, straight lines passing through baseline locations at 818.17 and 3605.47 cm^{-1} were subtracted from all the scaled spectra over the entire spectral range. Scaled and baseline corrected spectra were then converted to Kubelka-Munk format. Although fluctuations in peak maxima were greatly reduced by using this method, ambient temperature spectrum reproducibility was still superior.

Figure 3.23 shows an overlay of variable temperature single beam spectra after scaling and baseline correction. These spectra overlay better than before baseline correction (compare to Figure 3.20). Figure 3.24 shows an overlay of variable temperature reflectance spectra after scaling and baseline correction. These spectra also overlay better than before baseline correction (compare to Figure 3.21).

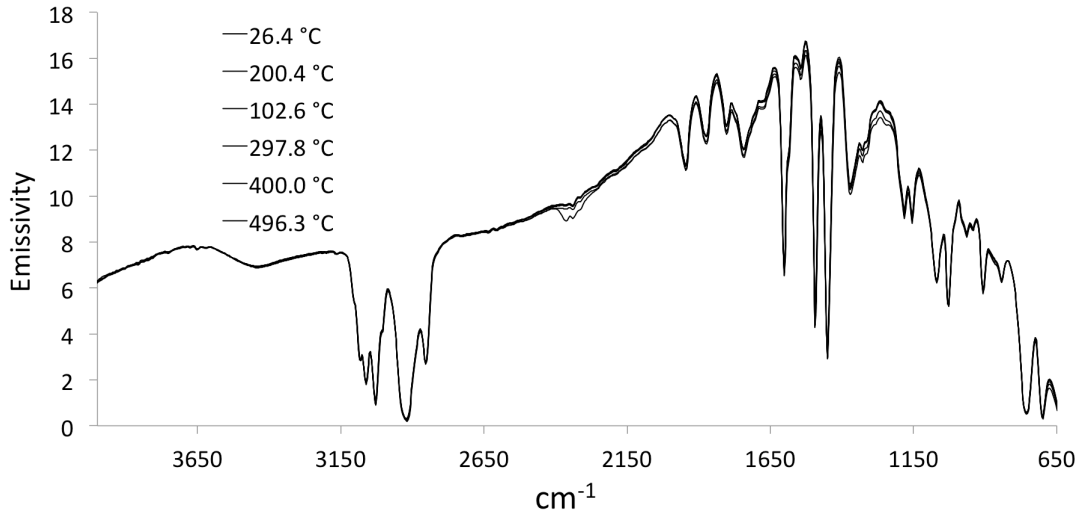

Figure 3.23 Overlay of scaled and baseline-corrected VT-DRIFTS polystyrene single beam spectra.

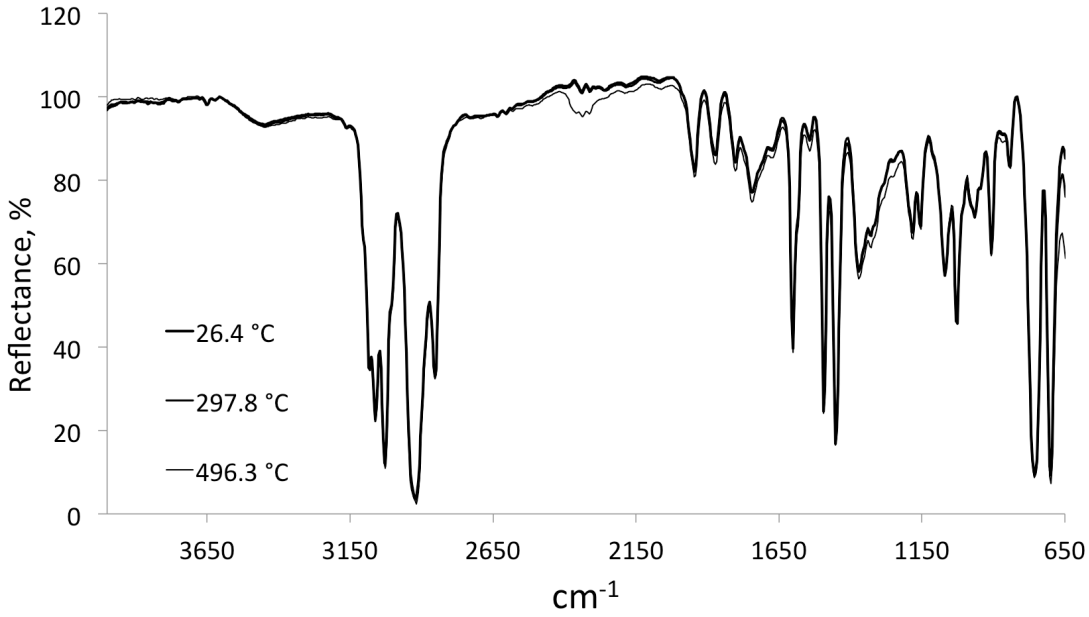

Figure 3.24 Overlay of scaled and baseline-corrected VT-DRIFTS polystyrene reflectance spectra.

Kubelka-Munk peak intensities were lower after baseline correction, as shown in Figure 3.25, compared to before baseline correction (Figure 3.22), and because reproducibility at higher Kubelka-Munk intensities was lower, it followed that the reproducibility of Kubelka-Munk intensities was improved after baseline correction. However, as shown by Figure 3.25, intensity fluctuations in corrected Kubelka-Munk intensities are still evident.

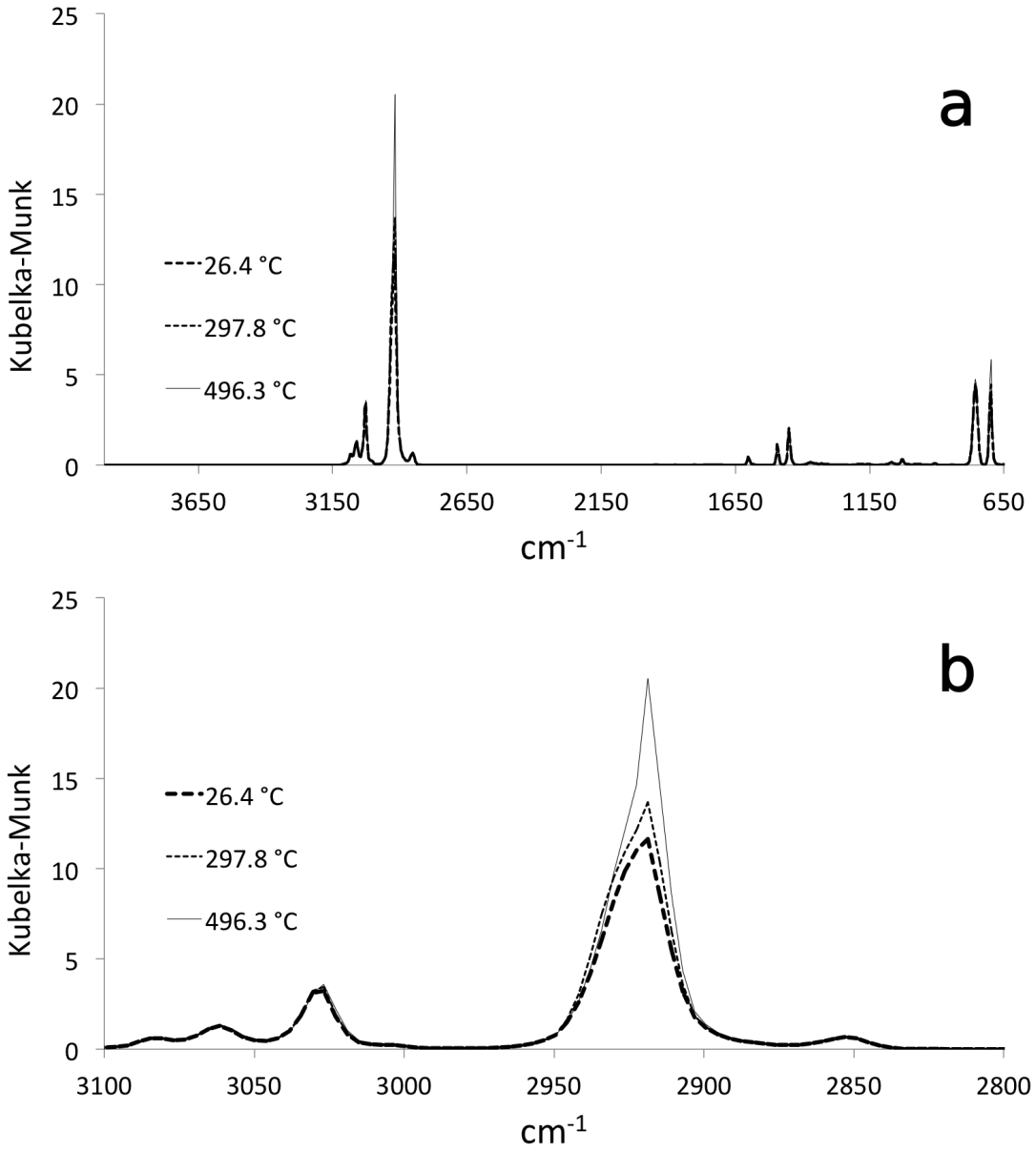

Figure 3.25 Overlay of scaled and baseline-corrected VT-DRIFTS Kubelka-Munk format spectra a) complete spectra and b) expansion of the C-H stretching region.

3.4 Comparison of Spectral Standard Deviations

Figure 3.26 shows the standard deviations at various absorption peak maxima derived from measurements made at room temperature (black), variable temperature (gray), variable temperature after scaling (open triangles), and variable temperature

after scaling and baseline slope removal (open squares). Figure 3.27 shows plots of these standard deviations as a function of Kubelka-Munk peak intensity.

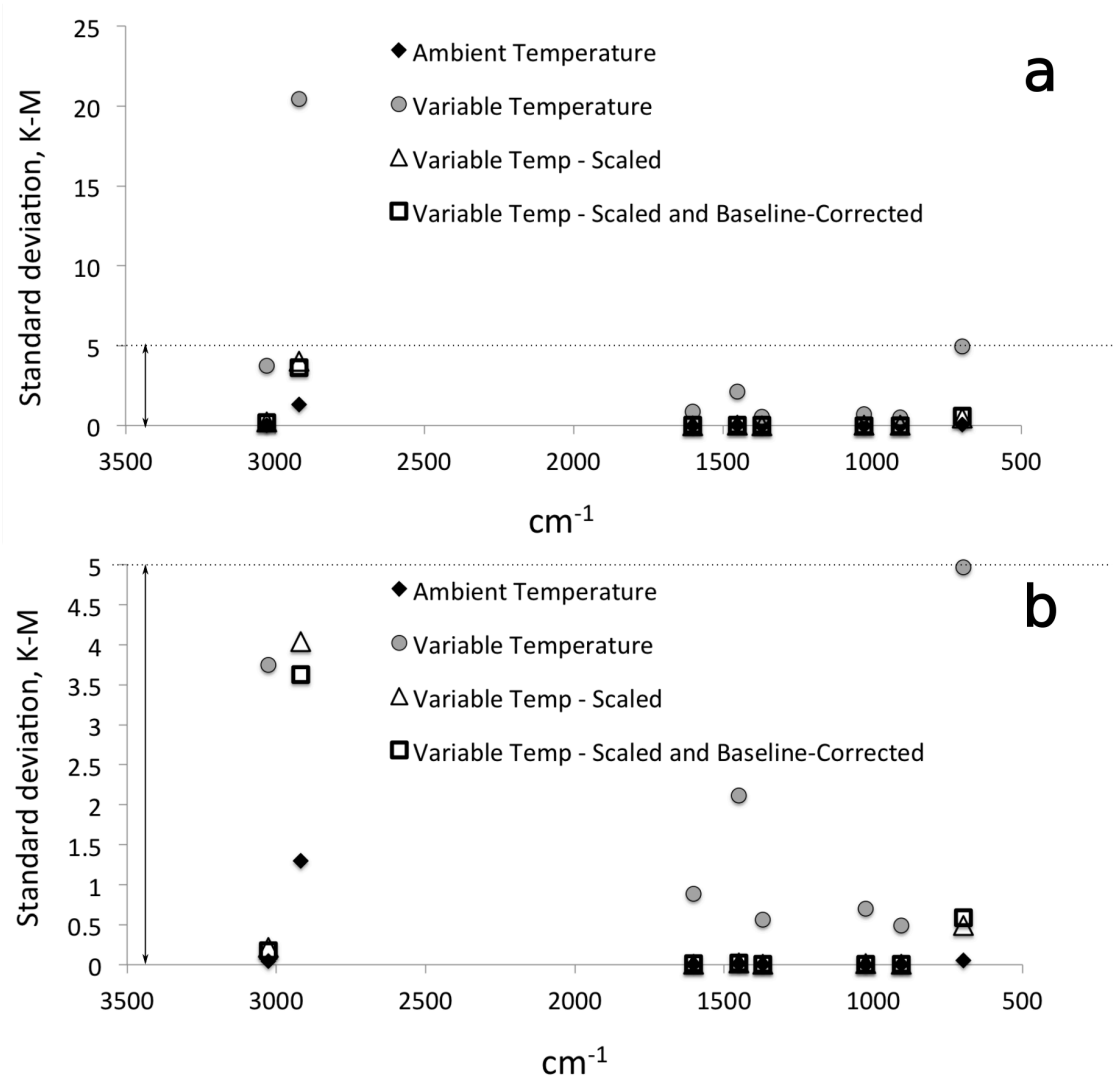

Figure 3.26 Peak intensity standard deviations as a function of wavenumber: a) complete data sets and b) expanded scale.

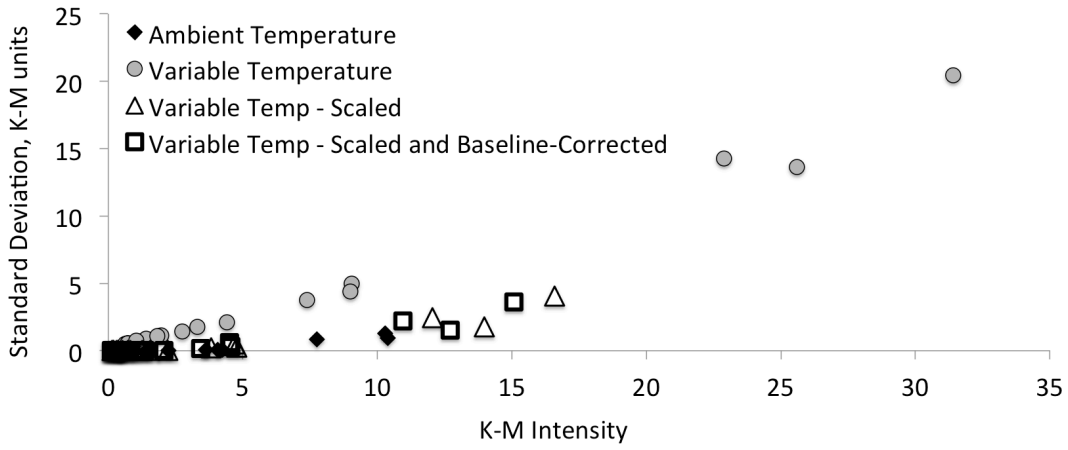

Figure 3.27 Peak intensity standard deviation as a function of Kubelka-Munk intensity.

Kubelka-Munk intensity was lowest for measurements made at ambient temperature and highest for uncorrected variable temperature measurements. Peak maximum standard deviations increased with increasing peak intensities. Note that scaling variable temperature spectra significantly decreased Kubelka-Munk peak intensities and standard deviations, but did not provide reproducibilities comparable to those obtained by ambient temperature measurements. Baseline correction further improved reproducibility, but ambient temperature measurement reproducibility was still superior.

A semi-quantitative comparison of the four sets of results can be provided by calculating the relative standard deviation of the measurements, which can be obtained from the slopes of standard deviation versus average peak intensity plots (Table 3.4).

Table 3.4 Comparison of the Relative Standard Deviations.

Data set	Slope ≈ RSD
Ambient temperature	0.092
Variable temperature	0.599
Variable temperature – scaled	0.183
Variable temperature – scaled and baseline corrected	0.181

The relative standard deviation of variable temperature measurements was 6.5 times greater than for ambient temperature measurements. Scaling sample single beam spectra lowered the RSD value to about twice the ambient temperature value. Baseline correction of scaled spectra had minimal effect on RSD. Although post-collection data manipulation improved the quality of variable temperature spectra, elimination or minimization of temperature-induced spectral artifacts would be preferred.

3.5 Effect of Sample Holder Heating on Baseline Slope

For quantitative infrared analysis, spectral peak intensities should depend on the amount of specific analyte present in a sample.[8] In VT-DRIFTS, sample heating can cause chemical structure changes, resulting in both positive and negative changes to spectral features. As demonstrated here, baseline offsets and slopes adversely affect the quantitative accuracy of Kubelka-Munk spectra. Therefore, when possible, VT-DRIFTS experiments should be designed to avoid baseline artifacts. When this is impossible, post-collection baseline correction techniques may be employed to minimize quantitative measurement inaccuracies. With properly aligned optics, FTIR spectra exhibit baselines without offset or significant sloping. However, heating

samples often results in curved or sloping baselines in spectra, and these artifacts become more severe at higher temperatures. Because it can be difficult to correct curved spectrum baselines, it is imperative that precautions be taken to prevent their occurrence. Thus, prevention of baseline variations should be a focus for VT-DRIFTS optimizations.

Figure 3.28 shows an example of baseline non-linearity resulting from sample heating. Single beam spectra for non-absorbing silver powder were measured at ambient temperature and at 200 °C. The ratio of these single beam spectra represents the instrument baseline, and should appear as a horizontal line in the reflectance spectrum. Instead, a sloping baseline was obtained in which the high wavenumber end of the spectrum exceeded 100% reflectance. Baselines such as the one shown in Figure 3.28 lead to large errors in Kubelka-Munk function representations of VT-DRIFTS spectra. If sloping baselines cannot be avoided, methods must be developed for minimizing their slopes before converting to Kubelka-Munk format.

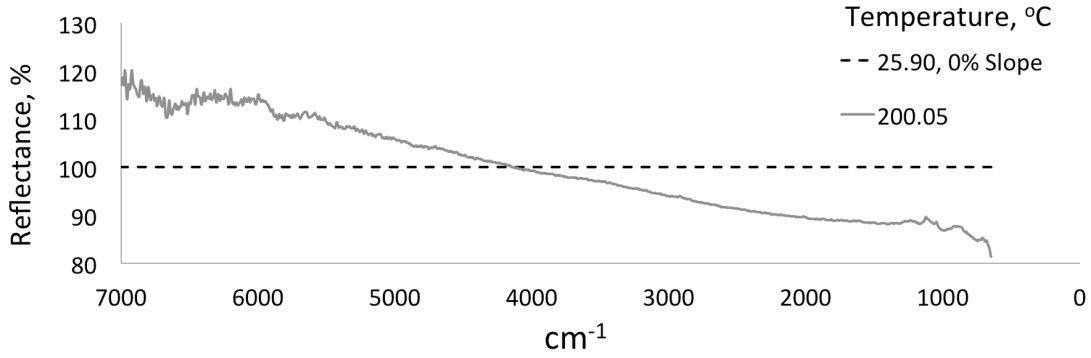

Figure 3.28 Baseline non-linearity caused by sample holder heating.

The infrared source emission spectrum, wavelength dependences of optical components (reflection and absorption), and the response function of the detector

determine the shape of FTIR single beam spectra. Single beam spectrum intensity varies with wavenumber, but relative intensities at all wavenumbers should be maintained unless one of these instrument factors change. VT-DRIFTS single beam spectrum emissivity decreases with sample heating due to detector saturation effects, but the shape of single beam spectra should not change. Changes in single beam spectrum shapes result in reflectance spectrum baseline slopes. Ideally, only sample absorptions should reduce reflectance values below 100%. Unfortunately, subtle changes in single beam spectrum shapes are often observed in VT-DRIFTS that affect reflectance spectrum baselines and lead to inaccuracies in Kubelka-Munk spectra.

3.5.1 Baseline Slope Characterizations

The magnitudes of VT-DRIFTS baseline slopes were estimated by calculating differences in reflectances near 4000 cm^{-1} and 2000 cm^{-1}. These spectral locations were selected because few samples absorb at these wavenumbers and they are not impacted by variations in instrument purge (i.e. changes in CO_2 and H_2O vapor absorptions).

Spectra were acquired for 10 hours with previously heated Ag powder in the sample holder. The following heating program was implemented: ambient for one hour, then heating to 200 °C at 5 °C/min, held at 200 °C for 4 hours, and then cooling to ambient while continuing to collect spectra for another 4.5 hours. Spectra collected in this manner provided information regarding fluctuations in baseline slopes at ambient temperature, baseline changes caused by sample heating, baseline fluctuations that occurred isothermally during sample heating, and trends in spectrum shape changes that occurred during cooling. Reflectance spectra were obtained by dividing each

consecutively measured single beam spectrum by the first acquired spectrum, which was measured at ambient temperature. Thus, the first "reflectance spectrum" was simply a 100% reflectance line with zero slope (and no noise) and zero difference between intensities at 4000 and 2000 cm^{-1}.

Figures 3.29 and 3.30 contain reflectance spectra overlays showing baseline slopes caused by sample holder heating and cooling. In Figure 3.29, the darkest lines denote spectra obtained near the beginning of the heating program (i.e. near ambient temperature), and lighter lines represent spectra obtained at higher sample holder temperatures. Spectra measured near ambient temperature did not exhibit significant deviations from 100% reflectance between 4000 and 650 cm^{-1}. Baselines in spectra collected at 200 °C were significantly tilted, with lower reflectance at low wavenumbers, which yielded positive calculated slopes. Figure 3.30 is an overlay of reflectance spectra obtained while the sample cooled from 200 °C to ambient temperature. The darkest lines represent spectra collected at 200 °C and lighter shade lines represent spectra acquired at lower temperatures. As the sample holder cooled, baseline slopes decreased and approached initial ambient temperature values.

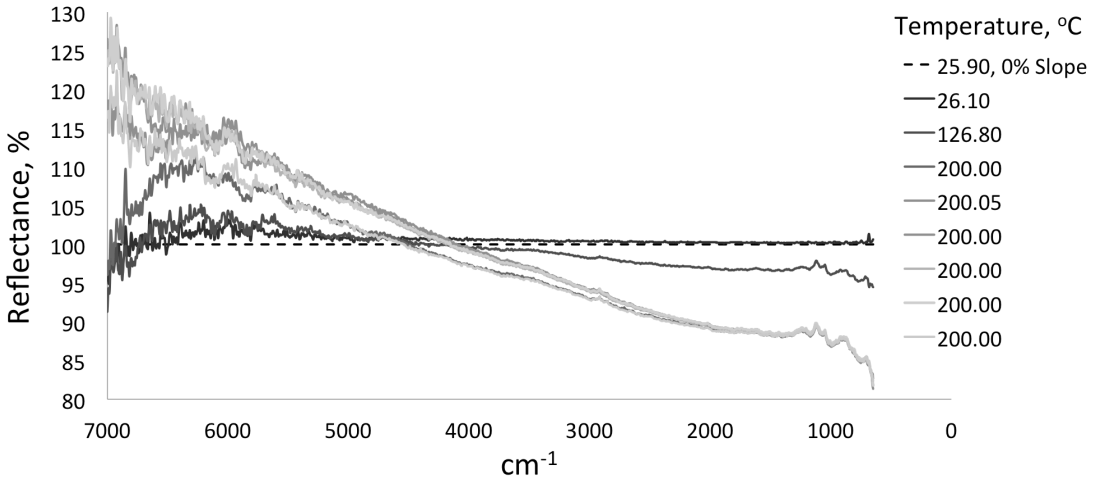

Figure 3.29 Baseline changes caused by sample heating.

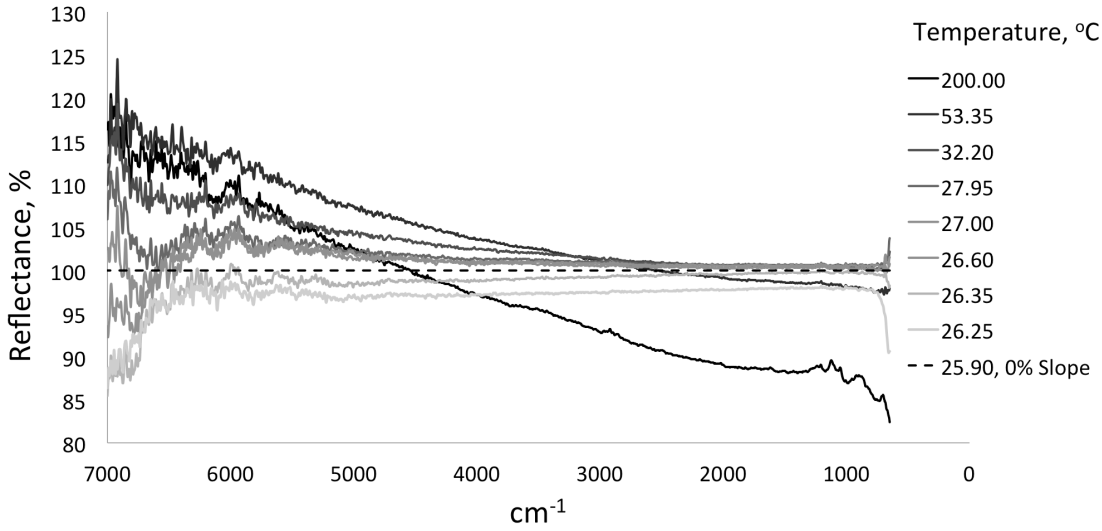

Figure 3.30 Baseline changes caused by sample cooling.

Figure 3.31 shows reflectance spectrum baseline slope (solid line) as a function of time during the heating profile. Measured sample holder temperatures (i.e. T_{Pt}) are represented in Figure 3.31 by the short dash line. Zero slope is indicated by the long dash line.

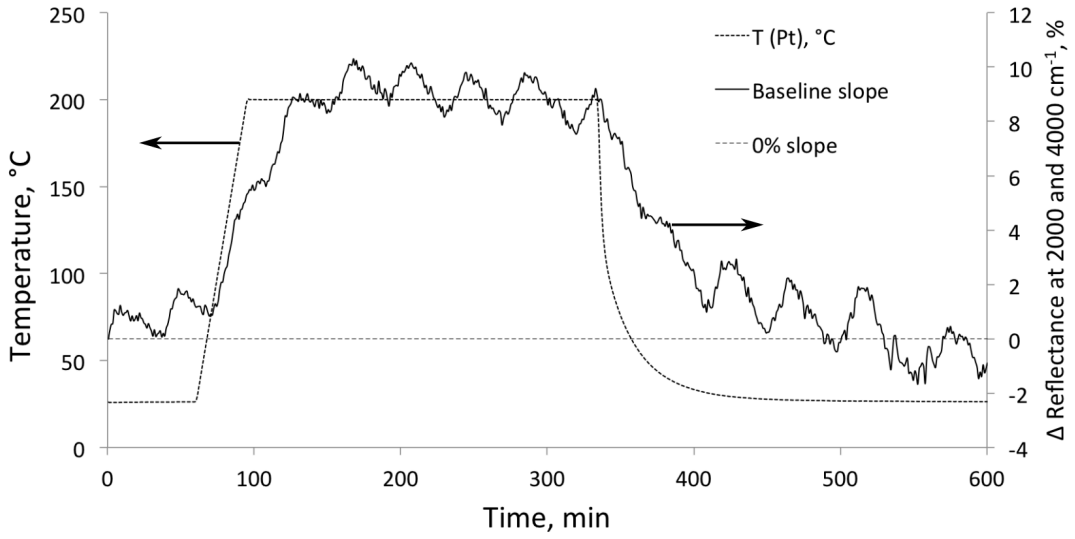

Figure 3.31 Baseline slopes of reflectance spectra (solid line) and sample holder temperature (short dash line) as a function of time during the heating profile.

The baseline slope plot consists of two components, a large increase with increasing sample holder temperature and a smaller oscillation superimposed on these changes. The initial baseline slope increase can be correlated with sample holder heating. When cooling, baseline slopes returned to near ambient temperature values. A delay in baseline slope increase was observed when the sample was initially heated and a similar delay in slope change was observed when the sample holder was cooled. Specifically, the sample holder reached 200 °C after 96 min, but baseline slope continued to gradually increase until it stabilized at about 135 min. The oscillation in baseline slope corresponded to about 1% cyclical changes and was detected throughout the heating and cooling process. Because these regular oscillations in the baseline slope repeated at about 40 min intervals, block average smoothing resulted in a curve with these oscillations removed. As shown in Figure 3.32, baseline slope initially increased from

0.8% near ambient temperature to 9.1% at 200 °C, then dropped to -0.8% when the sample holder cooled.

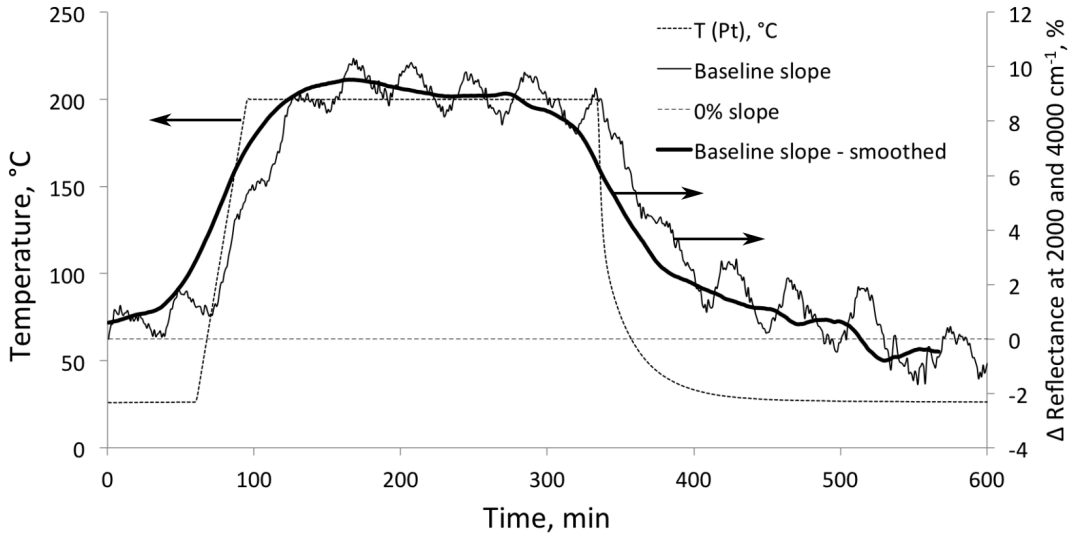

Figure 3.32 Baseline slope changes after block average smoothing.

Greater changes in intensity at higher wavenumbers (i.e. the shortest wavelengths) are consistent with variations in optical alignment, because interference for shorter wavelengths is most sensitive to small beam path length changes. The delay in baseline slope increase with sample holder heating and baseline slope decrease with sample holder cooling suggests that alignment variations caused by temperature changes to optical system components continued after the sample holder had equilibrated at 200 °C. The temperature changes for various instrument components caused by sample holder heating, which were responsible for baseline slope variations, are described in Chapter 4.

3.6 References

1. Spragg, R.A., B. Perston, and R.A. Hoult, Polystyrene Film as a Standard for Testing FT-IR Spectrometers*, Spectroscopy*, **28**(2), p. 38 (2013).

2. Gupta, D., L. Wang, L.M. Hanssen, J.J. Hsia, and R.U. Datla, *Polystyrene Films for Calibrating the Wavelength Scale of Infrared Spectrometers*, NIST Special Publication 260-122, National Institute of Standards and Technology: Gaithersburg, MD (1995).

3. Skoog, D.A., F.J. Holler, and S.R. Crouch, *Principles of Instrumental Analysis*, 6th ed., Thompson Brooks/Cole: Belmont, CA (2007).

4. Lin, R. and R.L. White, Effect of Diffuse Reflectance Fourier Transform Infrared Spectroscopy Sample Temperature on Photoconducting Semiconductor and Pyroelectric Infrared Detectors*, Analytical Chemistry*, **66**(18), p. 2976-2980 (1994).

5. Tripp, C.P. and R.A. McFarlane, Discussion of the Stray Light Rejection Efficiency of FT-IR Spectrometers: The Effects of Sample Emission on FT-IR Spectra*, Applied Spectroscopy*, **48**(9), p. 1138-1142 (1994).

6. *HgCdTe Detector. Serial # J-5385-2*, technical data, InfraRed Associates, Inc.: New Brunwick, NJ (1985).

7. *Mercury Cadmium Telluride Detectors*, data sheet, Teledyne Judson Technologies LLC: Mongomeryville, PA (2002).

8. White, R.L., Removal of Baseline Artifacts from Variable-Temperature Diffuse Reflectance Infrared Spectra*, Analytical Chemistry*, **64**(17), p. 2010-2013 (1992).

Chapter 4: Instrument Temperature Profiles

To better understand the effects of sample heating on the FTIR optical system, type K thermocouples were placed at various locations within the instrument, and temperature measurements were simultaneously made by using an Agilent 34970A Data Acquisition / Data Logger Switch Unit while heating the VT-DRIFTS sample holder. Silver powder that had been previously heated in the DRIFTS apparatus was left in the sample holder as a representative sample surface. Because the powder had been previously heated, it was more tightly packed into the sample holder, so there was minimal movement of the sample surface with successive heating ramps. Temperature measurements were obtained at 10 second intervals.

4.1 Thermocouple Calibration Procedure

To assure that thermocouples were properly calibrated and yielded consistent and accurate temperature measurements, they were bundled together to minimize temperature differences before calibration. Ice water and boiling water were used as temperature reference points, corresponding to 0 °C and 100 °C, respectively. Readings were collected at each reference temperature at about 10 sec intervals until all thermocouple measurements stabilized. Prior to calibration, all thermocouple

temperature readings were below ambient (by as much as 3 °C). However, each thermocouple provided stable readings over the course of 5 minutes. For each thermocouple, temperature variations were less than 0.1 °C at 100 °C and close to 0.05 °C at 0 °C. When temperature measurements from all thermocouples were statistically compared prior to calibration, standard deviations were about 1 °C at both 0 °C and 100 °C. After equilibration, the average temperature recorded over a 5 min interval for each thermocouple at 0 °C and at 100 °C was used to derive a calibration curve for that thermocouple. Calibration curves obtained by this method were used to modify the Agilent data logger software to correct thermocouple readings. After calibration, all temperature measurements were within 0.2 °C of reference temperatures, and standard deviations for all thermocouple readings were less than 0.03 °C.

4.2 Sample Holder Temperature Variations

Because infrared radiation reflects from the sample surface, front surface temperatures are most representative of the portion of the sample exposed to infrared radiation. Unfortunately, placing a thermocouple at this location is not practical because errors can be introduced into spectroscopic measurements due to blocking of incident radiation by the thermocouple. In addition, the thermocouple may move during heating either because of sample particle shifting or as a result of thermal expansion. Consequently, temperature-dependent random spectral variations that are unrelated to sample chemical composition changes may be caused by placing a thermocouple at the sample surface. To avoid these problems, temperatures were measured at the bottom of the powdered sample. A platinum foil was placed between the powdered sample and

the thermocouple so that the solid sample rested on top of the foil and a thermocouple was in contact with the bottom of the foil.

Ideally, samples should heat uniformly and temperature measurements should accurately reflect sample surface temperatures. Unfortunately, significant temperature variations were detected within the sample. The thermocouple employed by the temperature controller feedback control system to generate heating ramps was in contact with the platinum foil at the bottom of the sample, which was about 1 mm below the sample surface. Sample surface measurements indicated that surface temperatures differed from those at the Pt foil. Front surface temperatures were typically lower and sample temperature gradients increased with increased sample temperature.

To avoid potential spectral artifacts caused by placing a thermocouple at the sample surface, temperatures associated with specific VT-DRIFTS spectra were derived from Pt foil measurements (T_{Pt}) by means of calibration curves relating sample surface and Pt foil temperatures. Experiments were performed to determine temperature measurement reproducibility, the magnitudes of temperature gradients between the top and bottom of the sample, and effects of various environmental conditions on sample temperature readings.

To measure sample surface temperatures, a thermocouple was inserted through an opening at the bottom of the sample chamber and positioned so that it was in contact with the sample surface. By introducing the thermocouple in this manner, the top portion of the DRIFTS environmental chamber could be removed without disturbing the thermocouple. The thermocouple was sealed to the chamber by using high-temperature

cement. The thermocouple wire was insulated with ceramic tubing and secured to the sample holder post to prevent movement. The tip of the thermocouple was in contact with the sample surface at the center of the sample holder. This thermocouple placement would not be desirable when making VT-DRIFTS measurements, but the purpose of these experiments was to measure sample surface temperatures. Experiments were conducted to evaluate the reproducibility of temperature measurements made both beneath the sample (T_{Pt}) and at the sample surface (T_{surf}).

4.2.1 Effects of Sample Holder He Purge Rates

Temperatures were simultaneously measured beneath the sample and at the surface while heating the sample holder. Temperatures measured at the Pt foil were used by the temperature controller to adjust heater power. For heating ramps, T_{Pt} was held at room temperature for 2 min, increased to 300 °C at 5 °C/min, held at 300 °C for 5 min, and then the sample was allowed to cool by turning off the heater power. This heating profile was repeated while purging the sample compartment with 10 mL/min He and then with 100 mL/min He. Heating profile measurements at each purge rate were repeated 3 times. The sample temperature (T_{Pt}) exceeded 300 °C by 1 °C when the 5 °C/min heating ramp was employed, causing a small aberration in temperature versus time plots near 57 min.

Figure 4.1 shows an overlay of the average of three replicate T_{surf} measurements made while purging at 10 mL/min (dash-dot line) and 100 mL/min (solid line) along with standard deviations calculated for the 3 replicate measurements made at each He flow rate. The temperature versus time plots overlay very well, suggesting that

changing the He purge rate had minimal effect on sample surface temperatures. Although He purge rate changes did not significantly alter sample surface temperatures, measurement standard deviations were lower when purging at 100 mL/min (typically less than 0.05 °C) than when 10 mL/min (0.3 – 0.5 °C) was employed. After power to the heater was turned off, standard deviations calculated for measurements made while using the 10 mL/min He purge were significantly greater than when the 100 mL/min He purge was employed. Thus, although all standard deviations were less than 1 °C while heating, sample surface temperature measurement reproducibility was better when the 100 mL/min He purge rate was employed.

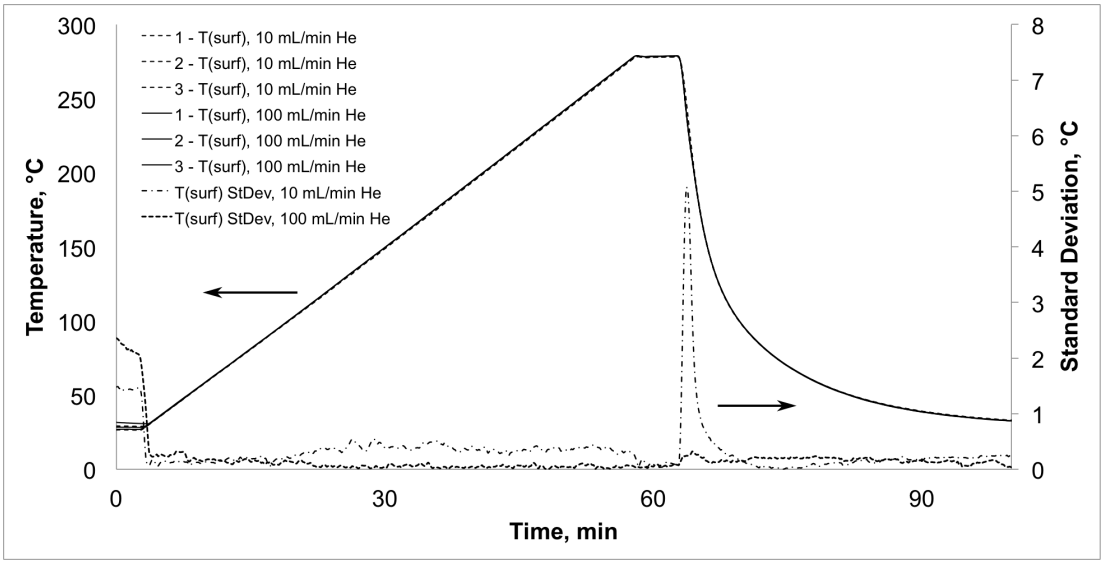

Figure 4.1 Sample surface temperatures and standard deviations for 3 replicate heating ramps with 10 (dash line) and 100 (solid line) mL/min He purge.

Figure 4.2 shows an overlay of the averages of 3 heating profile T_{Pt} measurements as a function of time made with 10 and 100 mL/min He purge. Standard deviations as a function of time for each set of 3 replicate measurements are also shown. Standard deviations were less than 0.5 °C with both He purge rates. During cooling, the

standard deviation was greater when purging at 100 mL/min He, which was the opposite of the sample surface temperature trends.

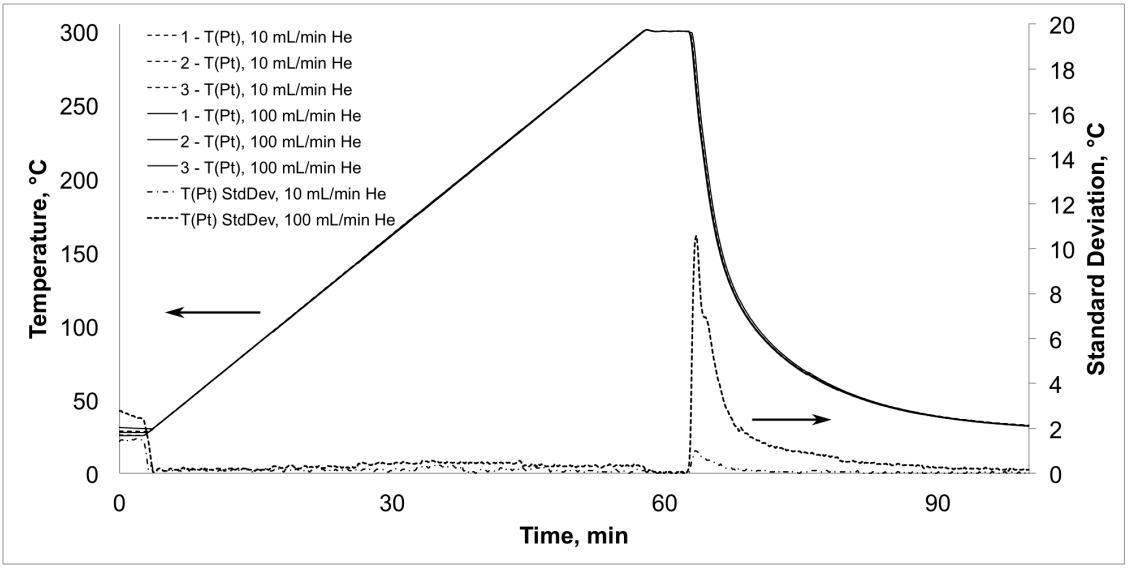

Figure 4.2 Temperature under the sample and standard deviations for 3 heating ramps with 10 (dash line) and 100 (solid line) mL/min He purge.

High standard deviations near the beginning of heating ramps were the consequence of slightly different starting temperatures. Sample surface temperatures were more reproducible with 100 mL/min He purge, and temperatures measured beneath the sample (T_{Pt}) were more reproducible for the 10 mL/min He purge. These trends were exaggerated during cooling, when power to the heater was removed. When purging at 100 mL/min He, the power provided to the heating element exhibited greater fluctuations. This caused greater fluctuations in T_{Pt}. Conversely, the sample surface was heated and cooled more reproducibly when the sample holder was purged with 100 mL/min He, therefore, sample surface temperature reproducibility was better when 100 mL/min He purge was employed compared to measurements with 10 mL/min He purge.

Figure 4.3 shows a comparison of T_{Pt} measurements (dotted line) and T_{surf} measurements (solid line) during heating profiles. These plots do not overlap. Sample surface temperatures were consistently below Pt foil temperatures, and the difference between these temperatures increased with increased heating. Because T_{Pt} and T_{surf} measurements were reproducible for repeated heating profiles, it should be possible to predict T_{surf} values from T_{Pt} measurements. However, such predictions require that the correlation function between T_{surf} and T_{Pt} be known. By plotting T_{surf} versus T_{Pt}, this correlation function can be determined by using best-fit linear regression. It should be possible to employ this correlation equation to predict T_{surf} based on T_{Pt} measurements.

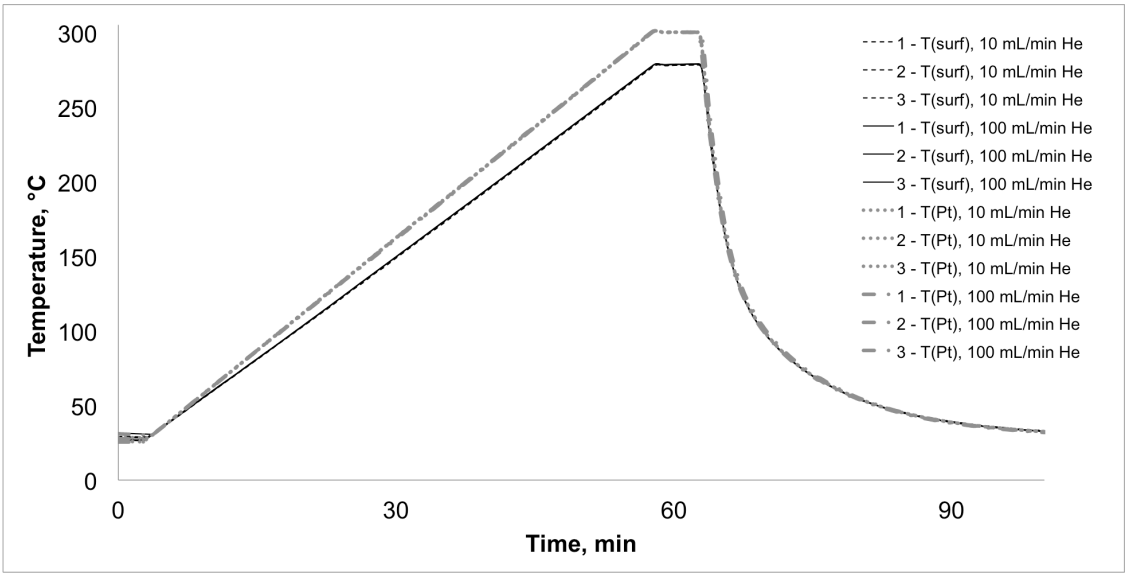

Figure 4.3 Correlation between temperature readings near the sample surface (T_{surf} – black) and beneath the sample (T_{Pt} – gray).

4.2.2 Effects of Sample Holder Heating Rates

Because VT-DRIFTS measurements made by using different sample heating rates are often used to elucidate temperature-dependent sample structure changes,

correlations between T_{surf} and T_{Pt} for a range of heating rates were examined. In addition to 5 °C/min (Figure 4.3), T_{surf} and T_{Pt} correlation functions were determined for 0.5, 1.0, and 2.0 °C/min heating rates. As previously described, heating profile experiments were performed by first measuring ambient sample temperatures for 2 min, followed by heating the sample to 300 °C (T_{Pt}) and then holding at 300 °C for 5 min. After a final 5 min isothermal period, the sample was allowed to cool by removing power to the heater. Because the 5 °C/min measurements revealed no significant difference in the correlation function when purging at 10 or 100 mL/min He, 10 mL/min He purge was employed for all heating rate experiments.

Heating ramp starting temperatures varied because of different cooling periods between successive experiments. In order to exclude successive measurement values with high standard deviations near ambient temperatures, correlation functions were derived from T_{Pt} measurements made between 35 and 300 °C. Experiments were initiated by simultaneously executing the PC heating ramp program and manually starting the data logger. Small differences in the times that heating ramps and temperature measurements were initiated likely contributed to T_{Pt} variations for values recorded at the same elapsed time for repeated heating ramps, but these contributions would be relatively constant. In general, repeated measurement standard deviations $\{\sigma(T_{Pt})\}$ increased with increasing heating rate, whereas standard deviations for surface temperature measurements $\{\sigma(T_{surf})\}$ did not exhibit a clear heating rate-dependent trend, and were ±0.11 °C on average with the highest standard deviation reaching ±0.17 °C for the 1 °C/min heating ramp (Table 4.1).

Table 4.1 Temperature Standard Deviations for Various Heating Rates

Heating rate	σ (T_{Pt})	σ (T_{surf})
0.5 °C/min	± 0.01 °C	± 0.08 °C
1 °C/min	± 0.04 °C	± 0.17 °C
2 °C/min	± 0.06 °C	± 0.10 °C
5 °C/min	± 0.13 °C	± 0.10 °C

Figures 4.4 and 4.5 illustrate the effects of sample heating rate on $\sigma(T_{Pt})$ and $\sigma(T_{surf})$. In both figures, the darkest color plot corresponds to results obtained at the lowest heating rate (0.5 °C/min) and the lightest color corresponds to results obtained at the highest heating rate (5 °C/min). Figure 4.4 shows that $\sigma(T_{Pt})$ values increased with increasing heating rate, but no significant change in $\sigma(T_{Pt})$ was observed with increasing sample temperature. In contrast, Figure 4.5 shows that plots of $\sigma(T_{surf})$ versus T_{Pt} generated from data acquired at different heating rates overlap. These plots also exhibit slight increases in $\sigma(T_{surf})$ with increasing temperature. Note that the plots in Figures 4.4 and 4.5 have different scales, and that $\sigma(T_{Pt})$ values were generally lower than $\sigma(T_{surf})$ values.

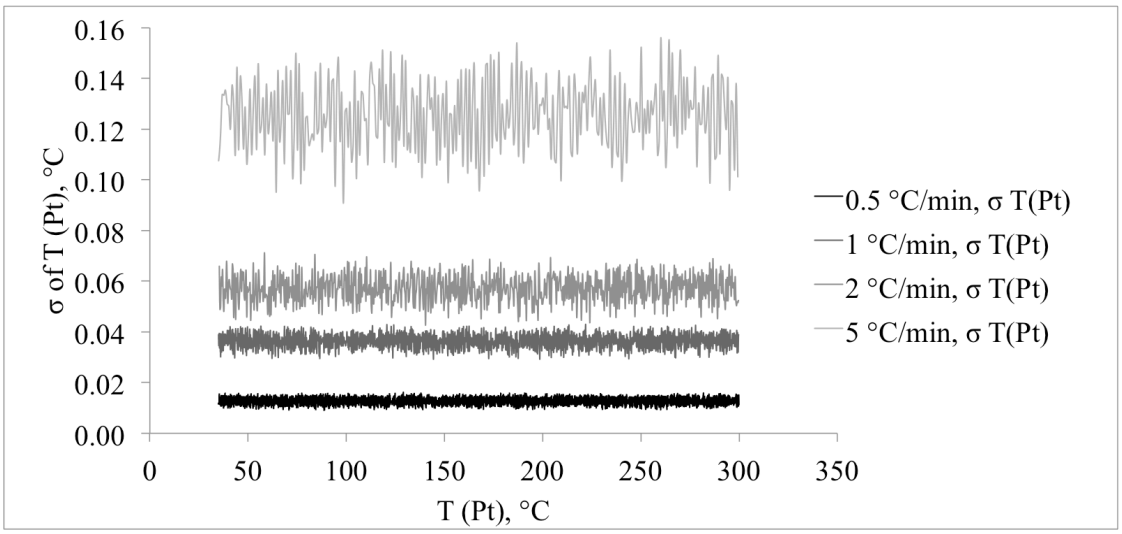

Figure 4.4 T_{Pt} measurement standard deviations for various heating rates.

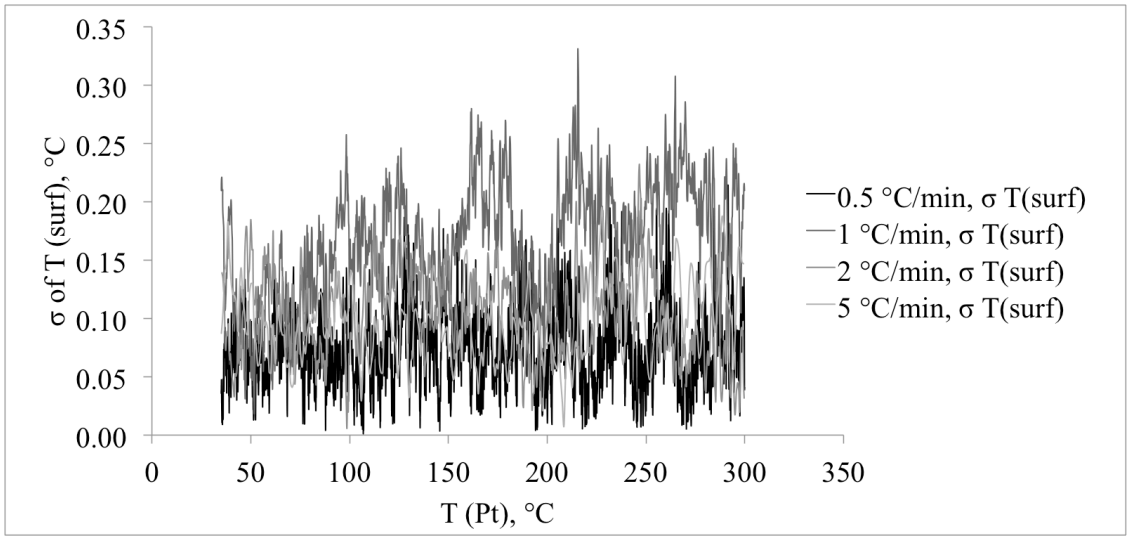

Figure 4.5 T_{surf} measurement standard deviations for various heating rates.

Figure 4.6 shows an overlay of T_{surf} versus T_{Pt} data for various heating rates (gray lines, left y-axis). The plots overlay more closely at low temperatures and deviate with increasing temperature. The temperature difference between T_{surf} and T_{Pt}, caused by a temperature gradient across the sample, is represented by:

$$\Delta T_S = T_{Pt} - T_{surf} \quad (4.1)$$

This maximum sample temperature difference (ΔT_S) increased with increasing temperature at each heating rate.

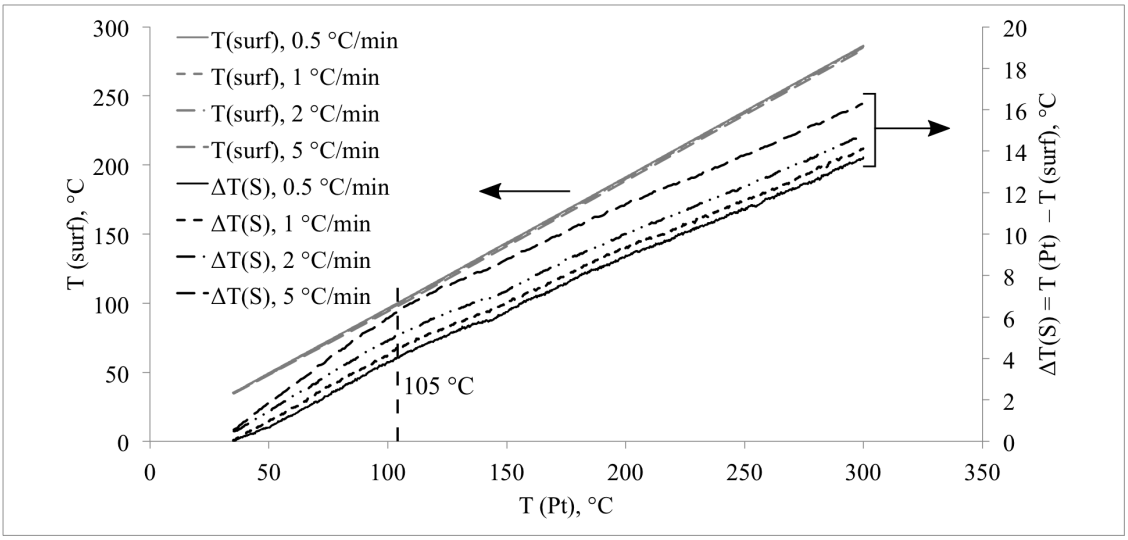

Figure 4.6 Correlations between T_{surf} and T_{Pt}.

Plots of T_{surf} versus T_{Pt} (Figure 4.6, gray plots) are nearly linear. However, slight deviations from linearity produce reproducible changes in maximum temperature difference plot slopes near 105 °C. Above 105 °C, slopes of ΔT_S versus T_{Pt} plots are similar for all heating rates. Below 105 °C, slopes of these curves increase with increasing heating rate. Notably, the change in the slope of the ΔT_S versus T_{Pt} plots occurs near the boiling temperature of water.

Because inflection points indicating slope changes occur in T_{Pt} versus T_{surf} curves near 105 °C, two linear regression equations were used to fit these curves, one for T_{surf} values below 105 °C, and a second for measurements made above 105 °C. Best fit regression equations describing the relationship '$T_{Pt} = m \times T_{surf} + b$' are listed in Table 4.2.

Table 4.2 Best Fit Regression Equations Describing the Relationship '$T_{Pt} = m \times T_{surf} + b$.'

Heating Rate, °C/min	For the data below T_{Pt} = 105 °C	For the data above T_{Pt} = 105 °C
0.5	y = 0.9398x + 2.257	y = 0.9512x + 0.9577
1	y = 0.9358x + 2.2138	y = 0.9511x + 0.5724
2	y = 0.9314x + 1.9564	y = 0.9509x – 0.0565
5	y = 0.9167x + 2.3184	y = 0.9497x – 1.2594

Slope values and intercept values were plotted as a function of heating rate. In Figures 4.7 and 4.8, triangles correspond to the data obtained below 105 °C and asterisks represent data obtained above 105 °C. Slope and intercept values follow opposite trends. Below 105 °C, slopes of T_{surf} versus T_{Pt} linear regressions decrease with increasing heating rate. Above 105 °C, slopes are similar, regardless of the heating rate. Intercept values, on the other hand, are comparable below 105 °C, but decrease with increasing heating rate above 105 °C.

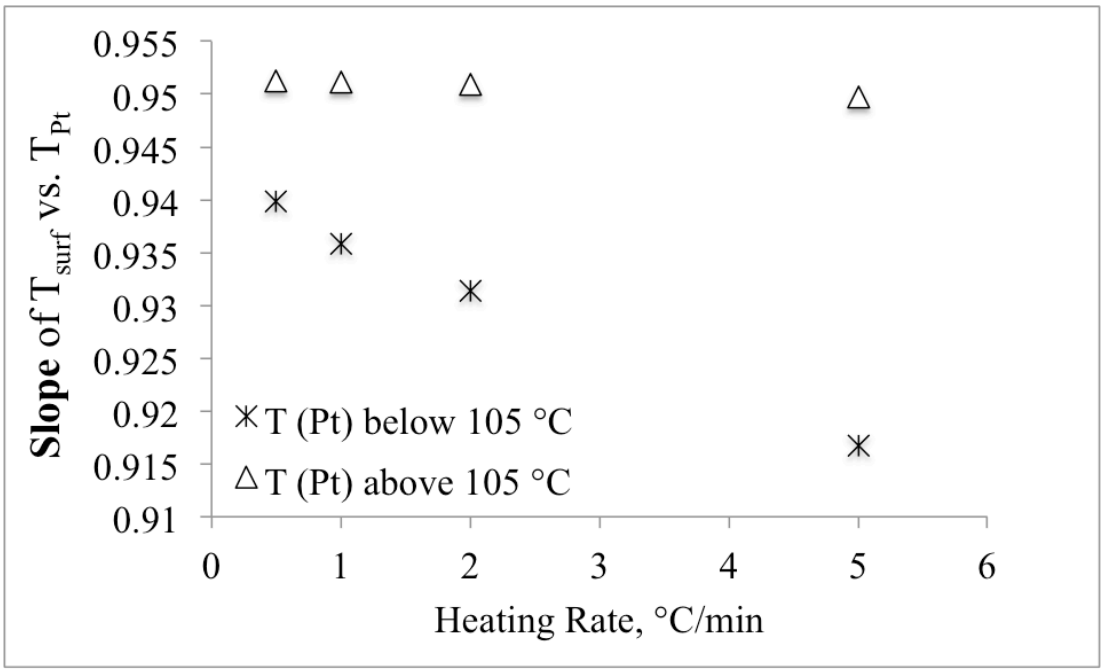

Figure 4.7 T_{surf} vs. T_{Pt} slopes versus heating rate.

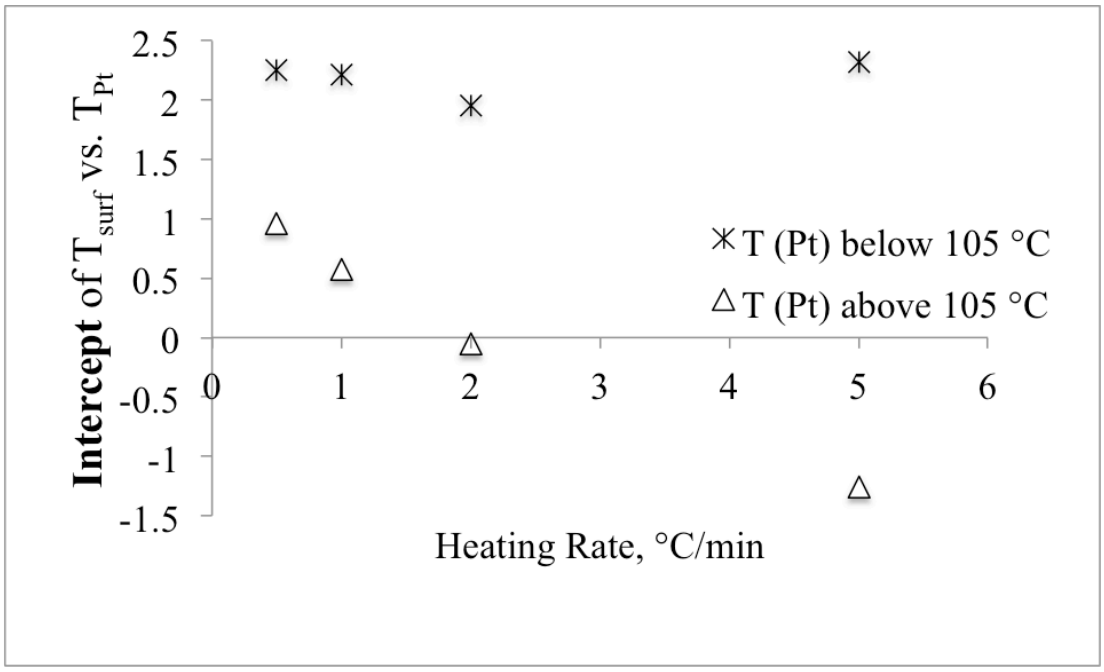

Figure 4.8 T_{surf} vs. T_{Pt} intercepts versus heating rate.

The slope is a coefficient that correlates T_{surf} with T_{Pt}. Below 105 °C, this coefficient is greatest at the lowest heating rate (i.e. 0.5 °C/min) and gradually decreases with increasing heating rate. Thus, T_{surf} values more closely match T_{Pt} values when the sample is heated more slowly, and increasingly lag behind T_{Pt} values with higher heating rates. Above 105 °C, slopes are comparable for all heating rates. The average slope above 105 °C was 0.9507 ±0.0007, indicating that sample surface temperatures were consistently about 95% of T_{Pt} values.

The linear regression intercept represents the initial difference between T_{surf} and T_{Pt}. All heating ramps started near ambient temperature. Thus, for linear regressions derived from measurements below 105 °C, intercept values represent the temperature difference between the sample surface and Pt foil at ambient temperature. The average intercept was 2.2 ±0.2 °C, indicating that initial sample surface temperatures were about 2 °C above the Pt foil temperature. This was likely the result of the infrared beam heating the sample surface and raising the temperature there compared to the temperature at the bottom of the sample. For measurements above 105 °C, intercepts represent cumulative temperature differences resulting from the lag in T_{surf} relative to T_{Pt} when the sample was heated. Because the highest heating rate produced the greatest lag, the intercept value for the 5 °C/min heating rate was the most negative (-1.2594 °C). Conversely, the intercept was most positive (0.9577 °C) for measurements made while heating at 0.5 °C/min. Because slopes were relatively constant above 105 °C, sample surface temperatures during 5 °C/min heating ramps were about 2 °C below those measured when a 0.5 °C/min heating rate was employed.

Temperature measurements made during heating profiles confirm the presence of a temperature gradient between the top and bottom of the powder sample. This gradient intensifies with increasing temperature. Gradient temperature variations depend on heating rate, but are reproducible, so that sample surface temperatures can be predicted based on T_{Pt} measurements. Sample surface temperatures could be predicted to within ±0.06 °C by using dual linear regression equations to characterize the lower and higher temperature regions separately. For all heating profiles, temperature differences across the sample were greatest between 35 and 105 °C. Above 105 °C, sample surface temperatures were about 95% of Pt foil values, regardless of heating rate. By using a 0.95 multiplier to convert T_{Pt} measurements to T_{surf} values for the four different heating rates, T_{surf} could be predicted with a maximum error of 1.95 °C (corresponding to 50 °C at 0.5 °C/min heating ramp) and with a standard deviation of ±1.04 °C for the average of three replicate measurements. Figures 4.9 and 4.10 show plots of ΔT_{err} versus T_{Pt} for the low and high temperature regions, respectively, obtained by using the dual linear regression method. For T_{Pt} values above 105 °C, errors were relatively constant. In fact, a linear regression equation of the form $y = 0.95x + b$ was found to predict T_{surf} values above 105 °C to within ~ ±0.5 °C for each heating rate, provided that the b value was systematically decreased as the heating rate increased from 0.5 to 5 °C/min. Below 105 °C, this approach was much less accurate. For temperatures below 105 °C, the linear regression slope must be systematically decreased when heating rates increase from 0.5 to 5 °C/min.

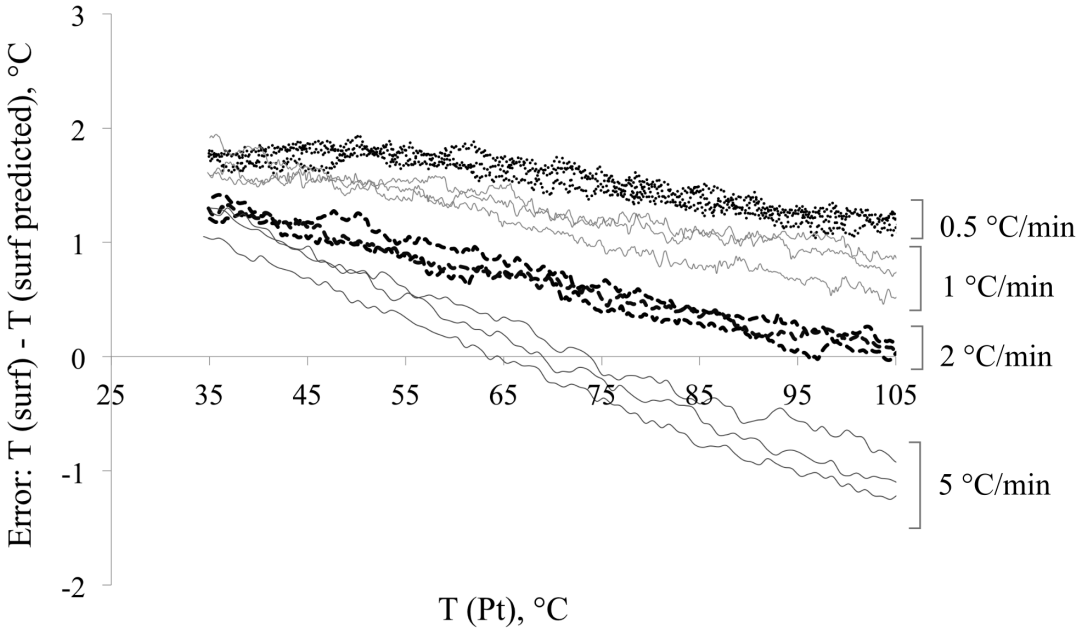

Figure 4.9 ΔT_{err} versus T_{Pt} for the low temperature region.

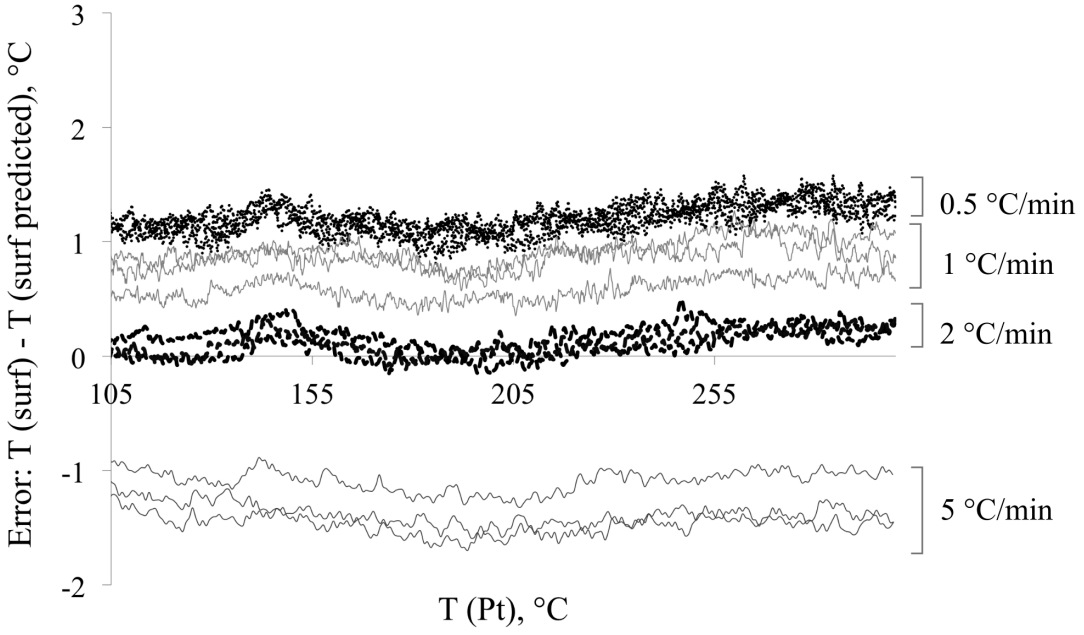

Figure 4.10 ΔT_{err} versus T_{Pt} for the high temperature region.

4.3 Temperature Changes Caused by Sample Heating

4.3.1 Effects of Sample Holder He Purge Rates.

To understand how temperatures at various locations near the sample holder vary when the sample is heated, thermocouples were placed near each ZnSe window location, on top of the sample chamber lid, and between the ellipsoid mirrors of the DRA, as shown in Figure 4.11.

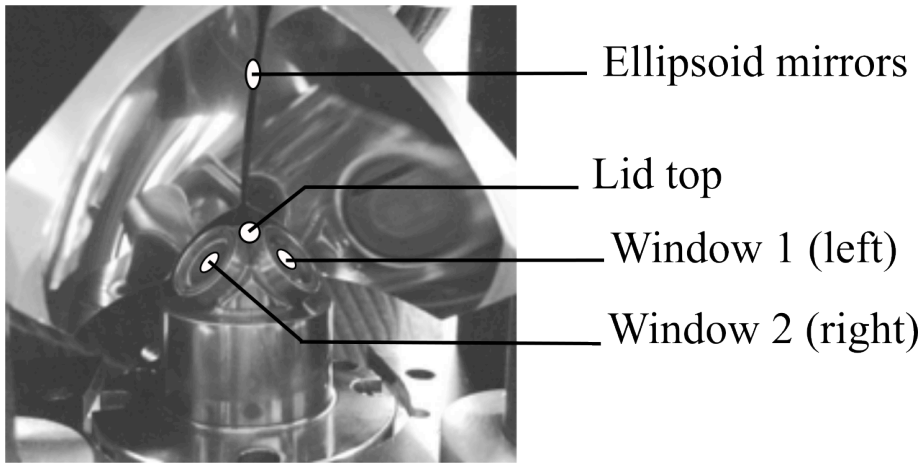

Figure 4.11 Thermocouple locations.

For temperature measurements, ZnSe windows were replaced with aluminum discs of the same dimensions with thermocouples inserted through the middle and secured with high temperature resistant cement. The aluminum disks were held in place by the compression nuts. In this manner, temperatures were measured within 1 mm of the ZnSe window location inside the environmental chamber (labeled "Window 1" and "Window 2" in Figure 4.11). Figure 4.11 shows the environmental chamber lid viewed from the back of the instrument. Therefore, when viewed from the front, window 1 is on the left, and window 2 is on the right. In figures 4.12 – 4.14 it can be seen that window temperatures were not the same. Window 2 was hotter than window 1 because

part of the nichrome wire heating element was close to it, causing it to heat to higher temperature.

To measure the temperature of the environmental chamber lid, a thermocouple was placed at the topmost point of the lid and secured with heat-resistant tape (labeled "Lid top" in Figure 4.11).

To measure the temperature of the ellipsoid mirrors, a thermocouple was threaded through a piece of high-temperature-resistant tape so that the tip of the thermocouple was not touching any part of the instrument and measured the temperature of the atmosphere close to the ellipsoid mirrors (within less than 1 mm of the reflective surface of the ellipsoid mirrors). All temperature measurements were correlated with T_{Pt} during VT-DRIFTS measurements.

With Ag powder in the sample holder, the following heating program was implemented: ambient for 5 min, then heating to 300 °C at 5 °C/min, held at 300 °C for 5 min, and then cooling to ambient after while continuing to monitor temperatures for 40 min. To test the effects of sample holder purge rate on instrument temperatures, sample holder purge was set to 10 mL/min and 100 mL/min, and experiment were repeated two times each to confirm reproducibility. The data presented here were collected with a fan secured to the instrument base in the front compartment to circulate CO_2-free dry air. Figure 4.12 shows an overlay of the instrument temperature profiles measured in two separate experiments while the 10 mL/min He purge was employed. Figure 4.13 shows an overlay of the same measurements made by using a 100 mL/min He purge. In both plots the curves for repeated experiments overlay very well, indicating reproducibility of temperature trends.

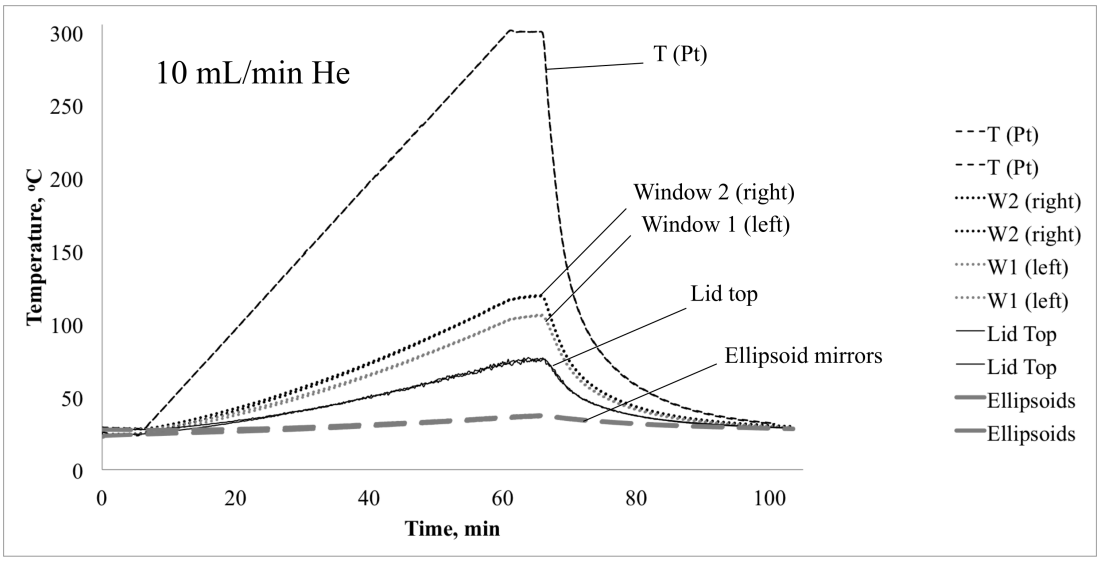

Figure 4.12 Instrument temperature profiles with 10 mL/min He purge.

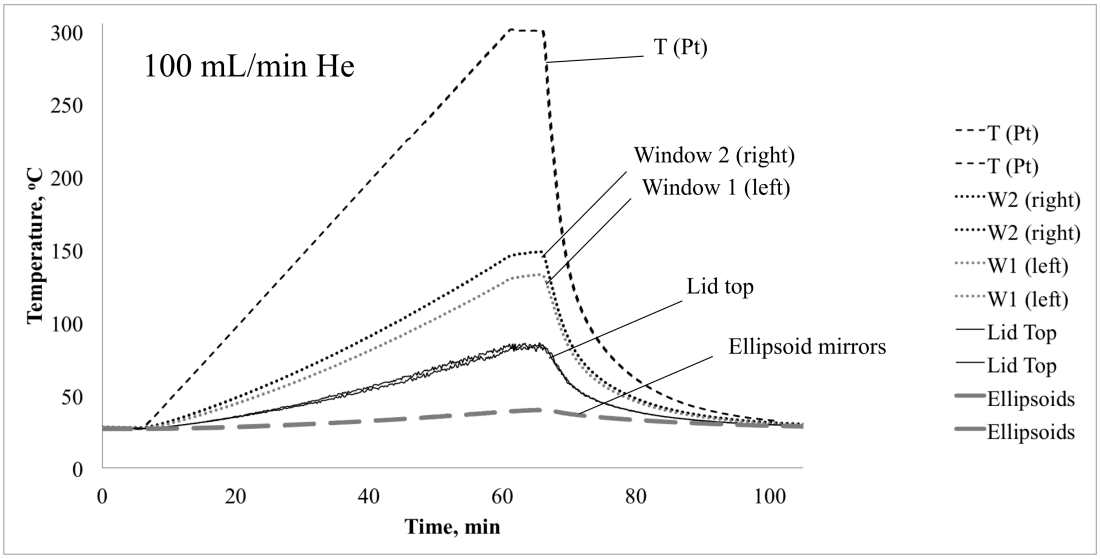

Figure 4.13 Instrument temperature profiles with 100 mL/min He purge.

A temperature gradient extending from the heater was observed, T_{Pt} was measured nearest the heater. The ZnSe window measurements were made less than 1 inch from the heater and reached 105.42 – 148.35 °C when the sample was heated to

300 °C. The top of the environmental chamber lid reached 74.26 – 85.77 °C, and the ellipsoid mirrors warmed from ambient to 36.66 – 40.00 °C during heating profiles.

Results described in Chapter 3 indicate that sample holder He purge rate did not significantly alter T_{surf} values. However, Figure 4.14 shows that temperatures at other locations were consistently greater when the higher He purge rate was employed. Figure 4.14 is an overlay of instrument temperature versus time plots obtained with 10 and 100 mL/min He purge rates. Black lines depict measurements made while purging at 10 mL/min He, and the gray lines represent the same measurements, but while purging at 100 mL/min He. The higher He purge flow rate resulted in greater heating of the chamber lid and ellipsoid mirrors. This was likely due to more efficient thermal conduction from the heater element to the environmental chamber lid when a higher purge flow rate was employed.

Based on these results, 10 mL/min He purge would be preferred over 100 mL/min He purge for VT-DRIFTS measurements because of reduced instrument component heating. In addition to lower cost (for He), lower He purge rates would yield less wear on the instrument components. Also, reduced heating of instrument optics should minimize temperature-dependent optical alignment variations, resulting in more accurate VT-DRIFTS measurements.

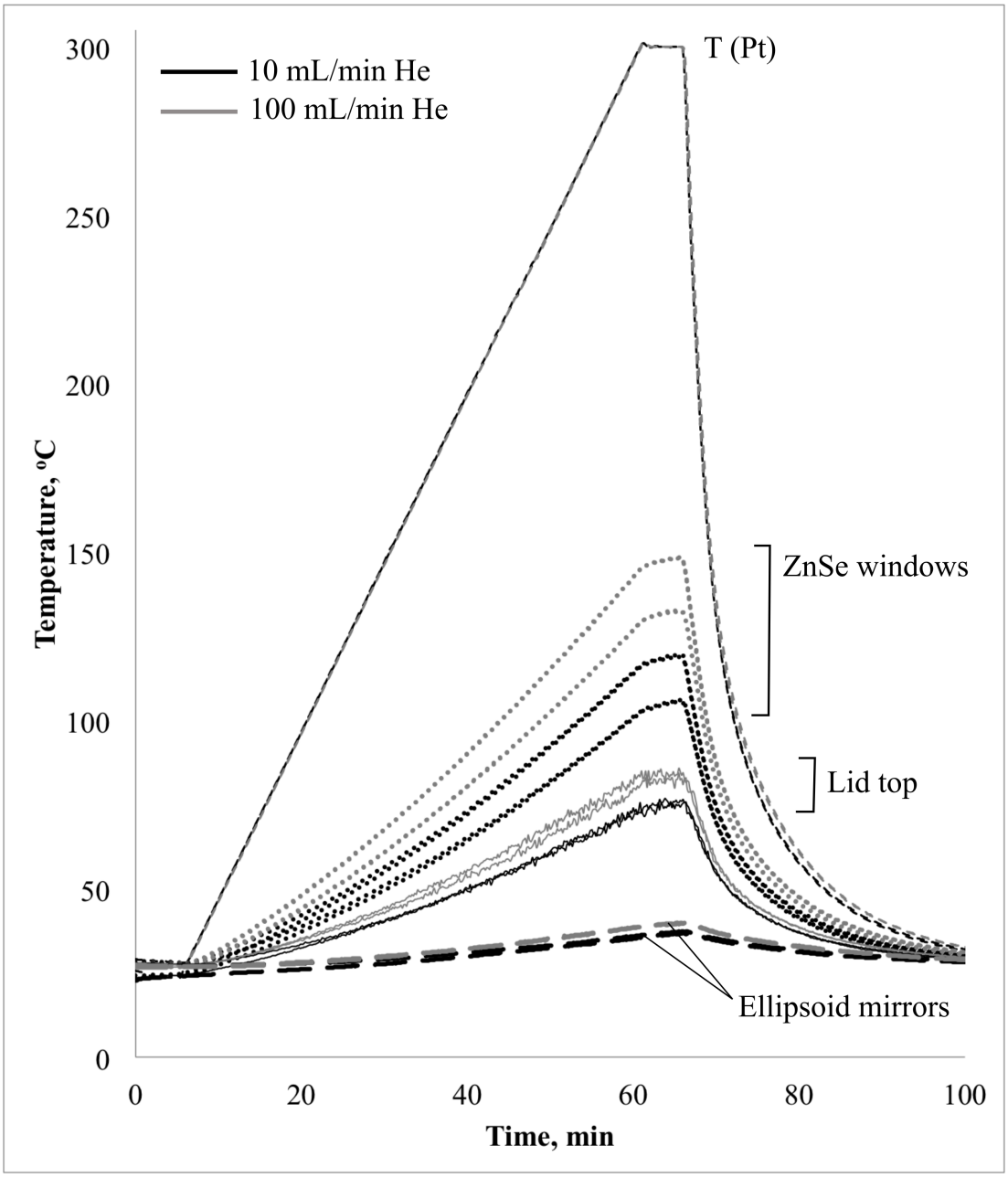

Figure 4.14 Comparison of the instrument temperature profiles obtained using 10 and 100 mL/min He flow.

Note that temperature stabilization at the isothermal region evident in the T_{Pt} versus time plots near 60 min becomes less distinct for environmental chamber components and ellipsoid mirrors, which are located further from the heating source.

This confirms that these instrument components continue to increase in temperature even when the sample temperature attains isothermal equilibrium. Continued heating of these components at sample isothermal temperatures contributes to optical alignment changes that may be responsible for the baseline slope change delays described in Chapter 3 (Figure 3.30).

4.3.2 Correlations Between Spectral and Temperature Data

To further investigate the nature of the temperature gradient that develops throughout the instrument when the sample is heated, thermocouples were placed near the interferometer (by the beamsplitter), on the DRA base, and on top of the sample chamber lid (as shown in Figure 4.11). The thermocouple near the beamsplitter measured air temperature near the interferometer. Thermocouples attached to the DRA and environmental chamber lid were in contact with the metal. Thermocouples were secured in position by using heat-resistant tape. In addition, two thermocouples were placed outside the instrument to measure the room temperature. All temperature measurements were compared with T_{Pt}, the VT-DRIFTS sample holder temperature.

With Ag powder in the sample holder, the following heating program was implemented: ambient for 1 hour, then heating to 300 °C at 5 °C/min, isothermal at 300 °C for 5 min, and then cooling to ambient temperature while continuing to monitor temperatures for a total of 1000 min. In addition to temperature measurements, VT-DRIFTS spectra were collected during the first 500 min. During heating profile measurements, the sample chamber was purged with 10 mL/min He. Results described here were obtained with a water-cooled heat sink mounted to the DRA. This heat sink

was employed to minimize ellipsoid mirror heating, but did not have a significant effect on measured spectrum quality. VT-DRIFTS heating profile measurements were repeated three times, yielding similar results.

Figure 4.15 shows overlays of temperature versus time plots representing heating at various locations within the instrument. Clearly, temperatures decreased at instrument locations further from the heat source. When the sample temperature (T_{Pt}) was heated to 300 °C, the sample surface temperature was 285.39 °C, the environmental chamber lid was 152.48 °C, and the DRA base temperature reached 33.05 °C.

Figure 4.16 shows an overlay of the interferometer and DRA base temperature versus time plots. The temperature of the DRA base increased from 26.42 to 33.05 °C, and interferometer temperature changed from 28.93 to 29.87 °C (< 1 °C). Periodic oscillations are apparent in both plots. Also, the DRA base and interferometer maximum temperatures were reached at different elapsed times, with the interferometer temperature increase lagging the DRA base temperature. The DRA base maximum temperature occurred slightly after the T_{Pt} maximum was reached (Figure 4.15). In contrast, the interferometer maximum temperature occurred about an hour later. Temperature maxima and the elapsed times required to reach these temperatures at the various instrument locations are listed in Table 4.3.

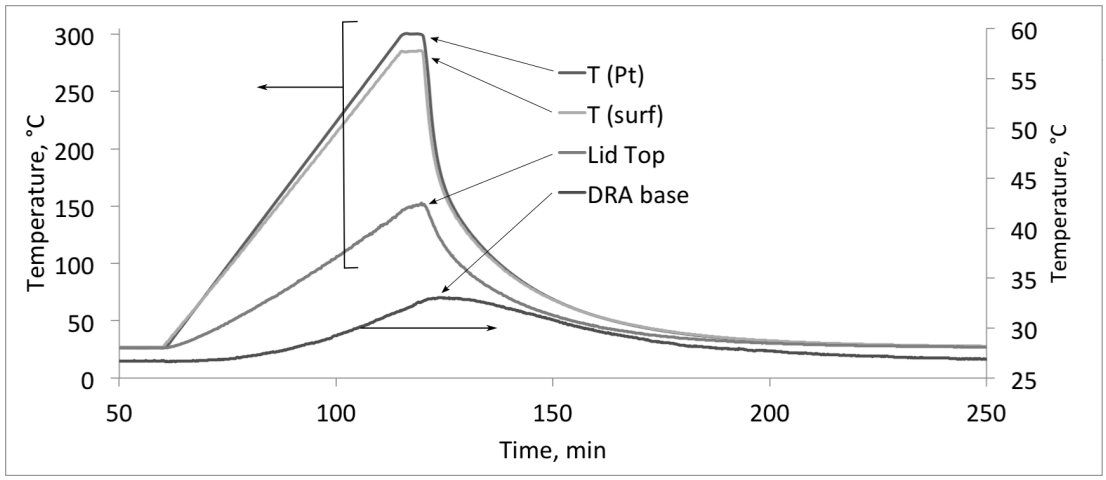

Figure 4.15 Instrument location temperature profiles.

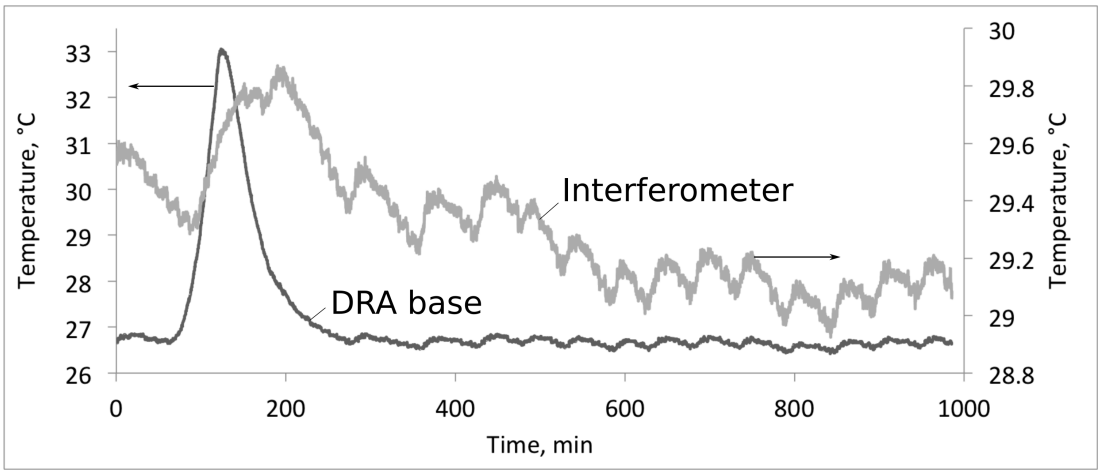

Figure 4.16 DRA base and interferometer temperature profiles.

Table 4.3 Instrument Location Maximum Temperatures and Elapsed Times.

	T (start), °C	T (max), °C	Time, min
T_{Pt}	26.30	300.50	116.05
T_{surf}	26.60	285.39	119.67
T (Lid top)	26.42	152.48	119.67
T (DRA base)	26.72	33.05	123.5
T (Interferometer)	29.53	29.87	190.17

At the end of the heating ramp, the sample holder temperature (T_{Pt}) exceeded the isothermal setting by about 0.5 °C and then quickly equilibrated at 300 °C. In contrast, the sample surface and environmental chamber lid reached their maximum temperatures near the end of the sample holder isothermal period at 300 °C. The DRA base reached its maximum temperature almost 4 min after sample holder cooling had begun, and the interferometer reached its maximum temperature 70.5 min after the start of the cooling phase. Thus, instrument temperatures continue to change long after sample holder temperatures have changed. These long-term temperature trends contribute to variations in optical alignment that affect measured spectra but are uncorrelated with temperature-dependent sample changes. More specifically, these optical alignment variations likely contribute to spectrum baseline artifacts (section 3.5).

Room temperature versus time plots derived from two separate thermocouples mounted outside the FTIR are shown in Figure 4.17. Room temperature control was achieved by periodically blowing warm air into the space. In Figure 4.17, room heating cycles are denoted by the repetitive room temperature spikes. Interestingly, an interferometer temperature cycling is repeated on a time scale that is similar to the room temperature spikes, but out of phase with room temperature changes. This phase difference was most likely due to the time required for interferometer heating after the increases in room air temperature. Figure 4.18 shows that VT-DRIFTS spectrum baseline slope changes exhibited a pattern that was similar to that for the interferometer temperature variations. In addition, baseline slope changes were in phase with interferometer temperature oscillations. This suggests that room temperature fluctuations caused slight interferometer temperature oscillations, resulting in periodic

optical alignment changes, which produced repetitive baseline slope artifacts in VT-DRIFTS spectra (Figure 3.31).

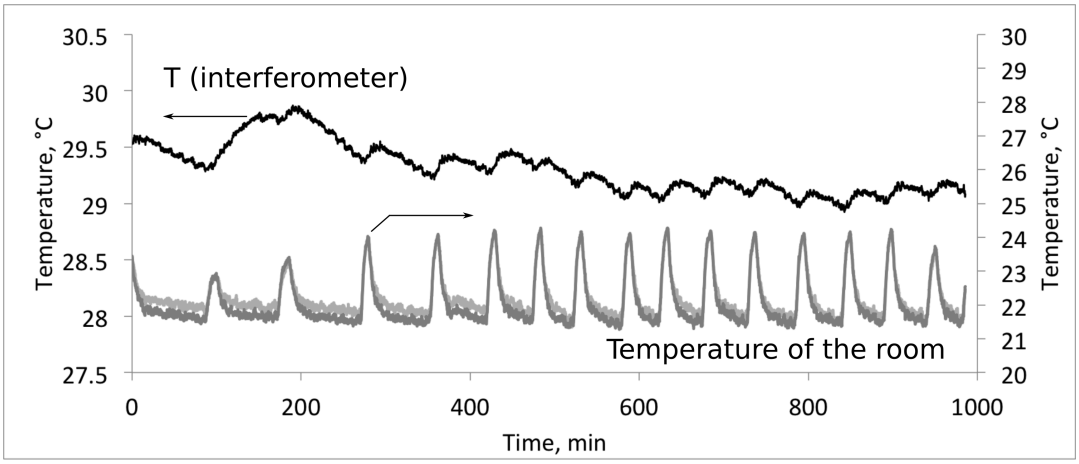

Figure 4.17 Correlation between interferometer and room temperatures.

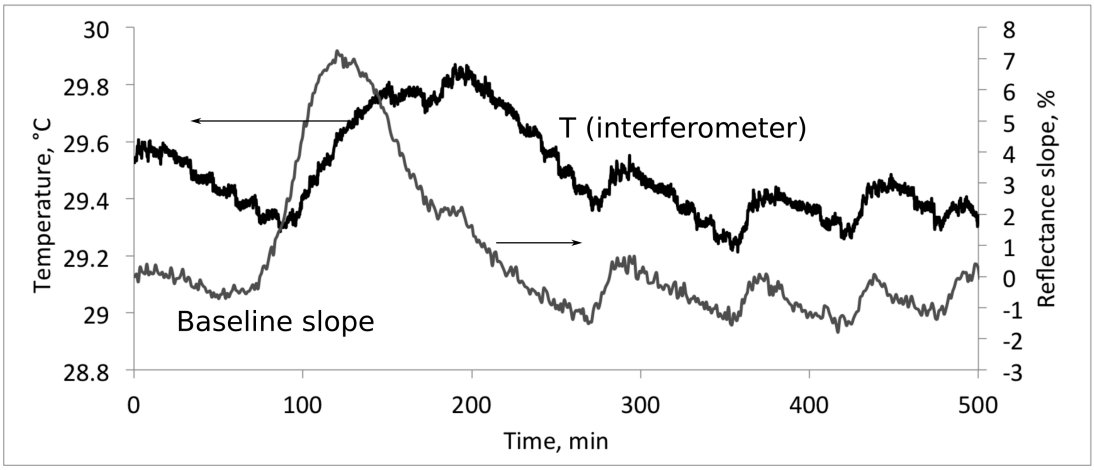

Figure 4.18 Correlation between baseline slope changes and interferometer temperature fluctuations.

The strong correlation between spectrum baseline slope oscillations and interferometer temperature indicates that interferometer alignment is an important factor in temperature-induced spectral artifacts. As described previously, larger changes at

higher wavenumbers are consistent with optical alignment effects, because interference for shorter wavelengths is more sensitive to beam path length changes. At the interferometer, a $\lambda/4$ moving mirror translation causes a shift from brightness to darkness at the detector (as discussed in section 2.3.1).[1] Over the 650 – 4000 cm^{-1} range, $\lambda/4$ distances are between 0.000385 and 0.0000625 cm. These path length increments are within the range expected for optical component thermal expansion.

4.4 Instrument Response to Temperature Manipulations

Various methods were evaluated for minimizing instrument component heating, both due to VT-DRIFTS sample heating, and room temperature fluctuations. Cooling of select instrument components during sample heating reduced sample temperature (T_{Pt}), requiring greater power to the heater to achieve desired temperatures. Thermally insulating the instrument from the environment by covering it with a blanket was not effective, possibly because the instrument was under constant CO_2-free dry air purge. Wrapping the CO_2-free dry air purge tube with heating tape served to increase the temperature inside the FTIR, but this also did not eliminate thermal oscillations. Immersing this tube in a temperature controlled water bath was also ineffective, possibly because there was insufficient time for temperature equilibration as the gas passed through the cooled portion of the tube. Incorporating insulation between the sample chamber and the DRA decreased the temperature change of the DRA during heating somewhat, but did not provide significant improvements to acquired VT-DRIFTS spectra. Incorporating a fan inside the sample compartment decreased noise in the temperature and the baseline slope oscillation patterns. However, increased

circulation of hot air through the instrument caused the temperature in interferometer compartment to increase. Considering that interferometer temperature changes of less than 1 °C can result in spectrum baseline artifacts (Figure 4.18), and that increased exposure of the detector to heat decreases signal intensity, the use of a fan to cool the sample chamber during spectral measurements is not recommended.

In an attempt to decrease the thermal gradient between the sample and optical components, a water-cooled heat sink was fabricated and attached to the back of the DRA ellipsoid mirrors. VT-DRIFTS measurements were made with the heat sink adjusted to ambient, 30, 50, and 80 °C. It was found that maintaining the heat sink temperature near ambient yielded the best results. Higher heat sink temperatures affected the thermal equilibrium of the instrument. In general, modifying and controlling temperatures far from the sample holder had little impact on VT-DRIFTS measurements. This makes sense, because the largest VT-DRIFTS thermal changes occur nearest the sample. In fact, sample holder thermal expansion was found to be the most important factor for determining VT-DRIFTS spectral quality (Chapter 5).

4.5 References

1. Ingle, J.D. and S.R. Crouch, *Spectrochemical Analysis*, Prentice Hall: New Jersey (1988).

Chapter 5: Effects of Sample Displacement on Spectral Features

5.1 Optimal Alignment: Effect of Sample Height

Prior to obtaining diffuse reflection spectra, instrument optics must be aligned to maximize single beam emissivity and to obtain accurate spectral features. Proper optical alignment assures that infrared source radiation is focused on the sample. For DRIFTS, proper alignment also requires that the amount of diffusely reflected radiation collected and delivered to the detector is maximized. When compared to transmittance spectroscopy, diffuse reflection optical alignment is more critical, because additional mirrors are needed to focus radiation on the sample and collect diffusely scattered radiation. The DRIFTS alignment procedure includes determination of the optimal 3-dimensional position of the sample. The best quality spectrum is typically obtained by an iterative approach in which all optical system components are sequentially adjusted to achieve the largest interferogram detector signal. During this process, individual optical components are moved until any alignment change results in a decrease in interferogram signal.

For the VT-DRIFTS apparatus used for studies described here, the horizontal sample holder position was optimized by attaching the sample chamber to a movable base plate and then moving the plate under the beam focusing optics until the largest detector signal was obtained. After the optimum horizontal sample position was found,

the plate was secured in place by setscrews. Next, the optimum sample height was determined by monitoring the interferogram signal while moving the sample holder up and down in small increments (e.g. thousandths of an inch). Sample height was arbitrarily defined here as the distance from the bottom surface of the sample compartment to the top surface of the sample holder. This distance was measured in inches by using a Vernier caliper.

After attaching a metal ruler "extension arm" to a Vernier height gauge, sample holder height could be measured to the nearest 0.001 in and was varied between 2.550 in and 2.600 in. An air bubble level was placed on the sample holder base during adjustments to assure that height adjustments did not result in horizontal movements. The measurement system is shown in Figure 5.1.

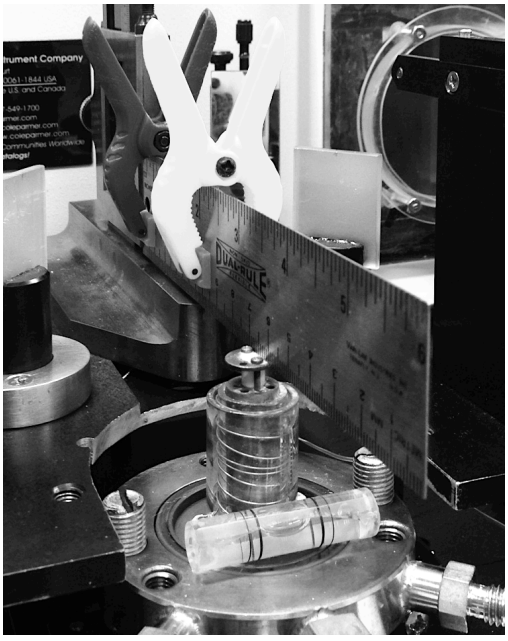

Figure 5.1 Vernier height gauge with extension arm and air bubble level.

To move the sample holder, two height adjustment screws (located to the left and right of the sample post in Figure 5.1) were rotated and then fixed in place with set

screws after checking that the sample holder was still aligned horizontally (based on the air bubble level indicator). Sample holder vertical positions were measured after each height adjustment by lowering the "extension arm" of the caliper to gently touch the top of the sample holder. For accuracy, the height was determined 3 separate times by the Vernier caliper after each sample height adjustment. Then, the environmental chamber lid and ellipsoid mirrors were secured in place, and the optics were aligned to attain the maximum interferogram signal.

In order to determine the optimal sample height, the optics were realigned after each height adjustment to optimize spectrum shape and intensity. Spectra collected at the optimal sample holder height yielded the greatest interferogram peak-to-peak (p2p) voltage, which corresponded to the highest single beam spectrum emissivity. Also, spectral features were checked to assure that they most accurately matched those for the material contained in the sample holder during alignment, which was silica gel (SiO_2).

Figure 5.2 shows the dependence of p2p interferogram voltage on sample holder height. The p2p voltage is directly proportional to the integrated intensity of the radiation striking the detector, and was used here as a measure of radiation transfer efficiency (i.e. from source to detector). Measurements were made with silica in the sample holder, a DTGS detector with gain set to 1, and without purging the instrument between measurements. Figure 5.2 shows interferogram signal variations resulting from moving the sample height from optimum, which was determined to be 2.581 in. Larger deviations from those shown in the graph yielded interferogram signals that were very small and insufficient to permit the instrument to initialize and provide a measurement. Figure 5.2 shows that within a window of about ±0.003 in from the

optimal sample height, the instrument optics could be aligned to provide a consistently high spectrum quality. However, larger deviations resulted in drastic interferogram voltage decreases of more than 50%. The slight decrease in p2p voltage at 0.000 (i.e. optimum) sample height may have been caused by the fact that the infrared beam intensity was not uniform across the diameter of the incident beam, which resulted in a slight reduction in radiation intensity even though the optics were optimally adjusted. It may also have been caused by changes in ambient water vapor and carbon dioxide concentrations, which were uncompensated during these measurements.

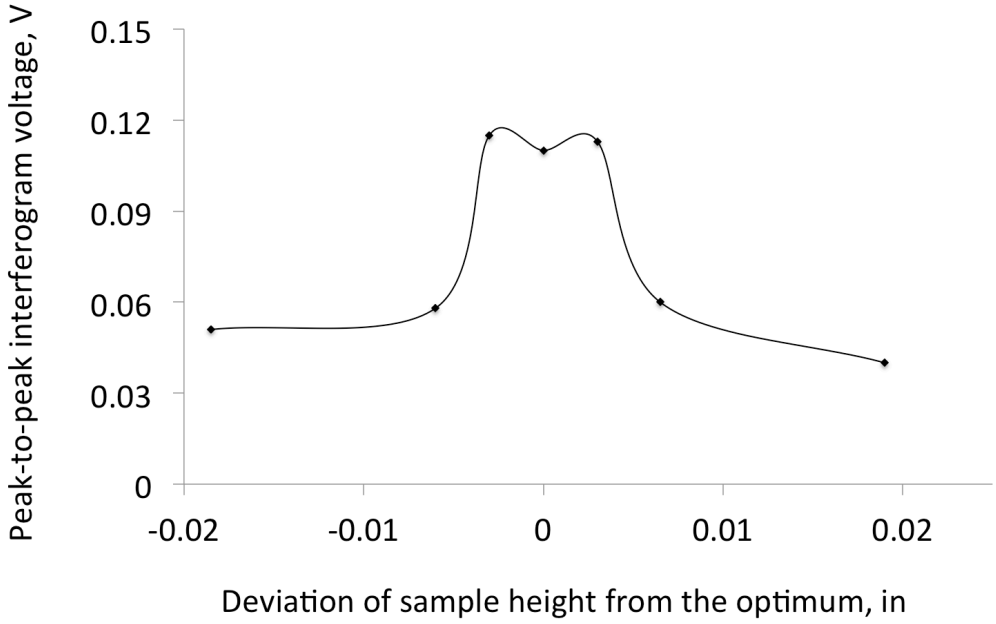

Figure 5.2 Effect of sample height on signal intensity.

Figure 5.2 shows that the vertical location of the sample is critical to signal intensity and spectrum quality, and if sample vertical movement occurs between measurements, such as due to thermal expansion during heating, spectrum quality will deteriorate. The results shown in Figure 5.2 were obtained by aligning the optics after

each sample height change. However, during VT-DRIFTS measurements, the optics would not be continually optimized. Therefore, loss of spectral quality resulting from temperature-dependent sample holder expansion during VT-DRIFTS measurements would be expected to exceed that depicted in Figure 5.2.

By comparing measurements made with and without the environmental chamber lid, it was found that the lid significantly decreased interferogram signal, but did not affect the optimal sample height location (Figure 5.3).

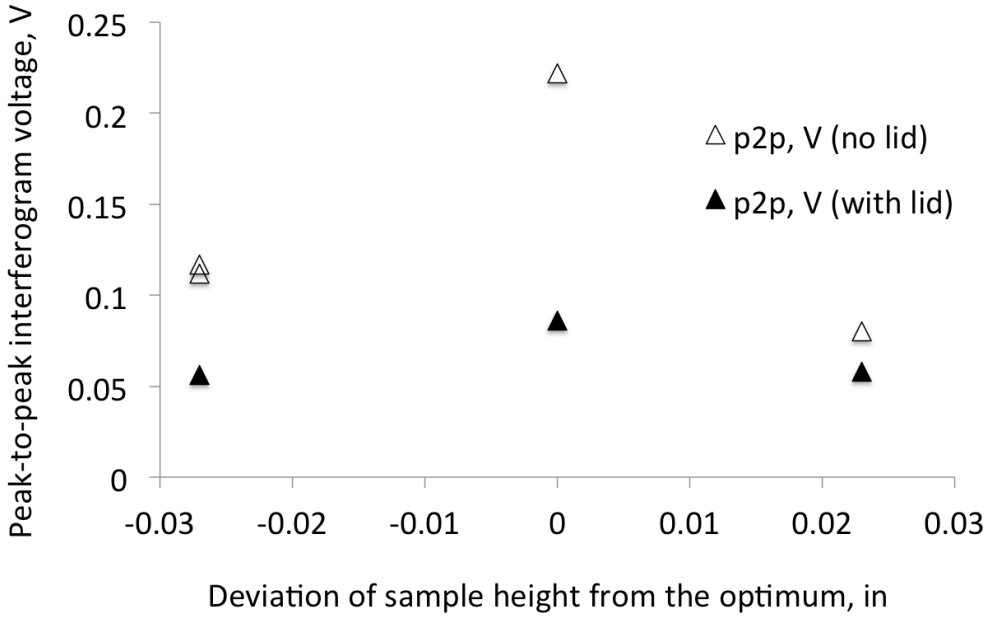

Figure 5.3 Effects of sample height and environmental chamber lid.

5.2 Eliciting Spectral Changes at Ambient Temperature

VT-DRIFTS measurements typically exhibit decreased interferogram signal and sloping baselines in spectra obtained while heating the sample. As shown in Figure 5.2, decreased interferogram signal occurs at ambient temperature when the sample is

moved away from the DRA focal point. In addition, baseline slope can be introduced into spectra by changing the sample location. Because sample height plays a major role in spectral quality, a device was built to facilitate sample height adjustments from outside the instrument, making it possible to change the sample height while collecting VT-DRIFTS spectra. A one inch travel micrometer was fastened to a metal plate supporting the sample holder and environmental chamber so that the height of the entire sample chamber assembly could be adjusted from outside the instrument sample compartment. The micrometer could be used to change the sample chamber height by a maximum of one inch, and measurements could be made to the nearest one thousandth of an inch. A photograph of the micrometer attached to the sample holder base plate is shown in Figure 5.4.

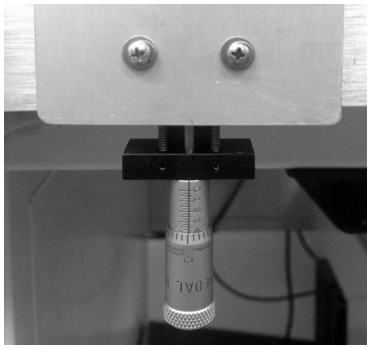

Figure 5.4 One inch travel micrometer attached to the sample holder base plate.

By varying the height of the sample from slightly above optimum alignment to slightly below optimum alignment, it was found that baseline slope and interferogram signal intensity could be varied in a manner similar to that observed when the sample was heated.

Figure 5.5 shows overlays of representative single beam spectra collected with the sample holder lowered by 0.008 in ±0.003 in below the optimal position (gray), raised by 0.014 in ±0.005 in above the optimal position (black), and at the optimal position ($\Delta h = 0$) both before and after moving the sample out of alignment (dots). For clarity, only 3 spectra for each height are shown. Spectra collected at the optimum height prior to and following the height adjustments overlay very well, indicating that the method for adjusting sample height provided reproducible sample positions and thus reproducible spectra. Moving the sample to 0.008 in ±0.003 in below and 0.014 in ±0.005 in above the optimum height caused signal intensity to decrease by about 30%, as determined by ratioing sample and reference single beam spectrum intensities. Note that below 1300 cm^{-1}, the gray lines are above the black lines, and that above 1300 cm^{-1}, the trend is reversed. This denotes a change in single beam spectrum shape.

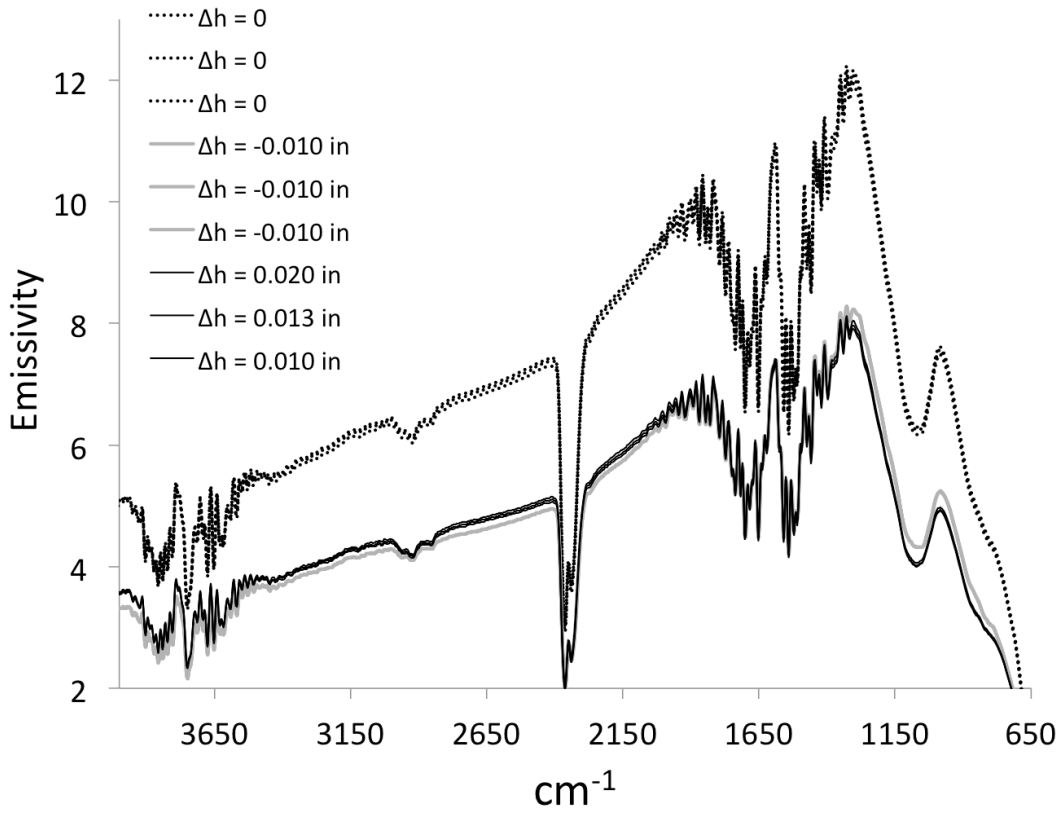

Figure 5.5 Single beam spectra measured at different sample holder heights: (a) optimum height (dots), (b) lowered by 0.008 ±0.003 in (gray), (c) raised by 0.014 ±0.005 in (black).

By ratioing single beam spectra collected at varying sample heights to a reference single beam spectrum collected at optimum sample height, a series of reflectance spectra were obtained representing baseline changes (Figure 5.6). Reflectance decreased by about 30% when the sample holder was displaced vertically in either direction, and a difference in baseline slope is apparent when comparing spectra generated with single beam spectra measured when the sample height was below optimum (thick gray dashes) and above optimum (thin short black dashes). Spectral features attributed to water vapor and CO_2 fluctuations, which resulted from the lack of

adequate instrument purge during measurements, are the only absorbance features that appear in reflectance spectra. In addition, small variations in the sample holder 3-dimensional location, caused by the fact that the baseplate attached to the micrometer was slightly tilted from horizontal due to the weight of the sample holder, may have contributed to baseline artifacts.

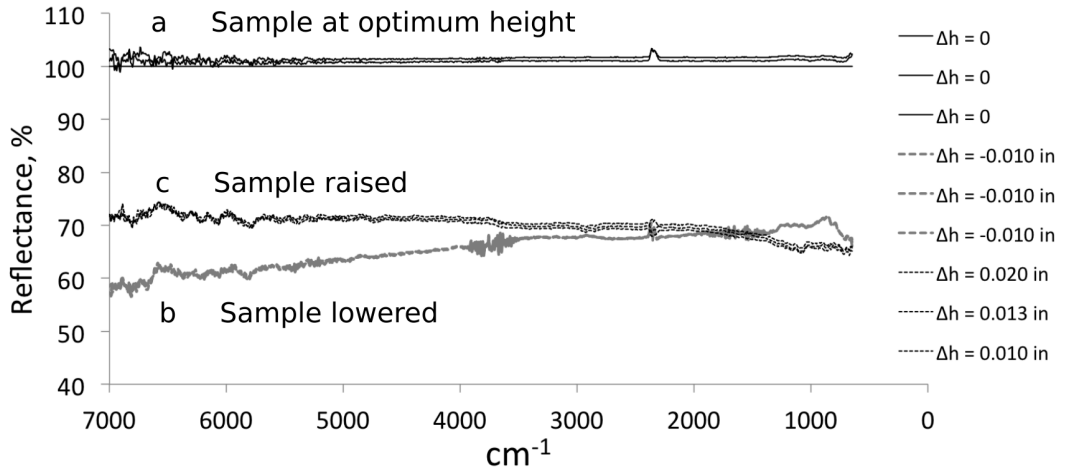

Figure 5.6 Reflectance spectra obtained at various sample holder heights: (a) optimum height, (b) -0.008 ±0.003 in, (c) +0.014 ±0.005 in.

Baseline slope (in % reflectance) was estimated by subtracting the reflectance value at 2000 cm^{-1} from the reflectance value at 4000 cm^{-1}. Figure 5.7 represents these differences (triangles) as a function of Δh, the deviation from optimum sample height. Positive Δh values correspond to spectra collected when the sample was located above the optimum height and negative values were derived from measurements made when the sample was located below the optimum height. The straight line through the data points represents the least squares fit to the data. The best-fit line has a positive slope, indicating that with increasing sample height, single beam spectrum intensity shifts to higher wavenumbers.

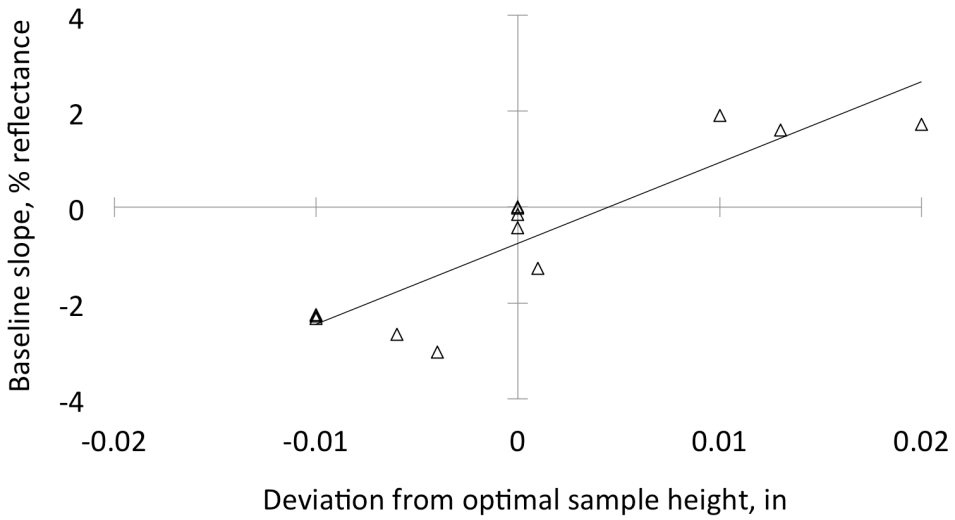

Figure 5.7 Baseline slope variations of reflectance spectra as a function of sample height.

Figure 5.7 shows that reflectance spectra baseline slopes can be introduced by isothermally moving the sample vertically. Although the magnitude of the slope is similar regardless of the direction in which the sample is moved, the sign of the baseline slope depends on the direction that the sample was moved. When sample height increased, baseline slope increased. When the sample was lowered, the baseline slope decreased. For a sample height change of about 0.01 in, a 30% decrease in reflectance was obtained along with a baseline deviation from horizontal on the order of 2%. These findings are summarized in Table 5.1.

Table 5.1 Effect of Sample Height on Reflectance Intensity and Baseline Slope.

Δh from $h_{optimum}$, in	Reflectance at 2000 cm^{-1}, %	Baseline slope (difference between reflectance at 4000 and 2000cm^{-1}), %
0	101.1 ±0.7	0.4 ±0.5
-0.008 ±0.003	68.7 ±0.7	-2.5 ±0.3
+0.014 ±0.005	69.5 ±0.6	+1.7 ±0.2

5.3 Sample Height Variations: Effect of the Environmental Chamber Lid

When the sample is heated during VT-DRIFTS measurements, thermal expansion of both the sample holder and the environmental chamber occur. The rate of expansion of the environmental chamber lid would be expected to be lower than the rate of expansion of the sample holder, due to a negative temperature gradient extending from the sample heater to the environmental chamber lid. If the change in environmental chamber lid height with respect to the optimum sample alignment position is represented by Δh_{lid}, this value will be positive when the lid is above the optimum alignment position and negative when it is below. Because the sample holder will expand faster than the environmental chamber lid during VT-DRIFTS sample heating, Δh_{lid} should decrease with increasing sample temperature. In order to simulate the relative movement of the environmental chamber lid with respect to the sample holder at ambient temperature, modifications to the environmental chamber were required. While keeping the sample holder at the same height, the lid was raised in small increments by inserting thin aluminum disks under the lid in three places, as shown in the Figure 5.8.

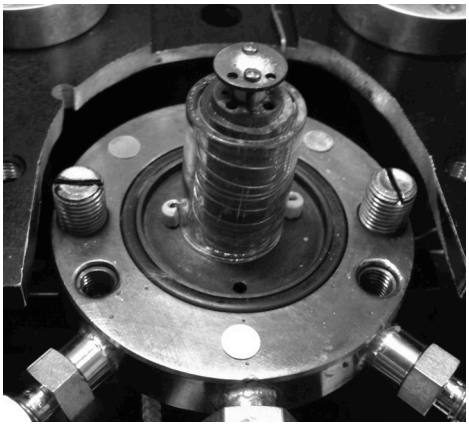

Figure 5.8 Environmental chamber base with aluminum disk spacers.

The thickness of each disk was about 0.002 in ±0.001 in (determined by measuring the thickness of 5 disks with digital Vernier calipers). However, the measured change in the vertical location of the environmental chamber lid was not found to be in increments of 0.002 in, but was slightly greater. Thus, the surfaces of the disks and/or the chamber base may not have been completely flat.

Figures 5.9a and 5.9b show single beam spectra obtained with the lid position at optimum alignment (i.e. Δh_{lid} = 0.000 in, depicted by the lightest gray line) and spectra obtained after raising the environmental chamber lid by varying amounts (i.e. successively darker lines with the black line depicting the spectrum collected when Δh_{lid} = 0.018 in). Figure 5.9b shows the same data as shown in Figure 5.9a, but with an expanded wavenumber scale. Single beam spectra overlays show that larger differences occur at higher wavenumbers. Figure 5.9c shows overlays of reflectance spectra obtained by ratioing single beam spectra measured with various Δh_{lid} environmental chamber lid heights to the initially measured single beam spectrum, which was

collected at the optimal lid height. The overlay of reflectance spectra shows a trend of increasingly negative baseline slope with increasing Δh_{lid} values.

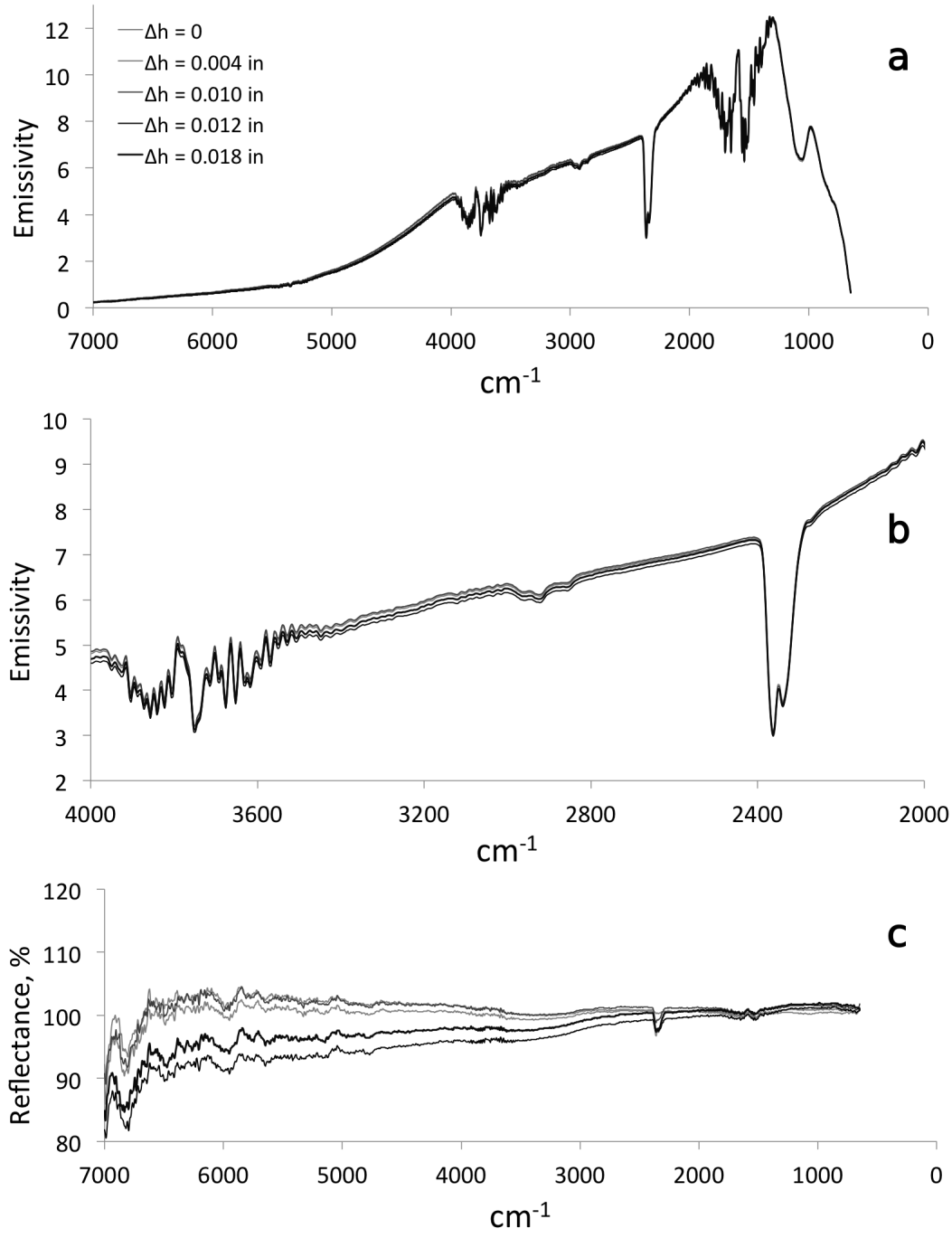

Figure 5.9 Effect of vertical displacement of the environmental chamber lid on a) single beam b) expanded scale single beam and c) reflectance spectra.

Although the data exhibits significant scatter, reflectance baseline sloping increases in magnitude when the environmental chamber lid is lifted above the optimal position relative to the sample surface (Figure 5.10). This is consistent with the appearance of a positive reflectance spectrum baseline slope that increases with increasing sample temperature. During heating, sample holder thermal expansion would move the sample surface closer to the environmental chamber lid. Thus, thermal expansion of the sample holder and environmental chamber lid would produce the opposite of the trend shown in Figure 5.10.

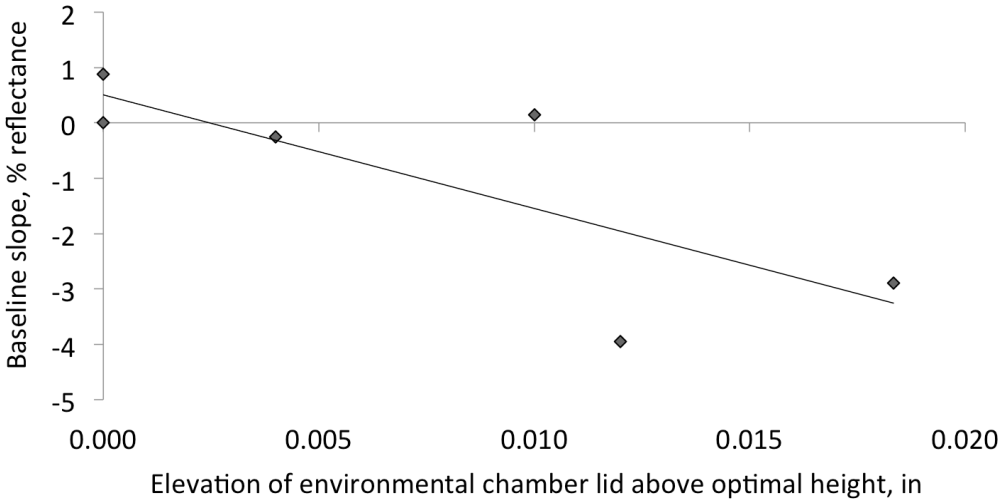

Figure 5.10 Reflectance baseline slope trend observed when the environmental chamber lid was lifted.

5.4 Thermal Expansion-Related Spectral Changes

Temperature measurements made by placing thermocouples throughout the diffuse reflection optical system confirmed that a large temperature gradient developed throughout the instrument, with the highest temperatures near the heater. Changes in

the sample holder position relative to the environmental chamber lid can cause reflectance spectrum baseline slopes similar to those observed with VT-DRIFTS measurements. To estimate the movement of the steel post due to thermal expansion, the temperature of the steel post was measured by using the Agilent Data Logger while the sample holder was heated with the following temperature program: hold for 10 min at ambient temperature, heat to 200 °C at 5 °C/min, hold for 10 min at 200 °C, heat to 500 °C at 5 °C/min, hold for 1 min at 500 °C, allow to cool by removing power to the heater.

Two thermocouples were placed on the metal sample holder to measure its temperature: one at the top, near the sample, and one at the environmental chamber base. The thermocouples were electrically isolated from the heating coil to prevent short circuits. Thermocouple placement is shown in the Figure 5.11 photograph. The environmental chamber lid was placed over the sample holder and thermocouple wires so that He purge gas could be passed into the chamber at a rate of 10 mL/min to simulate VT-DRIFTS measurement conditions.

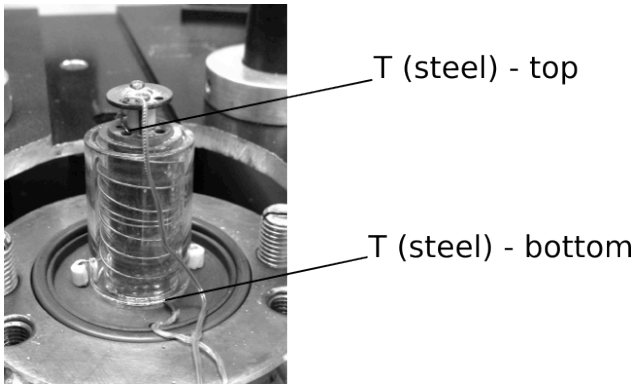

Figure 5.11 Location of thermocouples measuring the steel post temperature during sample heating.

Temperature versus time plots obtained during the heating program are shown in Figure 5.12.

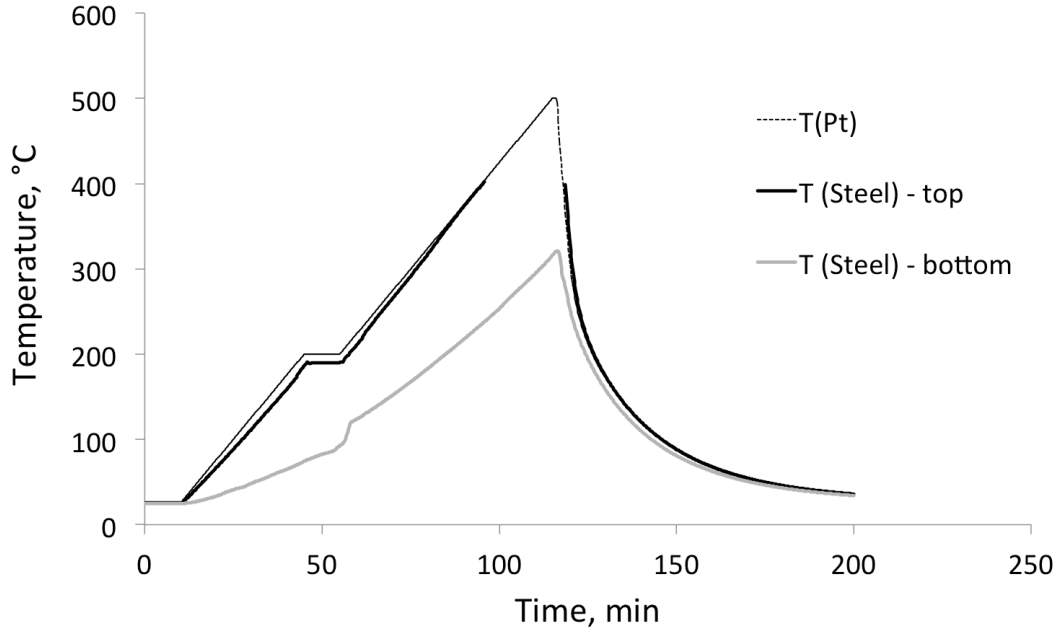

Figure 5.12 Steel post and sample temperatures during heating.

Initially, temperature readings at the bottom of the sample (T_{Pt}), the top of the sample holder, and at the environmental chamber base were similar. The average temperature of the steel post was 25.41 ±0.40 °C at ambient temperature over the 10 min isothermal period. The temperature measured near the top of the steel post (thick solid black line) closely matched T_{Pt} (thin dash black line), which was expected due to the proximity of these thermocouples. The steel post temperature near the environmental chamber base increased more slowly with time, because that location was farther from the heating source. As a result, a temperature gradient developed between the top and bottom of the steel post employed as the sample holder. During isothermal temperature periods, the temperature measured near the top of the steel post

was relatively constant, whereas the temperature near the bottom of the post continued to rise. Thus, although thermocouples located near the sample indicated that the temperature was fairly constant, the temperature gradient along the length of the steel post continued to change during isothermal periods, suggesting that optical alignment may have continued to change. When T_{Pt} was held at 200 °C, the temperature at the top of the steel post increased from 186.60 to 190.26 °C during the 10 min isothermal period, whereas the temperature near the bottom of the post increased from 74.39 to 92.64 °C. The continually changing steel post temperature gradient was likely responsible for spectral changes observed under isothermal conditions in spectra measured at elevated temperatures. When the heating ramp began following the isothermal period at 200 °C, the temperature near the bottom of the steel post increased sharply for about 2 min (from 55 to 57 min) and then the rate of increase stabilized.

When T_{Pt} reached 500 °C, the temperature near the bottom of the steel post was 316.29 °C and then increased to 320.46 °C after 1 min. Unfortunately, temperature data for the thermocouple placed near the top of the steel post could not be obtained above 404.16 °C due to failure of the twisted wire thermocouple junction. Apparently, thermal expansion caused the wires to move apart above 400 °C, making temperature measurements impossible. However, as shown in Figure 5.12, when the temperature dropped below 400 °C, thermocouple readings returned, most likely because the twisted pair of wires touched once again. T_{Pt} and the temperature recorded by the thermocouple placed near the top of the sample holder post were within 2 °C near 400 °C, indicating that the temperature at the top of the steel post and at the bottom of the sample were similar. Therefore, to estimate the magnitude of linear thermal expansion of the steel

post at 500 °C, the temperature at the top of the steel post was assumed to be approximately equal to T_{Pt} . The temperature of the steel post began to decrease immediately when the heater was turned off and the sample began to cool.

The linear thermal expansion of the steel post can be estimated based on these measurements by averaging the temperatures at the top and bottom of the steel post. Although this assumes temperature gradient linearity, which may not occur, it provides a rough estimate of the magnitudes of the sample height increases at various T_{Pt} values. Table 5.2 lists selected sample post temperatures and associated average temperatures.

Table 5.2 Sample Post Temperatures.

Ramp program time coordinate, min	**T_{Pt}, °C**	**$T_{top\ of\ post}$, °C**	**$T_{bottom\ of\ post}$, °C**	**T_{post} (Average) °C**
0.00	25.30	25.85	25.30	**25.41 ±0.40**
10.00	25.30	25.57	24.91	
45.00	200.00	186.60	74.39	**130.50**
55.00	200.00	190.26	92.64	**141.45**
115.00	500.00	≈ 500.00	316.29	**408.15**
116.00	500.00	≈ 500.00	320.46	**410.23**

5.4.1 Theoretical Expansion of Sample Support Post

Using the expression $\alpha_L = (1/L)(dL/dT)$, where α_L is the linear thermal expansion coefficient, L is the length of the material, and dL/dT is the change in length per change in temperature, the linear expansion of the sample support post can be estimated. Assuming that the thermal expansion coefficient was independent of temperature, the expression simplifies to:

$$\Delta T \times \alpha_L = \Delta L/L \tag{5.1}$$

The linear expansion coefficient of steel at 25 °C varies with composition, but α_L (steel) = 13.0×10^{-6} °C^{-1} is a reasonable estimate. "The Engineering Toolbox"[1]

The height of the steel post was measured to be 1.30 in ±0.01 in (an average of 6 measurements on different sides of the post).

Initially, the average temperature of the steel post was 25.41 °C. At the beginning of the 200 °C isothermal region, the average steel post temperature increased to 130.50 °C, and after holding at 200 °C for 10 min, the average steel post temperature was 141.45 °C. Thus, at the beginning of the 200 °C isothermal region:

$$\Delta L/L \text{ (steel)} = \Delta T \times \alpha_L = 13.0 \times 10^{-6} \text{ °C}^{-1} \times (130.50 - 25.41) \text{ °C} = 0.14 \% \tag{5.2}$$

$$\therefore \Delta L = (1.30 \text{ in} \pm 0.01 \text{ in}) \times 0.14\% = 0.0018 \text{ in} \tag{5.3}$$

Also, after holding the sample at 200 °C for 10 min:

$$\Delta L/L \text{ (steel)} = 13.0 \times 10^{-6} \text{ °C}^{-1} \times (141.45 - 25.41) \text{°C} = 0.15 \% \tag{5.4}$$

$$\therefore \Delta L = (1.30 \text{ in} \pm 0.01 \text{ in}) \times 0.15\% = 0.0020 \text{ in} \tag{5.5}$$

Thus, when the sample holder reached 200 °C, the sample height was estimated to increase by 0.0018 in, and after 10 min at 200 °C, the sample height would be expected to increase by an additional 0.0002 in.

When T_{Pt} reached 500 °C, the temperature measured at the bottom of the steel post reached 316.29 °C (average temperature 408.15 °C) and then rose to 320.46 °C after 1 min (average temperature 410.23 °C). Thus, when T_{Pt} reached 500 °C:

$$\Delta L/L \text{ (steel)} = \Delta T \times \alpha_L = 13.0 \times 10^{-6} \text{ °C}^{-1} \times (408.15 - 25.41) \text{ °C} = 0.50\% \tag{5.6}$$

$$\Delta L/L \text{ (steel)} = \Delta T \times \alpha_L = 13.0 \times 10^{-6} \text{ °C}^{-1} \times (410.23 - 25.41) \text{ °C} = 0.50\% \tag{5.7}$$

$$\therefore \Delta L = (1.30 \text{ in} \pm 0.01 \text{ in}) \times 0.50\% = 0.0065 \text{ in} \tag{5.8}$$

The value of ΔL would be expected to increase with time because the bottom of the sample holder post, and therefore the average steel post temperature, should gradually increase.

Note that the thermal expansion coefficient is not rigorously constant and should have some temperature dependence, so rather than calculating $\Delta L/L$, an appropriate function describing changes in length (also volume) should be integrated over the appropriate temperature range. Still, $\Delta L/L$ calculations provide rough estimates of steel post thermal expansions. The true expansion of the steel post may be even be greater than these estimates. Considering that interferogram signal intensity and spectrum quality begin to degrade when the sample height is varied by ±0.003 in from optimum, sample vertical position changes of 0.0020 in or 0.0065 in would be expected to have a significant impact on VT-DRIFTS spectra. It should be noted that the ±0.003 in tolerance value was obtained from measurements in which optical alignment was optimized after incremental sample height adjustments. However, for VT-DRIFTS measurements, continuous optical alignment is not viable, so the sample height tolerance would be expected to be less than ±0.003 in.

One solution to thermal expansion sample height changes would be to replace the steel sample holder post with one made from a material with a lower thermal expansion coefficient, like quartz. At 25 °C α_L for quartz is 0.55×10^{-6} /°C^{-1}.[2] Consequently, the thermal expansion of a quartz sample holder would be much less than steel:

$$\alpha_L \text{ (steel)} / \alpha_L \text{ (quartz)} = 13.0 \times 10^{-6} \text{ °C}^{-1} / 0.55 \times 10^{-6} \text{ °C}^{-1} = 23.6 \qquad (5.9)$$

By using the same calculation method employed for the steel sample holder post, the linear thermal expansion of a quartz post would be ~ 8.46×10^{-5} in when T_{Pt} is 200 °C and ~ 2.75×10^{-4} in when T_{Pt} reaches 500 °C. These values are less than the ±0.003 in estimated sample height tolerance for maintaining spectral quality.

5.4.2 Comparison of Steel and Quartz Sample Support Posts

A new sample holder was designed with the sample placed on top of a quartz support tube, with sample heating by using a cartridge heater inserted into a steel post that resided inside the quartz tube. The quartz tube was made longer than the steel post containing the heater, so that the sample never contacted the heated steel post. Unfortunately, this new design did not permit permanent installation of a thermocouple for measuring sample temperatures. To obtain sample temperature measurements, a thermocouple was inserted through an opening in the environmental chamber lid. The cartridge heater was connected to a variac and heating was accomplished by adjusting the variac setting.

Figure 5.13 shows photographs of the steel sample holder support post (a), the quartz tube sample support system (b), and the thermocouple in contact with the sample surface for the quartz support tube system as viewed through one of the environmental chamber lid windows (c).

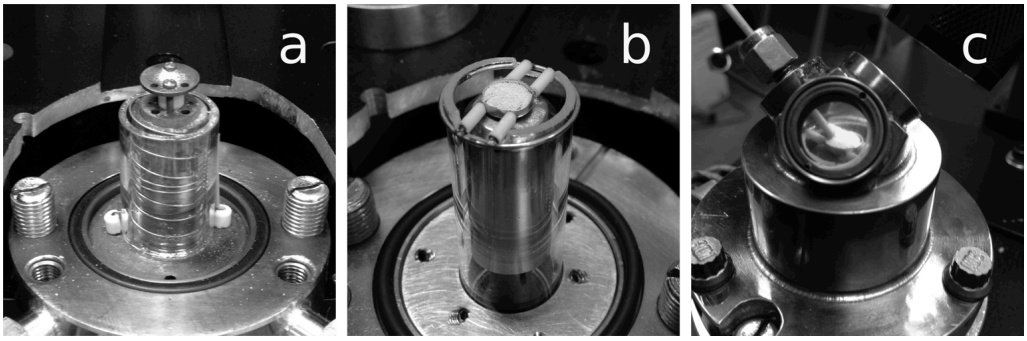

Figure 5.13 (a) Steel and (b) quartz sample holder support systems and (c) thermocouple for the quartz tube sample support system.

To compare results obtained with the quartz and steel sample support systems, samples in both arrangements were heated with a variac to similar temperatures. For the steel post sample holder, sample surface temperatures were estimated from T_{Pt} readings by using a 0.95 multiplier when temperatures exceeded 35 °C (i.e. $T_{surf} = 0.95T_{Pt}$). With silica powder in the sample holder on top of the quartz tube, the optimum sample height was determined, and the DRA optics were aligned for maximum interferogram signal and best silica absorption spectrum quality. After alignment, silver powder was loaded into the sample holder and then heated to various temperatures by adjusting the variac setting. Due to the tight fit of the quartz sample support inside the environmental chamber lid, sample temperatures were kept below 200 °C to avoid breaking the quartz tube.

Because silver powder does not undergo chemical changes below 500 °C, by comparing spectra at different temperatures, it was possible to characterize temperature-induced changes to the measurement system. To track temperature-dependent changes, single beam spectra were ratioed to a single beam spectrum acquired at ambient temperature, producing reflectance spectra with only baseline change information.

Figure 5.14a contains an overlay of single beam spectra collected with silver powder in the steel holder while heating the sample to 257 °C. Figure 5.14b shows an overlay of single beam spectra measured in a similar manner while heating to 212 °C, but by using the quartz tube sample holder system. Comparing the overlay plots in Figure 5.14 reveals that the temperature-dependent decrease in single beam intensity was less significant when quartz was employed.

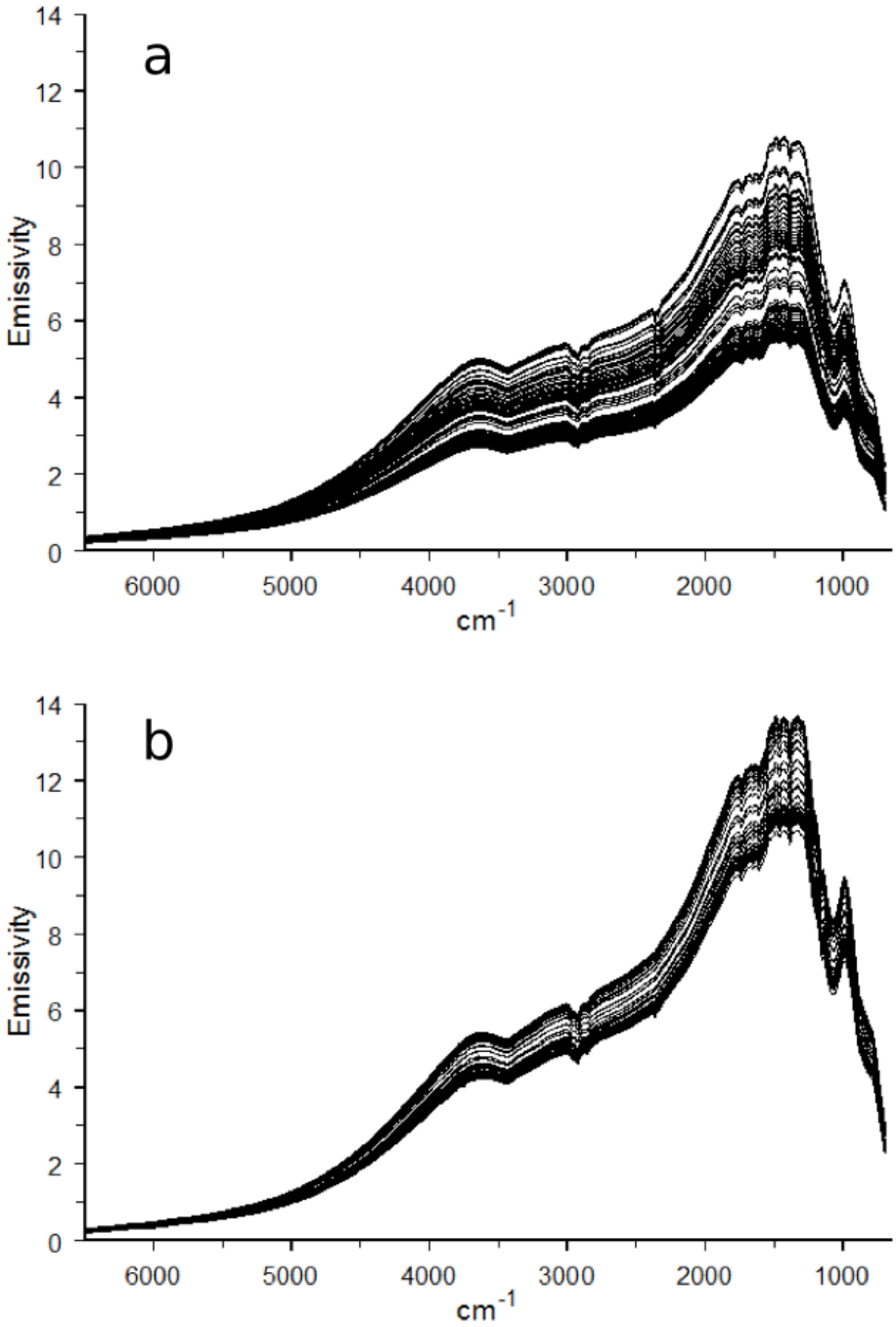

Figure 5.14 Overlay of single beam spectra obtained with the a) steel and b) quartz support systems.

Reflectance spectra obtained by ratioing variable temperature single beam spectra to the initially acquired single beam spectrum (i.e. ambient temperature) are shown in Figure 5.15. As expected, the decrease in reflectance was less significant when quartz was used, confirming the advantage of using a sample holder made of low thermal expansion material.

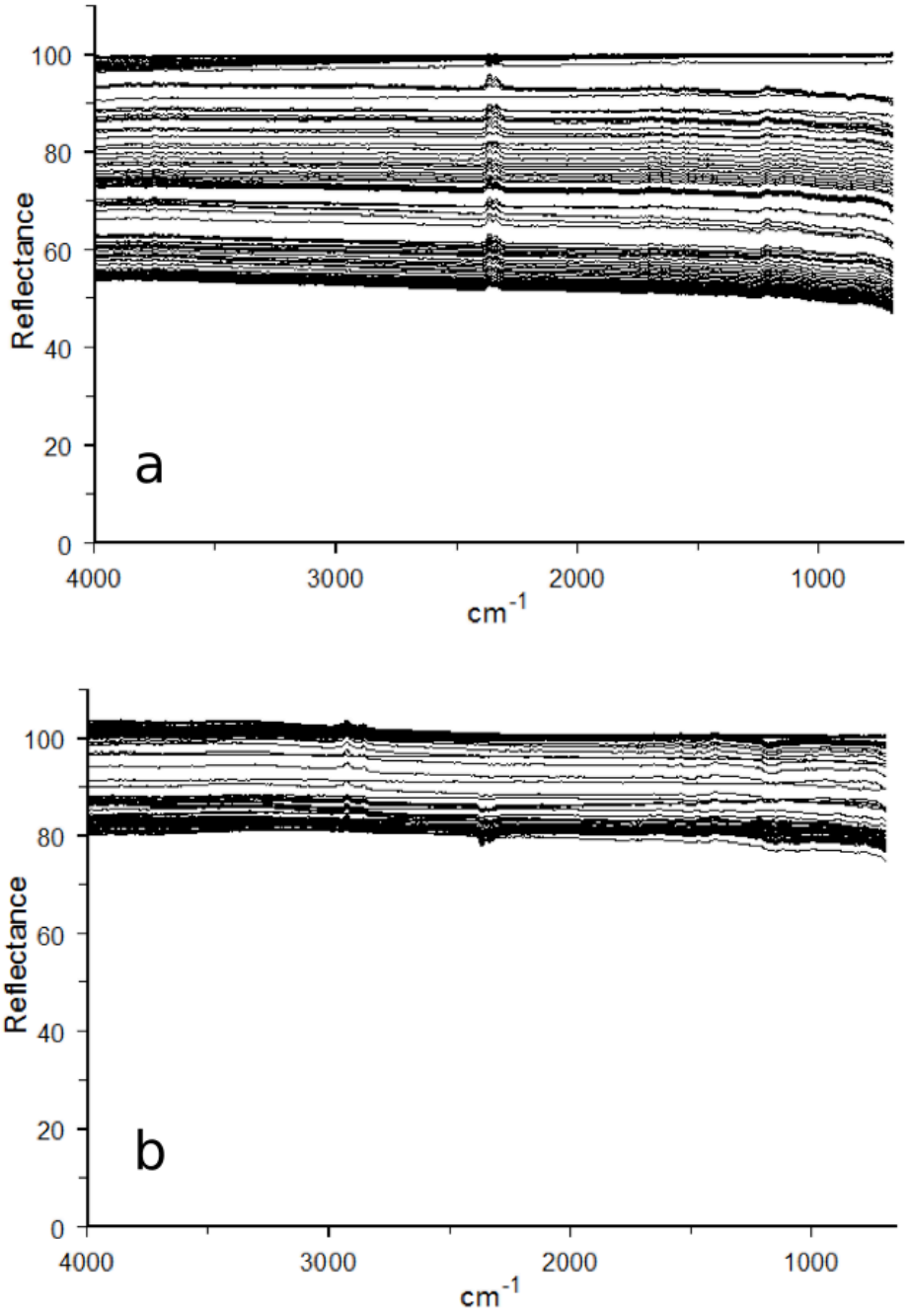

Figure 5.15 Overlay of reflectance spectra obtained with the a) steel and b) quartz support systems.

Although baseline shifts were less for the quartz tube compared to the steel post, reflectance values significantly decreased for both sample holder systems. One cause for this baseline offset was the effect of unmodulated sample emission on the infrared detector. Changes in alignment also appear to be a contributing factor because there are differences between the results obtained by using the two different sample supports. Figure 5.16 shows the trend in reflectance with temperature, specifically, reflectance values at 2000 cm^{-1}. Several measurement data sets collected by using the quartz sample support are represented by wireframe markers, whereas two sets of data collected with the steel support system are represented by filled markers (circles and triangles).

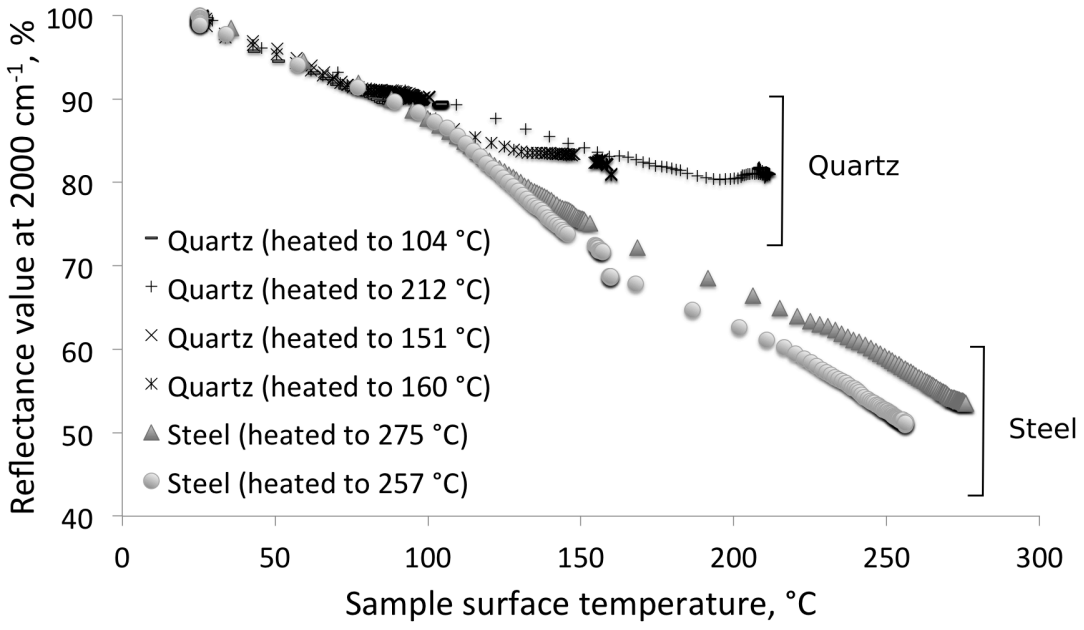

Figure 5.16 Reflectance at 2000 cm^{-1} as a function of temperature for steel and quartz sample supports.

For both sample holder systems, reflectance at 2000 cm^{-1} decreased with increasing temperature. No significant differences in reflectance variations were

detected below 100 °C. It is possible that the decline is signal intensity below 100 °C was primarily due to unmodulated sample emission effects, and not alignment changes. Above 100 °C, reflectance decreases were larger for the steel sample holder than for the quartz tube sample holder. When the sample surface temperature reached 212 °C for the steel holder, reflectance was 60-65% of the ambient temperature value. For the quartz holder at about the same temperature, reflectance was about 81% of the ambient temperature value.

By subtracting the reflectance value at 2000 cm^{-1} from the reflectance value at 4000 cm^{-1}, the magnitude of baseline slope was approximated. Figure 5.17 compares trends in baseline slope variations for measurements made by using the steel and quartz sample holders.

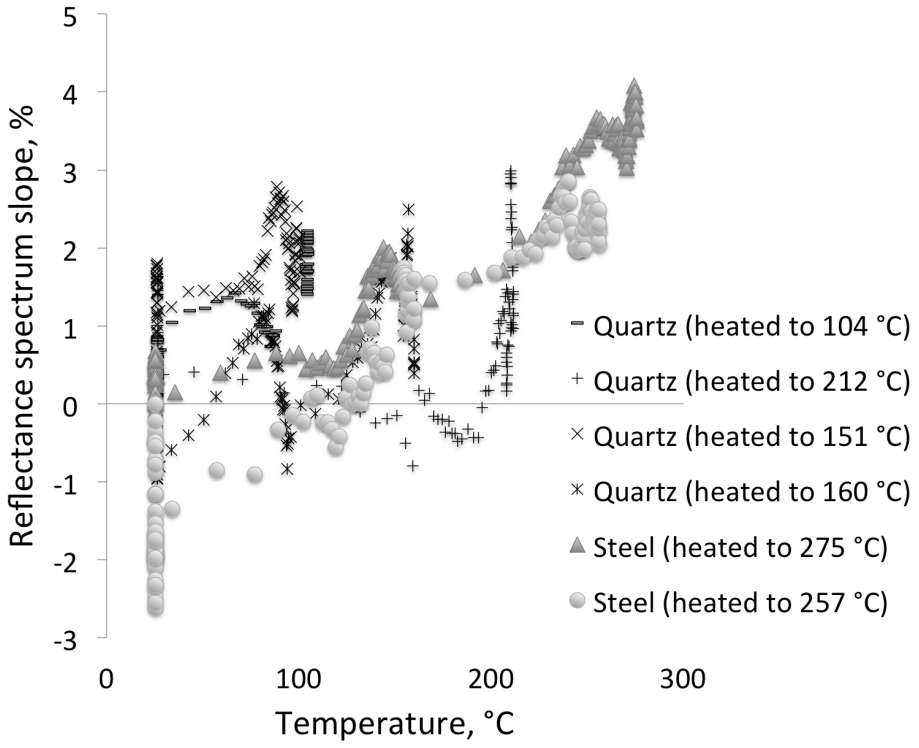

Figure 5.17 Baseline slope as a function of temperature for steel and quartz supports.

In general, baseline slopes increased gradually with increasing sample temperature because reflectance at higher wavenumbers was greater than reflectance at lower wavenumbers at higher temperatures. However, this gradual trend is obscured by variations due to other factors. When the sample (silver powder) was held at any temperature for a period of time, a cyclical pattern in baseline slope variation on the order of ±1.5% was observed.

5.4.3 Sample Height Adjustment to Compensate for Thermal Expansion

Using the micrometer sample height adjustment platform, the environmental chamber and sample holder assembly was moved vertically while the sample was held at elevated temperatures to compensate for spectral changes attributed to thermal expansion effects.

Figure 5.18 shows VT-DRIFTS results obtained when the steel sample holder was employed with Ag powder as the sample material. Sample temperature was held at ambient temperature for 40 min, then by increasing the variac voltage to 10% (of 120 V) for 100 min, the sample was heated to almost 150 °C. By then adjusting the variac to 14%, the sample was heated to 257 °C over a period of 100 min, after which the sample was allowed to cool by removing power to the heater. In Figure 5.18 sample surface temperature as a function of time is represented by the thin black line.

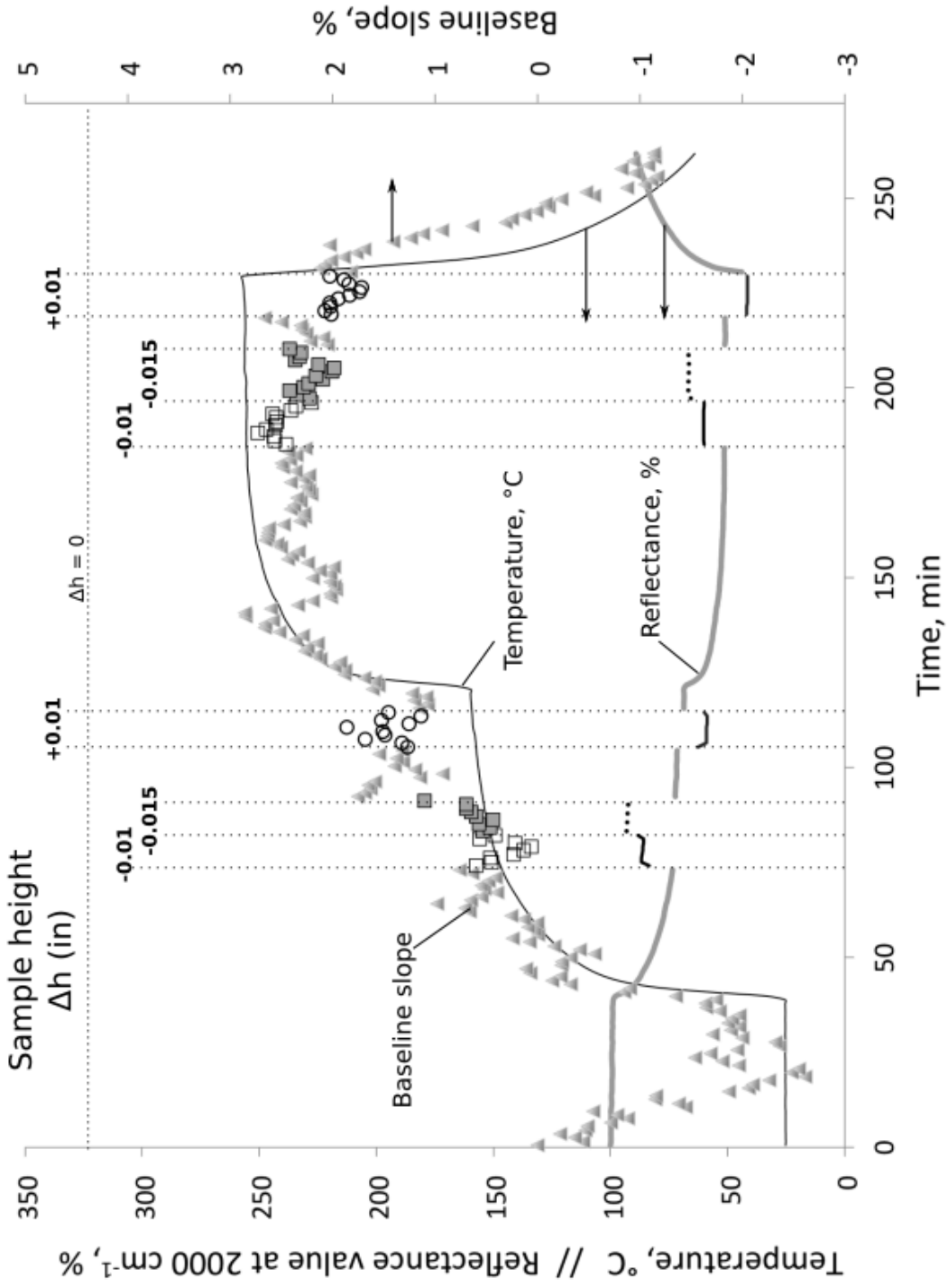

Figure 5.18 Baseline slopes (markers) at various sample heights (Δh) for the steel sample holder.

After the temperature stabilized near 147 °C, the sample chamber was incrementally moved vertically (Δh = 0.000 in, -0.010 in, -0.015 in, and +0.010 in). When moving the sample, decreasing the height brought reflectance closer to 100% and increasing the height decreased reflectance intensity. Percent reflectance in Figure 5.18 is shown by the thick line. The reflectance spectrum baseline slope, depicted in Figure 5.18 by markers (triangles for $\Delta h = 0.000$ in, squares for $\Delta h < 0$, and circles for $\Delta h > 0$), generally correlates with the temperature curve, but baseline fluctuations obscure this correlation. Possible effect of sample height changes on the baseline slope is also obscured by baseline fluctuations. When the sample was returned to its initial height, reflectance intensity returned to its previous value (thick gray line) indicating reproducibility in sample height positioning. Vertical displacement of the sample after the temperature stabilized near 257 °C showed the same results as at 147 °C.

Figure 5.19 shows results obtained when a similar experiment was conducted using the quartz tube sample holder system. The sample was held at room temperature for 30 min, then heated by adjusting the variac to 30% (of 120 V). After 60 min of heating, the sample reached 100 °C, where it was held for 2 hours before power to the heater was removed so that the sample cooled. While the sample was held at ~100 °C, the sample height was incrementally varied. Sample height was first decreased by 0.005 in, then in increments of 0.001 in, it was further decreased -0.011 in, and then returned to Δh = -0.005 in, followed by Δh = 0.000 in. As shown in Figure 5.19, reflectance decreased to about 90% of the ambient temperature value when the sample was near 100 °C. Decreasing the sample height caused reflectance values to increase (to 97.5% of ambient temperature values). Note that the most significant change in

reflectance corresponded to the initial movement from $\Delta h = 0.000$ in to -0.005 in, and very little change was observed when the sample was further moved from -0.005 in to -0.011 in. Bseline slope values (markers) decreased when the sample was lowered, but this change was obscured by the baseline oscillation (due to room temperature cycling). After cooling to ambient temperature, baseline slope values were somewhat greater than before heating, but lower than when the sample was held at 100 °C. This may indicate a permanent change to sample scattering coefficient caused by heating.

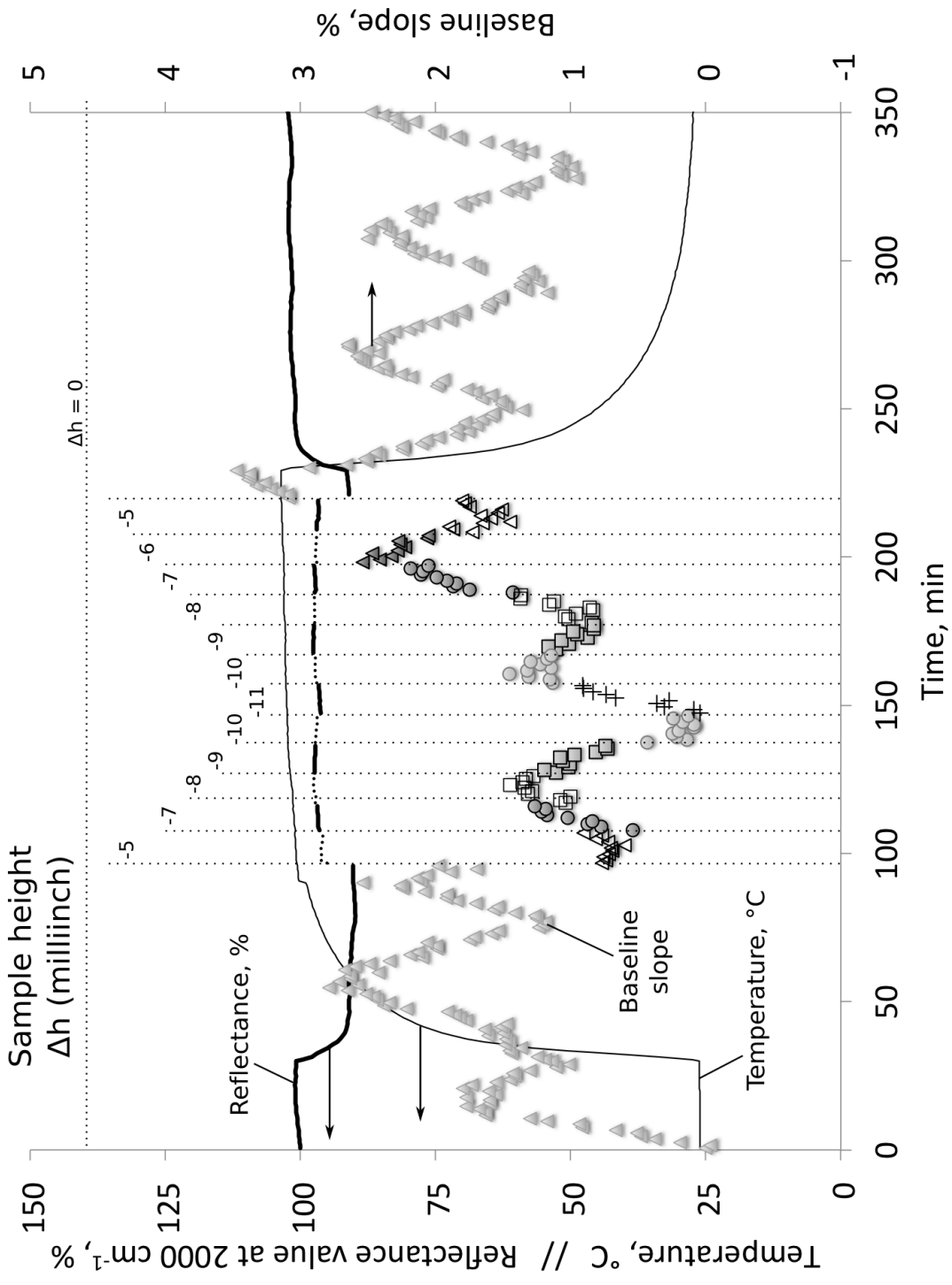

Figure 5.19 Baseline slopes (markers) at various sample heights (Δh) for the quartz sample holder.

5.5 Optimum Throughput VT-DRIFTS Sample Holder

VT-DRIFTS characterization studies (Chapter 3) indicate that thermal expansion of the sample holder affects alignment of the optical system when the sample is heated, which contributes to temperature-induced spectral artifacts. In addition, the presence of the environmental chamber lid decreases interferogram signal 10-fold, which decreases spectral SNR. When the sample holder is heated, a temperature gradient through the sample is formed. Consequently, sample surface temperatures must be determined from a correlation function that relates T_{surf} to T_{Pt}. Based on these findings, a new VT-DRIFTS sample holder design was developed to minimize inherent adverse effects. In the new design, the sample was suspended from a quartz tube in a similar manner to that described in section 5.4.2 (Figure 5.13b). However, the thermocouple employed for feedback temperature control was attached to the sample holder so that temperatures just below the sample surface could be measured, eliminating the need for a correlation function. Unfortunately, with this thermocouple placement, the environmental chamber lid could not be attached. Therefore, to minimize effects from sample oxidation and excessive DRA optics heating, VT-DRIFTS sample temperatures were limited to below 200 °C for this sample holder design. Eliminating the DRA environmental chamber lid significantly increased the interferogram voltage (Chapter 2) and yielded improved spectral SNR. Figure 5.20 shows photographs of the new quartz VT-DRIFTS sample holder.

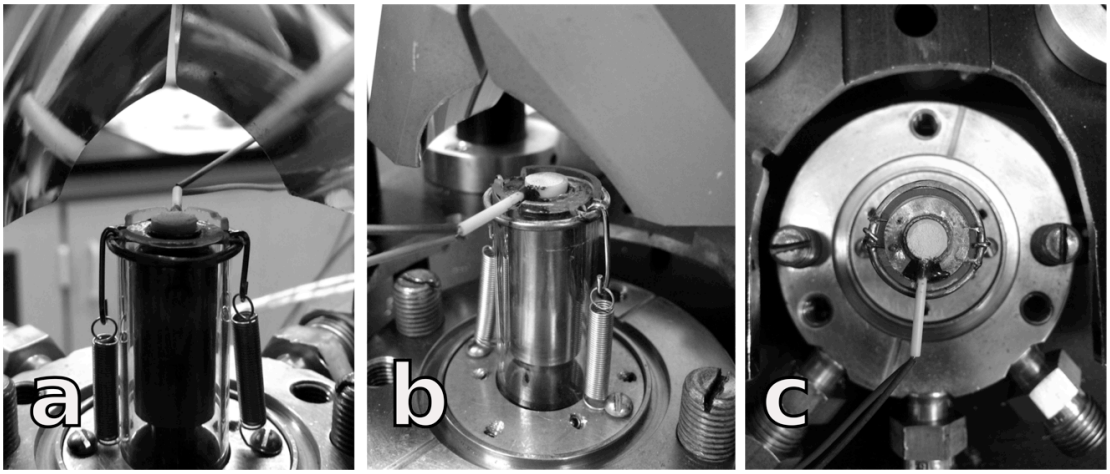

Figure 5.20 New VT-DRIFTS sample holder viewed from (a) behind, (b) front, and (c) top.

To create the new sample holder, a nickel disk was spot welded to two steel wires, which rested on grooves in the top of the quartz support tube. These wires were spot welded to a metal ring that slid around the quartz tube and centered the sample. Two springs were attached to this ring and secured to the sample holder base to prevent movement. (Figure 5.20, a and b). A ceramic ring about 2 mm in height with an inside diameter of 5 mm served as a cup to hold ~ 100 mg powder samples. The ceramic ring snapped into a metal retaining ring that was spot welded to the nickel disk. A thermocouple was passed through a small hole drilled in the side of the ceramic ring. The thermocouple wires that extended into the ceramic ring were placed so that the junction was located near the center and slightly below the top of the ring.

To test this new sample holder design, the experiments described in Chapter 3 were repeated. The same polystyrene film was placed in the infrared beam between mirror (7) and mirror (8) and secured in place by using magnets (Figure 3.1). The film location was adjusted to achieve a maximum interferogram signal. The KBr windows

used as heat barriers between the sample and interferometer compartments were removed to match the conditions employed for the measurements described in Chapter 3.

5.5.1 Reproducibility at Ambient Temperature

To characterize the instrument performance in the absence of sample heating, 50 spectra were successively collected at a rate of about 1 spectrum/min at ambient (i.e. room) temperature. Figure 5.21 shows an overlay of 6 single beam spectra over the 4000-650 cm^{-1} range collected in about 10 min increments (compare to Figure 3.4). Polystyrene absorption peaks are clearly visible, and spectra overlay very well, indicating high measurement reproducibility at ambient temperature. The overlay plots appear to be more reproducible than those shown in Figure 3.4, which would be consistent with a greater SNR associated with the absence of the environmental chamber lid.

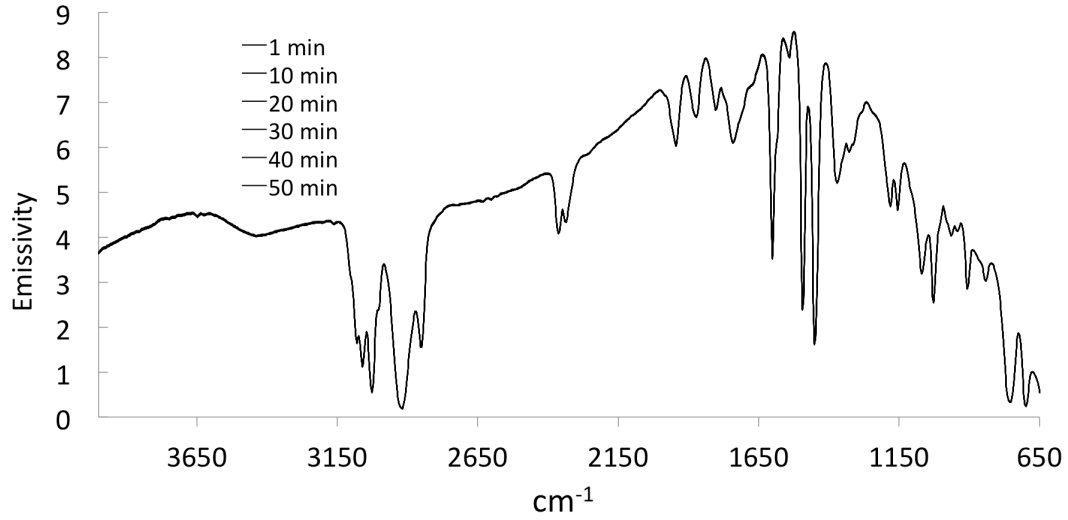

Figure 5.21 Overlay of single beam spectra collected at ambient temperature.

Because the environmental chamber lid was not used, interferogram voltage significantly increased, requiring the detector gain setting to be reduced from 4x to 2x. This resulted in a change of calculated single beam emissivity values. Consequently, the single beam emissivity scale depicted in Figure 5.21 differed from the scale shown in Figure 3.4.

Reflectance spectra were obtained by dividing polystyrene film single beam spectra by a reference background spectrum collected with the film removed and with Ag powder in the sample holder (Figure 5.22, compare to Figure 3.5). Because the cardboard sleeve holding the polystyrene film became the limiting aperture, reflectance spectra baselines were shifted below 100%. Because of the increased interferogram signal for the reference single beam measurement, reflectance values were baseline shifted more for the new sample holder design (~ 30%) compared to measurements made with stainless steel sample holder and with the environmental chamber lid in place (10%).

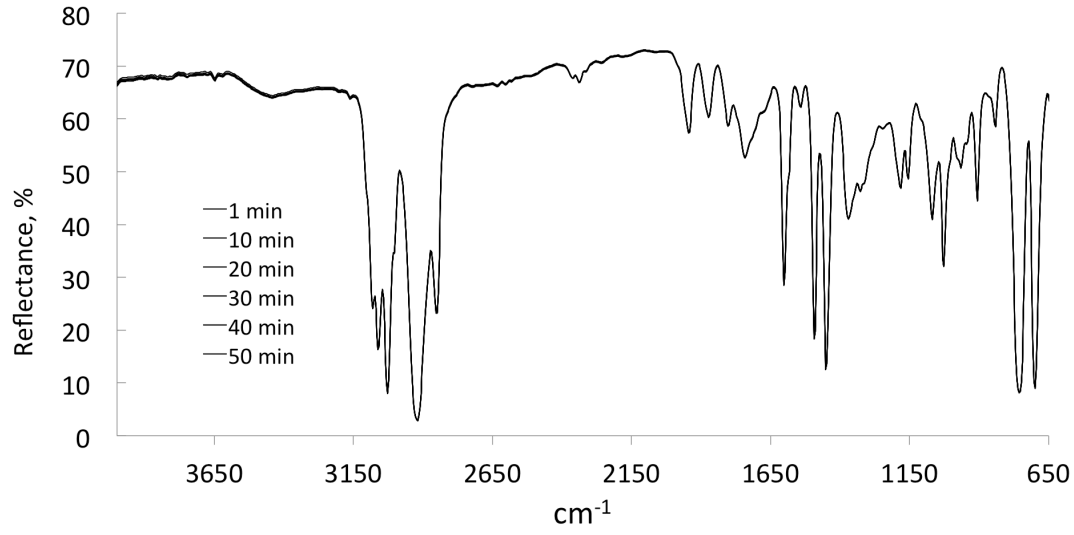

Figure 5.22 Overlay of reflectance spectra collected at ambient temperature.

The Kubelka-Munk spectra calculated from these reflectance spectra by using equation 1.33 are shown in Figure 5.23 (compare to Figure 3.6). The larger sample and reference single beam intensity differences caused Kubelka-Munk maxima to be greater when the new sample holder was employed for DRIFTS measurements.

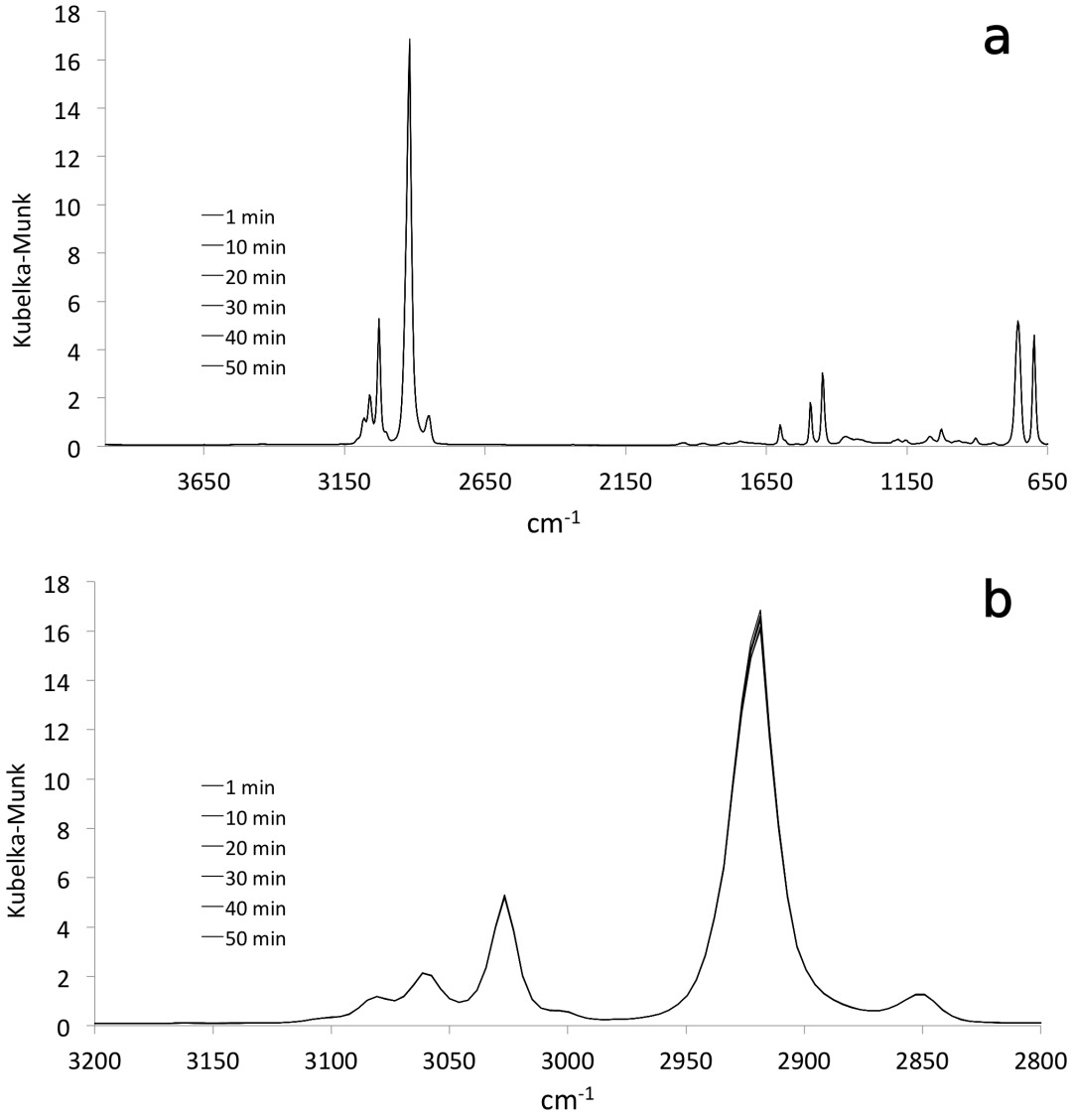

Figure 5.23 Overlay of diffuse reflectance spectra collected at ambient temperature: a) complete spectra and b) expansion of the C-H stretching region

Figure 5.24 compares overlays of ambient temperature C-H stretching region spectra in emissivity, reflectance, and Kubelka-Munk formats. This figure is analogous

to results shown in Figure 3.7. A comparison of Figure 5.24 with Figure 3.7 reveals that reproducibility was improved with the new sample holder.

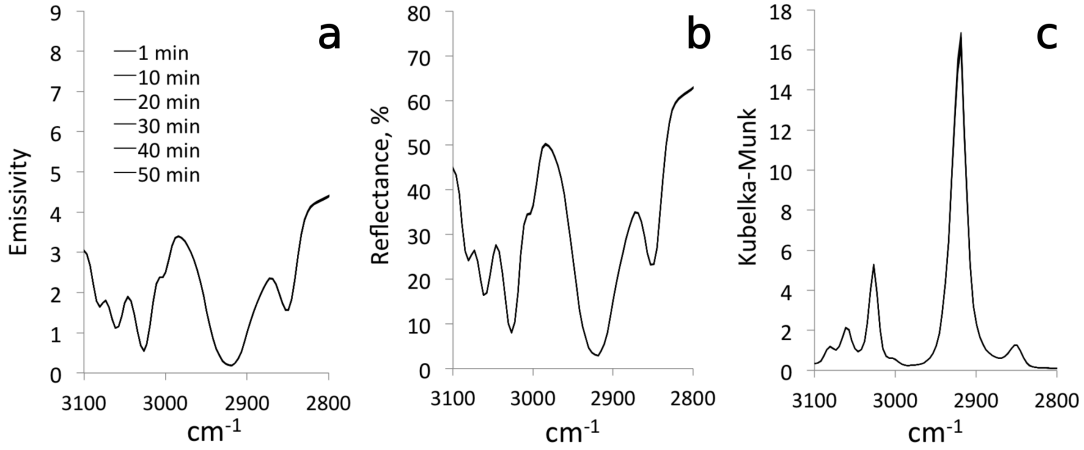

Figure 5.24 Overlay of the same ambient temperature C-H stretching region of spectra in a) emissivity, b) reflectance, and c) Kubelka-Munk formats.

Figure 5.25 compares selected absorption peak relative standard deviations calculated from 50 ambient temperature DRIFTS spectra obtained with the stainless steel and new sample holders. Crosses represent RSD values derived from steel sample holder measurements and diamonds denote RSD values calculated from spectra obtained with the new sample holder design. RSD values were lower for the new sample holder because of a greater SNR associated with the absence of the environmental chamber lid.

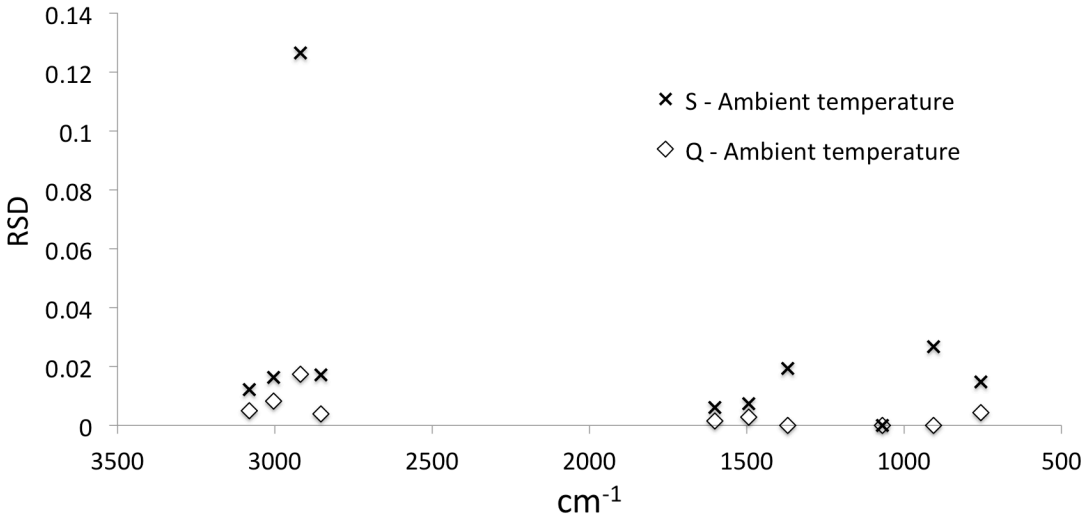

Figure 5.25 Relative standard deviations of ambient temperature Kubelka-Munk peak maxima obtained by using the stainless steel (S) and the new quartz (Q) sample holders.

The relative standard deviation was largest for the strong absorption peak at 2918.64 cm^{-1} in both cases. According to equation 1.33, DRIFTS measurements are most accurate for weak absorbers [3, 4] because high absorption coefficients (k) result in near-zero diffuse reflection (R_∞) values. Thus, for stronger absorptions, SNR is lower, resulting in large fluctuations in Kubelka-Munk peak intensities. Figure 5.26 shows the variation in RSD as a function of wavenumber (solid line) and the average single beam spectrum (dash line) for the 50 ambient temperature DRIFTS spectra. The RSD versus wavenumber plot exhibits a spike at the location corresponding to the highest absorption band maximum. To avoid this dramatic loss in reproducibility for high absorption spectral features, DRIFTS samples are typically diluted in highly reflective matrices [3-6].

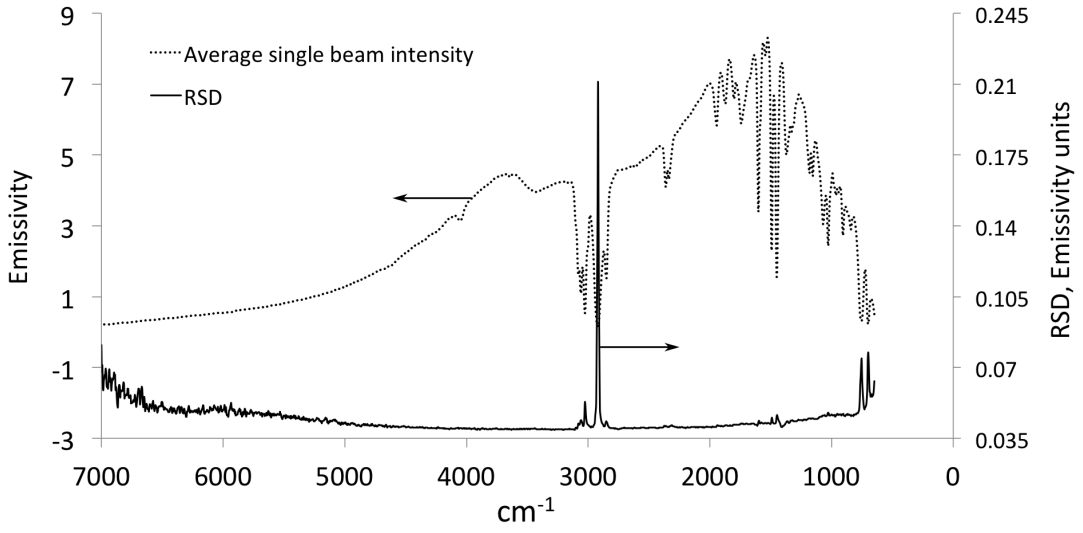

Figure 5.26 Average single beam spectrum and relative standard deviations at ambient temperature obtained with the new quartz sample holder.

5.5.2 VT-DRIFTS Polystyrene Spectrum Variations

After characterizing ambient temperature spectrum reproducibility, silver powder was heated in the new sample holder to 205.40 °C, measured near the sample surface. While heating, 100 spectra were sequentially obtained at about 1 minute intervals. A variac setting of about 50% was employed for heating.

Figure 5.27 compares single beam spectra measured with the new and stainless steel sample holders while heating to comparable temperatures. Polystyrene film absorptions were constant for all measurements, so single beam spectrum changes can be attributed to instrument variations that occurred while heating. The impact of these variations was less for the new sample holder design.

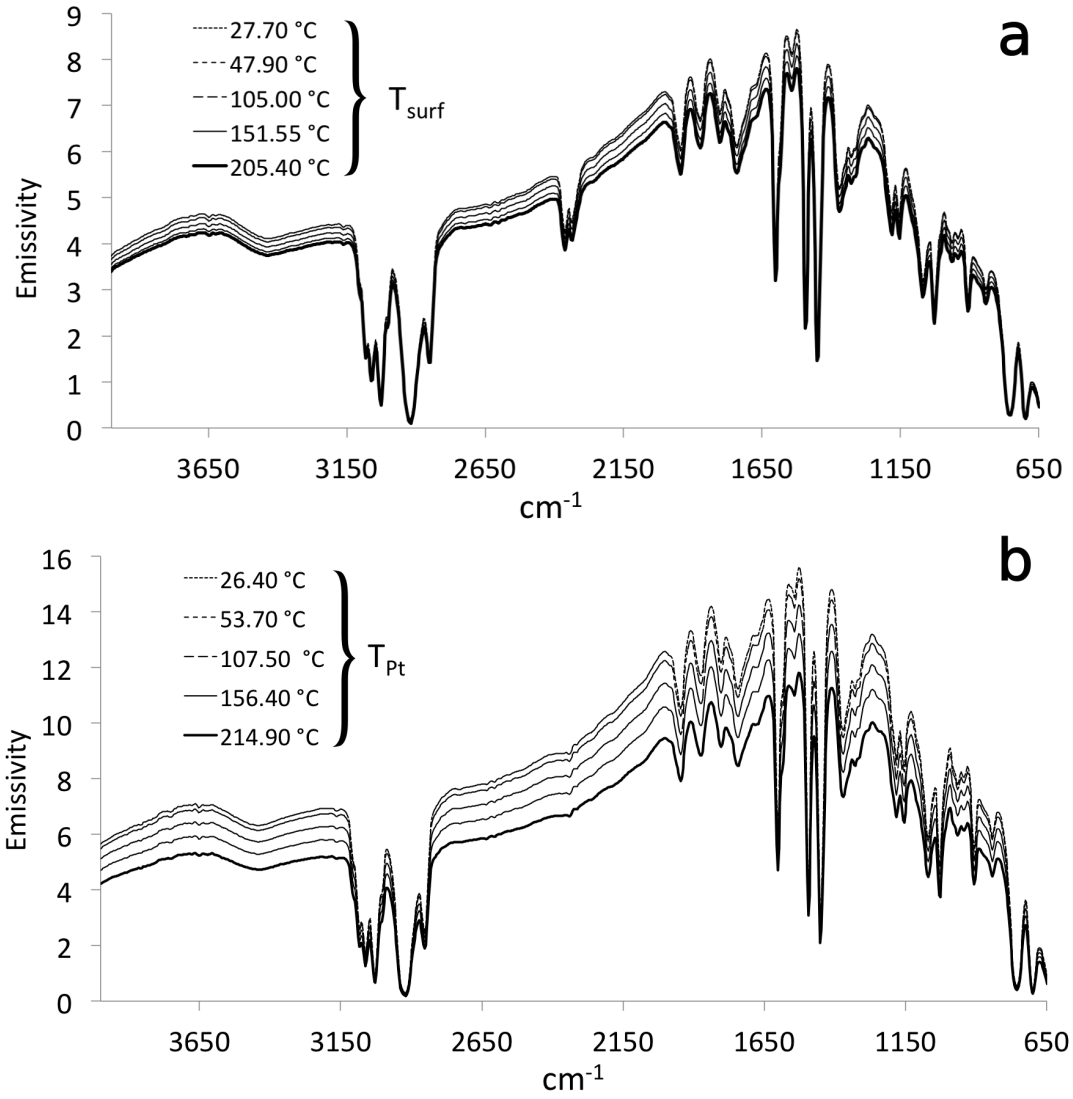

Figure 5.27 Overlay of polystyrene single beam spectra measured during sample heating for the (a) new quartz and (b) stainless steel sample holders.

Single beam spectra changes lead to "apparent" reflectance spectrum changes. Figure 5.28 shows overlays of polystyrene reflectance spectra obtained with the new quartz sample holder and with the stainless steel sample holder, calculated by ratioing single beam spectra to a reference background spectrum (Ag powder) collected at ambient temperature. Reflectance became lower with increasing temperature in both

plots, but shifts were smaller for the new sample holder (~ 5%) compared to the stainless steel holder (~ 15%).

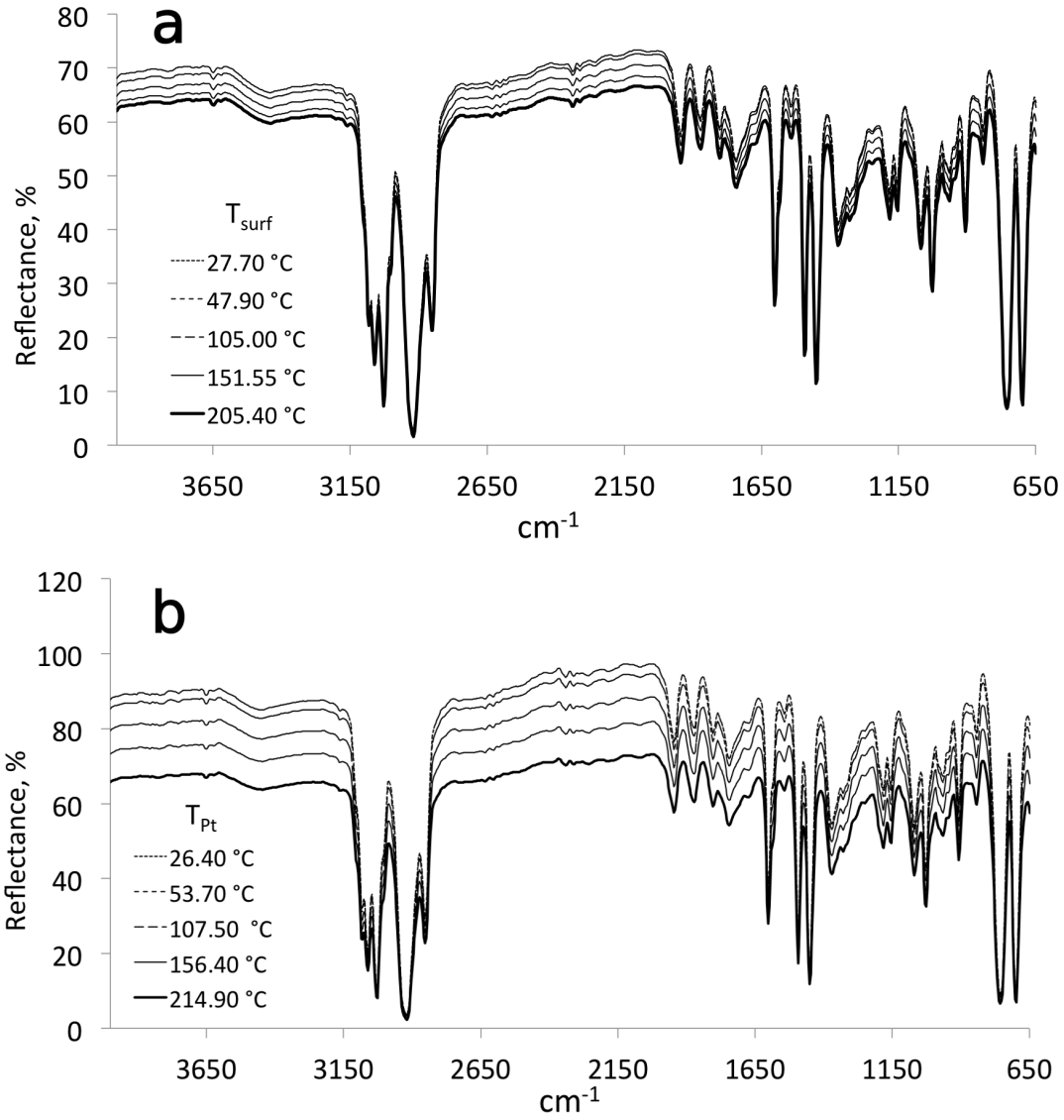

Figure 5.28 Overlay of VT-DRIFTS polystyrene reflectance spectra measured while heating the (a) new quartz and (b) stainless steel sample holders.

Conversion of reflectance spectra measured with the new quartz sample holder to Kubelka-Munk format resulted in the spectra shown in Figure 5.29. For comparison, spectra measured at similar temperatures but obtained with the stainless steel sample

holder are shown in Figure 5.30. Kubelka-Munk peak maxima for weaker absorbing peaks overlay better in spectra obtained with the new sample holder compared to measurements made with the stainless steel holder. Figures 5.29b and 5.30b show Kubelka-Munk spectrum overlays over the C-H stretching region.

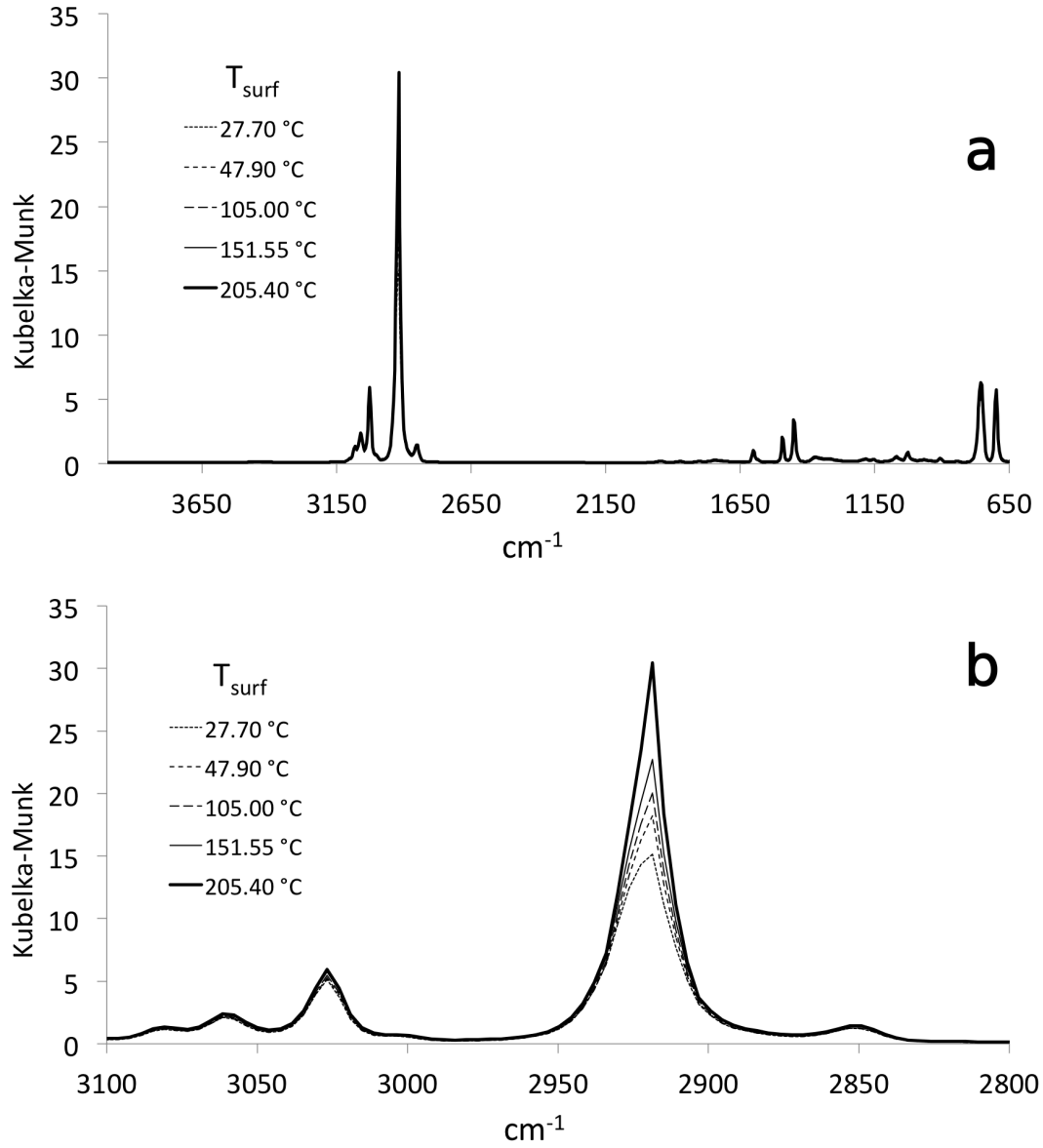

Figure 5.29 Overlay of VT-DRIFTS results obtained with the new quartz sample holder: a) complete spectra and b) expansion of the C-H stretching region.

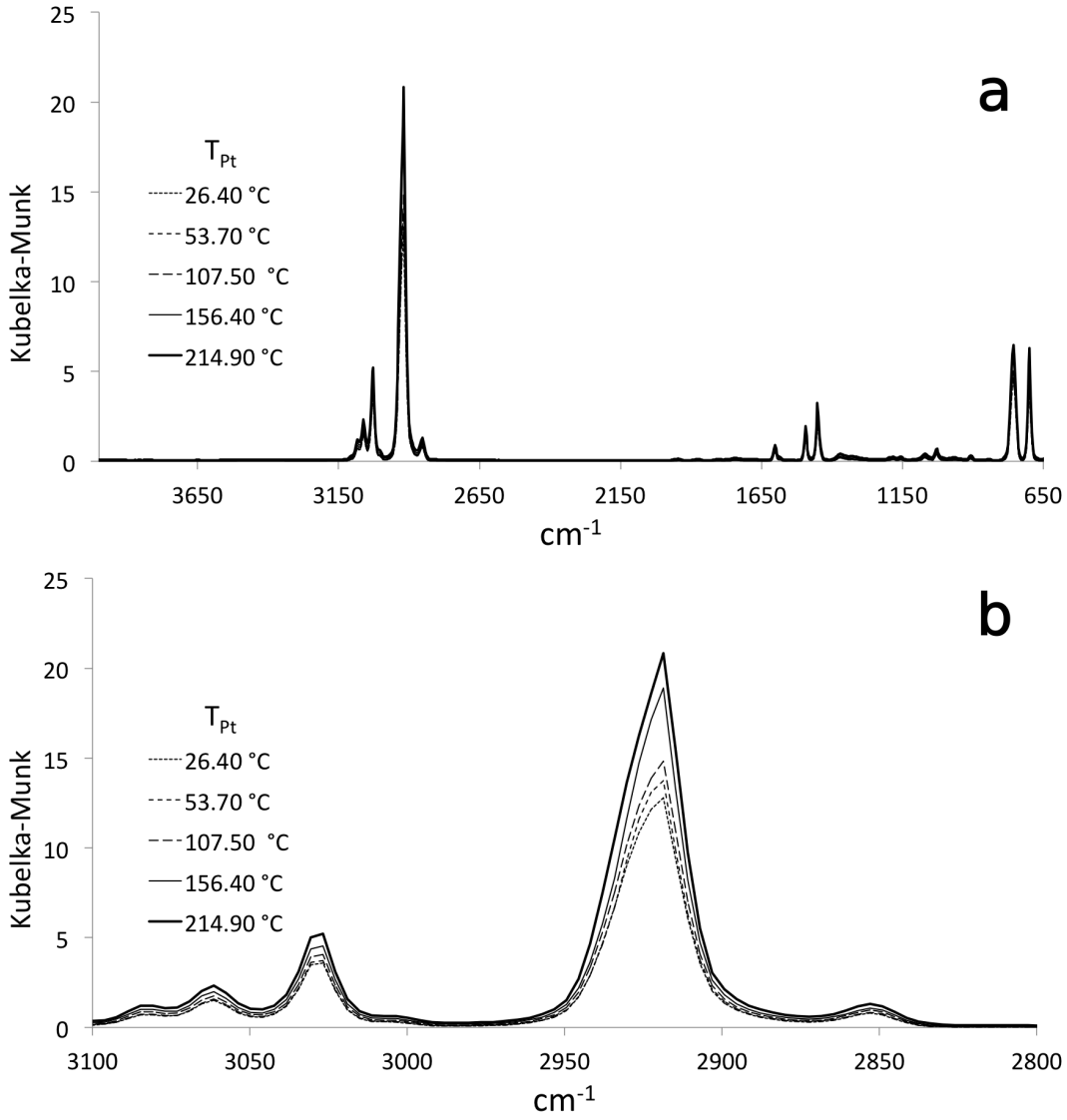

Figure 5.30 Overlay of VT-DRIFTS results obtained with the stainless steel sample holder: a) complete spectra and b) expansion of the C-H stretching region.

Figure 5.31 represents a comparison of relative standard deviations calculated for selected Kubelka-Munk peak maxima. Crosses represent RSD values derived from spectra measured with the stainless steel sample holder and diamonds represent RSD values calculated from spectra obtained with the new sample holder. Reproducibility was significantly better for the new sample holder compared to the stainless steel

sample holder. With the exception of the RSD values for the 2918.64 cm^{-1} absorption peak, reproducibility was between 6 and 7 times better for the new sample holder.

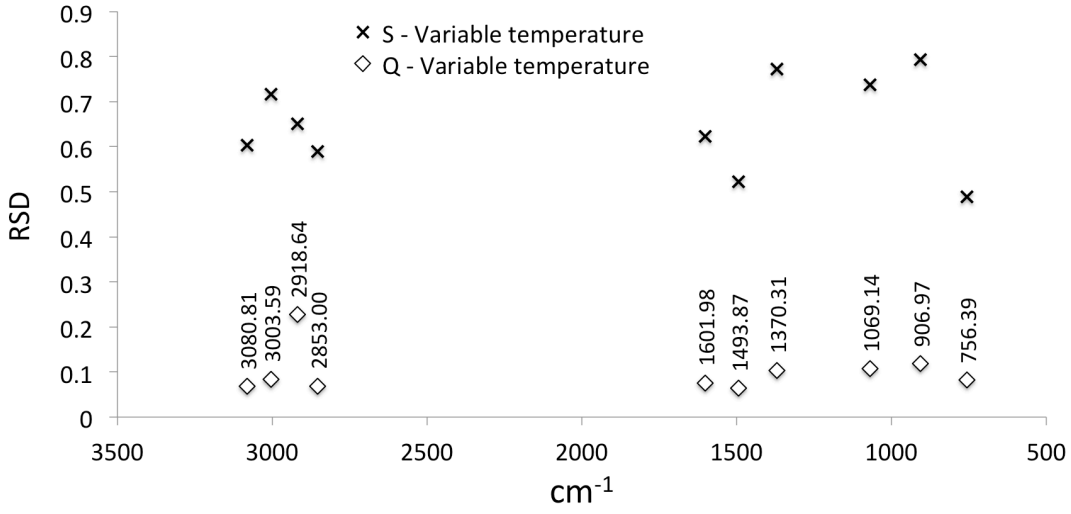

Figure 5.31 Relative standard deviations of VT-DRIFTS Kubelka-Munk peak maxima obtained by using the steel sample holder (S) and the new quartz sample holder (Q).

5.5.3 Effects of Single Beam Scaling

To compensate for the single beam intensity decrease with increasing sample holder temperature, spectra obtained with the new quartz sample holder design were scaled by using the method described in section 3.3.2. An overlay plot of the scaled single beam spectra is shown in Figure 5.32. The overlay plots of the corresponding reflectance spectra obtained by ratioing scaled single beam spectra to a reference background spectrum (Ag powder) measured at ambient temperature are shown in Figure 5.33. The Kubelka-Munk plots in Figure 5.34 were calculated from the reflectance spectra in Figure 5.33. The variable temperature single beam and reflectance overlay plots suggest that spectra matched well after the scaling procedure, even approaching ambient temperature reproducibility. However, there are some

fluctuations in both single beam and the reflectance spectra on either side of the wavenumber used for scaling (2107.80 cm^{-1}), indicating baseline slope variations.

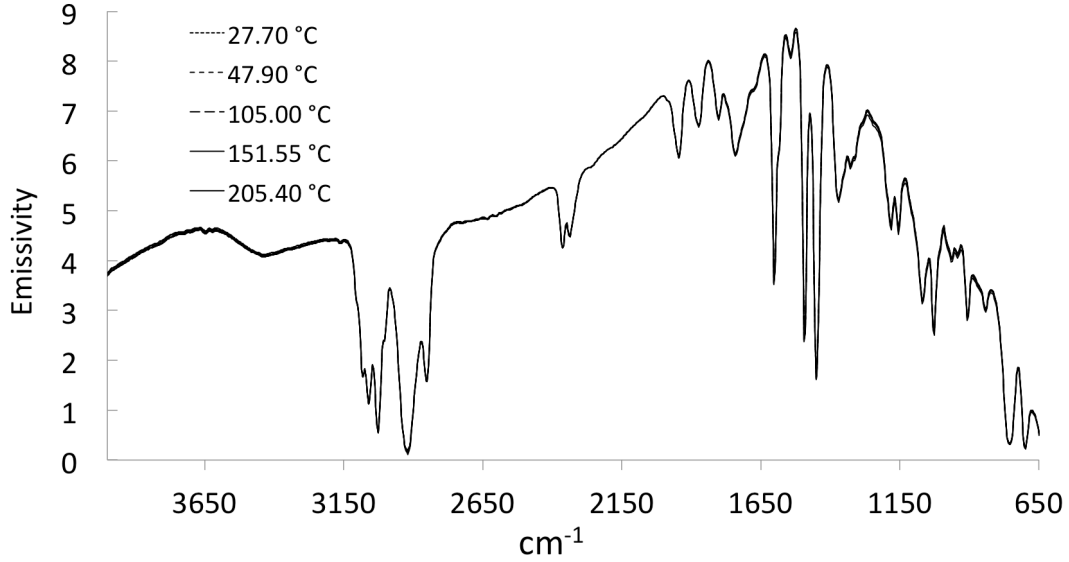

Figure 5.32 Overlay of scaled VT-DRIFTS single beam spectra obtained by using the new quartz sample holder.

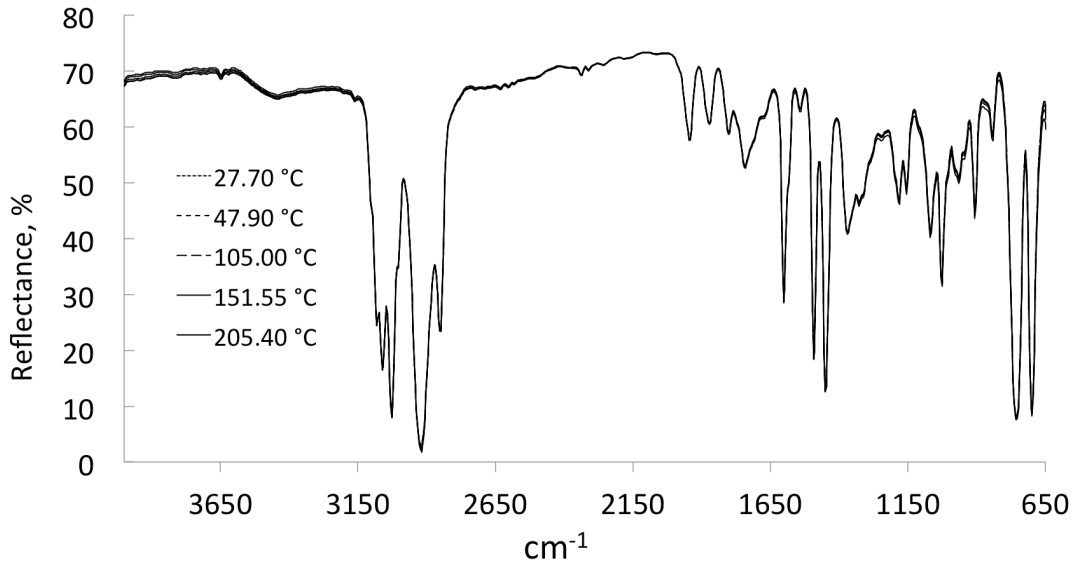

Figure 5.33 Overlay of VT-DRIFTS reflectance spectra derived from scaled single beam spectra.

The variable temperature Kubelka-Munk spectra derived from scaled reflectance spectra also overlay well, with the exception of the highly absorbing peak at 2918.64 cm^{-1}. Before scaling, the Kubelka-Munk intensity for the peak at 2918.64 cm^{-1} approximately doubled, from 15.16 to 30.43 Kubelka-Munk units when the sample holder was heated from ambient temperature to 205.40 °C. After scaling, Kubelka-Munk intensity for this peak maximum increased from 15.16 to 28.12 as a result of sample holder heating. Although improvement was made by scaling, reproducibility for this highly absorbing band maximum was still poor. In contrast, Kubelka-Munk peak maxima at 3003.59, 3026.73, and 3061.50 cm^{-1} were relatively constant regardless of sample holder temperature, as shown by the overlay plot in Figure 5.34b.

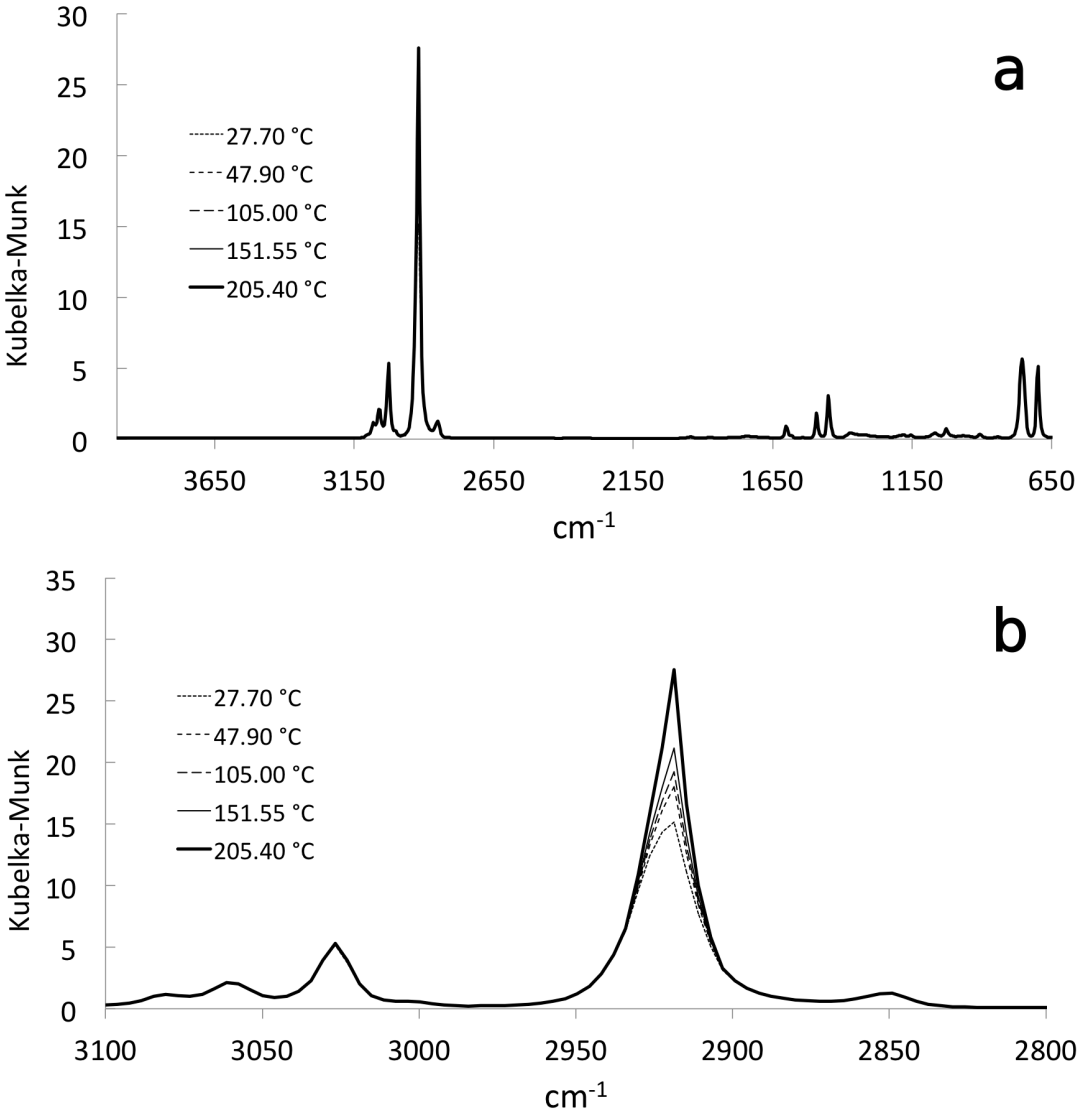

Figure 5.34 Overlay of scaled VT-DRIFTS Kubelka-Munk spectra obtained by using the new quartz sample holder.

To quantitatively assess the measurement reproducibility improvement afforded by the new quartz sample holder compared to the stainless steel holder, RSD values for selected peak maxima were plotted as a function of wavenumber in Figure 5.35. RSD values were lowest for peak maxima located near the wavenumber employed for scaling (i.e. 1601.98 and 1493.87 cm^{-1}). Relative standard deviations increased at lower

wavenumbers due to decreasing single beam intensity. Near 3000 cm^{-1}, RSD values tracked peak maxima trends. For all of the peak maxima, RSD values derived from scaled spectra were lower for measurements made by using the new quartz sample holder.

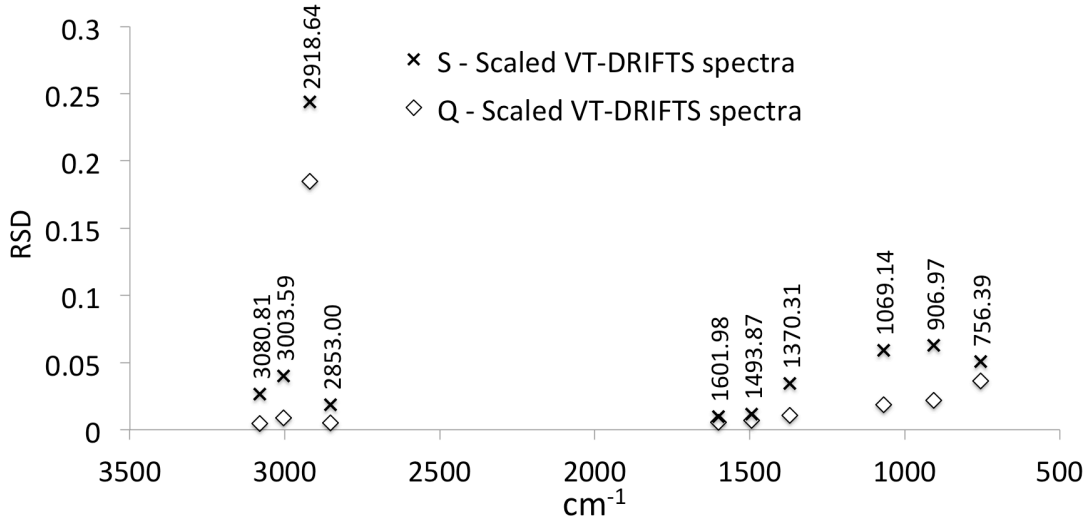

Figure 5.35 Relative standard deviations calculated for selected peak maxima in scaled VT-DRIFTS Kubelka-Munk format spectra obtained by using the stainless steel sample holder (S) and the new quartz sample holder (Q).

5.5.4 Effects of Baseline Slope Correction

To assess the impact of baseline slope on VT-DRIFTS RSD values, sloping lines were subtracted from scaled reflectance spectra by using the procedure outlined in section 3.3.3. Scaled and baseline corrected spectra were then converted to Kubelka-Munk format. Although fluctuations in peak maxima were greatly reduced by using this method, ambient temperature spectrum reproducibility was still superior. Figure 5.36 shows an overlay of variable temperature single beam spectra obtained by converting scaled and baseline corrected reflectance spectra to single beam format by multiplying by the reference background spectrum (i.e. Ag powder at ambient

temperature). These spectra overlay better than before baseline correction (compare to Figure 5.32).

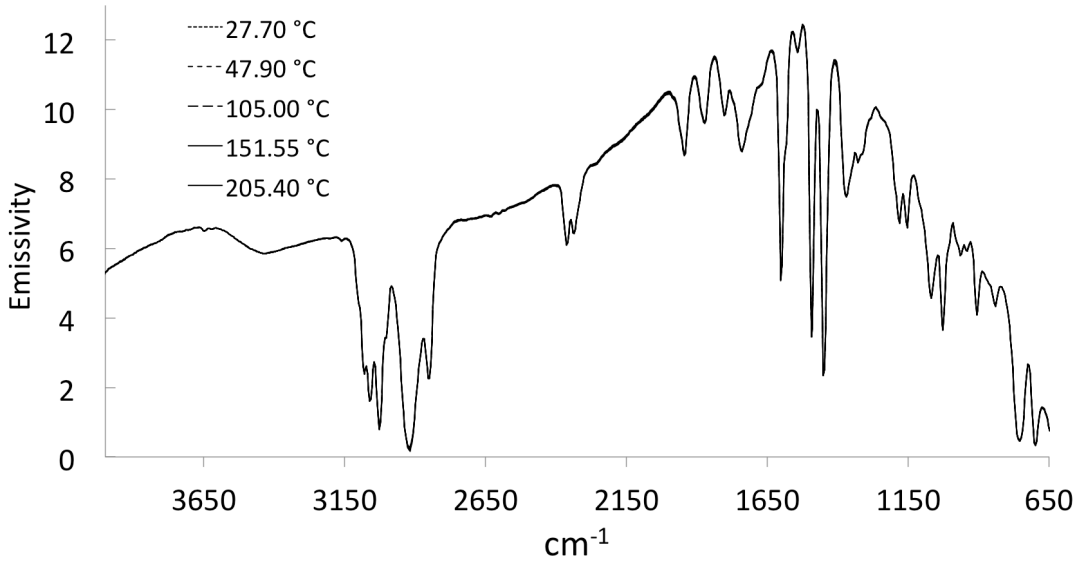

Figure 5.36 Overlay of scaled and baseline-corrected VT-DRIFTS polystyrene single beam spectra.

Figure 5.37 shows an overlay of scaled and baseline corrected VT-DRIFTS reflectance spectra. Like the corrected single beam spectra (Figure 5.36), these spectra overlay better than before baseline correction (compare to Figure 5.33).

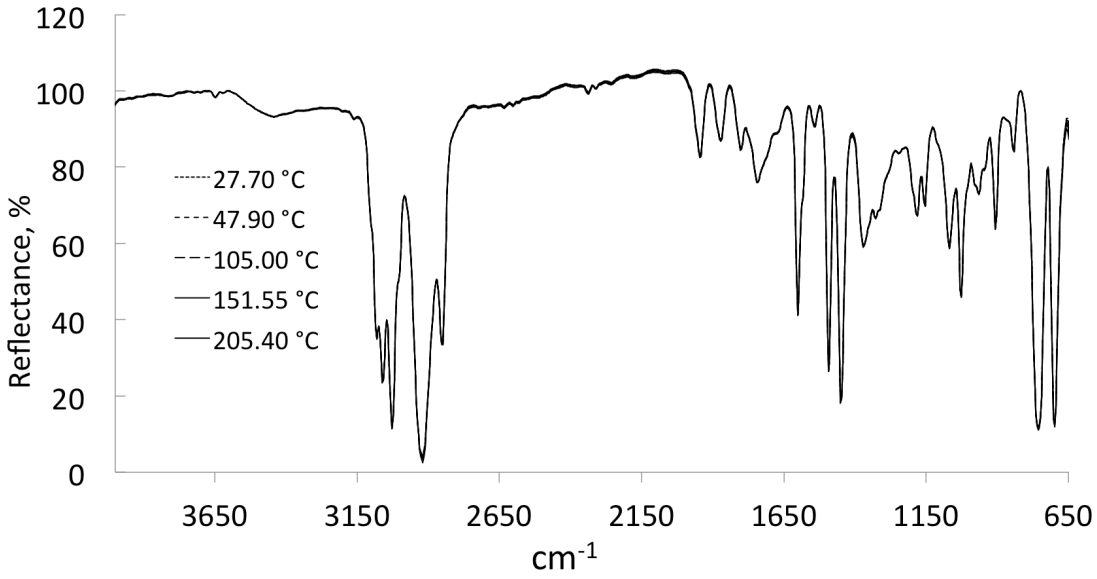

Figure 5.37 Overlay of scaled and baseline-corrected VT-DRIFTS polystyrene reflectance spectra.

Figure 5.38 shows Kubelka-Munk spectra derived from the reflectance spectra shown in Figure 5.37. Comparing the spectra in Figure 5.38 with those in Figure 5.34 reveals that peak maxima decreased after baseline correction. Also, because reproducibility decreases with increasing Kubelka-Munk values, it follows that the reproducibility of Kubelka-Munk peak maxima improved after baseline correction. However, as shown in Figure 5.38, intensity fluctuations for the 2918.64 cm^{-1} high absorption peak were significant even after baseline correction.

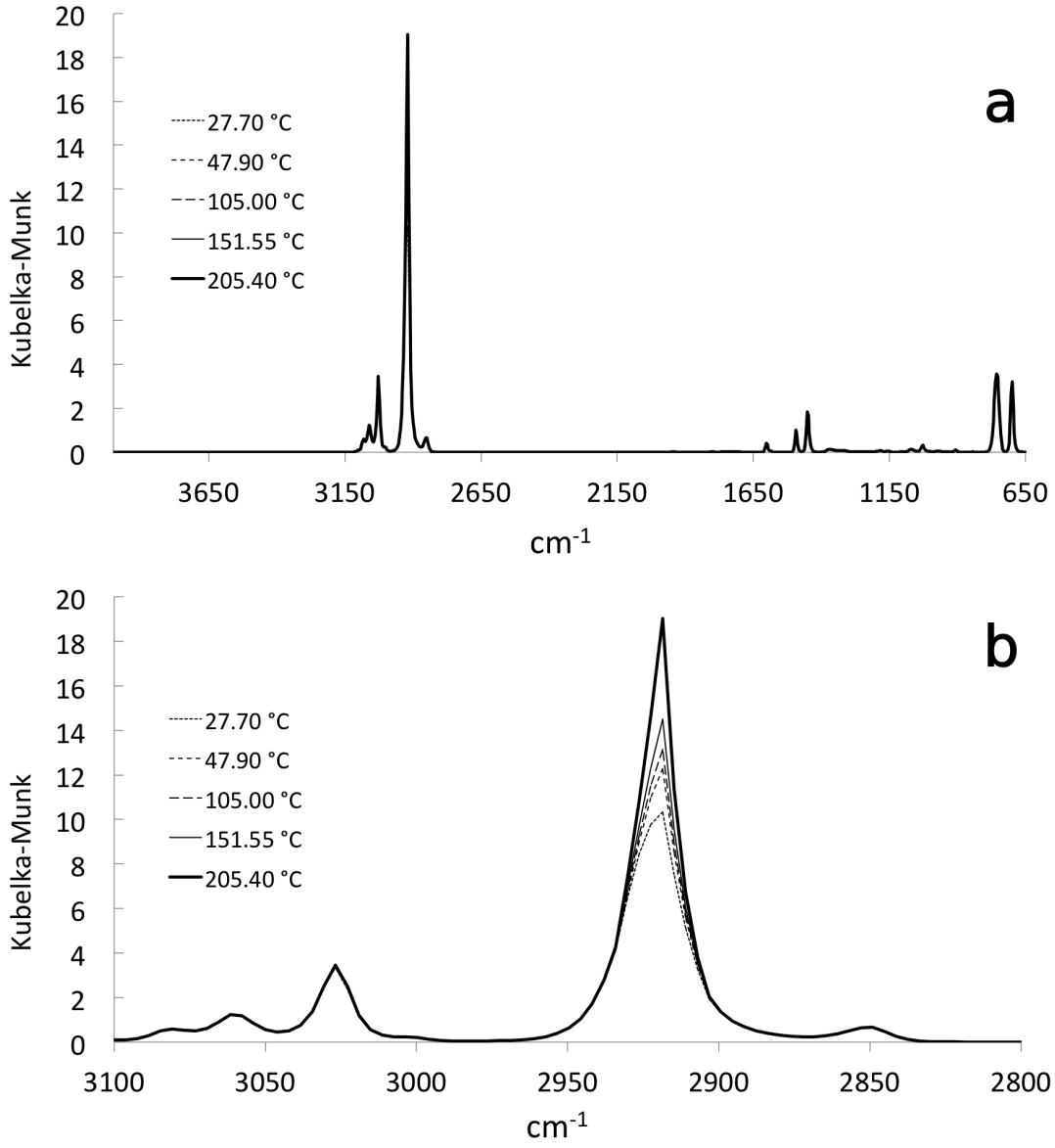

Figure 5.38 Overlay of scaled and baseline corrected VT-DRIFTS Kubelka-Munk format spectra obtained by using the new quartz sample holder: a) complete spectra and b) expansion of the C-H stretching region.

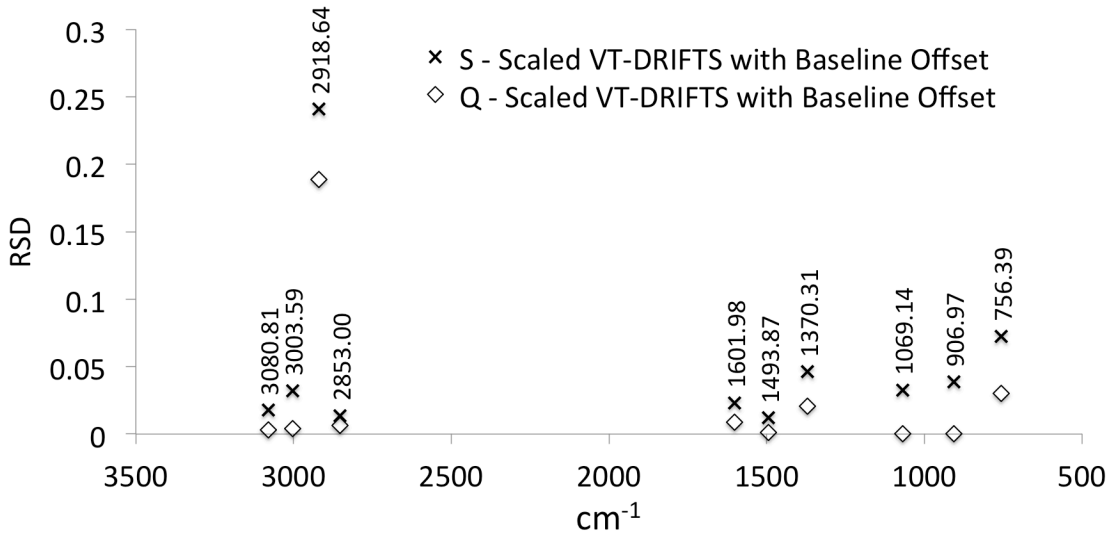

Figure 5.39 Relative standard deviations for scaled and baseline corrected VT-DRIFTS Kubelka-Munk peak maxima obtained by using the stainless steel sample holder (S) and with the new quartz sample holder (Q).

Relative standard deviations for scaled and baseline corrected spectra peak maxima were less than 0.05 Kubelka-Munk units for all except the 2918.64 cm^{-1} peak, as shown in Figure 5.39. For peak maxima in spectra obtained by using the new quartz sample holder, RSD values ranged from comparable to about 8.5 times lower compared to spectra obtained by using the stainless steel holder. The largest RSD values were associated with peaks located in low intensity regions of single beam spectra and the 2918.64 cm^{-1} peak. The relative standard deviation of the weak absorption at 1370.31 cm^{-1} was larger than the RSD values for other peaks due its very low intensity.

5.5.5 Comparison of Overall Spectral Standard Deviations

Results described in this section confirm the improvements in measurement reproducibility that can be derived by using a quartz sample support to decrease thermal

expansion spectral artifacts, and from increased SNR that results from removing the environmental chamber lid. Post-data collection scaling and baseline correction further reduced spectral artifacts. Reproducibility was consistently poor for highly absorbing peak maxima, suggesting that samples should be diluted to avoid strong absorptions.

Figure 5.40 shows plots of the standard deviations of selected Kubelka-Munk peak maxima as a function of intensity derived from spectra measured by using the stainless steel and new quartz sample holders. The overall RSD of peak maxima can be approximated by best fit slopes for the lines depicted in Figure 5.40, because RSD is the ratio of the standard deviation to the mean. These values are listed for both sample holders in Table 5.3. Due to strong absorption, the peak at 2918.64 cm^{-1} was not included in these RSD calculations.

In Figure 5.40, variable temperature results are indicated by grey circles and have the largest RSD values, whereas ambient temperature results, which are depicted by black diamonds, exhibit the lowest RSD values. Scaled spectra resulted in larger Kubelka-Munk intensities than scaled and baseline corrected spectra. Standard deviations for scaled and scaled and baseline corrected results obtained with the stainless steel sample holder were similar. In contrast, baseline correction decreased peak maxima standard deviations compared to scaled only spectra when the new quartz sample holder was employed. Kubelka-Munk peak maxima standard deviations derived from measurements made with the new quartz sample holder were significantly less (by ~ 10x) than the corresponding results obtained by using the stainless steel sample holder. However, although RSD values were significantly reduced by scaling and

baseline correction, ambient temperature measurements were consistently more reproducible than variable temperature measurements.

Table 5.3 Comparison of Overall Relative Standard Deviations.

Data set	Slope ≈ RSD	
	Steel sample holder	New VT-DRIFTS sample holder (Quartz)
Ambient temperature	0.0096	0.0055
Variable temperature	0.7995	0.0746
Variable temperature – scaled	0.0498	0.026
Variable temperature – scaled and baseline corrected	0.0913	0.0235

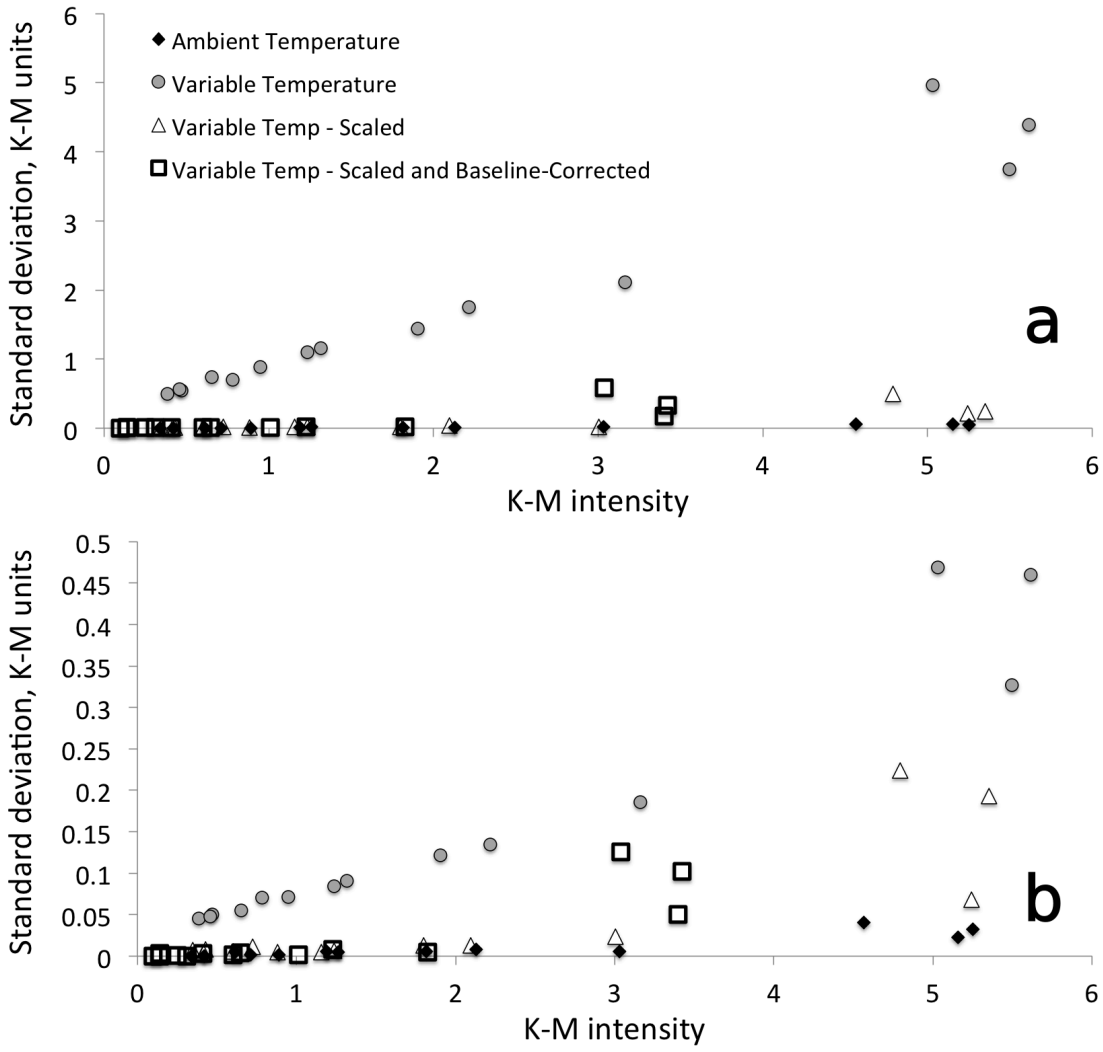

Figure 5.40 Peak maxima standard deviation as a function of Kubelka-Munk intensity for measurements made with the (a) stainless steel and (b) new quartz sample holders.

5.5 References

1. *Coefficients of Linear Thermal Expansion. Linear temperature expansion coefficients for aluminum, copper, glass, iron and other common materials*, The Engineering Toolbox: Thermodynamics, 2005, www.engineeringtoolbox.com/linear-expansion-coefficients-d_95.html. Accessed 8 Dec. 2016.

2. *Fused Silica Material Properties*, datasheet, Accuratus Ceramic Corporation: Phillipsburg, New Jersey (2013).

3. Milosevic, M. and S.L. Berets, A review of FT-IR diffuse reflection sampling consideration*, Applied Spectroscopy Reviews*, **37**(4), p. 347-364 (2002).

4. Handke, M., M. Milosevic, and N.J. Harrick, External Reflection Fourier-Transform Infrared-Spectroscopy - Theory And Experimental Problems*, Vibrational Spectroscopy*, **1**(3), p. 251-262 (1991).

5. White, R.L., Requirements for Thermal Analysis by Variable-Temperature Diffuse Reflectance Infrared Spectroscopy*, Applied Spectroscopy*, **46**(10), p. 1508-1513 (1992).

6. Maraoulaite, D.K., T.M. Nickels, A.L. Ingram, and R.L. White, VT-DRIFTS Investigations of Interactions Between Benzoic Acid and Montmorillonite Clay*, Spectroscopy*, **30**(10), p. 2-8 (2015).

Chapter 6: VT-DRIFTS Performance Characteristics

6.1 Introduction

Infrared spectroscopy has historically been an important analytical tool for the characterization of both organic and inorganic materials. Infrared spectra contain absorbance bands that uniquely represent molecular vibrations. Diffuse reflection infrared Fourier transform spectroscopy (DRIFTS) is particularly well suited for solid-state sample characterizations. Compared to film, pellet and mull techniques, DRIFTS is easier to implement and requires less sample preparation. Whereas conventional transmission infrared spectroscopy intensities are dependent on path length, which is difficult to reproduce for solid samples, DRIFTS band intensities depend on scattering coefficient, which is predominantly determined by particle size. DRIFTS is well suited for characterizing surface interactions between adsorbates and minerals. Consequently, it is often employed for soil contaminant studies.[1-4]

When using DRIFTS for adsorbate interaction studies, spectral subtractions are commonly employed to isolate selected infrared spectral features from large bulk sample absorbances. This is typically accomplished by subtracting reference spectra representing the sample matrix from spectra obtained for the same material, but also containing substances of interest. Often, pretreatment processes (e.g. extractions) are employed to remove these substances from the reference samples. As pointed out by

Thomas and Kelley,[5] careful reference and adsorbate spectrum measurements are critical for obtaining accurate difference spectra. For this reason, they reportedly avoided studies with montmorillonites. Unlike many other minerals, montmorillonite structures consist of a sandwich of two inorganic sheets around a variable thickness water layer. In order to measure an appropriate reference spectrum, it is necessary to precisely control the water content, which is difficult to accomplish. Thus, depending on environmental conditions, samples may contain different amounts of water and infrared spectra would therefore contain varying water absorbance contributions, which would be difficult to remove by using spectral subtractions.

To avoid difference spectrum artifacts not associated with substances of interest, a sample perturbation analysis method can be employed. This approach can be explained with the aid of the diagram shown in Figure 6.1. At the top of the diagram (A), the species of interest is represented by X, which may also exist in charge carrying forms (X^{n+} and X^{n-}), depending on its acid/base properties and local pH. Each form may interact differently with its surroundings, contributing different absorbance features to measured infrared spectra. The overlapping ellipses in Figure 6.1 represent X interactions with other organic substances (Org), water (H_2O), cations (+), anions (-), and inorganic oxides (M_aO_b) that may be present in the sample. The solid-state infrared spectrum measured for the system denoted in (A) will contain information regarding the vibrational modes of all constituents. After heating the sample represented by (A) to remove water (i.e. the perturbation), the resulting spectrum will represent a slightly different solid-state configuration (B). A difference spectrum computed by subtracting the infrared spectrum obtained for (A) from the spectrum measured for (B) will contain

spectral features representing the changes that occurred as a result of heating. Specifically, the difference spectrum will contain positive features representing vibrations formed after water removal (i.e. related to new interactions) and negative features corresponding to vibrational modes that were lost due to the configuration change. The size of the spectral features in difference spectra will depend on the number of perturbed species and the absorptivities of the affected absorbance bands. Negative spectral features provide insight into the interactions between X and water in the initial configuration (A). By continuing to heat the sample while measuring infrared spectra, the difference spectrum representing (C) – (B) sample configuration changes would contain negative features corresponding to vibrational modes associated with the dehydrated X molecule and its environment that were lost when it desorbed from the sample and the (D) – (B) difference spectrum would provide similar vibrational mode information, but for instances when X decomposed rather than desorbed. Additional information regarding decomposition mechanisms may be obtained by determining the amounts and identities of decomposition products (Y and Z). Figure 6.1 (A) potentially represents a very complicated system of simultaneous interactions. For example, soils typically contain numerous organic molecules, cations, anions, and inorganic oxides in differing amounts. Fortunately, appropriate sample composition simplifications can be made to design experiments that target specific molecular interactions. For example, the VT-DRIFTS study described here is focused on characterizing specific interactions between benzoic acid adsorbates and montmorillonite clay.

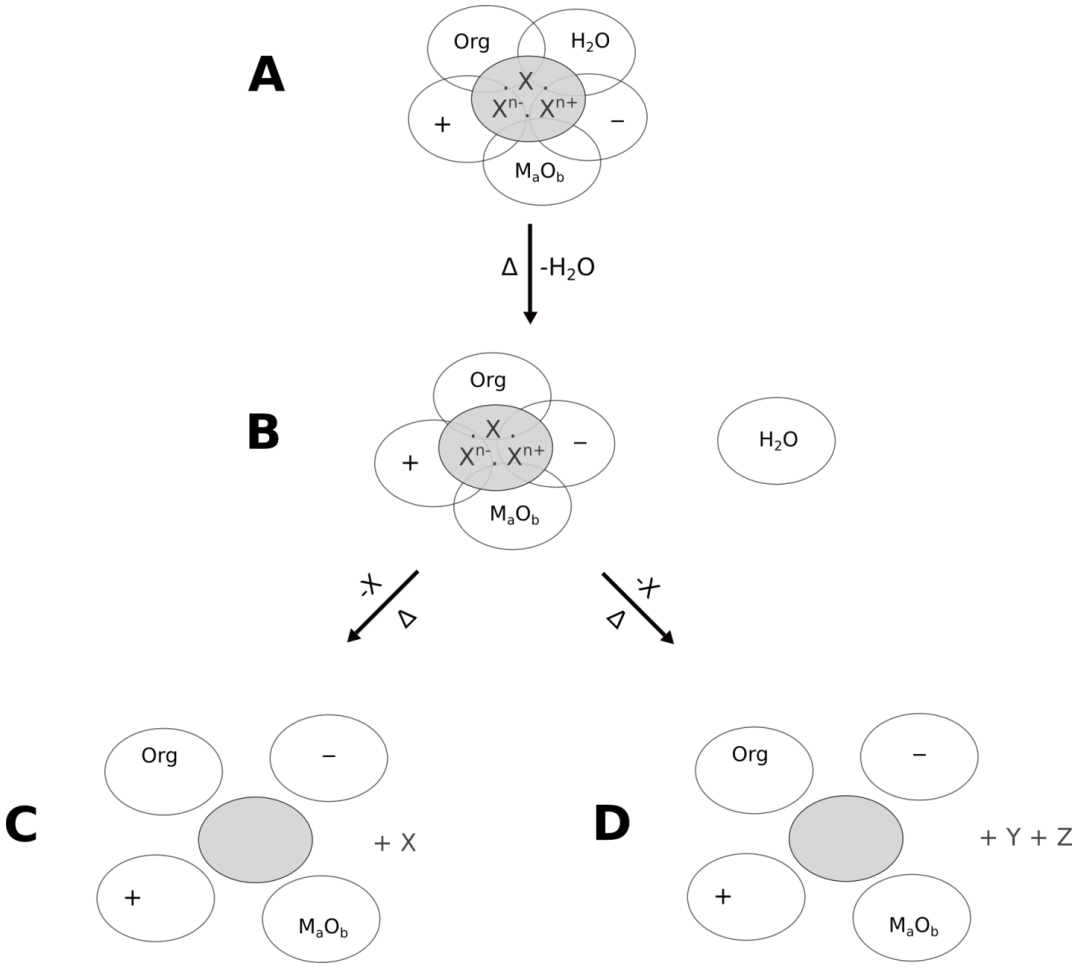

Figure 6.1 Representation of the X local environment (A) before heating, (B) after dehydration, (C) after X desorption and (D) after X decomposition.

6.2 Background – Benzoic Acid Interactions with Montmorillonite

The Environmental Protection Agency has identified organic acids as a primary source of contamination.[6, 7] Benzoic acid, which consists of an acid functionality attached to an aromatic ring, is the simplest aromatic acid. It can inhibit bacterial and plant growth and is extensively used as a food preservative.[8] In soils, it is typically adsorbed by the clay component.[9] Consequently, benzoic acid interactions with clays have been extensively studied.[5, 6, 9-14] These studies have primarily focused on

montmorillonites, because this type of clay is ubiquitous in soils. Montmorillonite clays have a unique structure, consisting of two negatively charged oxide layers separated by an interlayer space containing exchangeable cations and water.[15]

Interactions between benzoic acid and montmorillonite clays were previously studied by thermo-IR[10] and thermogravimetry[12]. By using thermo-IR, Yariv et al. reported that the C=O stretching vibration frequency of benzoic acid adsorbed on montmorillonite clays depended on the cation present in the interlayer space and on the extent of clay dehydration.[10] In a thermogravimetry study of benzoic acid – clay interactions, Lu et al. reported that the maximum rate of benzoic acid desorption from sodium montmorillonite occurred at 140 °C, which was significantly lower than from calcium montmorillonite (179 °C).[12] They attributed the higher desorption temperature for the clay containing calcium to stronger interactions between calcium ions and benzoic acid molecules.

To characterize benzoic acid – clay interactions in greater detail, in-situ analysis by using variable temperature diffuse reflection infrared Fourier transform spectroscopy (VT-DRIFTS) can be performed.[16, 17] VT-DRIFTS provides a sensitive means for discerning subtle temperature-dependent structural changes in solid materials. To obtain high quality VT-DRIFTS measurements, it is necessary to account for instrumental changes caused by heating the sample in addition to factors that must be considered when making isothermal DRIFTS measurements.[18-20] The methodology employed for VT-DRIFTS is outlined here, along with examples of results obtained from analysis of a sample consisting of 2% (w/w) benzoic acid adsorbed on montmorillonite clay.

6.3 VT-DRIFTS Experimental Conditions

Montmorillonite (K10) and benzoic acid were purchased from Sigma-Aldrich. Calcium chloride was purchased from Fischer Scientific. Silver powder (100 mesh, 99.95%) was purchased from Alfa Aesar. Carbon tetrachloride was purchased from JT Baker Chemical Company. All chemicals were used as received without additional purification. Montmorillonite clay with predominately Ca^{2+} interlayer ions (CaMMT) was prepared by cation exchange with the metal chloride solution by following previously described procedures.[21, 22]

The cation-exchanged clay was loaded with 2% (w/w) benzoic acid by incipient wetness. Benzoic acid was dissolved in carbon tetrachloride, and the solution was mixed with the montmorillonite clay. The mixture was stirred for 30 minutes at room temperature, then the solvent was removed by roto-evaporation for 90 minutes at room temperature. Samples were prepared for VT-DRIFTS analysis by diluting with silver powder in a 5-95 ratio by weight (e.g. 5% (w/w)). Silver powder diluent, which is highly scattering and inert for this application, was employed to eliminate spectral artifacts that appear in infrared spectra when neat samples are analyzed by DRIFTS (*vide infra*). Approximately 15 mg samples were employed for VT-DRIFTS analysis.

VT-DRIFTS measurements were made by using the apparatus described in Chapter 2. A linear sample heating ramp and 10 mL/min helium purge were used for analysis. The sample was heated at 5 °C/min beginning from ambient temperature. Infrared spectra were measured at 1 min (5 °C) intervals. Reflectance spectra were computed by dividing successively acquired infrared single beam spectra by diluent (i.e.

silver powder) reference single beam spectra. Reflectance spectra were baseline corrected prior to conversion to Kubelka-Munk format by following previously described procedures.[20]

6.4 VT-DRIFTS Spectral Results

DRIFTS measurements of neat calcium montmorillonite (CaMMT) exhibit artifacts caused by the Reststrahlen effect,[23] resulting in loss of spectral features over the affected wavelength range. Increased sample reflectance occurs near the intense 1050 cm^{-1} inorganic oxide absorption band due to high sample refractive index, which results in an apparent loss of absorbance (i.e. an increase in reflectance). As shown in Figure 6.2, this phenomenon results in a distorted reflectance spectrum when the neat clay is analyzed by DRIFTS. Fortunately, as illustrated by the dashed line spectrum in Figure 6.2, sample dilution can reduce the sample refractive index and eliminate this artifact. Thus, to avoid complications caused by Reststrahlen effects, the benzoic acid/CaMMT sample used for VT-DRIFTS studies was diluted in silver powder.

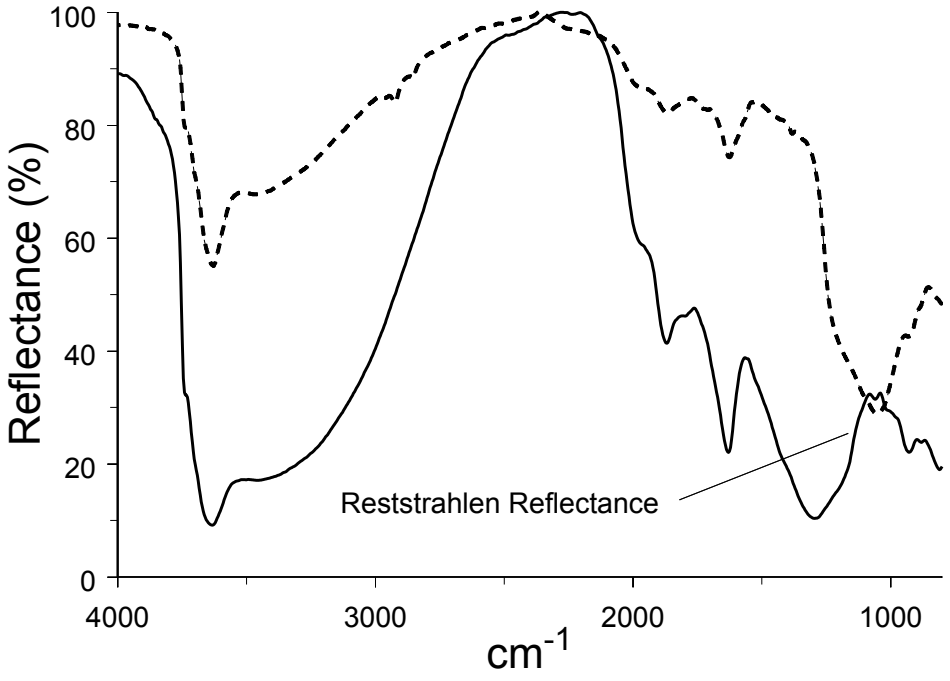

Figure 6.2 Reflectance spectra measured for neat (solid line) and 5% (w/w) clay diluted in silver powder (dashed line).

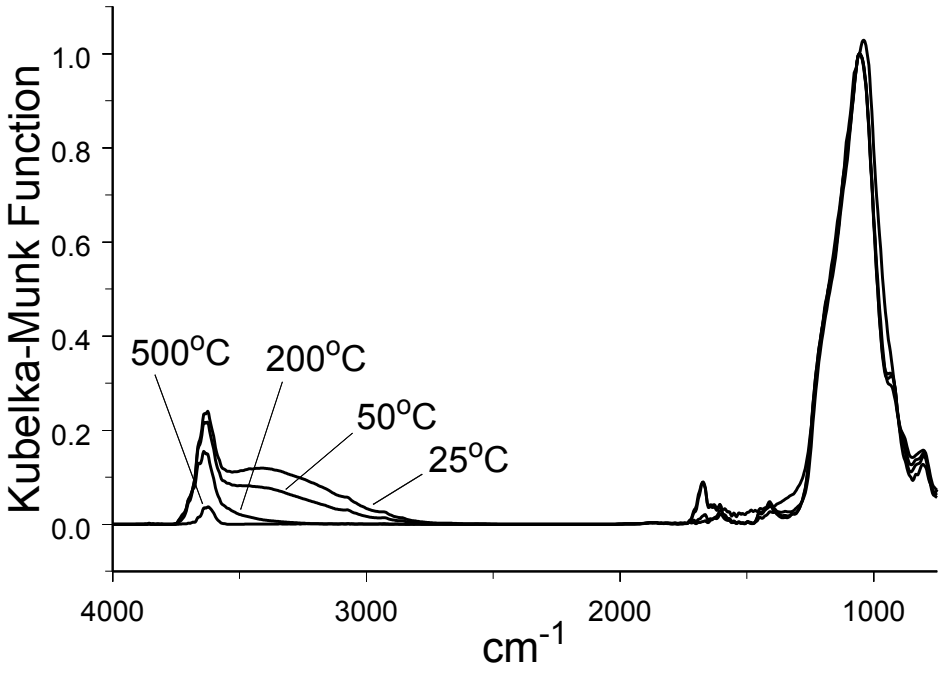

Figure 6.3 Overlay of VT-DRIFTS spectra obtained at different sample temperatures.

Figure 6.3 shows overlaid benzoic acid/CaMMT VT-DRIFTS spectra measured between 25 and 500 °C. The inorganic oxide absorbance at 1050 cm^{-1} is relatively constant as a function of temperature, but does exhibit an observable red shift in the spectrum measured at 500 °C. Smaller absorbances in the 1800-1400 cm^{-1} region are associated with benzoic acid adsorbate and interlayer water (i.e. H-O-H bending). Above 2500 cm^{-1}, spectral features represent -O-H stretching vibrations associated primarily with clay interlayer water molecules, but also benzoic acid and inorganic oxide hydroxyl groups. Thus, the VT-DRIFTS results depicted in Figure 6.3 contain

temperature-dependent functional group vibrational mode information regarding the inorganic oxide, interlayer water, and benzoic acid adsorbate sample components.

Heating the benzoic acid/CaMMT sample resulted in characteristic temperature-dependent functional group changes. These changes were profiled by plotting selected VT-DRIFTS spectral region integrated areas as a function of temperature. Three of these plots are shown in Figure 6.4. The 2500-3650 cm^{-1} integrated area plot represents the loss of hydrogen bonded hydroxyl groups as a function of sample temperature. The spectral intensity in this range is mainly representative of clay interlayer water content and the abrupt decrease upon heating denotes sample dehydration. The 1650-1700 cm^{-1} integrated area plot represents the loss of –C=O stretching vibration band intensity with increasing temperature. This plot primarily depicts benzoic acid desorption. The 3700-3750 cm^{-1} spectral region represents weakly hydrogen bonded inorganic oxide hydroxyl groups. Unlike the other profiles in Figure 6.4, the 3700-3750 cm^{-1} integrated area increases between 25 and 100 °C and then remains relatively constant until about 350 °C, at which point a gradual decline in integrated area is observed.

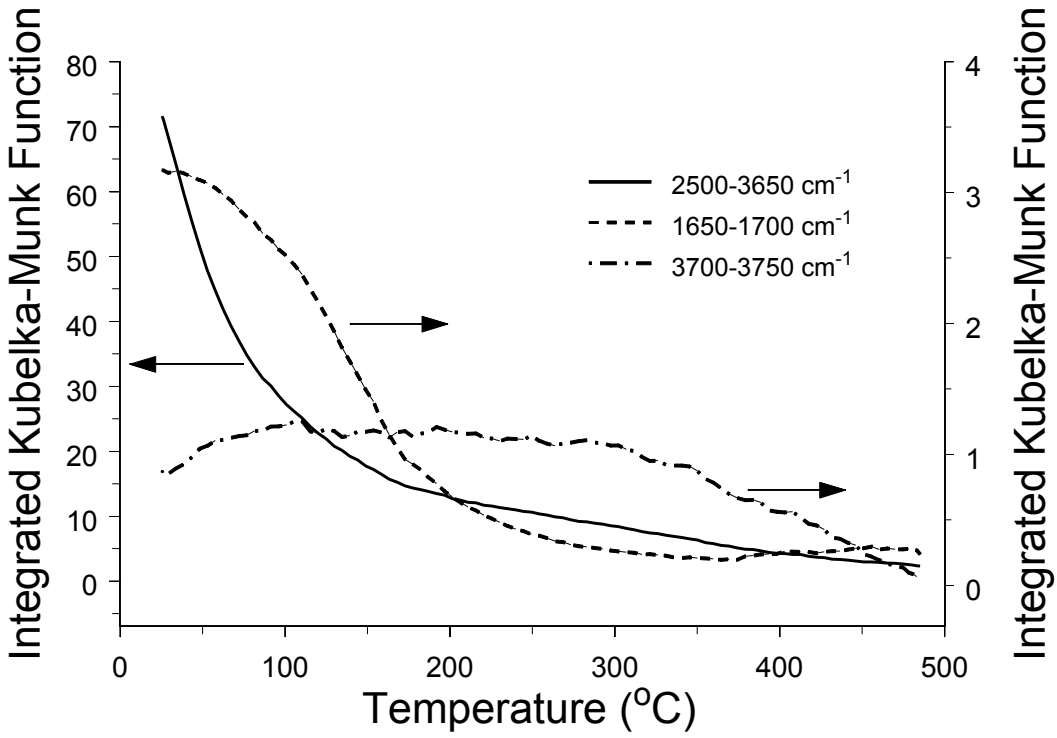

Figure 6.4 VT-DRIFTS integrated area temperature profiles.

Although the temperature profiles in Figure 6.4 show general trends in sample composition variations that occur with heating, they do not provide detailed information regarding molecular environment changes. However, the information provided by these temperature profiles can be used to select VT-DRIFTS spectra for difference calculations, from which information regarding molecular environment changes can be obtained. For example, Figure 6.5 shows the difference spectrum obtained by subtracting the ambient temperature (25 °C) spectrum from the VT-DRIFTS spectrum obtained at 50 °C. A DRIFTS spectrum for a 5% (w/w) calcium montmorillonite/silver powder sample (CaMMT) is provided at the bottom of Figure 6.5 for reference. As

expected, the difference spectrum contains negative features between 2800-3700 cm^{-1} and at 1630 cm^{-1} associated with loss of hydrogen bonded –O-H stretching vibrations and H-O-H bending vibrations respectively, which, at these low temperatures, are indicative of clay interlayer water loss. The positive band near 3750 cm^{-1} is associated with an increase in inorganic oxide hydroxyl group vibration frequency (i.e. a blue shift) due to loss of hydrogen bonding with water molecules. Spectral features in the 1200-800 cm^{-1} range reflect changes in inorganic oxide vibrations caused by water loss. The negative band at 1690 cm^{-1} in the difference spectrum can be assigned to the benzoic acid –C=O stretching vibration. The presence of this band is surprising because it cannot be attributed to benzoic acid desorption, because that occurs at temperatures above 50 °C.[16] Instead, this intensity decrease reflects a loss in –C=O stretching vibration band absorptivity caused by the loss of hydrogen bonding interactions between benzoic acid and clay interlayer water molecules.

Figure 6.4 shows that loss of –C=O stretching vibration intensity occurs mainly over the 50-200 °C sample temperature range. Figure 6.6 contains the 200 – 50 °C VT-DRIFTS difference spectrum and an ambient temperature DRIFTS spectrum measured for a sample containing 5% (w/w) benzoic acid mixed with silver powder. The difference spectrum in Figure 6.6 contains features primarily associated with the loss of benzoic acid. Spectral features attributed to loss of hydrogen bonded hydroxyl groups and inorganic oxide vibration changes are also present in this difference spectrum. In addition to the clearly visible negative band associated with loss of the benzoic acid –C=O stretching vibration band, smaller negative peaks can be assigned to the benzoic

acid aromatic ring (3077, 1606, and 1585 cm^{-1}) and to the –C-O-H functional group (1498, 1450, and 1415 cm^{-1}).

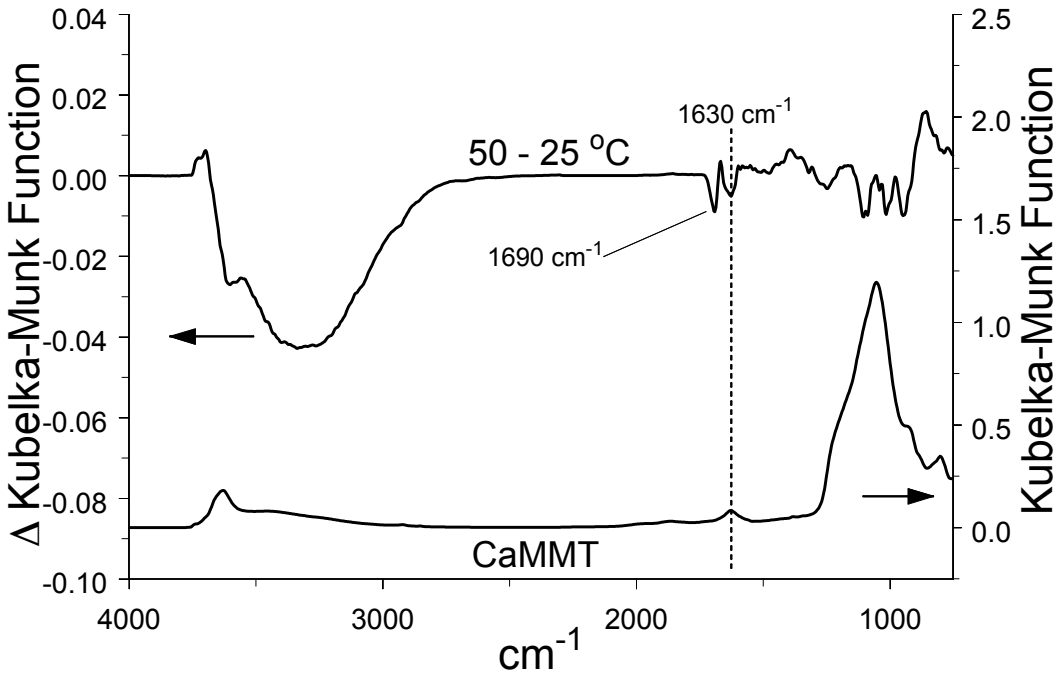

Figure 6.5 Difference spectrum computed by subtracting the spectrum measured at 25 °C from the spectrum measured at 50 °C (top) and a clay reference spectrum (bottom).

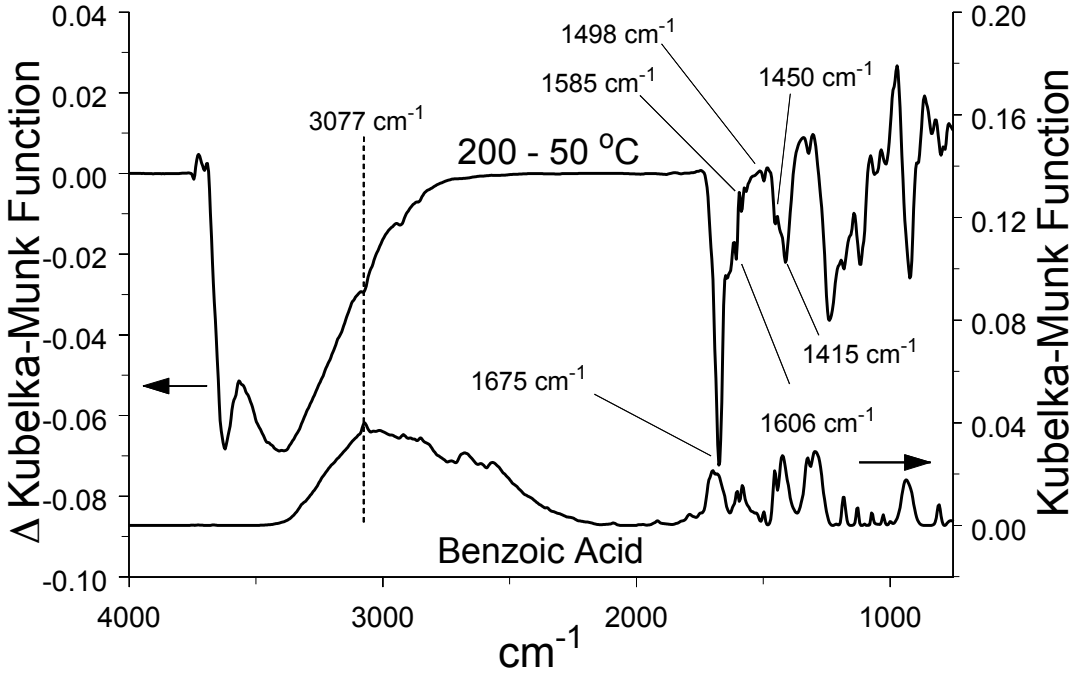

Figure 6.6 Difference spectrum computed by subtracting the spectrum measured at 50 °C from the spectrum measured at 200 °C (top) and a benzoic acid reference spectrum (bottom).

VT-DRIFTS spectral variations confirm that sample changes continued to occur above 200 °C (Figure 6.7). The dominant 500 – 200 °C difference spectrum features are associated with loss of weakly hydrogen bonded –O-H stretching vibrations and to inorganic oxide vibration band changes. The significant increase in intensity near 990 cm^{-1} likely results from the formation of metal-oxygen-metal inorganic oxide bridges resulting from high temperature dehydroxylation reactions.

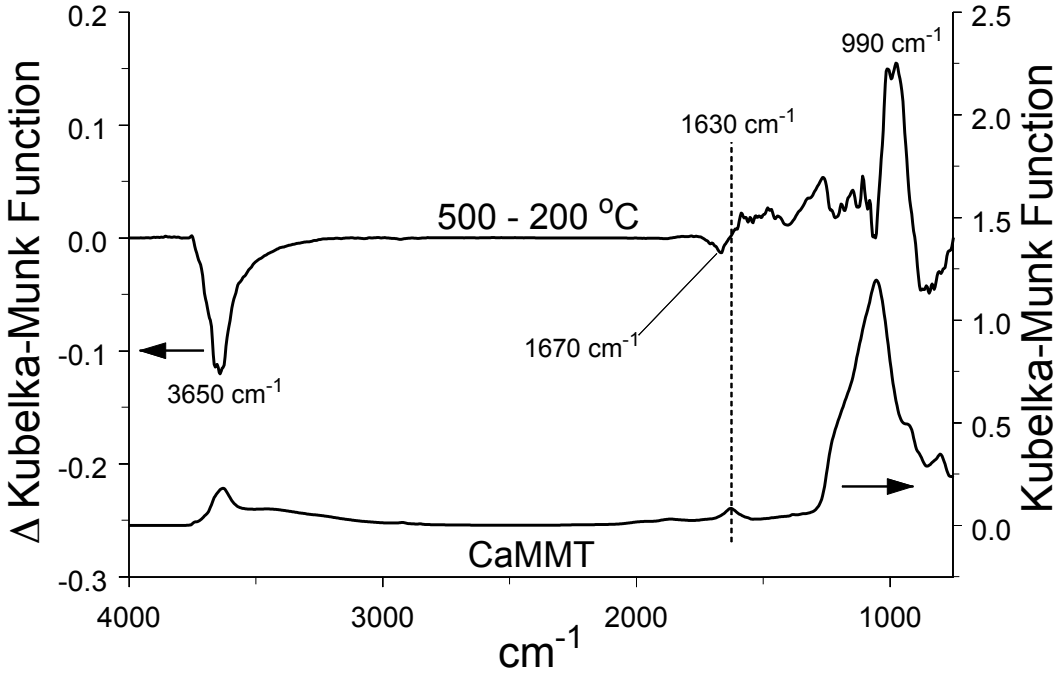

Figure 6.7 Difference spectrum computed by subtracting the spectrum measured at 200 °C from the spectrum measured at 500 °C (top) and the clay reference spectrum (bottom).

6.5 Conclusions

The VT-DRIFTS sample perturbation method described here constitutes a sensitive thermal analysis technique capable of providing detailed functional group specific information regarding temperature-dependent sample composition changes. Modern FTIR instruments provide sufficiently high scan-to-scan reproducibility to make sensitive VT-DRIFTS measurements possible, provided that temperature-dependent artifacts associated with the interferometer and detector are minimized.

Taking into account dilution, the ~15 mg benzoic acid/CaMMT sample quantity employed for the spectral measurements described here contained about 735 μg of clay and 15 μg of benzoic acid. Consequently, the relatively high signal-to-noise ratio for the 1650-1700 cm^{-1} integrated Kubelka-Munk function profile shown in Figure 6.4 suggests that VT-DRIFTS analysis can facilitate detection of adsorbate losses in the high nanogram range that occur between successive infrared measurements (i.e. 5 °C sample temperature intervals). This sensitivity may be improved by using slower heating ramp rates and increasing the number of signal averaged interferograms used to compute spectra.

The study of the temperature-dependent interactions between benzoic acid and montmorillonite clay described here illustrates the power of using VT-DRIFTS measurements for characterizing molecular environments. VT-DRIFTS spectra contained information regarding clay components (e.g. water and inorganic oxides) and specific benzoic acid functional groups (e.g. –C=O, -C-O-H, and C_6H_5 ring). However, interpretation of VT-DRIFTS analysis results can be difficult, because changes to all sample constituents are simultaneously detected. Overlapping positive and negative spectral features can occur, and intensity variations may be associated with changes in the number of absorbers, to changes in vibration band absorptivities, or to both.

Comparing the negative –C=O stretching vibration bands in difference spectra shown in Figures 6.5 – 6.7 reveals that the frequency for this vibration band loss decreases with increasing temperature from 1690 cm^{-1} in the lowest temperature difference spectrum to 1670 cm^{-1} in the highest temperature difference spectrum. This 20 cm^{-1} red shift is indicative of increasing strengths of interactions between the

benzoic acid –C=O functionality and its surroundings. This trend is reasonable because increasingly strong interactions require greater energies (i.e. temperatures) to disrupt them.

By studying samples containing larger amounts of benzoic acid adsorbed on montmorillonite clays containing different interlayer cations, a more comprehensive VT-DRIFTS study in which multiple benzoic acid adsorption sites were characterized has been reported.[16] Future VT-DRIFTS studies may include even more complicated solid state systems, such as soils containing multiple adsorbates. In fact, VT-DRIFTS may become a particularly important tool for studying the transport and fate of soil contaminants, because few other analysis methods provide comparable sensitivity and specificity.

6.6 Summary of Findings

DRIFTS is a powerful method for analysis of powders and rough surfaces. Unfortunately, DRIFTS is also considered an "energy starved" technique, which therefore necessitates significant attention to sample measurement conditions. To obtain high SNR spectra, the detector interferogram signal must be maximized. This requires high infrared source radiance, high optical throughput, and highly reflective samples.[20, 24] To achieve maximum optical throughput, the sample must be located at the infrared beam focal point, all optics must be properly aligned, and the FTIR must be purged with dry CO_2 free air. To eliminate spectral artifacts, samples should be diluted in a highly reflective, low absorbance matrix. This is particularly important for measurements of high absorption spectral bands, because Kubelka-Munk intensity

reproducibility decreases significantly with increasing absorbtivity. Powdered samples should contain small particles, because this maximizes the quantity of diffuse reflection.

The detailed characterization of VT-DRIFTS described here identified two contributions to measured spectra that depend on sample temperature, but do not result from sample composition changes. Changes in sample single beam emissivity result in Kubelka-Munk intensity errors. The primary cause for sample single beam intensity variations was found to be detector saturation from unmodulated radiation emitted from heated samples.[20] Temperature-dependent optical alignment variations produce baseline slopes in reflectance spectra. This primarily results from sample holder and environmental chamber thermal expansion and the temperature sensitivity of the interferometer.

Unmodulated infrared radiation from heated samples reduces interferogram voltages.[20] As described in Chapter 3, this reduction in single beam emissivity results in Kubelka-Munk peak maxima increases that depend exponentially on absorptivity. Post-data collection single beam spectrum scaling can be used to minimize these non-linear effects. By scaling VT-DRIFTS single beam spectra to match ambient temperature emissivity, reflectance spectrum baseline offsets can be removed,[19] as described in section 3.3.3. Removal of baseline offsets increases the accuracy of Kubelka-Munk spectral features, especially for highly absorbing bands.

By monitoring temperatures at various locations within the FTIR (section 3.5.1), long term (~ 40 min) baseline slope oscillations were correlated with small interferometer temperature changes caused by room temperature fluctuations (section 4.3.2). These baseline slope oscillations were detected at ambient temperature as well

as for VT-DRIFTS measurements. The extreme temperature sensitivity of the FTIR interferometer is evidenced by the fact that relatively small interferometer temperature variations cause these baseline oscillations. To minimize reflectance spectrum baseline slopes attributed to the interferometer, room temperature should be precisely controlled, or, the interferometer should be thermally isolated from room air. To eliminate reflectance spectrum baseline slopes that appear as a result of VT-DRIFTS sample heating, the interferometer compartment should be thermally isolated from the heated sample. Without adequate thermal isolation of the interferometer, a systematic change in baseline slope appears in VT-DRIFTS spectra that persists even after heating power is removed. This effect can be attributed to gradual temperature increases for instrument components. Instrument component temperature changes depend on sample temperature and proximity to the sample. Consequently, instrument component temperatures do not track with sample temperatures. In fact, temperatures for some components continue to increase while the sample cools after heating. Thus, sufficient time between VT-DRIFTS analyses is required to ensure that all components return to their initial temperatures. The sample environmental chamber helium purge rate also affects instrument component temperatures. Higher helium purge rates facilitate more efficient heat transfer to instrument components (Chapter 4). Consequently, lower sample purge rates are recommended for VT-DRIFTS measurements to minimize optical component temperature increases.

Trends in temperature- dependent baseline slope changes can be induced at ambient temperature by moving the sample up and down. This suggests that optical throughput variations are caused by sample holder thermal expansion during VT-

DRIFTS measurements. Temperature-dependent sample and optical component movements can be minimized by using materials with low thermal expansion coefficients, such as quartz (Chapter 5). In general, VT-DRIFTS baseline slope artifacts can be minimized by limiting optical component movements during sample heating.

When VT-DRIFTS sample temperature exceeds about 200 °C infrared significant radiation emitted by the sample passes through the interferometer and becomes modulated. This modulated sample emission is 180° out of phase with the modulated FTIR infrared source radiation, resulting in interferogram voltage reduction. When cube corner retroreflectors are employed in the interferometer, this effect can be eliminated by blocking one-half of the beam exiting the interferometer. Unfortunately, this approach also reduces interferogram voltages. [25]

Instrument temperature measurements confirm that a substantial temperature difference develops between the sample surface and the bottom of the sample, where the temperature control thermocouple is located. Although sample surface temperatures can be estimated from temperature controller readings by using an appropriate correlation function, the best approach for measuring sample temperatures is to place the thermocouple just under the sample surface. This results in accurate temperature measurements for the portion of the sample exposed to infrared radiation and avoids problems associated with radiation reflection by the thermocouple when it is placed on top of the sample (Chapter 4). Interestingly, studies show that surface temperature measurement reproducibility is not significantly affected by sample purge rates.

As described in section 2.4, the DRA optical components and environmental chamber employed for VT-DRIFTS decreased the FTIR optical throughput. Eliminating the environmental chamber lid increases interferogram voltage by about a factor of 10, yielding improved SNR for spectra. Although VT-DRIFTS measurements can be made without the environmental chamber, exceeding 200 °C is not recommended, because of potential sample oxidation and excessive optics heating at higher sample temperatures (section 5.5).

The instrument characterization studies described here have led to a better understanding of the VT-DRIFTS technique and significant improvements in measurement SNR and reproducibility. However, based on the thorough evaluation described here, additional improvements are possible. For example, better sample heating methods that transfer a greater fraction of energy to the sample would minimizing heat transfer to the sample holder and environmental chamber. This would reduce artifacts caused by thermal expansion of these components as well as reduce heating of the FTIR optical system. The current VT-DRIFTS design can provide high nanogram detection limits (Chapter 6), which is remarkable for an infrared analysis technique. By eliminating the environmental chamber lid, lower detection limits should be possible. Although measurements without the environmental chamber lid should be limited to below 200 °C, this is a sufficient temperature range to study a wide variety of sample change mechanisms. For example, interactions between molecules and water can be characterized by comparing spectra acquired before and after sample dehydration. The VT-DRIFTS sample perturbation technique outlined here (Chapter 6)

can be used to study adsorbate-water interactions even in the presence of complicated matrices, like those found in soils.

6.7 References

1. Janik, L.J., S.T. Forrester, J.M. Soriano-Disla, J.K. Kirby, M.J. McLaughlin, and C. Reimann, GEMAS: Prediction of Solid-Solution Partitioning Coefficients (K-d) for Cationic Metals in Soils using Mid-Infrared Diffuse Reflectance Spectroscopy*, Environmental Toxicology and Chemistry*, **34**(2), p. 224-234 (2015).

2. Fultz, L.M., J. Moore-Kucera, F. Calderon, and V. Acosta-Martinez, Using fourier-transform mid-infrared spectroscopy to distinguish soil organic matter composition dynamics in aggregate fractions of two agroecosystems*, Soil Science Society of America Journal*, **78**(6), p. 1940-1948 (2014).

3. Yang, X., An extension to "Mid-infrared spectral interpretation of soils: Is it practical or accurate?"*, Geoderma*, **226-227**(1), p. 415-417 (2014).

4. Reeves, J.B., III., Mid-infrared spectral interpretation of soils: Is it practical or accurate? *, Geoderma*, **189-190**, p. 508-513 (2012).

5. Thomas, J.E. and M.J. Kelley, Interaction of Mineral Surfaces with Simple Organic Molecules by Diffuse Reflectance IR Spectroscopy (DRIFT)*, Journal of Colloid and Interface Science*, **322**(2), p. 516-526 (2008).

6. Lu, L., J. Cai, and R.L. Frost, Near Infrared Spectroscopy of Benzoic Acid Adsorbed on Montmorillonite*, Spectroscopy Letters*, **43**(4), p. 266-274 (2010).

7. Jafvert, C.T., *Assessing the Environmental Partitioning of Organic Acid Compounds*, Research and Develoment, environmental research brief, USEPA, Env. Res. Lab: Athens, GA (1990).

8. Inderjit and P.C. Bhowmik, Sorption of Benzoic Acid onto Soil Colloids and its Implications for Allelopathy Studies*, Biology and Fertility of Soils*, **40**(5), p. 345-348 (2004).

9. Chefetz, B., S. Eldad, and T. Polubesova, Interactions of Aromatic Acids with Montmorillonite: Ca^{2+}- and Fe^{3+}-Saturated Clays versus Fe^{3+}- Ca^{2+}-Clay System*, Geoderma*, **160**(3-4), p. 608-613 (2011).

10. Yariv, S. and H. Cross, eds., *Organo-Clay Complexes and Interactions*, Marcel Dekker, Inc.: New York (2002).

11. Yariv, S., J.D. Russell, and V.C. Farmer, Infrared Study of the Adsorption of Benzoic Acid and Nitrobenzene in Montmorillonite*, Israel Journal of Chemistry*, **4**(5-6), p. 201-213 (1966).

12. Lu, L., J. Cai, and R.L. Frost, Desorption of Stearic Acid upon Surfactant Adsorbed Montmorillonite*, Journal of Thermal Analysis and Calorimetry*, **100**(1), p. 141-144 (2010).

13. Yan, L.G., J. Wang, H.Q. Yu, Q. Wei, B. Du, and X.Q. Shan, Adsorption of benzoic acid by CTAB exchanged montmorillonite*, Applied Clay Science*, **37**(3-4), p. 226-230 (2007).

14. Lu, L., R.L. Frost, and J. Cai, Desorption of Benzoic and Stearic Acid Adsorbed upon Montmorillonites: a Thermogravimetric Study*, Journal of Thermal Analysis and Calorimetry*, **99**(2), p. 377-384 (2010).

15. Bhattacharya, K.G. and S.S. Gupta, Adsorption of a Few Heavy Metals on Natural and Modified Kaolinite and Montmorillonite: A Review*, Advanced Colloid Interface Science*, **276**, p. 181-210 (2008).

16. Nickels, T.M., A.L. Ingram, D.K. Maraoulaite, and R.L. White, Variable Temperature Infrared Investigation of Benzoic Acid Interactions with Montmorillonite Clay Interlayer Water*, Applied Spectroscopy*, **69**(7), p. 850-856 (2015).

17. Nickels, T.M., A.L. Ingram, D.K. Maraoulaite, and R.L. White, Variable Temperature Infrared Spectroscopy Investigations of Benzoic Acid Desorption from Sodium and Calcium Montmorillonite Clays*, Applied Spectroscopy*, **69**(12), p. 1381-1389 (2015).

18. White, R.L., Requirements for Thermal Analysis by Variable-Temperature Diffuse Reflectance Infrared Spectroscopy*, Applied Spectroscopy*, **46**(10), p. 1508-1513 (1992).

19. White, R.L., Removal of Baseline Artifacts from Variable-Temperature Diffuse Reflectance Infrared Spectra*, Analytical Chemistry*, **64**(17), p. 2010-2013 (1992).

20. Lin, R. and R.L. White, Effect of Diffuse Reflectance Fourier Transform Infrared Spectroscopy Sample Temperature on Photoconducting Semiconductor and Pyroelectric Infrared Detectors*, Analytical Chemistry*, **66**(18), p. 2976-2980 (1994).

21. Stanley, D.A. and B.J. Scheiner, *Flocculation and Dewatering of Montmorillonite Modified by Ion Exchange*, RI 9021, U.S. Dept of Interior, Bureau of Mines: Avondale, MD (1986).

22. Stanley, D.A., S.W. Webb, and B.J. Scheiner, *Rheology of Ion-Exchanged Montmorillonite Clays*, RI 8895, U.S. Dept. of Interior, Bureau of Mines: Avondale, MD (1984).

23. Hapke, B., *Theory of Reflectance and Emittance Spectroscopy*, 2nd ed., Cambridge University Press: New York (2012).

24. Milosevic, M. and S.L. Berets, A review of FT-IR diffuse reflection sampling consideration*, Applied Spectroscopy Reviews*, **37**(4), p. 347-364 (2002).

25. Tripp, C.P. and R.A. McFarlane, Discussion of the Stray Light Rejection Efficiency of FT-IR Spectrometers: The Effects of Sample Emission on FT-IR Spectra*, Applied Spectroscopy*, **48**(9), p. 1138-1142 (1994).

Appendix A: Data Processing – File Types and Conversions

Information presented here was adapted from the FIRST™ Macros Fourier Infrared Software Tools User's Manual.[1]

In WinFirst, interferogram data is saved in a file with the extension **.igm* (for "interferogram") or **.big* (for "background interferogram").

The fast Fourier transform (FFT) algorithm is used to convert the interferogram into a single beam spectrum: **.sbm* (for "sample single beam") and **.bkg* (for "background single beam"). A detailed explanation of the FFT algorithm can be found in a number of references.[2]

To summarize, an interferogram is converted into a single beam spectrum by the FFT algorithm:

example.igm --- *FFT* --- *example.sbm*

example.big --- *FFT* --- *example.bkg*

The single beam spectrum represents the intensity of radiation reaching the detector as a function of radiation frequency (Figs. 2 and 3). A reflectance spectrum (for a diffuse reflection measurement) or a transmittance spectrum (for a transmission measurement) can be obtained by computing the ratio of the sample single beam spectrum (which lacks radiation that has been absorbed by the sample) to the background single beam spectrum (i.e. reference). The file extension for this ratio is **.ras*:

example.sbm / *example.bkg* = *example.ras*

example.sbm / *reference.sbm* = *example.ras*

The transmittance (*T*) or, in the case of diffuse reflection, the reflection spectrum (**.ras*) can be converted into an absorbance (*A*) spectrum (**.abs*) via the Beer-Lambert law,[3] which states that $T = 10^{-A}$. Thus,

$$\log (1/example.ras) = example.abs$$

However, whereas absorbance band intensities are proportional to the concentration of the species of interest in the case of transmittance measurements (according to Beer's law, $A = abC$, where A is absorbance, a is molar absorptivity in L/(mol×cm), b is path length in cm, and C is concentration in mol/L[3]), for a reflection spectrum, absorbance increases exponentially with increasing concentration. Therefore, a different mathematical operation is required to make band intensities directly proportional to the species concentration. This transformation is known as the Kubelka-Munk (K-M function), which converts **.ras* files to **.drt* files:

$$\text{K-M function } (example.ras) = example.drt$$

Appendix B: Software

B.1 Macro Programs

After the sample is loaded, the instrument is purged, and the heating program is specified, the operator launches *samcol_2.mac* (Appendix B.2) from the computer. On prompt, the operator specifies the data collection file name and the number of spectra to collect. At this point, the computer takes over and controls the operation of the spectrometer and the temperature controller. The macro *samcol_2.mac* creates a new data folder and files to store temperature and time information (\samtemps and \samtimes, respectively) and then calls the program *avrg_pid.exe* (Appendix B.3) to set the PID parameters (previously determined experimentally) on the temperature controller to optimize the power output for best correlation with the specified heating ramp. Immediately after this, the macro signals the temperature controller via *ramp_st.exe* (Appendix B.4) to begin the pre-programmed heating ramp.

After the heating program is initiated, the macro *Samcol_2.mac* starts a timer and records time zero to "\samtimes," writes the current temperature into "\samtemps" by accessing the temperature controller (using the program *rd_pv.exe* provided in Appendix B.5), and then directs the FTIR spectrometer to begin scanning. After the specified number of scans have been collected and signal averaged, the interferogram file is stored on the computer and another set of time and temperature values are recorded. Thus, time and temperature measurements are recorded by the macro before and after each new spectrum is collected. This loop is repeated *n* times (where *n* represents the number of spectra specified by the operator).

After data collection, the *samcol_2.mac* macro processes the files \samtimes and \samtemps by executing *samdata.exe* (Appendix B.6). The "before and after" temperature and time values collected for each spectrum are averaged, respectively, to obtain a temperature and time for each spectrum. The program records this information (spectrum number, average time, and average temperature for each scan) into a file named *samdata.txt*.

Here is an example of *samdata.txt* content:

1, 0.525000, 27.900002

2, 1.533333, 33.700001

3, 2.533333, 42.250000

The fist column represents the spectrum number, the second represents the number of minutes elapsed from the start of the experiment, and the last column is the average temperature in °C during data collection. To complete the process, the macro executes *w_spid25.exe* (Appendix B.7) to return the PID parameters and set-point value of the temperature controller back to ambient temperature settings.

B.2 samcol_2.mac

```
# samcol_2.mac = same as samcol.mac plus
# automatically starts Ramp Program1 on Eurotherm TC, and adjusts PID

let c 0
let s s_0

clrscr
comment PROGRAM FOR COLLECTING VT-DRIFTS SAMPLE SPECTRA
comment
comment     USING EUROTHERM TEMPERATURE CONTROLLER
label begin
comment
```

```
comment Enter the sample data storage name
enter a
comment
label getigms
exist &a\s_1.igm
if &z = 0
goto igmask
comment Sample spectra exist in &a directory
ask Do you want to overwrite? (Y/N)
goto askquit
goto igmask2

label askquit
ask Do you want to quit? (Y/N)
goto begin
exit

label igmask
dos mkdir &a
label igmask2
comment
comment Enter the number of sample spectra to collect
enter R

label start
# comment Initalizing - - Please Wait
mattscan parm=c:\first\macros\scanparm.dat actions=iq quiet=1
comment SAMPLE SCAN TEMPERATURES > &a\samtemps
comment SAMPLE SCAN TIMES (min) > &a\samtimes
# mattscan parm=c:\first\macros\scanparm.dat actions=iq quiet=1

# clrscr
system avrg_pid.exe
comment
comment Press the ENTER key to start data acquisition
enter e
system ramp_st.exe

timerStart
label loop
increment s
increment c
timerCheck
let B &z
system rd_pv.exe &a\samtemps
# mattscan parm=c:\first\macros\scanparm.dat actions=iq quiet=1
```

```
mattscan parm=c:\first\macros\scanparm.dat actions=sq file=&a\&s irdatatype=igm
quiet=1
system rd_pv.exe &a\samtemps
#
timerCheck
let A &z
+ &A &B
/ &z 120
comment >> &a\samtimes
comment &c , &z >> &a\samtimes
if &c < &R
goto loop
system samdata.exe &a
system w_spid25.exe
comment
```

B.3 avrg_pid.exe

```
// Part of Samcol_2 macro, works with
// Eurotherm Temperature Controller
//
// Program function:
// Adjusts PID parameters to the average good values
// determined experimentally for the range from 25C to 500C
// (Pb = 2.6, ti = 0.6, td = 0.1)
//
// 9/7/12 DKM

#include <bios.h>
#include <conio.h>
#include <ctype.h>
#include <dos.h>
#include <math.h>
#include <stdio.h>
#include <stdlib.h>
#include <string.h>
#include <time.h>

#define COM1            0
#define COM2            1
#define DATA_READY      0x100
#define STX    0x02
#define ETX    0x03
#define EOT    0x04
#define ENQ    0x05
```

```
#define ACK   0x06
#define NAK   0x15
#define TRUE 1
#define FALSE          0

#define SETTINGS    (0xE0 | 0x02 | 0x18 | 0x00)

float timer(void);
char mk_BCC_checksum(char *c_code);

char *r_str;
int status, n_retry = 0;

int main (void)
{
char *r_str, *send_str(), xx_strng[5], wt_xx[100], BCC;
float xx_val;

status = bioscom(0, SETTINGS, COM2);     /* set serial port parameters */

// Set and send Proportional band Pb
xx_val = 2.6;
sprintf (xx_strng, "%1.3f", xx_val);
sprintf (wt_xx, "XP%s%c", xx_strng, ETX);
BCC = mk_BCC_checksum(wt_xx);
sprintf (wt_xx, "%c0000%cXP%s%c%c", EOT, STX, xx_strng, ETX, BCC);
r_str = send_str(wt_xx);
printf ("\n Pb = %s", xx_strng);

// Set and send Integral time ti
xx_val = 0.6;
sprintf (xx_strng, "%1.3f", xx_val);
sprintf(wt_xx, "TI%s%c", xx_strng, ETX);
BCC = mk_BCC_checksum(wt_xx);
sprintf (wt_xx, "%c0000%cTI%s%c%c", EOT, STX, xx_strng, ETX, BCC);
r_str = send_str(wt_xx);
printf (" ti = %s\n", xx_strng);

return 0;
}

// The following subroutine includes steps for troubleshooting
// possible serial port communication errors

char *send_str(char *code)
{
```

```
char c, in_mesg[100];
int i, j, in, out, status, DONE, SAVE;
int count, reset;
float start_time, cur_time;

count = 0;
reset = 0;

com_loop:
   if(count > 5 && reset < 2)
          {
          reset++;
          count = 0;
          printf ("\nCount > 10.  Resetting serial port parameters.");
          status = bioscom(0, SETTINGS, COM2);     /* set serial port parameters */
          }

   if(count > 11)
          {
          printf ("\nTIMEOUT\n");
          printf ("\nstatus = %x", status);
          printf ("\nsent string = %s", code);
          printf ("\nsent string = ");
          i = 0;
          while((c = code[i++]) != '\0')
                    printf("%c", code[i]);
          leave();
          }

status = bioscom(3, 0, COM2);
while ((status & DATA_READY) != 0)        // clear out receive buffer
          {
          status = bioscom(2, 0, COM2);
          }

i = 0;
while((c = code[i++]) != '\0')
          {
     status = bioscom(1, c, COM2);
          }

status = 0;
j = 0;
DONE = FALSE;
SAVE = FALSE;
```

```
start_time = timer(); // used to determine timeout condition

while((status & DATA_READY) == 0) // check for input data
        {
        status = bioscom(3, 0, COM2);
        cur_time = timer();
        if ((cur_time - start_time) > 10)
                {
                count++;
                n_retry++;

                printf ("\nCP4 message sent to TC: %s", code);
        printf ("\nCount: %d.  Retry No.  %d.  Status: %d", count, n_retry, status);
                goto com_loop;          // timeout - resend command
                }
        }

while(!DONE)
        {
        status = bioscom(3, 0, COM2);
        if(status & DATA_READY)
        if((out = bioscom(2, 0, COM2) & 0x7f) != 0)
                        {
                        if((out & 0x7f) == ETX)
                                {
                                DONE = TRUE;
                                out = bioscom(2, 0, COM2);
                                break;
                                }
                        if(SAVE == TRUE)
                                in_mesg[j++] = out & 0x7f;
                        if((out & 0x7f) == 'V')
                                SAVE = TRUE;
                        if((out & 0x7f) == ACK)
                                {
                                DONE = TRUE;
                                }
                        }
        if ((status & DATA_READY) == 0)
                {
                start_time = timer(); // used to determine timeout condition
                while((status & DATA_READY) == 0)       // check for input data
                        {
                        status = bioscom(3, 0, COM2);
                        cur_time = timer();
                        if ((cur_time - start_time) > 10)
```

```
                                {
                                count++;
                                n_retry++;
        printf ("\nCP6 no response from TC for more than 10sec");
        printf ("\nCount: %d.  Retry No.  %d.  Status: %d", count, n_retry, status);
                                goto com_loop;          // timeout - resend command
                                }
                        }
                }
        }

in_mesg[j] = '\0';
return(in_mesg);

}

char mk_BCC_checksum(char *c_code)
{
int i;
char BCC;

   BCC = (c_code[0] ^ c_code[1]);
   for (i = 2; c_code[i] != '\0'; i++)
   {
      BCC = (BCC ^ c_code[i]);
   }
        return(BCC);
}

float timer()
{
   struct time t;
   float time_sec;

   gettime(&t);
   time_sec = (float) t.ti_hour * 3600 + (float) t.ti_min * 60 + (float) t.ti_sec + (float)
t.ti_hund / 100;
   return(time_sec);
}

int leave (void)          // Exit the program
{
printf ("\nNumber of COM Retries = %d\n", n_retry);
printf ("\npress any key to exit");
getch();
exit(1);// exit program
```

```
return;
}
```

B.4 ramp_st.exe

```
// Eurotherm Temperature Controller
//
// Program function: Start the heating ramp program
//
// DKM 05/12

#include <bios.h>
#include <stdio.h>
#include <conio.h>
#include <ctype.h>

#define COM1            0
#define COM2            1
#define DATA_READY      0x100
#define STX   0x02
#define ETX   0x03
#define EOT   0x04
#define ENQ   0x05
#define ACK   0x06
#define NAK   0x15
#define TRUE 1
#define FALSE           0

#define SETTINGS    (0xE0 | 0x02 | 0x18 | 0x00)

int mk_BCC_checksum(char *c_code);
int BCC;

int main(void)
{
char *r_str, rd_sl[100], wt_sl[100], wt_sl_BCC[100], *send_str(), sl_strng[5];
int status, sl_val;
char BCC_ch;

status = bioscom(0, SETTINGS, COM2);     /* set serial port parameters */

sprintf (sl_strng, "0002");
   fflush (stdin);
```

```
// Calculate checksum (BCC)
   sprintf(wt_sl_BCC, "OS>%s%c", sl_strng, ETX);
   mk_BCC_checksum(wt_sl_BCC);
   BCC_ch = toascii(BCC);

// Send command to set the setpoint
   sprintf(wt_sl, "%c0000%cOS>%s%c%c", EOT, STX, sl_strng, ETX, BCC_ch);
   r_str = send_str(wt_sl);
   printf("\n%s", r_str);

return 0;
}

char *send_str(char *code)
{
char c, in_mesg[100];
int i, j, in, out, status, DONE, SAVE;

i = 0;
while((c = code[i++]) != '\0')
        {
     status = bioscom(1, c, COM2);
         }

j = 0;
DONE = FALSE;
SAVE = FALSE;
while(!DONE)
        {
        status = bioscom(3, 0, COM2);
        if(status & DATA_READY)
        if((out = bioscom(2, 0, COM2) & 0x7f) != 0)
                        {
                        if((out & 0x7f) == ETX)
                                {
                                DONE = TRUE;
                                out = bioscom(2, 0, COM2);
                                break;
                                }
                        if(SAVE == TRUE)
                                in_mesg[j++] = out & 0x7f;
                        if((out & 0x7f) == 'L')
                                SAVE = TRUE;
                        if((out & 0x7f) == ACK)
                                {
```

```
                                DONE = TRUE;
                                }
                        }
        }
in_mesg[j] = '\0';
return(in_mesg);

}

int mk_BCC_checksum(char *c_code)
{
int i;

   BCC = (c_code[0] ^ c_code[1]);
   for (i = 2; c_code[i] != '\0'; i++)
   {
      BCC = (BCC ^ c_code[i]);
   }

return 0;
}
```

B.5 rd_pv.exe

```
// Read current temp (process value) from Eurotherm TC
// Print value to screen & to file passed via argc

#include <bios.h>
#include <conio.h>
#include <ctype.h>
#include <dos.h>
#include <math.h>
#include <stdio.h>
#include <stdlib.h>
#include <string.h>
#include <time.h>

#define COM1            0
#define COM2            1
#define DATA_READY      0x100
#define STX    0x02
#define ETX    0x03
#define EOT    0x04
#define ENQ    0x05
#define ACK    0x06
```

```
#define NAK  0x15
#define TRUE 1
#define FALSE          0

#define SETTINGS    (0xE0 | 0x02 | 0x18 | 0x00)

int status, n_retry = 0;
char filename[100];
float timer(void);

main (argc, argv)
int argc;
char *argv[];

{
char *r_str, rd_pv[100], *send_str();
FILE *fp, *fopen();

strcpy(filename, argv[1]);
fp = fopen(filename, "a+");
status = bioscom(0, SETTINGS, COM2);      /* set serial port parameters */
sprintf(rd_pv, "%c0000PV%c", EOT, ENQ);
r_str = send_str(rd_pv);
printf("%s\n", r_str);
fprintf(fp,"%s\n", r_str);
fclose(fp);
return 0;
}

// The following subroutine includes steps for troubleshooting
// possible serial port communication errors

char *send_str(char *code)
{
char c, in_mesg[100];
int i, j, in, out, status, DONE, SAVE;
int count, reset;
float start_time, cur_time;

count = 0;
reset = 0;

com_loop:
   if(count > 5 && reset < 2)
         {
         reset++;
```

```
            count = 0;
            printf ("\nCount > 10.  Resetting serial port parameters.");
            status = bioscom(0, SETTINGS, COM2);     /* set serial port parameters */
            }

    if(count > 11)
            {
            printf ("\nTIMEOUT\n");
            printf ("\nstatus = %x", status);
            printf ("\nsent string = %s", code);
            printf ("\nsent string = ");
            i = 0;
            while((c = code[i++]) != '\0')
                    printf("%c", code[i]);
            leave();
            }

status = bioscom(3, 0, COM2);
while ((status & DATA_READY) != 0)        // clear out receive buffer
            {
            status = bioscom(2, 0, COM2);
            }

i = 0;
while((c = code[i++]) != '\0')
            {
      status = bioscom(1, c, COM2);
            }

status = 0;
j = 0;
DONE = FALSE;
SAVE = FALSE;

start_time = timer(); // used to determine timeout condition

while((status & DATA_READY) == 0) // check for input data
            {
            status = bioscom(3, 0, COM2);
            cur_time = timer();
            if ((cur_time - start_time) > 10)
                    {
                    count++;
                    n_retry++;
                    printf ("\nCP4 message sent to TC: %s", code);
            printf ("\nCount: %d.  Retry No.  %d.  Status: %d", count, n_retry, status);
```

```
                goto com_loop;          // timeout - resend command
                }
        }

while(!DONE)
        {
        status = bioscom(3, 0, COM2);
        if(status & DATA_READY)
        if((out = bioscom(2, 0, COM2) & 0x7f) != 0)
                        {
                        if((out & 0x7f) == ETX)
                                {
                                DONE = TRUE;
                                out = bioscom(2, 0, COM2);
                                break;
                                }
                        if(SAVE == TRUE)
                                in_mesg[j++] = out & 0x7f;
                        if((out & 0x7f) == 'V')
                                SAVE = TRUE;
                        if((out & 0x7f) == ACK)
                                {
                                DONE = TRUE;
                                }
                        }
        if ((status & DATA_READY) == 0)
                {
                start_time = timer(); // used to determine timeout condition
                while((status & DATA_READY) == 0)       // check for input data
                        {
                        status = bioscom(3, 0, COM2);
                        cur_time = timer();
                        if ((cur_time - start_time) > 10)
                                {
                                count++;
                                n_retry++;
        printf ("\nCP6 no response from TC for more than 10sec");
        printf ("\nCount: %d.  Retry No.  %d.  Status: %d", count, n_retry, status);
                                goto com_loop;          // timeout - resend command
                                }
                        }
                }
        }
in_mesg[j] = '\0';
return(in_mesg);
}
```

```
float timer()
{
   struct time t;
   float time_sec;

   gettime(&t);
   time_sec = (float) t.ti_hour * 3600 + (float) t.ti_min * 60 + (float) t.ti_sec + (float)
t.ti_hund / 100;
   return(time_sec);
}

int leave (void)          // Exit the program
{
printf ("\nNumber of COM Retries = %d\n", n_retry);
printf ("\npress any key to exit");
getch();
exit(1);// exit program
return;
}
```

B.6 samdata.exe

```
#include <stdio.h>
#include <stdlib.h>

main (argc, argv)
int argc;
char *argv[];
{
char c, str[100], dirname[100], timename[100], tempname[100], dataname[100];
int i, n, num;
float stime, b_temp, e_temp, avetemp;
FILE *time, *temp, *data, *s_temps, *fopen();

strcpy(dirname, argv[1]);
strcpy(timename, dirname);
strcpy(tempname, dirname);
strcpy(dataname, dirname);
strcpy(str, dirname);
strcat(timename, "/REFTIMES");
strcat(tempname, "/REFTEMPS");
strcat(dataname, "/REFDATA.txt");
strcat(str, "/ra_temps.txt");
```

```
time = fopen(timename, "rt");
temp = fopen(tempname, "rt");
data = fopen(dataname, "wt");
s_temps = fopen(str, "wt");

fscanf(time, "REFERENCE SCAN TIMES (min)\n\n");
fscanf(temp, "REFERENCE SCAN TEMPERATURES\n");
while (1==1)
        {
        if ((fscanf(time, "%d %f\n\n", &num, &stime)) != 2)
                break;
        fscanf(temp, "%f\n", &b_temp);
        fscanf(temp, "%f\n", &e_temp);
        avetemp = (b_temp + e_temp)/2;
        fprintf(data, "%d, %f, %f\n", num, stime, avetemp);
        fprintf(s_temps, "%f\n", avetemp);
        printf("%d %f %f\n", num, stime, avetemp);
        }
fclose(data);
fclose(s_temps);
return;
}
```

B.7 w_spid25.exe

```
// Works with
// Eurotherm Temperature Controller
//
// Program function:
// Sets the set-point to 22C (below 25) and adjusts PID parameters accordingly
//
// 9/7/12 DKM

#include <bios.h>
#include <conio.h>
#include <ctype.h>
#include <dos.h>
#include <math.h>
#include <stdio.h>
#include <stdlib.h>
#include <string.h>
#include <time.h>
```

```
#define COM1            0
#define COM2            1
#define DATA_READY      0x100
#define STX   0x02
#define ETX   0x03
#define EOT   0x04
#define ENQ   0x05
#define ACK   0x06
#define NAK   0x15
#define TRUE 1
#define FALSE           0

#define SETTINGS    (0xE0 | 0x02 | 0x18 | 0x00)

float timer(void);
char mk_BCC_checksum(char *c_code);

char *r_str;
int status, n_retry = 0;

int main (void)
{
char *r_str, *send_str(), xx_strng[5], wt_xx[100], BCC;
float PV, xx_val;

status = bioscom(0, SETTINGS, COM2);     /* set serial port parameters */

PV = 22.00;  // set temperature below 25C to ensure 0 power output

// Calculate and send the appropriate Proportional band
xx_val = -0.00000001*PV*PV*PV + .00002*PV*PV - 0.011*PV + 4.3414;
sprintf (xx_strng, "%1.3f", xx_val);
sprintf (wt_xx, "XP%s%c", xx_strng, ETX);
BCC = mk_BCC_checksum(wt_xx);
sprintf (wt_xx, "%c0000%cXP%s%c%c", EOT, STX, xx_strng, ETX, BCC);
r_str = send_str(wt_xx);
printf (" Pb = %s", xx_strng);

// Calculate the appropriate Integral time ti and send
xx_val = .000004*PV*PV - 0.0026*PV + .9099;
sprintf (xx_strng, "%1.3f", xx_val);
sprintf(wt_xx, "TI%s%c", xx_strng, ETX);
BCC = mk_BCC_checksum(wt_xx);
sprintf (wt_xx, "%c0000%cTI%s%c%c", EOT, STX, xx_strng, ETX, BCC);
r_str = send_str(wt_xx);
printf (" ti = %s\n", xx_strng);
```

```
// Set temperature to 22C
sprintf (xx_strng, "%2.2f", PV);
sprintf (wt_xx, "SL%s%c", xx_strng, ETX);
BCC = mk_BCC_checksum(wt_xx);
sprintf (wt_xx, "%c0000%cSL%s%c%c", EOT, STX, xx_strng, ETX, BCC);
r_str = send_str(wt_xx);
printf ("\nSetpoint: %s", xx_strng);

return 0;
}

// The following subroutine includes steps for troubleshooting
// possible serial port communication errors

char *send_str(char *code)
{
char c, in_mesg[100];
int i, j, in, out, status, DONE, SAVE;
int count, reset;
float start_time, cur_time;

count = 0;
reset = 0;

com_loop:
   if(count > 5 && reset < 2)
         {
         reset++;
         count = 0;
         printf ("\nCount > 10.  Resetting serial port parameters.");
         status = bioscom(0, SETTINGS, COM2);     /* set serial port parameters */
         }

   if(count > 11)
         {
         printf ("\nTIMEOUT\n");
         printf ("\nstatus = %x", status);
         printf ("\nsent string = %s", code);
         printf ("\nsent string = ");
         i = 0;
         while((c = code[i++]) != '\0')
                  printf("%c", code[i]);
         leave();
         }
```

```
status = bioscom(3, 0, COM2);
while ((status & DATA_READY) != 0)        // clear out receive buffer
        {
        status = bioscom(2, 0, COM2);
        }
i = 0;
while((c = code[i++]) != '\0')
        {
    status = bioscom(1, c, COM2);
        }
status = 0;
j = 0;
DONE = FALSE;
SAVE = FALSE;
start_time = timer(); // used to determine timeout condition
while((status & DATA_READY) == 0) // check for input data
        {
        status = bioscom(3, 0, COM2);
        cur_time = timer();
        if ((cur_time - start_time) > 10)
                {
                count++;
                n_retry++;
                printf ("\nCP4 message sent to TC: %s", code);
        printf ("\nCount: %d.  Retry No.  %d.  Status: %d", count, n_retry, status);
                goto com_loop;          // timeout - resend command
                }
        }

while(!DONE)
        {
        status = bioscom(3, 0, COM2);
        if(status & DATA_READY)
        if((out = bioscom(2, 0, COM2) & 0x7f) != 0)
                        {
                        if((out & 0x7f) == ETX)
                                {
                                DONE = TRUE;
                                out = bioscom(2, 0, COM2);
                                break;
                                }
                        if(SAVE == TRUE)
                                in_mesg[j++] = out & 0x7f;
                        if((out & 0x7f) == 'V')
                                SAVE = TRUE;
                        if((out & 0x7f) == ACK)
```

```
                                {
                                DONE = TRUE;
                                }
                        }
        if ((status & DATA_READY) == 0)
                {
                start_time = timer(); // used to determine timeout condition
                while((status & DATA_READY) == 0)       // check for input data
                        {
                        status = bioscom(3, 0, COM2);
                        cur_time = timer();
                        if ((cur_time - start_time) > 10)
                                {
                                count++;
                                n_retry++;
        printf ("\nCP6 no response from TC for more than 10sec");
        printf ("\nCount: %d.  Retry No.  %d.  Status: %d", count, n_retry, status);
                                goto com_loop;          // timeout - resend command
                                }
                        }
                }
        }

in_mesg[j] = '\0';
return(in_mesg);
}
char mk_BCC_checksum(char *c_code)
{
int i;
char BCC;
   BCC = (c_code[0] ^ c_code[1]);
   for (i = 2; c_code[i] != '\0'; i++)
   {
      BCC = (BCC ^ c_code[i]);
   }
return(BCC);
}
float timer()
{
   struct time t;
   float time_sec;
   gettime(&t);
   time_sec = (float) t.ti_hour * 3600 + (float) t.ti_min * 60 + (float) t.ti_sec + (float)
t.ti_hund / 100;
   return(time_sec);
}
```

```
int leave (void)          // Exit the program
{
printf ("\nNumber of COM Retries = %d\n", n_retry);
printf ("\npress any key to exit");
getch();
exit(1);// exit program
return;
}
```

B.8 nproc2-1.mac

```
let c 0
clrscr

comment PROGRAM FOR PROCESSING VT-DRIFTS SAMPLE SPECTRA
comment References all data to s_1 in the Ref Data Folder
comment
comment Enter the directory name used for sample data storage
enter a
comment Enter the directory name used for reference data
enter r
comment

dos mkdir &a\nproc2-1
open 1 &a\sa_temps.txt
open 2 &r\ra_temps.txt

label loop
eof 1
if &z = 1
goto end

# This portion of the code can be unlocked to process Variable Temperature Data
# by rationing to corresponding Variable Temperature References
# instead of to a single reference spectrum collected at ambient
# let t 0
# let j 0
# let s 0
# input 1 t
# rewind 2
# let j 0
# label iloop
# eof 2
# if &z = 1
# goto end
```

```
# input 2 s
# increment j
# if &s <= &t
# goto iloop
# decrement j
# if &j <= 0
# let j 1

increment c
exist &a\s_&c.igm
if &z = 0
goto end
mattproc parms=c:\first\macros\procparm.dat s=&a\s_&c.igm r=&r\s_1.big
load &a\s_&c.ras
ras2abs
# show
save &a\nproc2-1\s_&c.abs
goto loop
label end
close 1
close 2
dos del &a\*.ras
```

Appendix C: Dimensions of the Optical Components

C.1 Losses at the transition from mirror (3) to the beamsplitter

For the system under investigation, the diameter of the collimated beam is ~ 3 in (based on the dimensions of mirror (3)), and the diameter of the beamsplitter opening is ~ 2.75 in. Projected areas A_p of the beam before and after the beamsplitter can be determined from the equation

$$A_p = A \times \cos(\theta) \tag{C.1.1}$$

where A is the area viewed from normal, A_p is the projected area, and θ is the angle between the line of observation and the normal.[4]

For mirror (3), width $d_1 = 3.312_5$ in, height $d_2 = 2.375$ in, and $\theta = 45°$. Cross-sectional area of the beam projected from mirror (3) onto the beamsplitter is estimated to be:

$$A_{p\,\mathrm{M3}} = \pi\, r_1\, r_2 \cos(\theta) = 6.179 \text{ in}^2 \times \cos(\theta) = 4.369 \text{ in}^2 \tag{C.1.2}$$

For the beamsplitter (4a), diameter = 2.75 in, $\theta = 45°$. Surface area of the beamsplitter is estimated to be

$$A_{4a} = \pi\, r^2 = 5.940 \text{ in}^2 \tag{C.1.3}$$

The area projected by the beamsplitter towards mirror (3) is less because the beamsplitter is positioned at a 45° angle relative to the incident beam, and is estimated to be:

$$A_{p\,4a} = A_{4a} \cos(\theta) = 4.200 \text{ in}^2 \tag{C.1.4}$$

The maximum fraction of radiation transferred from mirror (3) to the beamsplitter is estimated by:

$$A_{p\,4a} / A_{p\,M3} = 4.200\ \text{in}^2 / 4.369\ \text{in}^2 = 0.9600 = 96.00\% \qquad \text{(C.1.5)}$$

Thus, only ~ 96% of the beam from mirror (3) enters the interferometer (4) due to the limiting diameter of the beamsplitter.

C.2 Geometrical factors between the interferometer and mirror (5)

The diameter of the apertures connecting the front and rear instrument compartments is ~ 3.00 in. The area of the apertures viewed from normal is $\pi r^2 = 7.07$ in.

For mirror (5), width $d_1 = 4.125$ in, height $d_2 = 3.00$ in, and $\theta = 45°$. The projected area of mirror (5) from the beamsplitter is estimated to be:

$$A_{p\,M5} = \pi\, r_1\, r_2 \cos(\theta) = 9.72\ \text{in}^2 \times \cos(\theta) = 6.87\ \text{in} \qquad \text{(C.2.1)}$$

The projected area of the mirrors far exceeds the projected area of the collimated beam from (4), which is limited by the beamsplitter diameter: $A_{p\,4a} = 4.20\ \text{in}^2$.

C.3 Focal length and solid angle of mirrors (5) and (7)

Because (5) and (7) are F/1 mirrors, for each the focal length f equals the effective diameter D. Because the beam is reflected at a 45° in the horizontal plane, D = width of (5) = width of (7) = 4.125 in. The location of the 45° off-axis focal point of (5) and (7) can be calculated using the Pythagorean theorem:

$$l = (2f^2)^{1/2} = (2 \times 4.13^2)^{1/2} = 5.83\ \text{in} \qquad \text{(C.3.1)}$$

The solid angle Ω of the beam from (5) is calculated by

$$\Omega_{M5} = A_p / l^2 = 4.20\ \text{in}^2 / (5.83\ \text{in})^2 = 0.124\ \text{sr} \qquad \text{(C.3.2)}$$

C.4 Geometrical factors between mirror (7) and the detector

Radiation incident to mirror (5) is a collimated beam with a cross-sectional diameter ~ 4.20 in (determined by the beamsplitter diameter). Mirrors (5) and (7) are positioned so that they share a focal point, which means that the beam reflected from mirror (5) onto (7) has the same projected area and becomes collimated by mirror (7) after reflection.

Thus, the projected area of the beam traveling from (7) to the detector is ~ 4.20 in^2, and therefore it is not obstructed by the aperture between the front and rear of the instrument.

For mirror (8), width $d_1 = 3.3187_5$ in, height $d_2 = 2.50$ in, and $\theta = 45°$. The area of mirror (8) viewed from (7) is estimated by:

$$A_{p\,M8} = \pi\, r_1\, r_2 \cos(\theta) = 6.26 \text{ in}^2 \times \cos(\theta) = 4.43 \text{ in}^2 \qquad \text{(C.4.1)}$$

Thus, mirror (8) does not restrict the beam reflected to the detector.

C.5 Geometrical factors between mirrors (5) and (6-1)

The area of the mirror (6-1) $A_{(6\text{-}1)} \approx 1 \text{ in} \times 1 \text{ in} = 1 \text{ in}^2$, $\theta = 45°$. The distance from (5) to (6-1) is $l = 4.40$ in. The 45° off-axis focal point of (5) lies behind (6-1) at a distance of:

$$5.83 \text{ in} - 4.40 \text{ in} = 1.43 \text{ in} \qquad \text{(C.5.1)}$$

The projected area A_p subtended by the solid angle Ω_{M5} at $l = 1.43$ in from the off-axis focal point of (5) is:

$$A_p = \Omega_{M5} \times l^2 = 0.124 \text{ sr} \times (1.43 \text{ in})^2 = 0.254 \text{ in}^2 \qquad \text{(C.5.2)}$$

The area of mirror (6-1) viewed from the off-axis focal point of mirror (5) is:

$$A_{p\,M(6\text{-}1)} = A \times \cos(\theta) = 1\ \text{in}^2 \times \cos(45°) = 0.707\ \text{in}^2 \qquad \text{(C.5.3)}$$

Thus, mirror (6-1) is large enough to capture the solid angle from mirror (5) Ω_{M5} = 0.124 sr, as determined in Appendix C.3.

C.6 Geometrical factors between mirrors (6-1), (6-2), and (6-3)

The area of mirror (6-2) $A_{(6\text{-}2)} \approx 1$ in × 2 in = 2 in^2, $\theta = 45°$. The distance from (6-1) to (6-2) is ~ 3.66 in. This means that the focal point is between (6-1) and (6-2). The distance from the focal point to (6-2) is 3.66 in – 1.43 in = 1.23 in, which is smaller than the distance from (6-1) to the focal point. This means that the beam projected onto (6-2) is smaller than the area projected onto (6-1), and the solid angle is conserved. No losses are expected at mirror (6-2) due to the dimensions of the mirror.

After mirror (6-2), the beam irradiates the ellipsoid mirror (6-3). The distance between (6-2) and (6-3) is ~ 6.625 in, and from the focal point to (6-3) the distance is ~ 8.85 in. The Ω_{M5} is conserved, and the area of the beam projected onto (6-3) is A_p = Ω_{M5} × (8.85 in)^2 = 0.124 sr × (8.85 in)^2 = 9.71 in^2. It is difficult to determine precisely whether the ellipsoid mirror is large enough to capture the entire beam, but it seems reasonable to expect that the DRA was designed to capture the entire beam. Assuming that the beam has a circular projected area, the projected diameter of the beam at (6-3) is ~ $D = ((A_p \times 4)/\pi)^{1/2}$ = 3.52 in, which is smaller than the apparent diameter of mirror (6-3).

Appendix D: scale.mac

```
int choice
int done
done = 0
while (done == 0)
{
choice = menu "drt;abs;ras;bkg;big;sbm;igm"
if(choice == 1)
        e = ".drt"
else if (choice == 2)
        e = ".abs"
else if (choice == 3)
        e = ".ras"
else if (choice == 4)
        e = ".bkg"
else if (choice == 5)
        e = ".big"
else if (choice == 6)
        e = ".sbm"
else if (choice == 7)
        e = ".igm"
done = 1
}
enter w "Enter wavenumber to use for scaling"
enter n "Enter number of files to scale"

dos mkdir "scaled"
fopen 1 "scaled\info.txt"

c = 1
f = buildstring "s_" c e
exist f
if (z == 0)
        exit
load f
v = value w
fprint 1 "Spectra scaled to value of y at" w "cm-1 in" f
fprint 1 "At" w "cm-1, y =" v

for c = 1 to n step 1
   begin
        f = buildstring "s_" c e
        h = buildstring "scaled\s_" c e
        load f
        value w
```

```
        g = v/z
        scale g
        save h
    end
fclose 1
closeallwindows
```

Appendix E: Baseline Offset. slope.mac

```
int choice
int done
float slope
slope = 0
done = 0
while (done == 0)
{
choice = menu "drt;abs;ras;bkg;big;sbm;igm"
if(choice == 1)
        e = ".drt"
else if (choice == 2)
        e = ".abs"
else if (choice == 3)
        e = ".ras"
else if (choice == 4)
        e = ".bkg"
else if (choice == 5)
        e = ".big"
else if (choice == 6)
        e = ".sbm"
else if (choice == 7)
        e = ".igm"
done = 1
}
if (stringcompare e ".big" || stringcompare e ".igm")
        {
        enter a "Enter starting (smaller) data point"
        enter b "Enter ending (larger) data point"
        }
else
        {
        enter a "Enter starting (smaller) wavenumber"
        enter b "Enter ending (larger) wavenumber"
        }
c = 1
f = buildstring "s_" c e
exist f
if (z == 0)
        exit
n = 1
while (z == 1)
        {
        increment n
```

```
        f = buildstring "s_" n e
        exist f
        }
n = n - 1
s = 1
i = buildstring a b ".txt"
fopen 1 i
fprint 1 e "slope calculated between" a "and" b
for c = 1 to n step 1
   begin
        closeallwindows
        slope = 0
        g = buildstring "s_" c e
        load g
        verbose "on"
        value a
        v = z
        value b
        w = z - v
        slope = w/(b - a)
        verbose "off"
        fprint 1 c slope
   end
fclose 1
closeallwindows
```

References

1. *FIRST™ Macros Fourier Infrared Software Tools User's Manual*, user's manual, Mattson Instruments, Inc.: Madison, WI (1991).

2. James, J.F., *A Student's Guide to Fourier Transforms with Applications in Physics and Engineering*, 3rd ed., Cambridge University Press: New York (2011).

3. Skoog, D.A., F.J. Holler, and S.R. Crouch, *Principles of Instrumental Analysis*, 6th ed., Thompson Brooks/Cole: Belmont, CA (2007).

4. Ingle, J.D. and S.R. Crouch, *Spectrochemical Analysis*, Prentice Hall: New Jersey (1988).